2014

A multi-proxy study of the Palaeocene - Eocene Thermal Maximum in northern Spain

Hayley Manners

PHD

A multi-proxy study of the Palaeocene - Eocene Thermal Maximum in northern Spain

Manners, Hayley

Award date:
2014

Awarding institution:
University of Plymouth

A MULTI-PROXY STUDY OF THE PALAEOCENE – EOCENE THERMAL MAXIMUM IN NORTHERN SPAIN

HAYLEY RACHAEL MANNERS

A thesis submitted to the University of Plymouth in partial fulfilment for the degree of

DOCTOR OF PHILOSOPHY

School of Geography, Earth and Environmental Science

Faculty of Science and the Environment

February 2014

Signed: 

Dated: 4th February 2014

‘Education is the path from cocky ignorance to miserable uncertainty.’

Mark Twain (1835 – 1910)

A MULTI-PROXY STUDY OF THE PALAEOCENE – EOCENE THERMAL MAXIMUM IN NORTHERN SPAIN, HAYLEY RACHAEL MANNERS

At the boundary between the Paleocene and Eocene epochs (ca. 56 Ma) a significant global warming event, termed the Paleocene-Eocene Thermal Maximum (PETM), occurred. Records of this event are characterised by a negative carbon isotope excursion (CIE) which has been associated with the release of thousands of petagrams of isotopically light carbon into the ocean-atmosphere system, initiating changes in the carbon cycle, the climate system, ocean chemistry and the marine and continental ecosystems. The amount of isotopically light carbon that was required to cause the event, its source and the rapidity of its release are, however, are still debated. This study uses $\delta^{13}C_{TOC}$, $\delta^{13}C_{n\text{-alkane}}$, $\delta^{13}C_{CARB}$ and palynological data to evaluate the PETM CIE in terms of the magnitude of the CIE in both continental and marine settings, rapidity of release and drawdown of carbon, and mobilisation of different organic matter (OM) pools as a response to the climate change. The sections studied span a continental to marine transect in northern Spain. This represents the first organic geochemical study of these PETM sections, one of the first comparisons of CIE magnitude between continental and marine sections within the same sediment routing system, and one of the first comparisons of the same OM proxies within different depositional environments. The data suggest that different OM pools were mobilised in response to the PETM, with reworking of older material, soil residence times, and contemporaneous vegetation all contributing. CIE profile shapes predominantly suggest a rapid onset and recovery from the event. The magnitude of the CIE was also assessed. The current resolution of the data suggests that the differences between continental and marine CIE magnitudes could be minimal within a single sediment routing system, perhaps establishing a realistic CIE magnitude for the PETM, for use in future modelling scenarios.

CONTENTS

LIST OF FIGURES AND PLATES

LIST OF TABLES

ACKNOWLEDGEMENTS

I owe a lot of people a massive thank you in this section for their support, encouragement, and inspiration throughout my PhD. To start with, I would like to say a huge thank you to my Director of Studies, Dr Steve Grimes, who has always encouraged, directed and brainstormed with me to achieve my goals. At times when I have got excited and possibly gone off on a tangent, Steve has always known how to tactfully put me back on the right path without causing upset. I consider him a good friend with a great sense of humour and he is a constant source of support. At this point I would also like to thank Steve's inquisitorial squad (Lily Grimes), for her motivational ice cream breaks and constant concern as to how my "book writing" is going. You make quite the team! Second, I would like to say a massive thank you to my second supervisor, Dr Paul Sutton, without whom this project wouldn't have been possible. At times when things have seemed impossible, he motivated me and helped me arrive at logical solutions, as well as making lab work much more fun. Paul has also become a very good friend, and through means of coffee breaks (and the occasional beer) has been an understanding and inspirational fountain of knowledge. I couldn't have asked for kinder, more understanding and supportive first and second supervisors, and I feel extremely lucky to have worked with them both. I would also like to thank Prof. Malcolm Hart, not only for his thoughts and near-instantaneous feedback on work (!), but also for sharing his office – it has been motivational and fun, and Prof. Richard Twitchett for his detailed comments and ideas throughout the project. Also, whilst not strictly a supervisor, I would like to say a massive thank you to Prof. Rich Pancost, for his constant enthusiasm, energy and ideas. Rich has helped me to structure my arguments, introduced new ideas and has always been more than willing to read and comment on anything I send him at lightning speed! Finally, I would like to say a huge thank you to Kernow Analytical Technology (KAT), in particular Dr Neil Chilcott, for trusting me with T-SEP^{TM}! This equipment was not only a saviour academically where other techniques were unsuccessful, but by working with KAT in a consultancy role it allowed me to fund my write-up year. Neil has also become a very good friend, so I would like to thank him for the academic (and non-academic) advice throughout the last four years. At this point I should therefore also say a big thank you to Frankie Morgan (AKA The Creator), for building, maintaining and upgrading T-SEP^{TM}.

My PhD research was funded by Plymouth University, and as such I would like to thank the University for this opportunity, with particular thanks due to the Centre for Research in Earth Sciences (CRES). From the word go this department has been a fun and friendly department to work in, and I have felt very welcomed and part of the family – I am grateful to have worked with you all. I would also like to thank Prof. Steve Rowland and the petroleum and environmental geochemistry group (PEGG), for allowing me to use their labs throughout my research, and for friendly and informative

discussion. In particular I would like to thank Anthony Lewis for giving me a home throughout my PhD! I will always have very fond memories of 1a Prince Maurice road.

Throughout my research I have been lucky enough to work with a number of external contacts. I would particularly like to thank Drs Laura Domingo, Tom Dunkley Jones and Rob Duller for their support (both monetarily and academically) throughout my field seasons and subsequent paper writing. All three are very knowledgeable, interesting and fun to work with, and I consider them friends. From this work I met Dr Phil Jardine, without whom the palynological aspect of this project would not have been feasible, so I would like to thank him for his assistance, as something that started as a small idea turned into a really interesting part of the project. I would therefore also like to acknowledge the British Geological Survey (BGS) for preparing the palynological samples, and The Society for Organic Petrology (TSOP) for providing a grant for this work. Isotope analyses were carried out at the NERC Isotope Geosciences Laboratory (NIGL; Keyworth) and the Bristol Life Sciences Mass Spectrometry Facility (LSMSF). During my time at NIGL, Prof. Melanie Leng and her colleague Chris Kendrick provided assistance in sample preparation and analysis, and Melanie has also helped in the formulation of papers since. At the LSMSF, Dr Ian Bull and technicians James Williams and Alison Kuhl were always willing to help, and provided assistance whenever necessary. When I was pushed for time they were extremely flexible, and allowed me free reign with the GC-IR-MS, for which I am extremely grateful. I have also been grateful to attend a variety of conferences throughout my PhD, which would not have been possible without the aid of travel grants, so I would like to acknowledge the geochemistry group of the Geological Society of London, and the British mass spectrometry society for funding travel to conferences such as Climate and Biota of the Early Paleogene, and the international meeting on organic geochemistry.

Finally, I owe a huge thank you to my friends and family, who have tolerated my madness throughout, and have believed in me at times when I haven't. First, a big thank you to Mum, Dad and Lewis, for endless chats on the phone and helping me to put things into perspective – it's good to have a non-academic view on things from time to time. Second, to Andy and Debbie, for the afternoon tea breaks and general gossips – I couldn't have asked for better office mates. Also to Andy and Matt for the pranks, banter, and social life – you have made the whole PhD experience a lot more fun. It seems fitting here to also mention our second home, the JSV, for a constant supply of "refreshments" and friendliness. Last but by no means least, I probably owe my biggest thanks to Dan, for keeping me sane throughout the last four years, listening to my worries and ideas at all hours of the day and night, and allowing me to turn the house into a second office.

AUTHORS DECLARATION

At no time during the registration for the degree of Doctor of Philosophy has the author been registered for any other University award without prior agreement of the Graduate Committee. This study was financed with the aid of a studentship from Plymouth University.

Relevant scientific seminars and conferences have been regularly attended during the course of this research and findings have been presented at conferences in the form of oral and poster presentations. Three manuscripts have been prepared for publication, one of which has been published in a peer reviewed journal, and two are currently in preparation. During this research, several travel grants were awarded by the Geological Society of London Geochemistry Group and the British Mass Spectrometry Society for travel to conferences, and a grant for palynological sample preparation was awarded by The Society for Organic Petrology.

Peer reviewed publications:

PEER REVIEWED PUBLICATIONS

Manners, H.R., Grimes, S.T., Sutton, P.A., Domingo, L., Leng, M.J., Twitchett, R.T., Hart, M.B., Dunkley Jones, T., Pancost, R.D., Duller, R., Lopez-Martinez, N. 2013. Magnitude and profile of organic carbon isotope records from the Palaeocene–Eocene Thermal Maximum: evidence from northern Spain. Earth and Planetary Science Letters 376, 220-230.

Belt, S. T., Vare, L. L., Massé, G., Manners, H. R., Price, J. C., MacLachlan, S. E., Andrews, J. T., Schmidt, S., 2010. Striking similarities in temporal changes to spring sea ice occurrence across the central canadian arctic archipelago over the last 7000 years. Quaternary Science Reviews 29, 3489-3504.

PUBLICATIONS IN PREPARATION

Manners, H.R., Dunkley Jones, T., Sutton, P.A., Jardine, P.E., Pancost, R.D., Taylor, K.W.R., Domingo, L., Leng, M.J., Hart, M.B., Grimes, S.T., A multi-proxy study of the Zumaia section, northern Spain. In prep.

Manners, H.R., Grimes, S.T., Sutton, P.A., Pancost, R.D., Taylor, K.W.R., Jardine, P.E., Dunkley Jones, T., Domingo, L., Duller, R., Leng, M.J., Hart, M.B., A multi-proxy study of the Claret section, northern Spain. In prep.

PUBLISHED ABSTRACTS

Manners, H.R., Grimes, S.T., Sutton, P.A., Domingo, L., Pancost, R.D., Leng, M.J., Twitchett, R.T., Hart, M.B., Taylor, K.W.R. 2013. An organic geochemical multi-proxy study of the Palaeocene – Eocene Thermal Maximum: Evidence from northern Spain. Organic Geochemistry: Trends for the 21st Century 2, 346-347.

Manners, H.R., Grimes, S.T., Sutton, P.A., Domingo, L., Pancost, R.D., Leng, M.J., Twitchett, R.T., Hart, M.B., Taylor, K.W.R. 2012. An organic geochemical multi-proxy study of the Palaeocene – Eocene Thermal Maximum: Evidence from northern Spain. AGU Fall Meeting, control ID 1480481.

Manners, H.R., Grimes, S.T., Sutton, P.A., Domingo, L., Pancost, R.D., Leng, M.J., Taylor, K.W.R., Twitchett, R.T., Hart, M.B., Lopez-Martinez, N., 2011. A high resolution compound specific carbon isotope study of the PETM in Northern Spain. 25th International Meeting on Organic Geochemistry Abstract Volume, 67.

Manners, H.R., Grimes, S.T., Sutton, P.A., Domingo, L., Pancost, R.D., Leng, M.J., Taylor, K.W.R., Twitchett, R.T., Hart, M.B., Lopez-Martinez, N., 2011. A high resolution compound specific carbon isotope study of the PETM in Northern Spain. Berichte Geol. B.-A., 85 (ISSN 1017-8880) – Climate and Biota of the Early Palaeogene Abstract Volume, 113.

Manners, H.R., Grimes, S.T., Sutton, P.A., Twitchett, R.T., Hart, M.B., Pancost, R.D., Domingo, L., Lopez-Martinez, N., 2010. Understanding the sensitivity of the Earth's climate to CO_2 forcing: comparative organic geochemistry of hyperthermal events. Polish Geological Institute (ISBN 978-83-924869-6-1) – 1st students international geological conference, Krakow, 16th – 19th April, Abstract, 30.

Manners, H.R., Grimes, S.T., Sutton, P.A., Twitchett, R.T., Hart, M.B., Pancost, R.D., Domingo, L., Lopez-Martinez, N., 2010. Understanding the sensitivity of the Earth's climate to CO_2 forcing: comparative organic geochemistry of hyperthermal events. Carbon System Science Geochemistry Group Research in Progress Meeting, London, March 4th.

Presentation and Conferences Attended:

- 26th International Meeting on Organic Geochemistry, Tenerife. **Poster presentation.** September 2013
- British Organic Geochemistry Society (BOGS) conference, Bristol, UK. **Attendance only.** July 2013
- American Geophysical Union Fall Meeting, San Francisco, USA. **Oral presentation** (presented on my behalf by Rich Pancost). December 2012
- Centre for Research in Earth Sciences (CRES), Plymouth, UK. **Research seminar.** May 2012
- Biogeochemistry Research Centre (BGC) annual conference, Plymouth, UK. **Session chair**. December 2011
- Palaeontological Association Annual Meeting, Plymouth, UK. **Poster presentation.** December 2011
- CRES Postgraduate annual conference, Plymouth, UK. **Session chair.** November 2011
- International Meeting on Organic Geochemistry conference, Interlaken, Switzerland. **Oral presentation.** September 2011
- Climate and Biota of the Early Palaeogene conference, Salzburg, Austria. **Poster presentation.** June 2011
- BGC annual conference, Plymouth, UK. **Oral presentation.** December 2010
- 1st CRES Postgraduate annual conference, Plymouth, UK. **Oral presentation.** November 2010
- Palaeo-CO_2 meeting, Bristol, UK. **Poster presentation.** July 2010
- 1st Students International Geological conference, Krakow, Poland. **Poster presentation.** April 2010
- Geochemistry Group Research in Progress Meeting, London, UK. **Oral presentation.** March 2010
- BGC annual conference, Plymouth, UK. **Oral presentation.** December 2009
- Association of Polar Early Career Scientists (APECS) UK Polar Network (UKPN) conference, Plymouth, UK. **Session demonstrator.** October 2009
- British Organic Geochemistry Society (BOGS) conference, Bristol, UK. **Attendance only.** July 2009

External Contacts:

Professor Richard D Pancost
Professor of Biogeochemistry
Organic Geochemistry Unit
University of Bristol

Dr Tom Dunkley Jones
Royal Society Dorothy Hodgkin Research Fellow
School of Geography, Earth and Environmental Sciences
University of Birmingham

Dr Robert Duller
Lecturer in Earth Sciences
School of Environmental Sciences
University of Liverpool

Dr Phillip Jardine
Post-Doctoral Research Associate
Department of Environment, Earth & Ecosystems
The Open University

Dr Laura Domingo
Post-Doctoral Research Associate
Departamento de Ingeniería Geológica.
Universidad Politécnica de Madrid

Professor Melanie J Leng
Professor of Isotope Geosciences
Department of Geology
University of Leicester
And
NERC Isotope Geosciences Laboratory,
Kingsley Dunham Centre,
Keyworth,
Nottingham
NG12 5GG

Dr Kyle W R Taylor
Post-Doctoral Research Associate
Organic Geochemistry Unit
University of Bristol

Word count of main body of thesis: 40,000 words

Signed: 

Date: 4th February 2014

CHAPTER 1

1 INTRODUCTION

1.1 RATIONALE

During the early Palaeogene, carbon cycle perturbations in the form of the catastrophic release of large quantities of carbon into the atmosphere occurred, causing several abrupt transient global hyperthermal events to take place (Zachos *et al.* 2001; 2008). The Palaeocene/Eocene boundary interval (ca. 56 Ma) is characterised by one such hyperthermal event which is termed the Palaeocene – Eocene Thermal Maximum (PETM). This event lasted between 120 – 220 ka (Farley and Eltgroth 2003; Rohl *et al.* 2003, 2007; Aziz *et al.* 2008; Murphy *et al.* 2010) and is considered the most dramatic and rapid global warming event of the Cenozoic (Dunkley Jones *et al.* 2010). The PETM is recorded in sediments from environments as disparate as terrestrial soils and the deep ocean (Bowen *et al.* 2004; Zachos *et al.* 2005; McInerney and Wing 2011). To date, sedimentary records from more than 165 locations have been studied in relation to this event (McInerney and Wing 2011). Current research is driven by the need to constrain the rate, rapidity, and magnitude of isotopically light carbon released, and the mechanisms of carbon release at the onset and drawdown at the termination of the event (Dickens 1995, 2003, 2011; Svensen *et al.* 2004, 2007; Zachos *et al.* 2008; Zeebe *et al.* 2009; Bowen and Zachos 2010; Cui *et al.* 2011; DeConto *et al.* 2012).

In this study the magnitude of the carbon isotope excursion (CIE) associated with the PETM is compared between different depositional environments, and profile shape is assessed in terms of modes of release and potential sequestration mechanisms. Studies of this type may be beneficial in understanding future climate scenarios, given

the current rate of CO_2 release. Understanding past climate events like the PETM may hold the key in determining potential CO_2 impact on the Earth's climate in the next few centuries (Zeebe *et al.* 2011). By studying sedimentary records of the PETM, a better understanding of the Earth system response to such climatic upheaval can be formulated.

1.2 AIMS AND OBJECTIVES

This study has three principle work packages (WPs), which were designed to be independent publications. The aims and objectives of each theme are outlined below.

Work Package 1: Assessment of the CIE using bulk parameters (Chapter 2).

Aims:

1) Study the magnitude and profile shape of PETM CIEs in northern Spain, and compare these between sections within a linked sediment routing system.
2) Evaluate local sedimentary system response to such climatic perturbations.

Objectives and outputs:

To achieve these aims, six sections in northern Spain were chosen for this study. Bulk total organic carbon (TOC) isotope analysis ($\delta^{13}C_{TOC}$) was conducted and the magnitude of the CIE calculated and compared at sites across the region. The onset and recovery of all isotope records were compared to sedimentary features that had previously been linked to the PETM interval, and conclusions drawn as to how the sedimentological system responded to the changing hydrology in the region.

Work Package 2: Evaluation of marine and terrestrial CIEs recorded at a single marine section (Chapter 3).

Aims:

1) Evaluate the magnitude of the CIE as recorded by marine and terrestrial proxies at a single marine section (i.e., Zumaia).
2) Assess likely controls on both magnitude and profile shape of the CIE associated with the PETM at this marine section.

Objectives and outputs:

To achieve these aims, compound specific carbon isotope analysis of *n*-alkanes derived from leaf waxes and bulk carbonate isotopes were measured at the marine section of Zumaia, in order to provide a continental CIE and a marine CIE, respectively. Likely controls on the CIE magnitude and profile shape were assessed using *n*-alkane proxy measurements (carbon preference index; CPI, and odd over even predominance; OEP) and palynological data. This enabled an evaluation of source inputs into the environment and reworking was evaluated via palynological data. Previously published data were also used (e.g., kaolinite data at the Zumaia section; Schmitz and Pujalte 2003) to elucidate reworking and changing source inputs.

Work Package 3: Evaluation of terrestrial CIEs within a linked sediment routing system (chapter 4).

Aims:

1) Compare the magnitude and profile shape of the CIE in the terrestrial and marine realms, as recorded between sections within a linked sediment routing system.

2) Evaluate how regional sedimentary systems respond to such climatic perturbations.
3) Determine whether a change in plant community coincident with the onset of the CIE could be identified, thereby testing the relevance of the theory commonly termed the "plant community change hypothesis" (Smith *et al.* 2007).

Objectives and outputs:

To achieve these aims, compound specific isotope analysis of *n*-alkanes were measured at the continental section of Claret and compared to the *n*-alkane isotope data generated for the Zumaia section, thus allowing the magnitude of the CIE to be compared regionally within one linked sediment routing system. Comparison of the CIE onset using both bulk TOC and *n*-alkane isotope records, combined with CPI, OEP and palynological data, allowed evaluation of how different pools of organic matter were mobilised in relation to the onset of the CIE. The onset and recovery of all isotope excursions were compared to sedimentary features that had previously been linked to the PETM interval, enabling conclusions to be drawn as to how the sedimentological system responded to changing hydrology in the region. Finally, the relative contributions of different palynomorph taxa throughout the Claret and Zumaia sections were compared in combination with the average chain length of extracted *n*-alkanes, to determine if a plant community change was recorded in association with the PETM CIE onset.

1.3 BACKGROUND

Current trends in the Earth's climate suggest that it is gradually moving away from the ice-house world of the last ~34 Ma and into a greenhouse state, a situation which may be exacerbated by the continued release of carbon derived from anthropogenic activity. Studies of palaeoclimate where carbon was rapidly injected into the atmosphere are, therefore, important for understanding the consequences of anthropogenic related carbon emissions in the near future. The PETM is thought to be the most appropriate analogue of the Cenozoic for the rapid injection of carbon into the climate system, and provides insight into how the Earth system responds to rapid carbon cycle perturbation (Dunkley Jones *et al*. 2010). The nature of this event which was, in effect, a greenhouse gas forced period of global warming superimposed upon an already warm world compared to today, has made it the focus of intensive research over the past two decades. It is now clear that this rapid climate perturbation is coincident with biotic extinctions, migrations and turnover, significant shifts in the global hydrological cycle and major transient changes in ocean chemistry (Kennett and Stott 1991; Dickens *et al.* 1995; Schmitz and Pujalte 2003, 2007; Svensen *et al.* 2004; Zachos *et al.* 2005; Wing *et al.* 2005; Bowen *et al.* 2006; Lopez-Martinez 2006; Nunes and Norris 2006; Smith *et al.* 2006; Sluijs *et al.* 2007; Sluijs and Brinkhuis 2009). Global surface temperatures are estimated to have risen by ca. 5 °C in less than 10,000 years, and by up to 9 °C at high latitudes (Kennett and Stott 1991; Zachos *et al.* 2006; Tripati and Elderfield 2004; Sluijs *et al*. 2007; Dunkley Jones *et al.* 2010), making this one of the most extreme and transient warming events in the geological record. An ocean acidification event occurred alongside the PETM (Zachos *et al.* 2005; Gibbs *et al.* 2010) which was attributed to the release of substantial amounts of carbon to the

atmosphere. This carbon was then dissolved and permanently sequestered in the Earth's oceans via silicate weathering, as indicated by a prominent clay layer in the oceanic sedimentological record which is suggestive of a shoaling of the carbonate compensation depth (CCD; Zachos *et al.* 2005). Carbon release and subsequent global warming throughout the PETM was also the cause of the most severe benthic foraminiferal extinction seen in the past 90 Ma, resulting in the loss of 35 – 50 % of deep sea benthic foraminiferal species (Thomas *et al.* 1998; Bowen *et al.* 2006). Changes in mammalian taxonomic diversity (Clyde and Gingerich 1998) and transient body size reductions occurred (Gingerich 2003), whilst floras extended northwards up to ca. 1500 km during the PETM (Wing *et al.* 2005). This transient period of extreme change coincided with the appearance of modern orders of mammals (i.e., primates) and the mammalian dispersal event (MDE), where large mammals migrated from Asia to North America (Smith *et al.* 2006; Beard 2008).

The PETM was first documented by Kennett and Stott (1991). Since then, more than 165 PETM sites have been discovered and studied worldwide, ranging from the Southern Ocean to Asia, Europe, America, Africa and the Arctic. The Palaeocene-Eocene (P/E) boundary has been defined by the placement of a Global Boundary Stratotype Section and Point (GSSP) in the Dababiya Quarry section of Egypt (Aubry *et al.* 2007). The age of the boundary has recently been estimated as 56.011 – 56.293 Ma using radiometric dates derived from marine ash layers and orbital tuning of marine sediments (Westerhold *et al.* 2009). The onset of the PETM is characterised by a negative CIE (Kennett and Stott 1991; Koch *et al*. 1992) and a dramatic shoaling of the carbonate compensation depth (Zachos *et al*. 2005), both of which document the

large-scale input of isotopically light carbon (as methane or carbon dioxide) to the ocean-atmosphere system (Zeebe *et al.* 2009). Reliable quantification of the amount and source of the released carbon to the atmosphere is one of the major outstanding issues, with current estimates ranging from 1,500 Gt to 12,000 Gt of carbon (Dickens 1995, 2003, 2011; Bice and Marotzke 2002; Panchuk *et al.* 2008; Zeebe *et al.* 2009; Cui *et al.* 2011). Accurate estimation of carbon release is further complicated by a difference in the magnitude of the CIE recorded in different environments: e.g., 4.7 ± 1.5‰ CIE from terrestrial records and 2.8 ± 1.3‰ CIE from marine records (McInerney and Wing 2011; Figure 1.1). Two hypotheses proposed to explain this difference are the "marine modification", and "plant community change" hypotheses (Smith *et al.* 2007). The "marine modification" hypothesis suggests that carbonate dissolution and poor carbonate preservation due to ocean acidification may have reduced the recorded CIE in many marine sections, especially in the deep sea. However, even the most complete marine records do not record a CIE much in excess of 4 ‰ (Zachos *et al.* 2007). The "plant community change" hypothesis proposes that the magnitude of the CIE is greater in the terrestrial realm as a result of major changes in floral composition during the PETM from mixed angiosperm (flowering plants)/gymnosperm (conifers) flora to a predominantly angiosperm flora (Smith *et al*. 2007; Schouten *et al*. 2007). This North America and Arctic Ocean derived plant community change hypothesis also predicts that the magnitude and pattern of amplification of CIEs will vary regionally depending on the extent of the replacement of gymnosperms by angiosperms during the PETM (Smith *et al.* 2007). Recently, however, it has been shown that angiosperms produce, on average, around 200 times more *n*-alkanes than gymnosperms (Diefendorf *et al.* 2011), with the latter sometimes synthesising no *n*-

alkanes at all. This suggests that the *n*-alkane record would almost entirely comprise an angiosperm $\delta^{13}C$ signal and, therefore, that even if a change in the plant community was observed it would be unlikely to significantly affect $\delta^{13}C_{n\text{-alkane}}$ values.

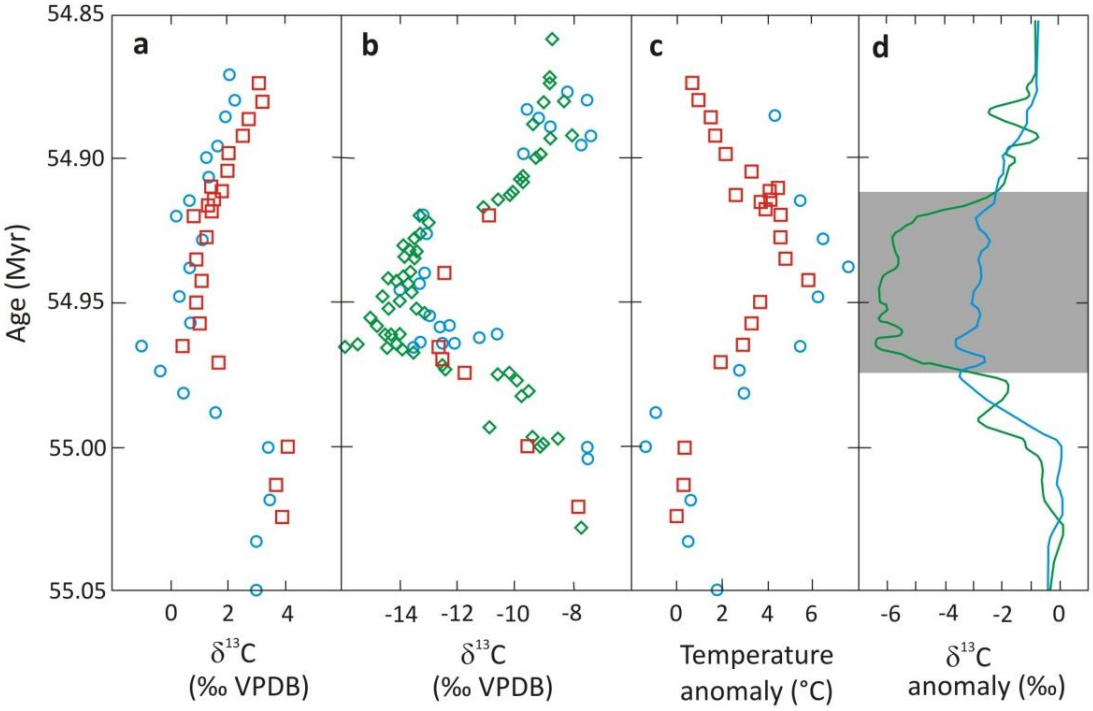

Figure 1.1. Graphic illustration of the difference in magnitude of the recorded CIE as measured in the marine and terrestrial realm. Modified from Bowen *et al.* (2004).

a) Marine record from *Acarinina* (= Southern ocean, = Pacific Ocean)
b) Terrestrial paleosol carbonate record (= Northern Spain, = China, = USA)
c) Temperature anomalies between the two marine sites
d) Discrepancy in CIE observed in the marine ( ) and terrestrial records ( )

1.4 SOURCES AND MECHANISMS OF CARBON RELEASE

Although a large carbon release at the PETM is accepted, the source and mass of the carbon are still debated. Because different sources of carbon have different $\delta^{13}C$ signatures, differential loadings of carbon would be required to cause the same magnitude CIE.

One of the most widely accepted theories of carbon release remains via the release of methane or gas hydrates and its subsequent oxidation to carbon dioxide (Dickens *et al.* 1995). Methane hydrates consist of methane molecules enclosed in a matrix of water,

forming a structure similar to ice. They are stable in deep-sea sediments, but can be easily destabilised. Several mechanisms have been proposed for this including cometary impact (Kent *et al.* 2003; Cramer and Kent 2005), slope failure, or increasing ocean temperature caused by changes in ocean circulation, specifically, a switch in the location of deep water formation from the South Atlantic to the North Atlantic (Kennett and Stott 1991; Bice and Marotzke 2002; Nunes and Norris 2006). Cometary impact remains a controversial theory, suggested as a result of the presence of magnetic nanoparticle material in kaolinite-rich shelf sediments on the Atlantic Coastal Plain (Kent *et al*. 2003). Researchers have since challenged this theory, suggesting that the magnetic material was of biogenic origin, produced by magnetotactic bacteria, and that its presence reflected environmental changes rather than a cometary impact (Kopp *et al.* 2007; Lippert and Zachos 2007).

Present day known methane hydrate reserves are located around North America and Greenland (Dickens *et al.* 1997). It has been suggested that if PETM methane hydrate reservoirs were similarly located, a switch in deep water formation from the Southern Hemisphere to the Northern Hemisphere (e.g., as evidenced by Nunes and Norris 2006), could have caused the temperature increase necessary to destabilise and release the methane hydrates (Bice and Marotzke 2002; Thomas *et al.* 2003). This change in oceanic circulation is suggested to have been driven by either increased ocean temperatures, decreasing the pole-to-equator sea surface temperature gradients, or by changes in continental freshwater run-off (Thomas *et al.* 2003; Nunes and Norris 2006). Applying this scenario to the present day suggests that future global warming could again affect ocean circulation, which in turn could trigger another

release of methane hydrates, accelerating the warming caused by anthropogenic activities (Thomas *et al.* 2003; Bowen *et al.* 2006).

If the terrestrial CIE magnitude is an accurate representation of the change recorded in the entire ocean-atmosphere carbon reservoir, then marine gas hydrates could only be solely responsible for the PETM if the climate sensitivity to CO_2 around the PETM was much higher than currently assumed (Pagani *et al.* 2006). However, current debates suggest that gas hydrates could not be the only source of carbon causing the PETM, owing to the required magnitude of carbon release exceeding the estimated amount of carbon stored in gas hydrate reservoirs at the time of the event (Higgins and Schrag 2006). Furthermore, no direct physical evidence has been found for the release of large volumes of methane hydrates (Dickens 2004).

"Contemporary opinion" is that methane hydrates are unlikely to be the sole source of carbon responsible for the PETM climate change but may be partially responsible in combination with other sources. Consequently, other sources have been hypothesised as the source of the released carbon, including thermogenic methane as a direct source of the ^{13}C-depleted carbon by means of sill emplacement (Svensen *et al.* 2004; 2010). Injection of magma into organic-rich sediments may have caused the explosive release of large quantities of thermogenic methane to the ocean/atmosphere system (Svensen *et al.* 2004; Bowen *et al.* 2006). Seismic data from the Norwegian Sea indicate the presence of sills and associated hydrothermal vent complexes, which have been dated radiometrically to have been emplaced approximately synchronous with the PETM (Svensen *et al.* 2010). It is estimated that a 5000 km^3 dolerite could

generate between 125 – 450 Gt carbon if intruded as a 100 m thick sill, with 1 – 3 wt% total organic carbon transferred to carbon gas (Svensen *et al.* 2004; Svensen *et al.* 2007). This indicates that methane could have potentially been produced in significant enough quantities by means of sill emplacement to have caused the CIE associated with the PETM. However, thermogenic methane as a potential source of the released carbon has been challenged due to the rate of release required; it has been estimated that a 100-fold increase in the rate of volcanic outgassing would be needed to cause the release of the amount of carbon required over the period of time estimated, which is geologically improbable (Dickens *et al.* 1995; Dunkley Jones *et al.* 2010; Dickens *et al*. 2011).

Another suggested source of carbon to initiate the PETM is the burning of extensive peat and coal deposited through the Palaeocene, via extensive wildfires (Kurtz *et al.* 2003). Evidence to support this theory came from carbon and sulphur stable isotope records, coincident with the onset of the PETM, in which a peak in organic carbon burial was accompanied by remarkably low pyrite sulphur burial rates. Kurtz *et al.* (2003) suggested that this may reflect organic burial being dominated by terrestrial environments, where sulphate was limited in supply. Coals of Palaeocene age were suggested as a potential source of the carbon, due to the volumes of coal being sufficient to account for the required burial of organic carbon coupled with their low sulphur content, consistent with the high organic carbon/pyrite sulphur burial ratios recorded. Mechanisms to initiate the proposed wildfires included increasing atmospheric O_2, dryer climates, and/or uplift of coal basins (Kurtz *et al.* 2003). However, no increase in combustion by-products, such as soot and graphitic black

carbon, was observed in PETM cores from the Atlantic or the Pacific (Moore and Kurtz 2008), and the by-products recorded appeared to be sourced from contemporaneous (P/E boundary) biomass, not geologically old carbon. Furthermore, Higgins and Schrag (2006) suggested that in order for wildfire burning to cause the carbon release estimated for the PETM interval, it would require an order of magnitude increase in the amount of carbon stored in peat and all the known peatlands to burn simultaneously. Moore and Kurtz (2008) suggested that these data refuted, but could not completely rule out, biomass burning as the sole cause for the PETM event, although it may have made a contribution to the carbon release.

Tectonically-driven isolation of an inland sea (epicontinental seaway) by means of volcanism or continental collision has also been suggested as a potential source and mechanism of release of the necessary carbon to cause the PETM. Epicontinental seaway isolation would have led to desiccation and oxidation of organic matter and would have removed a large source of moisture for the continental interior, subsequently resulting in further desiccation and oxidation of adjacent terrestrial wetlands (Higgins and Schrag 2006). However, although vast areas of central Asia were covered by shallow seaways in the Palaeocene-Eocene, there is no evidence that any dried up at a time coincident with the PETM (Gavrilov *et al.* 2003).

Finally, DeConto *et al.* (2012) suggested that the rapid thawing of permafrost deposits may have been responsible for the release of carbon at the P/E boundary. During the Palaeogene Antarctica did not support a large ice cap and may, therefore, have stored vast quantities of carbon as permafrost and peat (McInerney and Wing 2011).

DeConto *et al.* (2012) used an astronomically calibrated PETM record to show that the hyperthermal events were occurring during high eccentricity and obliquity orbits, and suggested that orbitally-triggered decomposition of soil organic carbon in the Arctic and Antarctic terrestrial permafrost may have had the potential to release large quantities of carbon into the ocean-atmosphere system. Furthermore, they suggested that following peak-warming, replenishment of permafrost carbon stocks may have contributed to the rapid recovery from the event. This hypothesis was also applied to subsequent early Eocene hyperthermals, suggesting that this carbon would provide a sensitive reservoir for the next hyperthermal. Whilst this hypothesis provides a reasonable explanation for both onset and termination of the PETM event, the termination would need to be in combination with another mechanism. DeConto *et al.* (2012) suggested that the extent of permafrost recovery after each hyperthermal would have declined resulting in a successively smaller carbon pool for each hyperthermal and thus a smaller hyperthermal event.

Whether any one of these proposed sources of carbon is solely responsible for the carbon release to cause the PETM, or a combination of sources, is still debated. Mass balance calculations, models and further PETM records may help to constrain the size of the magnitude of the CIE associated with the PETM, which in turn may help to identify more likely sources of the carbon (Figure 1.2).

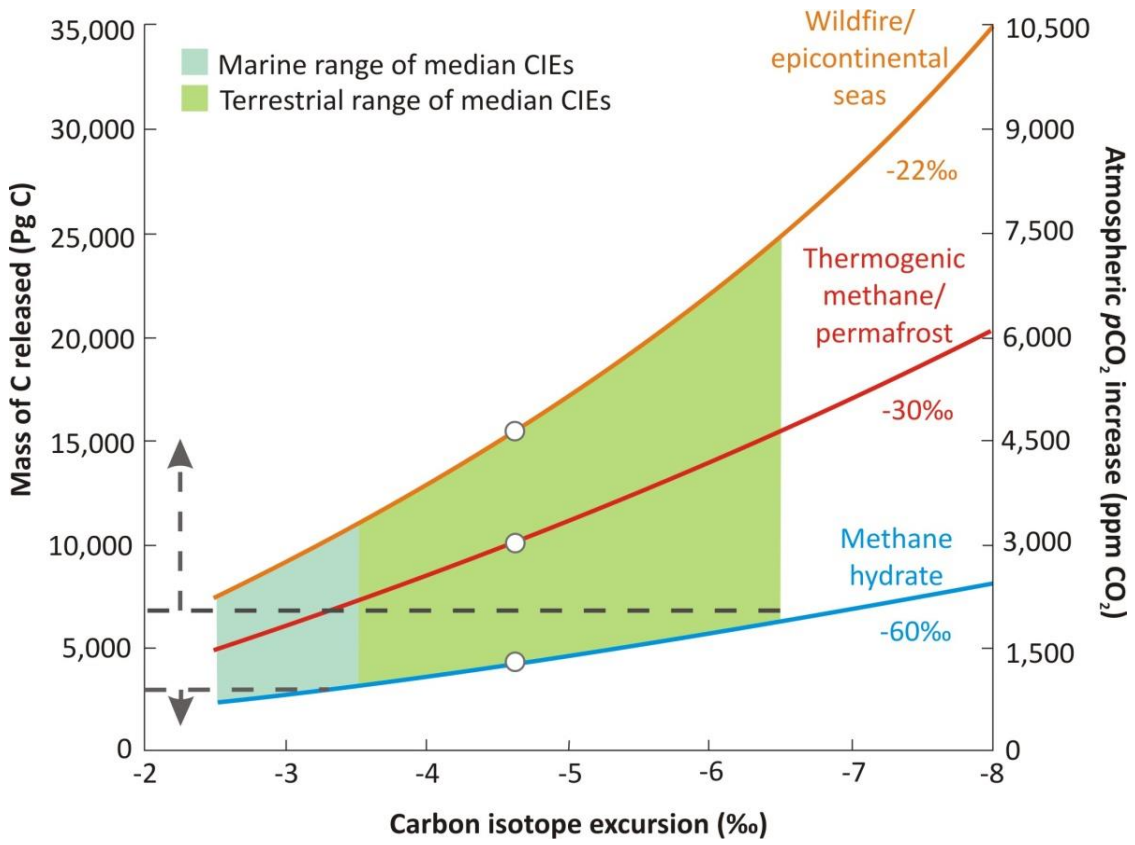

Figure 1.2. Mass balance estimates of mass of carbon released from different sources of carbon, over a range of absolute values for the CIE, as discussed in the text. Modified from McInerney and Wing (2011).

1.5 RECOVERY FROM THE PETM

How the Earth climate system recovered from the PETM warming event is still not well understood and alternative hypotheses have been proposed. The recovery period is estimated to have lasted ca. 83 Ka (Murphy *et al*. 2010) and reflects natural carbon sequestration and negative feedbacks that brought about termination of the event. Three mechanisms have been proposed to account for the drawdown of CO_2 at the termination of the event. Kelly *et al.* (2005, 2010) and Torfstein *et al.* (2010) proposed enhanced silicate weathering and runoff from land as a recovery mechanism. They suggest that this resulted in increased carbonate precipitation and preservation in the ocean. Evidence for this theory came from increased coccolithophore blooms and

kaolinite abundance (Kelly *et al.* 2005), which together were suggested to reflect a transient climate state and enhanced continental weathering and carbonate precipitation. Silicate weathering is, however, a slow process, and due to the relatively short timescales of recovery, Bowen and Zachos (2010) suggested that a process that preferentially sequestered ^{13}C-depleted carbon would likely be required.

An alternative explanation proposed an increase in the intensity of the marine biological pump, resulting in increased CO_2 fixation and subsequent sequestration of carbon via burial in marine sedimentary organic matter (Bains *et al.* 2000). Evidence for this theory derived from increased accumulation rates of biogenic barium, indicative of export palaeoproductivity. However, this idea was refuted by Torfstein *et al.* (2010), who argued that increased export production occurred ca. 70 ka after the onset of the CIE, implying that it could not be responsible for rapid removal of excess carbon from the atmosphere.

Finally, increased carbon storage in the terrestrial biosphere was suggested as a potential recovery mechanism from the PETM interval (Beerling 2000; Bowen and Zachos 2010). Rates of carbon isotope change in well-dated marine and terrestrial sediments spanning the PETM were constrained, resulting in a calculated rate of recovery that was an order of magnitude more rapid that that expected for carbon drawdown from silicate weathering alone (Bowen and Zachos 2010). This led to the hypothesis that regrowth of terrestrial biospheric carbon stocks that were released at the onset of the event may have occurred, because to recover from the PETM on such

a rapid timescale it was estimated that 2,000 Pg of carbon had to be sequestered in 30 – 40 ka (Bowen and Zachos 2010).

Research based on the mode of recovery from the PETM interval is still relatively new, and as such all three mechanisms discussed herein are considered plausible. It is likely, as with the source of the carbon released to cause the event, that recovery occurred by means of several mechanisms. However, further work is needed to determine which mechanisms are most plausible, and thus to understand better how the Earth system responds to climate change.

This study aims to address three important debates associated with the PETM.

1) The magnitude of PETM CIEs in northern Spain is evaluated through the comparison of continental and marine CIEs within a linked sediment routing system.

2) The profile shape of the different CIE records is assessed, with inferences drawn on the rate and rapidity of release and drawdown of carbon.

3) Evaluation of how the sediment system responds locally to such climatic perturbations is achieved through the comparison of features in the sedimentary record, in relation to the onset and recovery from the CIE.

1.6 NORTHERN SPAIN

The sections studied in this research represent a series of well-known PETM sections in northern Spain, spanning continental to marine depositional environments within the same depositional system (Schmitz *et al.* 2001). These sections are unique in providing a series of expanded and accessible PETM sedimentary successions. The PETM has already been located by carbonate $\delta^{13}C$ stratigraphy in most of the sections (Schmitz *et al.* 1997, 2001; Schmitz and Pujalte 2003, 2007) and many bio-, magneto- chemo- and lithostratigraphic studies have been conducted across the region identifying the PETM (Canudo and Molina 1992; Canudo *et al.* 1995; Schmitz *et al.* 1997; Baceta *et al.* 2000; Schmitz *et al.* 2001; Domingo *et al.* 2009).

The data presented in this study represents the first organic geochemical data for the Zumaia, Ermua Campo and Esplugafreda sections and the first compound specific organic geochemical data for all of the sections. The study area is one of only a limited number of places worldwide where comparisons of marine and terrestrial CIEs within the same sediment routing system and indeed within one section (Zumaia) can be made.

CHAPTER 2

2 MAGNITUDE AND PROFILE OF ORGANIC CARBON ISOTOPE RECORDS FROM THE PETM: EVIDENCE FROM NORTHERN SPAIN

ABSTRACT

The Palaeocene – Eocene Thermal Maximum (PETM), a hyperthermal event that occurred ca. 56 Ma, has been attributed to the release of substantial amounts of carbon, affecting the atmosphere, biosphere and the oceans. Current issues with respect to our understanding of the PETM include the amount of carbon released, the duration of carbon release, and the mechanism(s) of release, all of which are related to the magnitude and profile of the associated Carbon Isotope Excursion (CIE). High-resolution organic carbon profiles ($\delta^{13}C$) of six PETM sections in northern Spain are presented that span a transect from continental to marine environments. These data represent the highest-resolution isotope records for these sections and allow a comparison of the magnitude of the excursion, the shape of the vertical $\delta^{13}C$ profile during the PETM episode, and the relative timing of the onset of the excursion across a linked sediment routing system. Previous studies using carbonate $\delta^{13}C$ data have suggested that the continental Claret Conglomerate, found in this region, formed synchronously with a marine, clay-rich, siliciclastic unit, with these key lithological changes interpreted to be driven by increased seasonal rainfall-runoff in the warmer PETM climate. The data presented here suggest that deposition of these units did not immediately follow the CIE onset, indicating that there may be a temporal lag between the onset of the PETM warming and the response of the depositional systems in northern Spain. No systematic variation in the magnitude of the CIE between different depositional environments was found; the marine CIE magnitudes are at the higher

end of those previously described (3.7 ±1.4‰), and the continental ranges are lower (3.1 ±1.3‰).

2.1 INTRODUCTION

The Palaeocene – Eocene Thermal Maximum (PETM; ca. 56 Ma) is the most dramatic and rapid global warming event of the Cenozoic Era, with global surface temperatures estimated to have risen by 5 – 9°C in less than 10,000 years (Dickens *et al.* 1995; Thomas *et al.* 2002; Wing *et al.* 2005; Zachos *et al.* 2005; Rohl *et al.* 2007; Sluijs *et al.* 2007; Zeebe *et al.* 2009; Dunkley Jones *et al.* 2010). Geological and geochemical evidence indicate that this warming was driven by a major perturbation to the global carbon cycle, with the release of several thousand gigatons of isotopically light carbon as methane or carbon dioxide to the ocean-atmosphere system (Dickens *et al.* 1995, 1997, 2011; Panchuk *et al.* 2008; Zeebe *et al.* 2009; Cui *et al.* 2011).

One of the major unresolved questions surrounding the PETM is the precise magnitude of the carbon release. Current estimates range from 1,500 Gt to 12,000 Gt of carbon (Dickens 1995, 2003, 2011; Panchuk *et al.* 2008; Zeebe *et al.* 2009; Cui *et al.* 2011), depending on the carbon source and its isotopic composition. A key constraint on estimates of the PETM carbon cycle perturbation is the magnitude of the accompanying negative Carbon Isotope Excursion (CIE), which, at the resolution of current data, is recorded simultaneously in environments as disparate as continental soils and deep ocean sediments (Koch *et al.* 1992; Bowen *et al.* 2004; Zachos *et al.* 2005). There is, however, a discrepancy in the magnitude of the recorded negative CIE

between continental and marine sediments, with the continental CIE consistently recorded as around 2 to 4‰ greater than the marine CIE shift (continental CIE ~3 to 7‰; marine CIE ~2.5 to 5.5‰; Pagani *et al.* 2006; Smith *et al.* 2007; Zachos *et al.* 2007; Handley *et al.* 2008; Bowen and Zachos, 2010; McInerney and Wing 2011). Carbonate dissolution and poor preservation may have dampened the CIE recorded in many marine sections, especially in the deep sea (Zachos *et al.* 2005; McCarren *et al.* 2008), although the most complete marine records do not record a CIE much in excess of 4‰ (Zachos *et al.* 2007). In contrast, amplification of the CIE in the continental realm has been attributed to increased moisture availability (Beerling, 1996; Bowen *et al.* 2004; Ward *et al.* 2005) allowing continental plants to increase $\delta^{13}C$ discrimination (Bowen et al, 2004), temperature effects on carbon isotope fractionation (Edwards *et al.* 2000); and possible changes in soil productivity and organic matter turnover rates (Bowen *et al.* 2004). An additional problem is that many previous studies comparing continental and marine sections are at a low resolution, an issue that is exacerbated when records derive from sections located in different basins (Koch *et al.* 1992; Schmitz and Pujalte 2003; Bowen *et al.* 2004; Wing *et al.* 2005; Pagani *et al.* 2006; Handley *et al.* 2011; Bowen and Zachos 2010; Tipple *et al.* 2011). Another un-resolved issue is the variability in the PETM isotopic profiles. The overall structure of (presumably) complete profiles is defined by three phases: initiation, alternate semi-stable state, and recovery (Bowen *et al.* 2006). However, not all sections exhibit the semi-stable state.

Differences among sites are typically interpreted with respect to how rapidly carbon was added to, and removed from, the ocean-atmosphere reservoir. For example, from studies of carbonate $\delta^{13}C$ values, Zachos *et al.* (2008) showed that at several South Atlantic ODP sites a rapid PETM onset occurred, followed by a gradual recovery that they attributed to silicate weathering feedback (Zachos *et al.* 2005, 2008). This is considered the classical model, and is exemplified by a triangular-shaped CIE profile (Figure 2.1 (1)). In contrast, well-dated marine bulk-carbonate and terrestrial soil-nodule carbonate $\delta^{13}C$ records from ODP Site 690 and Polecat Bench respectively, imply both a rapid release and drawdown of carbon at the onset and termination of the PETM (Bowen and Zachos 2010), with an expanded alternate semi-stable state, leading to a box-shaped CIE profile (Figure 2.1 (2)). Bowen and Zachos (2010) considered that this rapid recovery was inconsistent with the expected ~100 kyr response time of the silicate weathering feedback and, instead, explained it by the rapid re-growth of biospheric carbon stocks that may have been released at the onset of the event. Furthermore, a semi-stable state may suggest continued release of ^{13}C-depleted carbon during the event; an idea also proposed by Zeebe *et al.* (2009), who hypothesised that to maintain the negative body of the CIE, pulsed releases of carbon throughout the CIE may be necessary. Currently there is no consensus on whether one profile is a better reflection of the CIE associated with the PETM, or whether other factors, such as sedimentation rates and/or decompaction, may be biasing all recorded shapes (McInerney and Wing 2011).

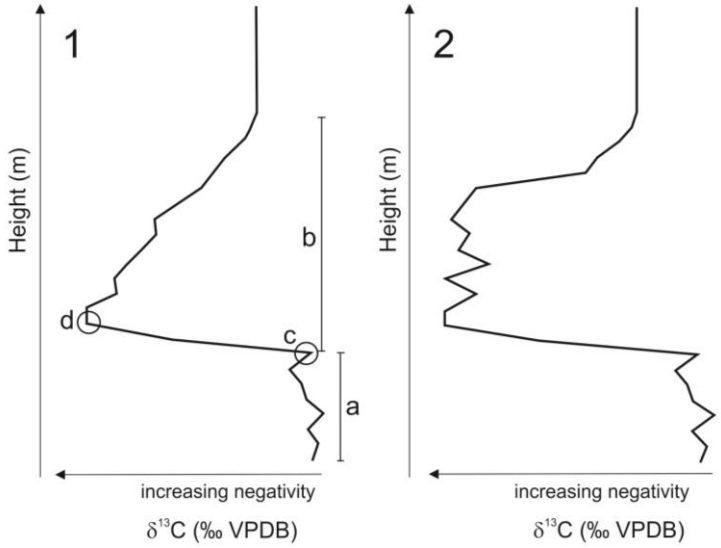

Figure 2.1. Exemplar CIE profile shapes illustrating: 1) the triangular profile (Zachos *et al.* 2008), and 2) the box profile (Bowen and Zachos 2010). The data used to generate the profiles is for illustrative purposes only. Methods for calculating CIE magnitude are shown on the triangular profile (1). Previous studies have subtracted the pre-CIE average (a) from the CIE average (b). This study subtracts the most positive $\delta^{13}C_{TOC}$ value immediately prior to the negative $\delta^{13}C_{TOC}$ shift (c), from the most negative $\delta^{13}C_{TOC}$ value at the base of the CIE (d).

This study presents a series of high-resolution $\delta^{13}C$ profiles from organic matter in six well-known PETM sections in northern Spain, spanning continental to marine depositional environments. This provides an opportunity to track changes in the recorded CIE across various palaeoenvironments. Previous stable isotope studies in northern Spain have presented either low-resolution soil nodule carbonate or bulk marine carbonate $\delta^{13}C$ excursions from the same sections (Schmitz and Pujalte, 2003, 2007), or organic carbon $\delta^{13}C$ excursions from individual sections (Domingo *et al.* 2009; Storme *et al.* 2012). The CIE magnitudes and profiles across this continental to marine transect are compared, providing new insights into the depositional control on the recorded CIE and the sedimentological response to the PETM warming episode.

2.2 SAMPLE LOCATIONS AND METHODOLOGY

2.2.1 GEOLOGICAL SETTING

The Tremp-Graus and Basque-Cantabrian basins of northern Spain are unique in providing a series of expanded and accessible PETM sedimentary sections that span the continental to marine realms within the same depositional system (Schmitz *et al.* 2001). The PETM has already been located by carbonate $\delta^{13}C$ stratigraphy in most of the sections (Schmitz *et al.* 1997, 2001; Schmitz and Pujalte 2003, 2007), which are, from east to west (Figure 2.2.), the continental sections of Claret (N 042°09´14.1", E 000°51´58.4"), Tendrui (N 042°10´07.2", E 000°51´25.3"), and Esplugafreda (N 042°14´47.3", E 000°45´22.7"), the transitional mixed shallow marine and continental deposits of Campo (N 042°23´24.5", E 000°23´50.2"), and the marine sections of Ermua (N 043°10´44.1", W 002°29´49.1") and Zumaia (N 043°18´4.5", W 002°15´31.2").

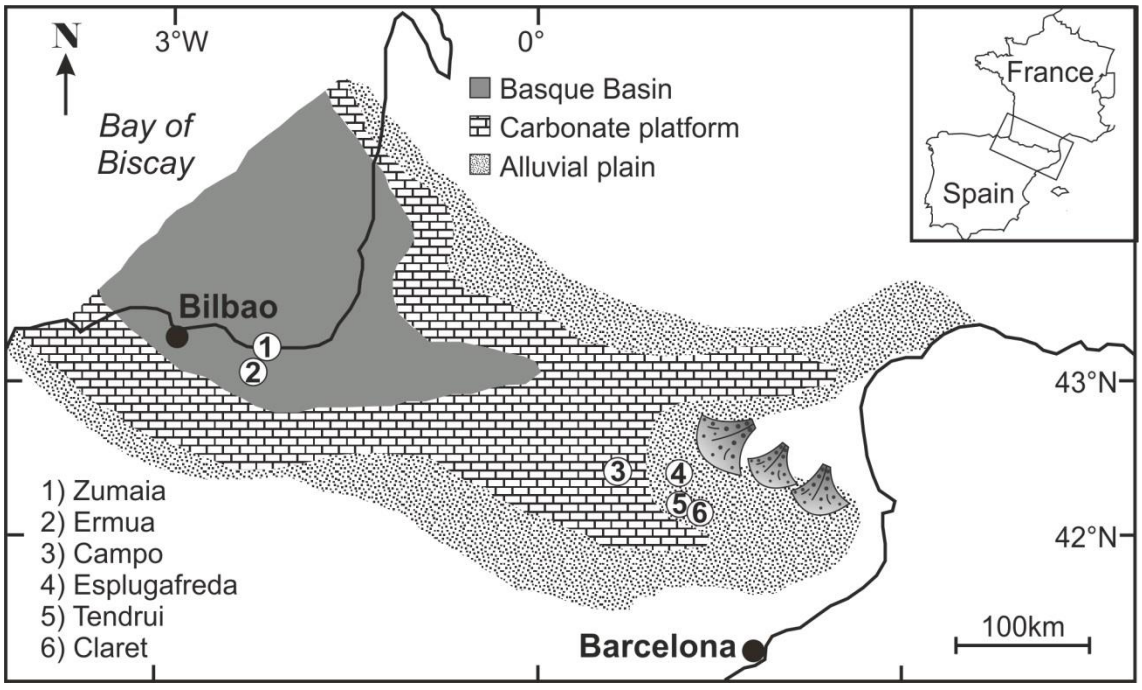

Figure 2.2. Palaeogeographic reconstruction and location map (redrawn from Schmitz *et al.* 2003). Numbers on map represent studied sections, which are: 1) Zumaia, 2) Ermua, 3) Campo, 4) Esplugafreda, 5) Tendrui and 6) Claret.

The lithological logs produced in this study (Figure 2.3.) are similar to those published previously for all sections (Schmitz *et al.* 1997, 2001; Schmitz and Pujalte 2003, 2007; Domingo *et al.* 2009). The continental sections have been correlated predominantly using fossil mammal sites comprising, for example, dental remains of the condylarth genus *Paschatherium* found at Claret and Tendrui. These are dated as late Palaeocene and occurring before the mammalian dispersal event (MDE), placing the sections close to the Palaeocene – Eocene boundary (Lopez-Martinez and Pelaez-Campomanes 1999; Lopez-Martinez *et al.* 2006; Domingo *et al.* 2009). In addition to fossil sites, chemostratigraphic features such as the CIE and lithostratigraphic marker horizons such as the Claret Conglomerate and *Alveolina* Beds have been used in correlation (Molina *et al.* 2000; Pujalte *et al.* 2000a; Schmitz and Pujalte 2007). The *Alveolina* Beds are a prominent marker bed in the Ilerdian representing a shallow marine environment associated with a basin-wide transgression in the early Eocene (Molina *et al.* 2000). Biostratigraphic correlations are discussed in further detail in Chapter 3 and Chapter 4 and illustrated in Figure 3.2.

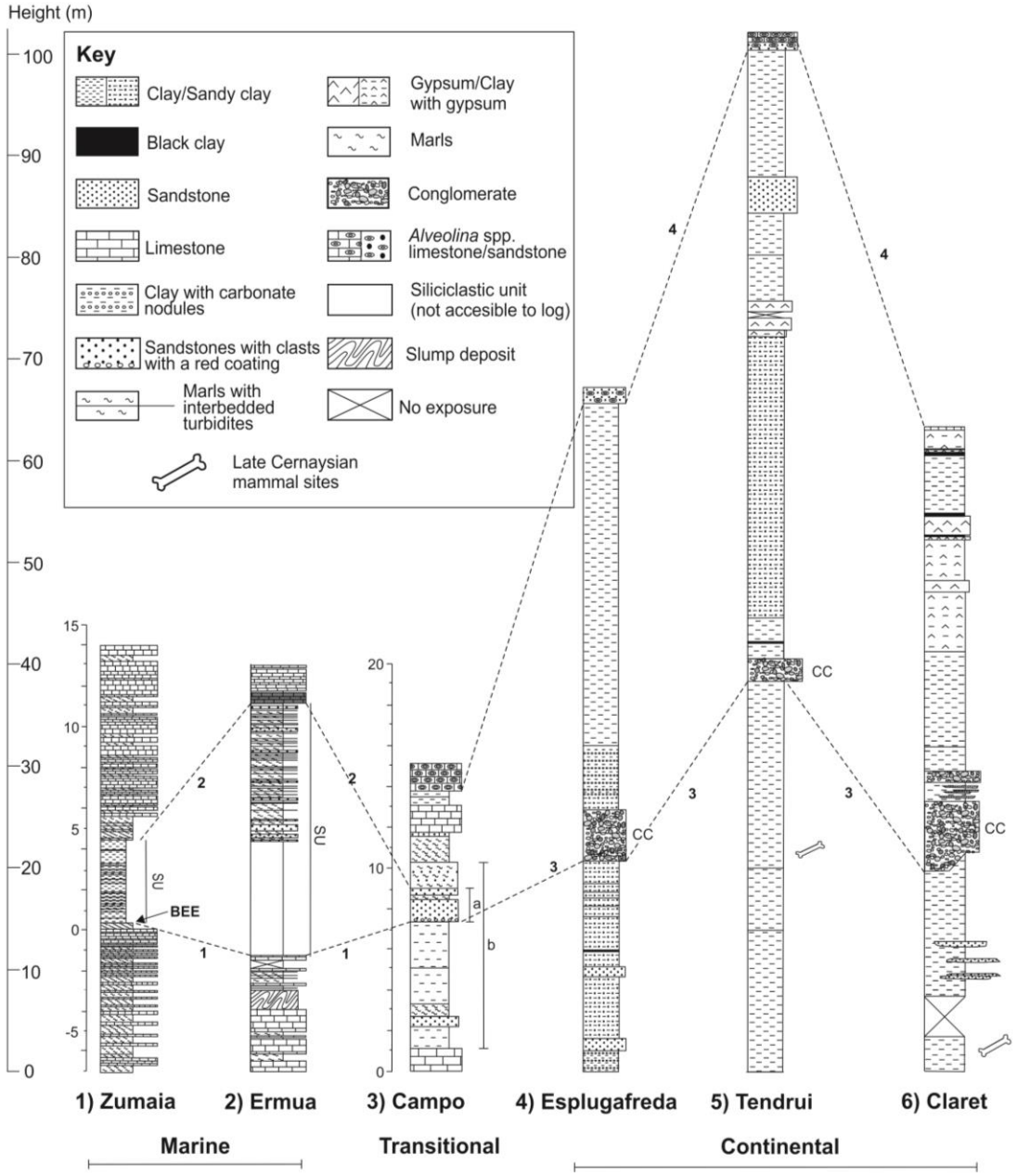

Figure 2.3. Lithological logs with proposed correlation points from the marine to continental realm (West to East), from Schmitz and Pujalte (2003), based upon carbon isotope stratigraphy and lithology. Note different scales used for Zumaia and Campo. BEE = Benthic Extinction Event. Numbered/lettered lines indicate proposed tie points/key lithological features: **1&2)** Bottom and top of the marine Siliciclastic Unit (SU on figure), respectively (Schmitz *et al.* 2001). Using isotope stratigraphy and lithology the Siliciclastic Unit has been suggested to experience a lateral change of facies towards a more detritic nature and can be linked to two sandstone beds at the transitional section of Campo (Schmitz and Pujalte 2003). **3)** Bottom of the Claret Conglomerate (CC on figure: Schmitz and Pujalte 2007). **4)** *Alveolina* Beds associated with a marine transgression throughout the entire terrestrial region (Molina *et al.* 2000, 2003). **a)** Sandstone beds interpreted to be the distal equivalent of the Claret Conglomerate (Schmitz and Pujalte 2003). **b)** Continental interval of the Campo section (Schmitz and Pujalte 2003).

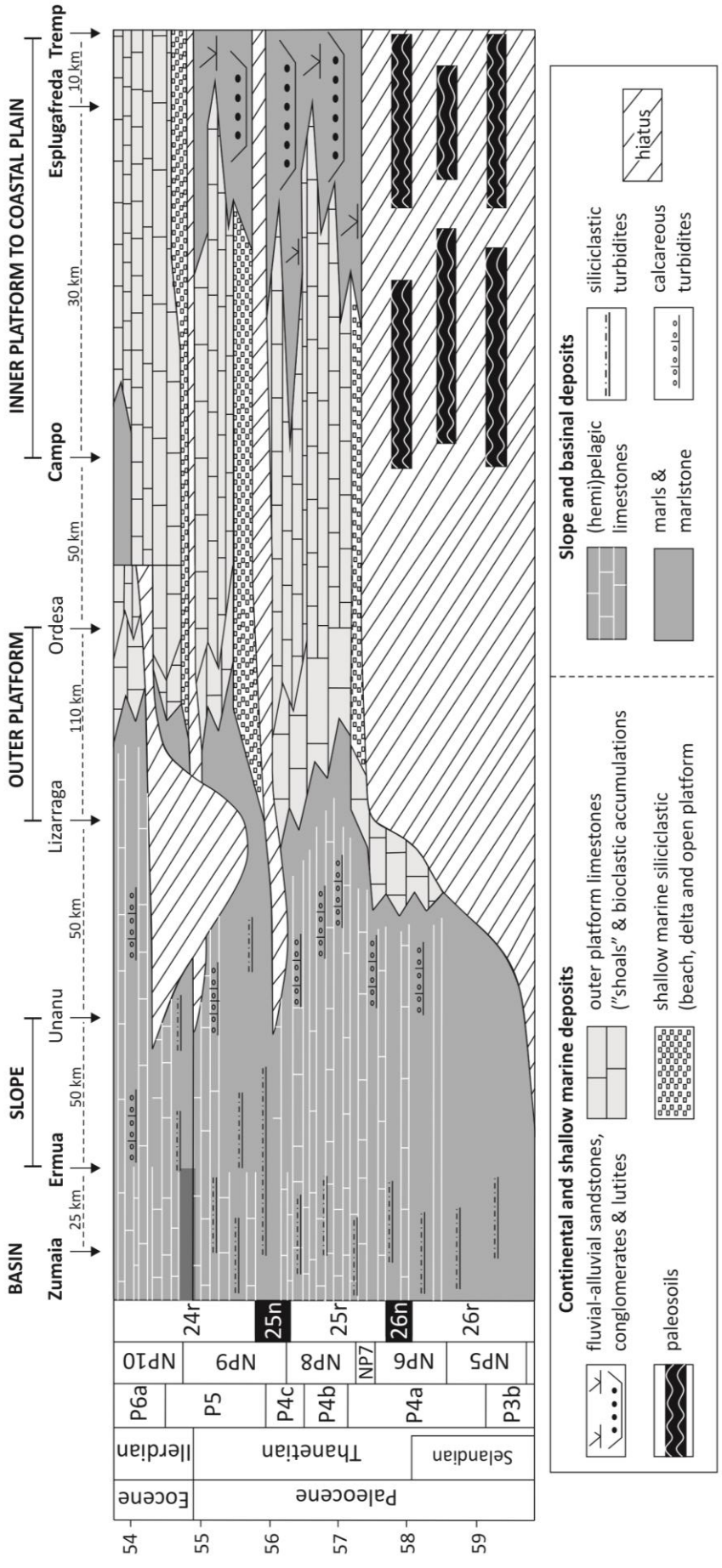

Figure 2.4. Correlation between all sections across the region; based upon previously published lithological tie points (Section 2 Figure 2), biostratigraphy, and carbonate $\delta^{13}C$ stratigraphy (Schmitz *et al.* 1997; Baceta *et al.* 2000; Molina *et al.* 2000; Nunez-Betelu *et al.* 2000; Pujalte *et al.* 2000a; Molina *et al.* 2003; Schmitz and Pujalte 2003).

The marine sections of Zumaia (bathyal) and Ermua (base-of-slope-apron; Schmitz and Pujalte 2003) and the mixed marine/continental section at Campo, have been correlated to each other using biostratigraphic (Molina *et al.* 2000; Nuñez-Betelu *et al.* 2000; Orue-Etxebarria *et al.* 2001), chemostratigraphic (Schmitz and Pujalte, 2003) and lithostratigraphic (Pujalte *et al.* 2000a; Schmitz and Pujalte 2007) methods. Pujalte *et al.* (2000) constructed a shelf to basin tentative correlation in the Pyrénées using four main lithological tie points, whilst Molina *et al.* (2000) undertook a detailed bio- and chemostratigraphic study at Campo to identify the PETM. Orue-Etxebarria *et al.* (2001) used these data and data from a palynological study by Nuñez-Betelu *et al.* (2000) to correlate Campo to the Benthic Extinction Event (BEE), recorded at Zumaia and Ermua, respectively (Schmitz *et al.* 1997; Schmitz and Pujalte 2007). Further correlative studies have also been undertaken in this region linking basin, slope and mixed marine PETM settings (Orue-Etxebarria *et al.* 1996; Baceta *et al.* 2000; Molina *et al.* 2003).

Correlation between the continental and marine sections in northern Spain has been achieved by Schmitz and Pujalte (2003) using a combination of all the bio-, litho- and chemostratigraphic techniques previously discussed (Figure 2.4.). The Claret Conglomerate is a continental feature propagating westwards toward the marine sections, whilst the *Alveolina* Beds are a marine unit that transgresses eastwards, both of which can be seen at the transitional section of Campo (Molina *et al.* 2000, 2003; Schmitz and Pujalte, 2007). Campo is, therefore, a fundamental section in this correlation, owing to its marine sediments immediately above and below the PETM, and the transition to continental deposition during the PETM (Molina *et al.* 2000;

Orue-Etxebarria *et al.* 2001; Schmitz and Pujalte 2003, Pujalte *et al.* 2009a). Carbonate $\delta^{13}C$ profiles have been used to further confirm correlation between sections (Schmitz *et al.* 2001; Schmitz and Pujalte 2003, 2007).

2.2.2 METHODS

All sections have been logged and 285 samples collected and analysed for organic carbon content and $\delta^{13}C$ (Table 2.1.). Results for Claret and Tendrui were added to the previously published data of Domingo *et al.* (2009) to provide a total of 98 samples at Claret and 94 samples at Tendrui. Sampling frequency varied according to the length and exposure of each section, with shorter sections (<25 m) ideally being sampled at 30 cm resolution, whilst longer sections (>25 m) were sampled at 50 cm intervals where possible.

Table 2.1. The $\delta^{13}C_{TOC}$ data used for calculating the magnitude of the CIE in this study. Superscripted numbers in the case of Campo refer to the values taken for the CIE calculation as pre-CIE values vary depending on where the onset of the CIE is placed. Total number of samples means all samples from this study and those used from Domingo *et al.* (2009), upon which all statistical analysis has been conducted. Number of samples indicates the new samples for which $\delta^{13}C_{TOC}$ data has been generated in this study.

Section	Total no. of samples	No. of samples this study	Min. $\delta^{13}C_{TOC}$ (‰)	Max. $\delta^{13}C_{TOC}$ (‰)	CIE calculation values (‰)		CIE magnitude
					Pre-CIE	Body-CIE	
Claret	98	20	–27.8	–21.7	–23.3	–26.8	3.5
Tendrui	94	28	–26.7	–22.9	–24.7	–26.4	1.7
Esplugafreda	80	80	–26.5	–21	–21.9	–26	4.1
Campo	34	34	–28.9	–21.3	-23.5^{1} /-26.2^{2}	–28.3	$2.1^{1} - 4.8^{2}$
Ermua	46	46	–29.5	–22.4	–22.4	–27.2	4.8
Zumaia	77	77	–28.4	–23.9	–24.3	–28.4	4.1

Whole rock samples were oven dried (30°C, 24 hours), crushed using a granite pestle and mortar and de-carbonated following the methodology of Domingo *et al.* (2009) using excess hydrochloric acid (10% v/v) until any visible sign of reaction had ceased. This was followed by repeated washing with deionised water until a neutral solution was obtained, then oven drying (30°C, 24 hours). Stable isotope analyses were conducted at the NERC Isotope Geosciences Laboratory. Total organic carbon (TOC) content was measured using a Carlo Erba 1500 elemental analyser with acetanilide used as the calibration standard. Replicate analyses indicated a precision of ±0.1% in well-mixed samples (1 Standard Deviation, SD). For $\delta^{13}C$ analysis a Carlo Erba 1500 EA online coupled to a VG TripleTrap was used. This setup also included a secondary cryogenic trap in the mass spectrometer for samples with very low carbon content. The mean standard deviation on replicate $\delta^{13}C$ analyses of laboratory standard broccoli (BROC1) and soil (SOILB) was between 0.1 and 0.4‰. The carbon isotope composition of the TOC within the samples is referred to as $\delta^{13}C_{TOC}$.

Two different methods are commonly used for calculating CIE magnitude. For example, in some instances, the average of $\delta^{13}C_{TOC}$ values preceding the CIE are taken and subtracted from the average of $\delta^{13}C_{TOC}$ values during the CIE (Domingo *et al.* 2009; Figure 2.1.). This averaging approach inevitably leads to some smoothing of the peak CIE magnitude at the very start of the PETM, especially if there was a relatively rapid transient negative spike at the onset. Instead, here, a "maximum CIE" approach is used that identifies the most positive $\delta^{13}C_{TOC}$ value immediately prior to the negative $\delta^{13}C_{TOC}$ shift (Figure 2.1., point c), and the most negative $\delta^{13}C_{TOC}$ value at the base of the PETM

(Figure 2.1., point d; Table 2.1.). This maximum CIE approach is appropriate for a comparison between sections which have varying degrees of noise superimposed on the CIE, most likely due to the inclusion and reworking of variable amounts of older, non-CIE related organic material. It assumes that this reworking most likely smooths and dampens the actual magnitude of the CIE. However, caution must also be taken in using the maximum CIE approach, as it is possible that over-emphasis of CIE magnitude may occur as a result of including spikes in the CIE magnitude calculation. Therefore, identifying differences in magnitude between disparate records may become challenging if the different methods are employed, i.e., observed differences in magnitude may be an artefact of the method used rather than a reflection of the environment of deposition.

Regression analysis was used to assess whether there was a significant logarithmic correlation between $\delta^{13}C_{TOC}$ values and % weight of organic carbon (wt%TOC; Figure 2.5) for the continental sections of Claret, Tendrui, and Esplugafreda. If correlation was not significant (95% confidence interval; low r^2), it is tentatively assumed that $\delta^{13}C_{TOC}$ values are independent of lithological change. For all sections, wt%TOC remained low (generally <1% TOC); independence of wt%TOC and lithological change was assessed using the student's t-test at the 95% confidence interval (Tables 6.1.1 – 6.1.6 of Appendix 1). Where $p < 0.05$, a significant difference between wt%TOC and different lithologies may be observed, as discussed in the results, otherwise wt%TOC was considered independent of lithological change. Comparison with carbonate records (where present) was also used to assess similarity, increasing confidence in the $\delta^{13}C_{TOC}$

records reflecting a primary signal and thus atmospheric CO_2 values. A t-test on each section, comparing $\delta^{13}C_{TOC}$ values during the CIE to those before the CIE, determines if a significant shift in $\delta^{13}C_{TOC}$ values occurred during the CIE (Table 2.2.).

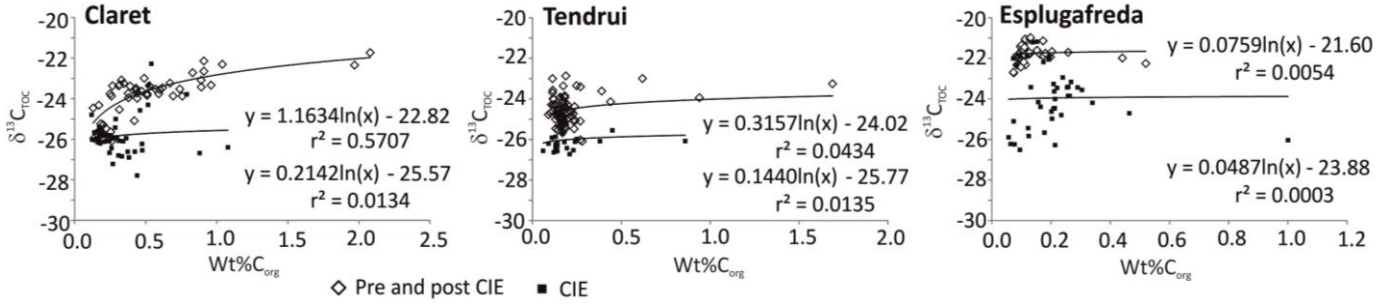

Figure 2.5. Regression analysis plots. Cross plots showing correlations between $\delta^{13}C_{TOC}$ and weight % organic carbon (Wt%TOC) for each continental section studied.

Table 2.2. Associated statistical tests performed on the data (regression analysis and *t*-tests) comparing $\delta^{13}C$ and wt%TOC. For regression analysis, pre- and post-CIE values were combined, and CIE values were analysed separately to determine if a logarithmic relationship was observed in any of the sections. *t*-tests were conducted comparing only pre-CIE values to CIE values to determine if a statistically significant shift was recorded. For this second analysis post-CIE values were ignored, as they do not return to pre-CIE values, and as such may bias the test.

Section	Data used for regression analysis	R^2 values comparing $\delta^{13}C_{TOC}$ and wt%TOC	Data used for comparison in *t*-tests	*t*-test results for $\delta^{13}C_{TOC}$ values
Claret	Pre/post CIE	0.57	Pre/during CIE	t = 12.32
	During CIE	0.01		p < 0.001
Tendrui	Pre/post CIE	0.04	Pre/during CIE	t = 10.36
	During CIE	0.01		p < 0.001
Esplugafreda	Pre/post CIE	0.005	Pre/during CIE	t = 7.08
	During CIE	0.0003		p < 0.001
Campo	Not calulcated due to the nature of the sections (continental-marine, or entirely marine).		Pre/during CIE	t = 3.67
				p < 0.001
Ermua			Pre/during CIE	t = 13.70
				p < 0.001
Zumaia			Pre/during CIE	t = 10.93
				p < 0.001

To define the magnitude of any CIE, the start, or onset, of the CIE in any given section must be determined. The onset of the CIE in this study is defined by a negative isotope shift of at least ca. 2‰ to continuous values of< –25‰. For Claret, Esplugafreda, Ermua, and Zumaia this resulted in an unambiguous identification of the CIE onset. However, Tendrui and Campo proved more challenging and, as such, to confirm that the shift observed was in fact the CIE associated with the PETM, the onset of the CIE in this study was compared to previously published data and lithological tie points (Figure 2.3.). Finally, a return to less negative values similar to those preceding the event, was used to determine the termination of the CIE. The $\delta^{13}C_{TOC}$ results for all 6 sections are presented in Figure 2.6. (continental sections) and Figure 2.7. (marine sections; also Tables 6.1.7 to 6.1.12 of Appendix 1).

2.3 RESULTS

The $\delta^{13}C_{TOC}$ CIE magnitudes range between 1.7 to 4.8‰ among the six sections (Table 2.1.). The highest recorded $\delta^{13}C_{TOC}$ CIE magnitude for the continental sections is that of Esplugafreda (4.1‰; Figure 2.6), whilst for the marine sections it is Ermua (4.8‰; Figure 2.7.). Using the defined parameters for the CIE onset, combined with correlative data from previous studies (Schmitz and Pujalte 2003, 2007; Pujalte *et al.* 2009a), a CIE magnitude of 2.1‰ at Campo is suggested (Figure 2.7.). However, interpretation of the CIE onset at Campo was more difficult due to its stepped nature (Figure 2.7.), leading to a range of potential CIE magnitudes, depending on where the onset was placed (2.1 – 4.8‰). Among the continental sections of Claret, Tendrui, and Esplugafreda the magnitude of the CIE varies, despite their proximity (Table 2.1.),

but in the case of Claret and Tendrui, the onset of the excursion occurs prior to the deposition of the Claret Conglomerate, and the peak of the CIE occurs after conglomerate deposition (Figure 2.6). Comparison between the marine sections illustrates variability in terms of the magnitude, onset, and shape of the CIE profiles (Figure 2.7.).

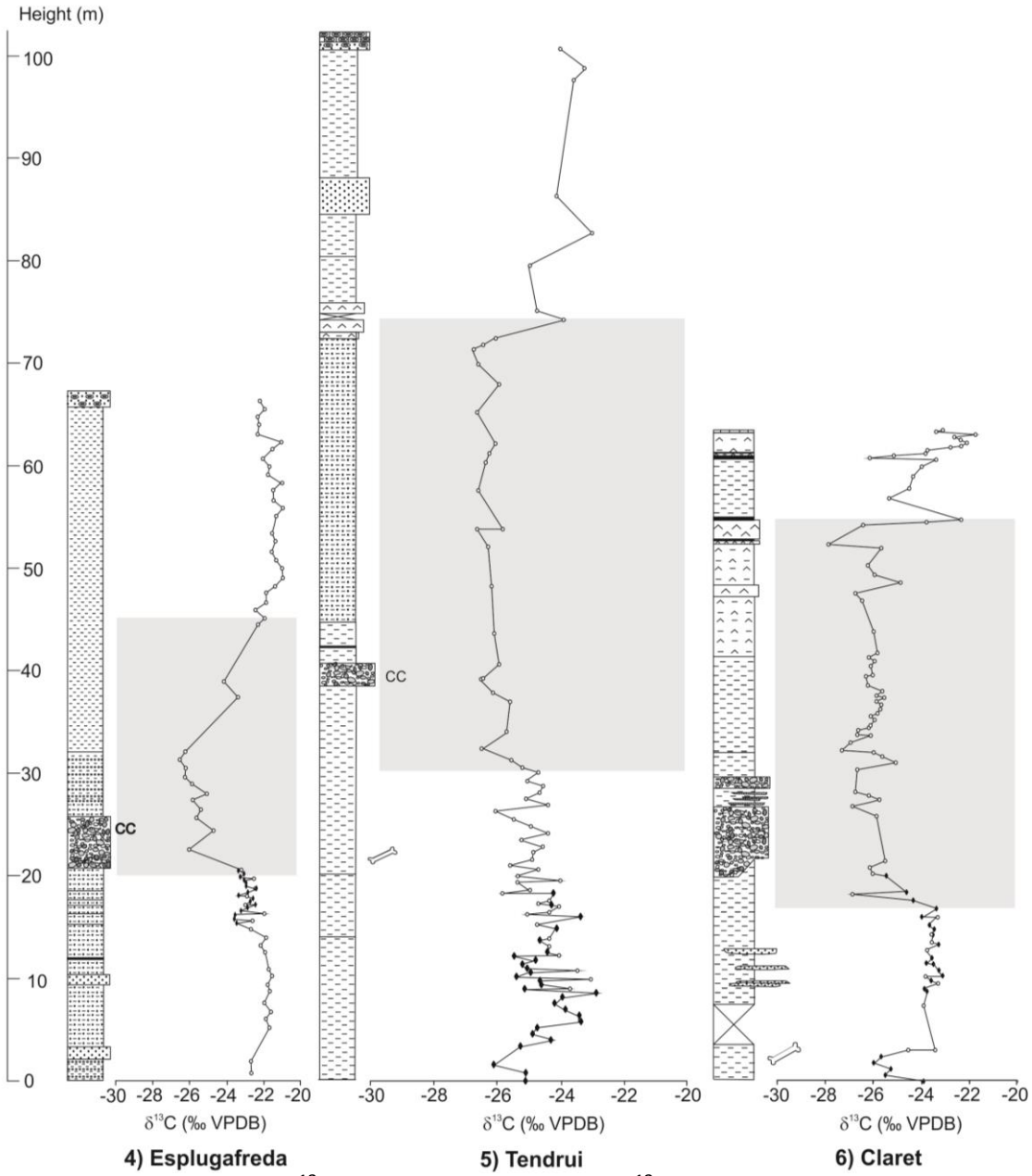

Figure 2.6. Continental $\delta^{13}C_{TOC}$ data. Lithology and $\delta^{13}C_{TOC}$ for the continental sections only. Grey boxes indicate inferred CIEs associated with the PETM; clear circles indicate previously published data (Domingo *et al.*, 2009), filled diamonds indicate new data from this study. See Figure 2.3 for lithological key.

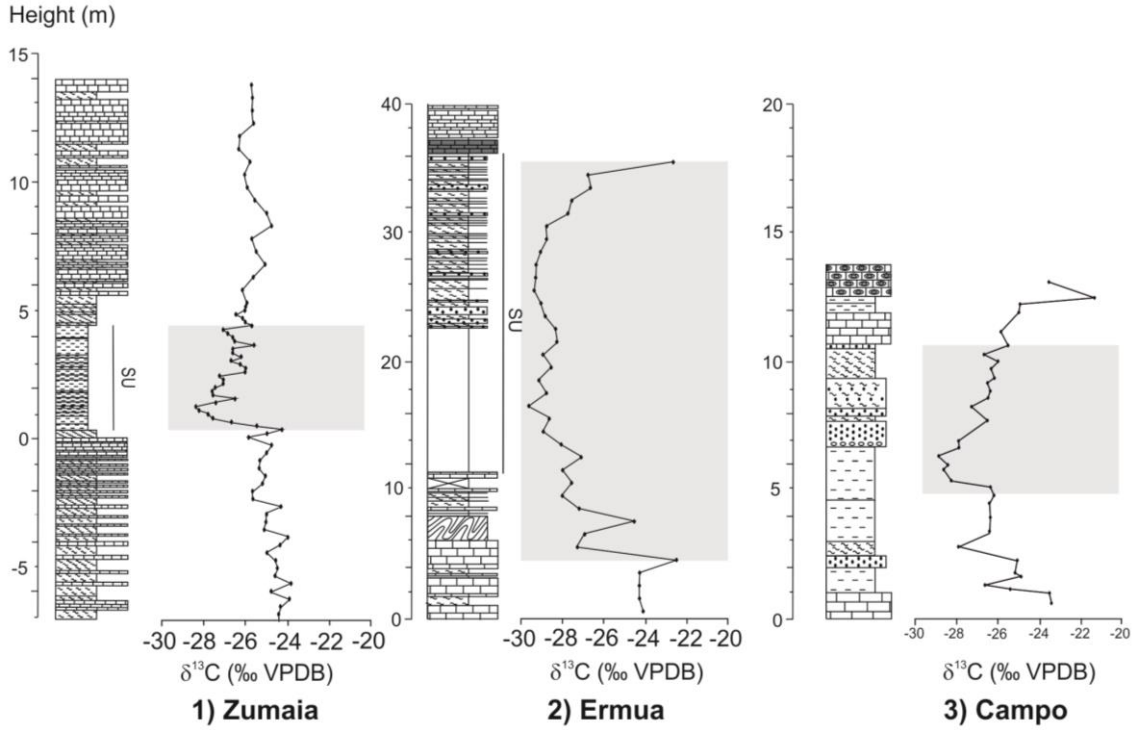

Figure 2.7. Marine $\delta^{13}C_{TOC}$ data. Lithology and $\delta^{13}C_{TOC}$ for the marine and transitional sections only. Grey boxes indicate inferred CIEs associated with the PETM. SU = Siliciclastic Unit. See Figure 2.3 for lithological key and Figure 3.2 for biostratigraphical information. Note different scales used throughout.

Regression analysis was conducted to determine if a significant logarithmic correlation between $\delta^{13}C_{TOC}$ and wt%TOC is present for the continental sections, in either pre- plus post- CIE sediments or CIE sediments. For most of the sections a significant correlation was not observed ($r2 \leq 0.19$, Table 2.2., Figure 2.5), although the pre- and post-CIE correlation coefficient for Claret is 0.57, indicating a possible logarithmic relationship between the $\delta^{13}C_{TOC}$ and wt%TOC of the samples in this section. A similar relationship has been observed by Wing *et al.* (2005), Wynn *et al.* (2005) and Wynn (2007), who suggested that a logarithmic relationship may imply further decomposition of organic matter after burial. Care must be taken when interpreting results where such a logarithmic relationship is observed. The dependence of wt%TOC on lithology was assessed using the students t-test. Results indicate that wt%TOC may be dependent on certain lithological types in the sections (Tables 6.1.1 to 6.1.6 of Appendix 1). Although

statistically significant differences are observed between some pairs of lithologies, they do not necessarily correspond to the lithologies observed throughout the CIEs. Furthermore, those differences do not exhibit consistency among sections. This would be indicative of the independence of the wt%TOC and the sampled lithology. Further statistical tests comparing pre-CIE to CIE $\delta^{13}C_{TOC}$ values demonstrate that statistically significant differences occur between CIE $\delta^{13}C_{TOC}$ values and those from before the CIE (Table 2.2.) in all sections. The $\delta^{13}C$ CIE magnitudes are consistently higher in the marine sections than previously published data based on carbonates (Table 2.3.), whilst the opposite is true for continental sections; both methods however show no apparent relationship between magnitude of the CIE and depositional environment. This verifies the results of previous studies in this region using the $\delta^{13}C$ values of carbonates, which also illustrate no observable relationship between the magnitude of CIE and depositional environment (Schmitz *et al.* 1997, 2001; Molina *et al.* 2003, Schmitz and Pujalte 2003, 2007).

Table 2.3. Comparison of $\delta^{13}C_{TOC}$ CIE magnitude calculated using different methods and previously published $\delta^{13}C$ measured from carbonates. Method 1 refers to the method used in this study (see text for an explanation; termed "maximum CIE" approach); Method 2 refers to the method used in previous studies (termed "average CIE" approach. [1.] Schmitz and Pujalte (2007); [2.] Schmitz and Pujalte (2003); [3.] Schmitz *et al.* (2001); [4.] Schmitz *et al.* (1997).

Section	Setting	Published CIE magnitudes for carbonate carbon (‰ VPDB)	CIE magnitude calculation		Difference
			Method 1 (‰ VPDB)	Method 2 (‰ VPDB)	
Claret	Continental	6.0 – 7.0[1]	3.5	1.9	1.6
Tendrui		6.0 – 7.0[2]	1.7	1.4	0.3
Esplugafreda		6.0 – 7.0[2]	4.1	2.0	2.1
Campo	Transitional	-	2.1 – 4.8	1.0 – 2.9	1.5
Ermua	Marine	5.0[3]	4.8	3.8	1.0
Zumaia		2.0[4]	4.1	1.7	2.4

2.4 DISCUSSION

2.4.1 MAGNITUDE OF CIE

There is low but sufficient TOC (ca. 0.2 – 2%) within the sediments through all six sections to generate high-resolution isotope curves from which the PETM can be identified. Differences in carbon sources or even changes in source(s) through the PETM in each section could contribute to the recorded differences in the magnitude of the CIE between sections. Some will comprise of a mixture of marine and continental organic matter (i.e., Zumaia, Ermua and Campo) and some exclusively continental organic matter (i.e., Claret, Tendrui, and Esplugafreda). It is widely known that $\delta^{13}C$ values can vary dramatically with changing sources due to differences in isotopic fractionation during initial photosynthetic fixation of carbon (O'Leary, 1981; Diefendorf *et al.* 2010), subsequent biochemical partitioning of carbon amongst different compound classes (Hayes 2001), and differential degradation of isotopically distinct compound classes (Lockheart *et al.* 1997). To some extent, these issues can be negated in well-mixed sediments of varying provenance, although even in these settings the isotopic signature of sediments can be biased by organic matter degradation and selective preservation (Bowen *et al.* 2004; Magioncalda *et al.* 2004; Poole *et al.* 2004; Wynn *et al.* 2005; Smith *et al.* 2007).

The magnitude of the $\delta^{13}C_{TOC}$ CIE at Zumaia, Ermua, and Campo ranges from 2.1 to 4.8‰, comparable to marine CIEs recorded elsewhere (2‰ to 5.5‰: Zachos *et al.* 2005; Schmitz and Pujalte 2007; Bowen and Zachos 2010; McInerney and Wing 2011; Tipple *et al.* 2011). Schmitz *et al.* (2001) measured a ca. 5‰ excursion in carbonate

$\delta^{13}C$ values at Ermua, whilst here a $\delta^{13}C_{TOC}$ excursion of 4.8‰ is reported. However, at Zumaia, only a 1.5 to 2‰ excursion is recorded by bulk carbonate (Schmitz *et al.* 1997), whilst the $\delta^{13}C_{TOC}$ excursion is 4.1‰.

Calculation of the magnitude of the CIE at Campo is more difficult, possibly due to the potential for alternating continental and marine organic matter sources before, during, and after the CIE interval. Several studies have suggested that Campo was located in a shallow marine setting before and after the CIE, but that continental deposition dominated during the CIE (Molina *et al.* 2000; Schmitz and Pujalte 2003). Molina *et al.* (2003) attempted to identify the PETM CIE using carbonate $\delta^{13}C$ stratigraphy at Campo, but they concluded that diagenetic overprinting made this impossible. Schmitz and Pujalte, (2003) also attempted to identify the PETM CIE using soil carbonate $\delta^{13}C$ values. However, no magnitude was calculated due to low sample resolution making determination of the CIE challenging, although they did tentatively identify the onset (Section 2.4.2). Results from this study record a stepped nature of the onset, which means that the 2.1‰ estimate for the magnitude of the CIE is tentative at Campo.

The three continental records (Claret, Tendrui, and Esplugafreda) show broadly similar $\delta^{13}C_{TOC}$ magnitudes (Figure 2.6., Table 2.1.). Domingo *et al.* (2009) published the first $\delta^{13}C_{TOC}$ results for Claret and Tendrui, and demonstrated that in both cases the magnitude of the CIE was smaller and the onset occurred earlier than that previously recorded in soil carbonate nodules (carbonates $\delta^{13}C$ = 6-7‰) from the same and

neighbouring sections of the Pyrénées (Schmitz and Pujalte 2003, 2007). Here, the magnitudes of the CIE are also smaller than that of carbonate $\delta^{13}C$ data (3.5‰ at Claret, 1.7‰ at Tendrui, and 4.1‰ at Esplugafreda), and other studies have also reported smaller PETM CIEs from $\delta^{13}C_{TOC}$ than carbonate $\delta^{13}C$ (e.g. Smith *et al.* 2007).

Studies of continental records will always be biased by changes in fractionation and reworking of organic matter, as well as changes in sedimentation rate, all of which can affect the magnitude and profile shape to varying degrees. The greater the number of records available for comparison however, the better informed any conclusions pertaining to localised and global changes will be. The data presented in this study add six new PETM records to this discussion and are derived entirely from sections from neighbouring basins within the same sediment routing system, therefore allowing more direct comparison of magnitudes. So far the data from this transect suggest that for a given system, the difference between continental (average this study: 3.1 ±1.25‰, average other studies: 4.7 ± 1.5‰; McInerney and Wing 2011) and marine (average this study: 3.7 ±1.40‰, average other studies: 2.8 ±1.3‰ McInerney and Wing 2011) organic carbon CIEs could be minimal.

2.4.2 ONSET AND RECOVERY FROM THE CIE

The higher-resolution $\delta^{13}C_{TOC}$ records presented in this study suggest differences in the timing of the CIE onset in the Iberian continental settings, compared to the carbonate $\delta^{13}C$ data obtained by Schmitz and Pujalte, (2003, 2007), where lower-resolution analysis of soil carbonate nodules placed the onset of the CIE within, and above, the

Claret Conglomerate. The discrepancy between the CIE onsets recorded here and those recorded in soil carbonate nodules may be due to sampling resolution, or the time taken for soil development, with the carbonate data recording the isotopic composition of local soil CO_2, in turn reflecting plant respiration and fractionation (Cerling 1991). Hence, it is expected that the isotopic composition of soil-nodule carbonate follows that of organic carbon causing a delay in the record of the CIE onset in carbonate nodules due to the more protracted time of soil formation. The incorporation of CO_2 with pre-CIE $\delta^{13}C$ values into the carbonate could result in a smoothed record and apparently later onset. Furthermore, a paucity of carbonate $\delta^{13}C$ data directly below the Claret Conglomerate may also mean that previous studies have not detected the true onset of the CIE.

Sedimentological studies carried out by Schmitz and Pujalte (2003, 2007) indicated that the Claret Conglomerate formed as a series of alluvial megafans which, in conjunction with carbonate $\delta^{13}C$ data, were suggested to be induced by extreme hydrological changes related to the onset of the PETM (Schmitz and Pujalte, 2007). Here it is demonstrated that the onset of the $\delta^{13}C_{TOC}$ CIE occurs prior to the deposition of the Claret Conglomerate in the Claret and Tendrui sections, and in the lower few metres of the Claret Conglomerate at Esplugafreda. Because peak CIE values occur after the conglomerate deposition (Domingo *et al.* 2009), and the onset of the CIE has been suggested to occur in ca. 15kyr (Bowen *et al.* 2006), these revised records indicate a small time-lag (<15 kyr) in the response of the landscape and depositional system, to the climate perturbation (previously assumed to be coincident with onset of

the CIE). This is in agreement with Domingo *et al.* (2009) who estimated a time-lag between the onset of the CIE and the deposition of the Claret Conglomerate of around 4-9 kyr based on sedimentation rates calculated for the Claret and Tendrui sections. This time-lag is potentially seen in the comparison of the continental and continental-marine records; the source of the Claret Conglomerate has been mapped and suggested to originate "more than 10 km to the north of the present day outcrops" (Schmitz and Pujalte, 2007; Figure 2.2.). Comparing this to the CIE recorded at each section potentially shows how the onset of the CIE records this time-lag. If deposition of the Claret Conglomerate is time transgressive then it would be expected that the stratigraphical lag recorded between the onset of the CIE and the Claret Conglomerate would vary between sections according to the distance from the source. This appears to be the case for these sections (Figure 2.6); Esplugafreda is geographically nearest to the alluvial megafans suggested to be responsible for Claret Conglomerate deposition (Figure 2.2.), whilst the sections of Claret, Tendrui, and Campo are more distal. Consequently, Esplugafreda appears to have a briefer stratigraphic lag between the onset of the CIE and the deposition of the Claret Conglomerate than the time-lags at Claret, Tendrui and Campo. However, scouring probably removed some of the underlying strata during conglomerate deposition, such that even this higher-resolution record remains imperfect, complicating the comparison of any time-lag between the onset of the CIE and Claret Conglomerate deposition.

Two sandstone beds separated by a marly interval occur at Campo ca. 6 m above the lithological change from marine to continental deposits; these beds have previously

been interpreted as the lateral equivalent of the Claret Conglomerate (Schmitz and Pujalte, 2007) and, specifically, progression of the megafan conglomeratic deposits into lower energy environments. Pujalte *et al.* (2009) suggested that the Palaeocene – Eocene boundary coincides with the base of the sandstone beds, interpreted to be the lateral equivalent of the Claret Conglomerate, based upon extensive mapping of the area, biostratigraphy, and carbonate $\delta^{13}C$ data. The $\delta^{13}C_{TOC}$ data from this study support several different interpretations, due to the stepped nature of the profile. When, however, compared to Pujalte *et al.* (2009), the onset of the CIE as recorded by $\delta^{13}C_{TOC}$ occurs just below the sandstone units, at ca. 5m height (Figure 2.7.). This suggests that this is analogous to the situation at Claret and Tendrui, where the onset of the CIE occurs prior to the Claret Conglomerate.

Differences are also recorded in the timing of the onset of the CIE in the marine realm. Schmitz *et al.* (2001) concluded that the onset of the CIE at Zumaia, based upon a carbonate record, occurs simultaneously with the lithological change to siliciclastic deposits, directly above a thick limestone bed (ca. 0.75 m thick) and coincident with a marl bed (ca. 0.30 m thick), inferring that the sedimentological change was brought about by the PETM. The onset of the CIE at Zumaia derived from $\delta^{13}C_{TOC}$ values occurs at the top of the ca. 0.30 m marl unit coincident with the start of siliciclastic deposition. This later onset suggests that the sedimentological changes may have occurred prior to the onset of the CIE.

At Ermua, however, the onset of the CIE occurs within the limestones below the lithological change to predominantly siliciclastic deposition (Figure 2.7.). This contradicts the findings of Schmitz *et al.* (2001), who found the CIE onset occurred simultaneously with siliciclastic deposition. However, Schmitz *et al.* (2001) also suggested that the carbonate isotope signals at Ermua had been diagenetically altered to a much greater extent than those of surrounding sections (e.g., Zumaia and Trabakua). Previous studies have suggested that where diagenetic overprinting is observed, isotopic analyses on organic matter could give more reliable results (Molina *et al.* 2003), due to organic matter being more resistant to acidic degradation than carbonate material. The onset of the CIEs at Ermua and Zumaia, therefore, both appear to be rapid, but occur at different lithological horizons, which is contrary to that shown by Schmitz *et al.* (2001). If the onset of the CIE associated with the PETM is assumed to be globally synchronous, this indicates that the lithological beds previously used to correlate between sections may in fact be diachronous events within the study area, and as such a time transgressive element may have to be considered. Alternatively, it may reflect limitations for the TOC-derived $\delta^{13}C$ records; for example, the apparently later CIE at Zumaia could be a consequence of organic matter source mixing associated with the sedimentological changes. Further analysis of $\delta^{13}C_{n\text{-alkanes}}$ may also help to constrain the differences recorded in $\delta^{13}C_{TOC}$ at these sections.

Recovery from the CIE in the Claret and Tendrui sections has been linked to the occurrence of a gypsum layer, suggesting a return to drier conditions and intense evaporation rates towards the end of the PETM (Domingo *et al.* 2009). However, a

comparison of CIE recovery in relation to the stratigraphic framework for other sections is lacking. A marker bed associated with a marine transgressive event in the early Eocene, known as the *Alveolina* Beds, occurs in all continental and continental-marine sections (Claret, Tendrui, Esplugafreda and Campo, respectively). The diachronous nature of this transgression is recorded in the isotope records at each section. Figure 2.2. illustrates section location in relation to the Bay of Biscay; the transgression occurred from a south-westerly direction across the region and, as such, the CIE recovery in relationship to this marker bed can be assessed. As would be expected, the CIE recovery occurs much closer to the *Alveolina* Beds at sections geographically closer to the source of the transgression. As such, Campo records the CIE recovery closest to the *Alveolina* Beds (ca, 2 m below), whilst the more distal sections of Claret, Tendrui, and Esplugafreda record the recovery from the CIE much further below the *Alveolina* Beds (ca. 20 to 25 m).

Comparison can also be made between the CIE recovery and the top of the Siliciclastic Unit at Ermua and Zumaia. Ermua is interpreted as a base-of-slope apron, whilst Zumaia is more bathyal in nature. The Siliciclastic Unit is interpreted as the product of increased continental erosion coupled with reduced hydrodynamic energy of freshwater entering the ocean (Schmitz *et al.* 2001). Ermua records the recovery almost coincident with the top of the Siliciclastic Unit, whilst at Zumaia recovery from the CIE occurs within the Siliciclastic Unit itself. Schmitz and Pujalte (2003) showed an enhanced kaolinite influx in the Siliciclastic Unit at both sections (Section 3, Figure 3.8). This enhanced kaolinite signal closely parallels the CIE, terminating coincidentally with

the top of the Siliciclastic unit at Ermua but within the Siliciclastic Unit at Zumaia. Schmitz and Pujalte (2003) argued that the increase in kaolinite content reflects deeper physical continental erosion and thus, an enhancement of terrestrial runoff, consistent with other low and mid-latitude investigations (Schmitz and Pujalte, 2003; Handley *et al.* 2012; Stassen *et al.* 2012). Therefore, these sections show a clear synchroneity between the lithological expression of the PETM and the CIE within these marine sections.

For the continental sections and the continental-marine section at Campo, the presence and cause of a time-lag between the onset of the CIE and the sedimentological response has fundamental implications for how we decode the impact of abrupt climate forcing and the sedimentary record. Assuming the near-geologically instantaneous uptake of the atmospheric carbon isotopic signature by terrestrial vegetation, and the subsequent deposition of this vegetation in terrestrial sediments, there are two potential explanations for the time-lag between the recorded bulk organic CIE and the observed sedimentological response to warming in these sediments. First, there was a genuine lag between the input of light carbon to the atmosphere and the expression of its full forcing effect on the climate system in terms of warming and hydrological change (Pagani *et al.* 2006; Secord *et al.* 2010; Rohling *et al.* 2012). To account fully for the time-lags observed between the carbon isotope and sedimentological records in these sections, this would assume that the sedimentological response to changing hydrological regimes is near-instantaneous. Second, the observed time-lag is largely due to the timescales of response of sediment

source and routing systems to a shift in hydrological regime. Given the relatively short timescales involved, of the order of 10 kyr or less, it is likely that some component of both these mechanisms is operating, and the deconvolution of each of these is challenging. Indeed, the interesting constraint for future studies would be to understand the speed with which these alluvial fan sediment systems are responding to rapid climate change. This study presents new and remarkably well-resolved constraints on the maximum response time of the systems of ~10 kyr, which should be a target for future sedimentological and geomorphological studies.

2.4.3 CIE PROFILES

The profiles recorded for each section vary with respect to the length of the CIE onset and recovery, and also to the general shape of the main body of the CIE. All profiles are generally triangular-shaped (Figure 2.1 (1)) as presented by Zachos *et al.* (2008), or box-shaped (Figure 2.1 (2)) as proposed by Bowen and Zachos (2010), although it is accepted that the shape is most likely influenced by reworking and sediment mixing. The CIEs recorded at Zumaia and Campo are similar to those recorded by Zachos *et al.* (2008) from three deep-sea sections in the Southern Ocean, Central Pacific and South Atlantic. Specifically, all records document a relatively rapid CIE onset, followed by a gradual return to pre-CIE $\delta^{13}C$ values (Figure 2.1 (1)). In contrast, the sections of Claret, Tendrui (both continental), and Ermua (marine) are similar to those of Bowen and Zachos (2010), in that all achieve a semi-stable state following the rapid onset, before finally recording a relatively rapid return to pre-CIE $\delta^{13}C$ values (Figure 2.1 (2)). The Esplugafreda section is more difficult to interpret due to low sample resolution in

the recovery section of the CIE profile, although, data around the onset appear to follow the box profile of Bowen and Zachos (2010) in that a continued negative excursion is recorded post-onset.

Sedimentation rates are important in determining the shapes of the CIE profiles; higher sedimentation rates may lead to the onset of the CIE appearing more gradually, and vice versa. Such rates are notoriously challenging to determine for continental settings due to a lack of robust age control. For the marine sections, Schmitz *et al.* (2001) apply different sedimentation rates to the Siliciclastic Unit at Zumaia and Ermua based on carbon isotope stratigraphy. Their carbonate isotope results suggest the Siliciclastic Unit formed synchronously at both sections, and as such a much higher sedimentation rate is calculated for Ermua (Siliciclastic Unit thickness ca. 20m), than that for Zumaia (Siliciclastic Unit thickness ca. 5m). The higher-resolution data presented here agree with the carbonate $\delta^{13}C$ data at Zumaia, but not at Ermua where $\delta^{13}C_{TOC}$ data suggest an earlier onset of the CIE, an observation in agreement with previous work (Orue-Etxebarria *et al.*, 1996) where the base of the Siliciclastic Unit at Zumaia was correlated with the base of the slump deposit seen at Ermua using sequence stratigraphy. This may suggest even higher sedimentation rates recorded at Ermua than previously calculated.

In this study, the CIE at Zumaia and potentially Campo follow the classical profile, but all the other sections do not. The fact that both profiles are present within the same and neighbouring basins clearly indicates that localised factors, such as changing

sedimentation rates, differential compaction, or depositional hiatuses in the record, are contributing to profile shape, likely in marine and terrestrial settings.

2.5 CONCLUSIONS

$\delta^{13}C_{TOC}$ and TOC data from six sections spanning a continental to marine transect through the PETM in northern Spain are presented. These data represent the highest-resolution $\delta^{13}C$ records for these sections to date, and the first organic data from four of the sections (Esplugafreda, Campo, Ermua and Zumaia). Regression analyses indicate that $\delta^{13}C_{TOC}$ values are independent of wt%TOC, suggesting that lithological changes have not impacted the isotopic records of the continental sections, and *t*-tests indicate the CIE is of statistically significant magnitude. The magnitude of the CIE amongst the six sites is variable, ranging from 1.7 to 4.8‰, with no consistent relationship between magnitude and depositional environment. The continental sections in this study record a greater CIE magnitude than the average recorded for marine sections globally, although there is no offset between the terrestrial and marine CIEs within this given depositional system. Different CIE profile shapes are recorded for different sections, fitting both the triangular profile described by Zachos *et al.* (2008) and the box profile proposed by Bowen and Zachos (2010). The variability in both CIE magnitude and shape, within a single terrestrial to continental margin depositional system, clearly demonstrates the significant effects that organic matter reworking and transport can have on the preserved carbon isotope signals.

The onset of the CIE appears to have occurred prior to the base of the Claret Conglomerate in most of the continental sections, whilst at the marine section of Ermua the CIE onset occurred prior to the base of the Siliciclastic Unit. This is in contrast to previous studies which have placed the CIE above or coincident with lithological changes in both the continental and marine realms. The data presented in this study, therefore, suggest that a lag occurred between the onset of the PETM and changes in the weathering/erosional regime, similar to findings of previous workers (e.g., Handley *et al.* 2012).

3 A MULTI-PROXY STUDY OF THE PETM AT THE ZUMAIA SECTION, SPAIN

ABSTRACT

The Palaeocene – Eocene Thermal Maximum (PETM) is thought to be the most appropriate analogue of the Cenozoic for rapid injection of carbon into the global climate system, and provides insight into how the Earth system responds to rapid carbon cycle perturbation. However, debate continues over the amount, source and mechanisms of carbon release. Here, data is presented for total organic carbon ($\delta^{13}C_{TOC}$), bulk carbonate ($\delta^{13}C_{CARB}$), and *n*-alkane ($\delta^{13}C_{n\text{-alkane}}$) $\delta^{13}C$ profiles across the PETM at the marine section of Zumaia, northern Spain. This represents the first $\delta^{13}C_{n\text{-alkane}}$ record for this section and the highest resolution $\delta^{13}C_{CARB}$ record, allowing comparison of terrestrial and marine carbon isotope excursions (CIEs) within one section. The bulk $\delta^{13}C_{TOC}$ profile records a CIE magnitude of 4.1‰, whilst the terrestrial $\delta^{13}C_{n\text{-alkane}}$ profile records 5.5‰ and the marine $\delta^{13}C_{CARB}$ values record 6.0‰. This demonstrates that no obvious difference is recorded in the $\delta^{13}C_{n\text{-alkane}}$ (terrestrial) and $\delta^{13}C_{CARB}$ (marine) CIE magnitudes at this site, contrary to observations reported between other widespread localities. Unusually, a sharp ^{13}C-enrichment is recorded in both $\delta^{13}C_{n\text{-alkane}}$ and $\delta^{13}C_{CARB}$ values immediately following the onset of the CIE, which is interpreted as potentially reflecting a changing palaeohydrological regime and the associated reworking of ancient carbon in the system. Palynological data are used to assess the extent of reworking and degradation, and also to determine the dominant palynomorph types throughout the section. At the current data resolution, no shift in the dominant vegetation from mixed gymnosperm/angiosperm to purely angiosperm flora was detected at this locality, although transport bias has to be taken into account in this interpretation.

3.1 INTRODUCTION

The PETM is characterised by a prominent negative carbon isotope excursion (CIE) in both marine and continental records and has been of interest to the scientific community since its discovery more than two decades ago (Kennett and Stott 1991). This interval was a hyperthermal event that is estimated to have lasted 120 – 220 ka (Farley and Eltgroth 2003; Rohl *et al.* 2003, 2007; Aziz *et al.* 2008; Murphy *et al.* 2010). It is postulated to be one of the most abrupt and extreme climate events documented in the geological record, with profound effects recorded in the atmosphere, biosphere and geosphere (Bowen *et al.* 2006). Since its discovery, 165 PETM sections have been identified and studied worldwide (McInerney and Wing 2011).

One of the major challenges in investigating the PETM is investigating the source and mechanism of release of the carbon responsible for the CIE. Current suggestions include methane clathrate destabilisation ($\delta^{13}C$ ~ –60‰; Dickens *et al.* 1995, 1997; Katz *et al*. 1999), burning of peat and coal deposits through wildfires ($\delta^{13}C$ ~ –22‰; Kurtz *et al*. 2003), injection of magma into organic rich sediments leading to thermogenic methane release ($\delta^{13}C$ ~ –30‰; Svensen *et al*. 2004, 2010; Westerhold *et al.* 2009), and permafrost thawing ($\delta^{13}C$ ~ –30‰; DeConto *et al.* 2012). Each source of carbon has a characteristic $\delta^{13}C$ signature, meaning that the requisite mass of each carbon source necessary to cause the CIE varies, but can be estimated (McInerney and Wing, 2011). Currently, estimates range from 1,500 Gt to 12,000 Gt of carbon (Dickens *et al.* 1995; Dickens 2003, 2011; Panchuk *et al.* 2008; Zeebe *et al*. 2009; Cui *et al*. 2011), dependant upon carbon source, isotopic composition and, crucially, the inferred magnitude of the CIE.

A MULTI-PROXY STUDY OF THE PETM AT THE ZUMAIA SECTION, SPAIN

The Zumaia section, located in the Gipuzkoa Province, northern Spain, is one of the best known and most studied PETM sections worldwide (Canudo and Molina, 1992; Canudo *et al*. 1995; Schmitz *et al*. 1997, 2001; Baceta *et al*. 2000; Bernaola *et al.* 2006; Dinares-Turell *et al.* 2007; Alegret *et al*. 2009; Storme *et al*. 2012). Numerous bio-, magneto- chemo- and lithostratigraphic studies have been conducted at Zumaia, identifying the PETM and associated impacts on the sedimentology, hydrology, and biology of the region during this time (Canudo and Molina 1992; Canudo *et al.* 1995; Schmitz *et al.* 1997; Baceta *et al.* 2000; Schmitz *et al.* 2001). Previous studies have linked a Siliciclastic Unit found at Zumaia and in the surrounding region to the CIE associated with the PETM (Schmitz *et al*. 2001). It was suggested that the Siliciclastic Unit reflects a change in the climate and hydrology toward a warmer and seasonally drier climate, leading to vegetational collapse and subsequent increased continental erosion. Schmitz *et al.* (2001) used carbonate nodules to measure the CIE associated with the PETM, and suggested that the change to siliciclastic deposits was coincident with the onset of the CIE. Manners *et al.* (2013) found through the measurement of bulk total organic carbon that a time-lag between CIE onset and siliciclastic deposition occurred, suggesting that whilst this sedimentological change was most likely a consequence of the PETM, a time-lag may have occurred between climatic change and sedimentological response (see also Chapter 2).

This study presents high resolution $\delta^{13}C$ profiles of total organic carbon (TOC), *n*-alkanes (C_{29} and C_{31}), and new carbonate data from the Zumaia section, building upon the work of Manners *et al.* (2013) and Chapter 2. Onset of the CIE in relation to the Siliciclastic Unit is assessed and compared to previous interpretations (Schmitz *et al.*

2001). This is one of the few sections in the world where marine and terrigenous isotope profiles can be compared, both in terms of magnitude and profile shape. The profiles do vary among the records, although mixed sources and reworking may also be controlling the structure to some extent; therefore, controls on the CIE are tentatively examined. The terrigenous *n*-alkane $\delta^{13}C$ profile is evaluated in terms of potential reworking, extent of degradation of samples, and source changes using palynological and other *n*-alkane-specific proxy data such as average chain length (ACL; nC_{27-33}), carbon preference index (CPI; nC_{27-33}), and odd-over-even predominance (OEP; nC_{27}, nC_{29} and nC_{31}). Vegetational change across the boundary is also assessed using palynological data and compared with other proxy data.

3.2 SAMPLE LOCATIONS AND METHODOLOGY

3.2.1 GEOLOGICAL SETTING

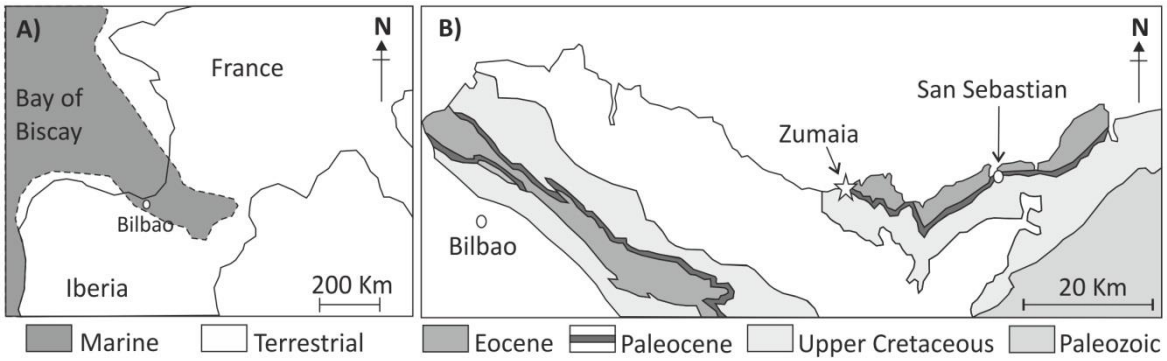

Figure 3.1. A) Palaeogeographical map of western Europe; B) simplified geological map of the study region showing the most important Palaeocene outcrops and the location of the Zumaia beach section. Modified from Schmitz *et al*. (2011).

The Zumaia section (N 043°18´4.5", W 002°15´31.2") is located on the Itzurun Beach in the Basque Basin of northern Spain (Figure 3.1). It contains a biostratigraphically

complete and well-preserved record of the PETM (Figure 3.2; Schmitz and Pujalte 2003; Bernaola *et al.* 2006; Alegret *et al.* 2009; Schmitz *et al.* 2011).

High sedimentation rates are documented at this section during the PETM interval, resulting in it being recognised as one of the most expansive open marine sections of the Palaeocene (Schmitz *et al.* 2001; Bernaola *et al.* 2006). Upper Palaeocene and lower Eocene deposits are thought to have been deposited in a middle or lower bathyal environment (Canudo *et al.* 1995) with sedimentation in an estimated 1000m water depth (Baceta *et al.* 2000). The bulk of the P/E BI comprises hemipelagic limestone and marlstones (Figure 3.3) with a ca. 0.7 m thick limestone unit in the uppermost Palaeocene. This limestone is capped by a ca. 30 cm thick marlstone bed, above which there is a ca. 4 m thick interval known as the Siliciclastic Unit composed of clay. Above the Siliciclastic Unit (lowermost Eocene), a thick bed of marlstones (ca. 1 m) is capped by hemipelagic limestones and marls, much like those recorded below the Siliciclastic Unit.

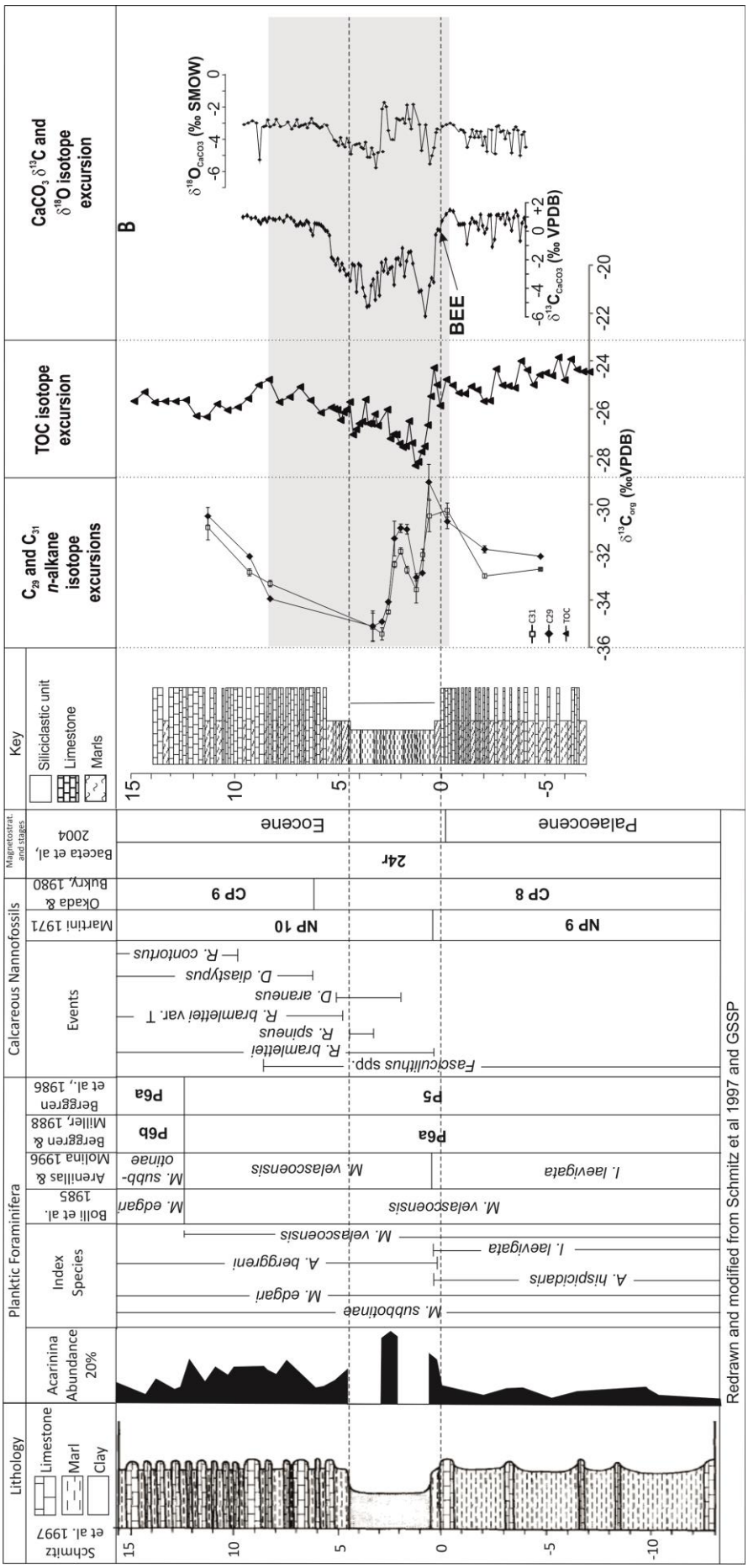

Figure 3.2. Biostratigrahical panel for the Zumaia section modified from Schmitz *et al.* (1997) showing biozones, magnetostratigraphy and the benthic extinction event (BEE) associated with the PETM across the Paleocene/Eocene boundary interval. This is correlated to data from this study on the right hand side of the panel. Grey box indicates all recorded CIEs.

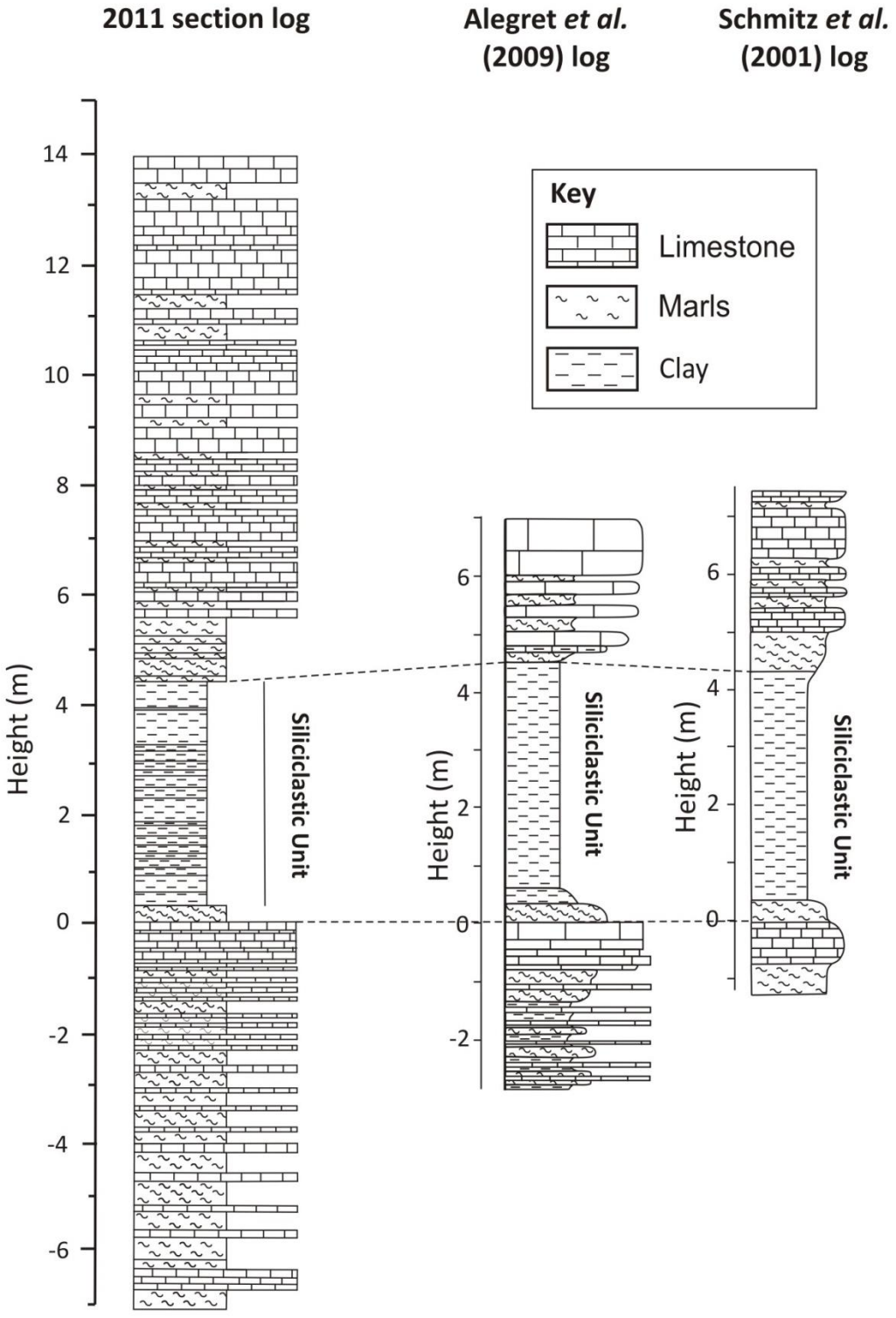

Figure 3.3. Zumaia section log produced in this study (left) compared to previously published logs (centre, Alegret *et al.* 2009; and right, Schmitz *et al.* 2001. This lithological log is consistent with both Schmitz *et al.* (2001) and Alegret *et al.* (2009) and, as such, the start of the log is defined at the same lithological horizon (the base of the Siliciclastic Unit).

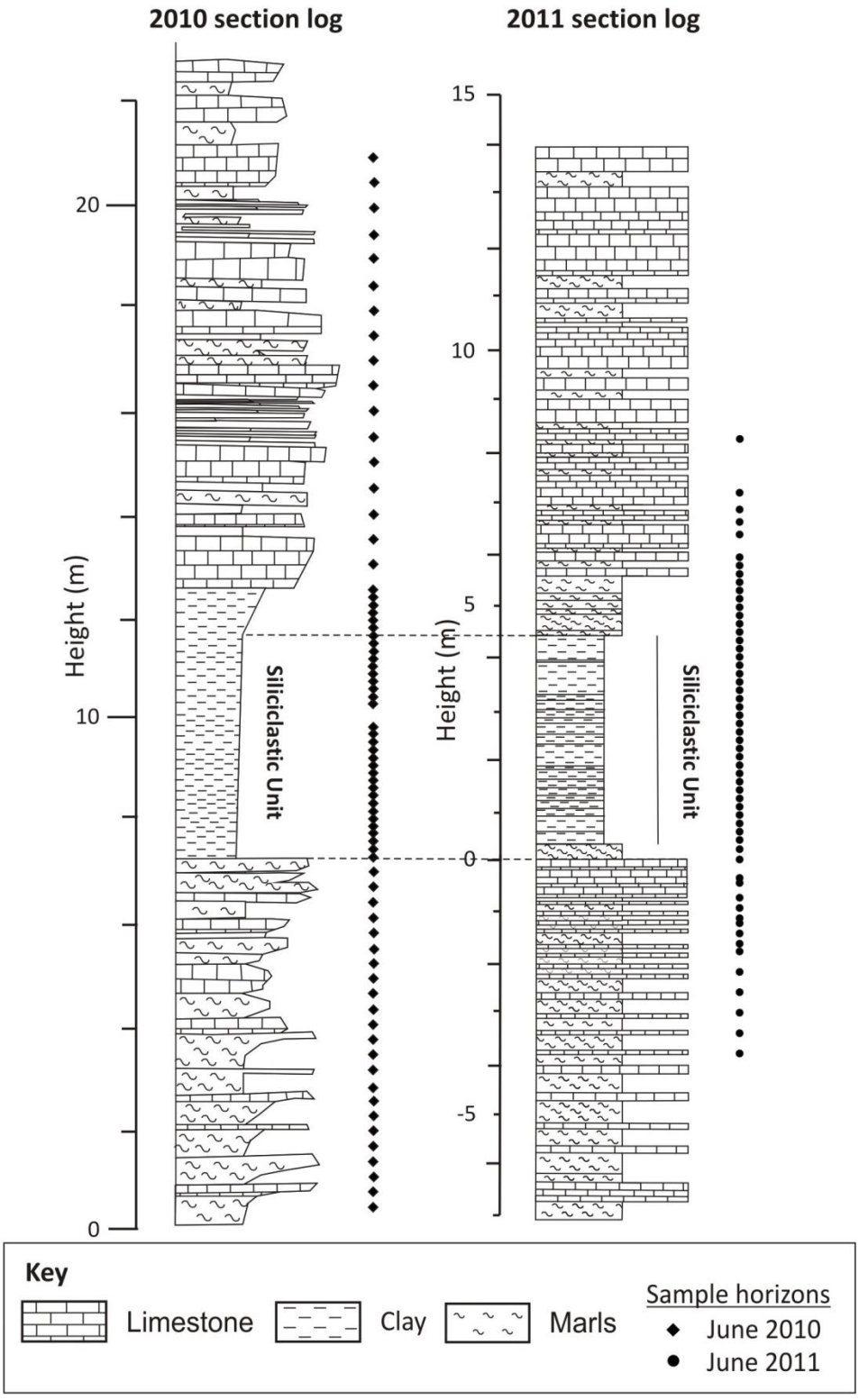

Figure 3.4. Lithological correlation for the Zumaia section to correlate samples collected during 2010 and 2011 field seasons. Dotted lines indicate same horizons on both logs.

3.3 METHODS

In total, 135 samples were collected from the Zumaia section over two field seasons (79 in June 2010 collected by H.R.M and L.D., and 56 in June 2011 collected by H.R.M. and T.D.J.). Sampling frequency varied between the two field seasons, with a mean sampling resolution of 30 cm in June 2010, and 20 cm in June 2011. Logs created over the two field seasons were correlated to each other by means of a simple lithological correlation in order to place samples in the correct stratigraphic order. Section heights were similar for both logs (Figure 3.4) with the only correlative marker bed (the Siliciclastic Unit) having a similar thickness in both instances. Lithological correlation was, therefore, achieved by setting the base of the Siliciclastic Unit as 0 m and adjusting all sample heights for both logs relative to this datum. Sample heights for both field seasons were then combined and arranged in height order against the log created in 2011. Prior to any chemical treatment all whole rock samples were oven dried (30°C, 24 hours) and powdered using a granite pestle and mortar.

3.3.1 TOTAL ORGANIC CARBON (TOC) AND TOTAL NITROGEN (TN): DETERMINATION OF WT% TOC, TN AND $\delta^{13}C_{TOC}$

Seventy-nine samples were powdered using a granite pestle and mortar. Decarbonation was conducted following the methodology of Domingo *et al.* (2009) using excess hydrochloric acid (10% v/v) until any visible sign of reaction had ceased. The sample was repeatedly washed with deionised water until a neutral solution was obtained, then oven dried (30°C, 24 hours). Total organic carbon (TOC) and total nitrogen (TN) content were measured at the NERC Isotope Geosciences Laboratory (NIGL; Keyworth, Nottingham) using a Carlo Erba 1500 elemental analyser with acetanilide used as the calibration standard. Replicate analyses indicated a precision of

±0.1 wt% in well-mixed samples (1 Standard Deviation, SD). Stable isotope $\delta^{13}C_{TOC}$ analysis was also conducted at NIGL using a Carlo Erba 1500 EA online coupled to a VG TripleTrap. This setup also included a secondary cryogenic trap in the mass spectrometer for samples with very low carbon content. The mean standard deviation on replicate $\delta^{13}C_{TOC}$ analyses of laboratory standard broccoli (BROC1) and soil (SOILB) was between 0.1 and 0.4‰. $\delta^{13}C_{TOC}$ are reported in standard ‰ notation relative to Vienna Pee Dee Belemnite (VPDB).

3.3.2 CARBONATE (CARB): DETERMINATION OF WT% CARB, $\delta^{13}C_{CARB}$ AND $\delta^{18}O_{CARB}$

One hundred and twenty samples were prepared for weight percent calcium carbonate (wt% $CaCO_3$), $\delta^{13}C_{CARB}$ and $\delta^{18}O_{CARB}$ determination and analysed at NIGL. Sample material was powdered using an agate pestle and mortar and enough sample to yield 10 mg carbonate was reacted with anhydrous phosphoric acid *in vacuo* overnight at a constant 25°C. Liberated CO_2 was separated from water vapour under vacuum and collected for analysis. Measurements were made on a VG Optima mass spectrometer (standard reproducibility of < ±0.2‰). $\delta^{13}C_{CARB}$ and $\delta^{18}O_{CARB}$ values are reported in standard ‰ notation relative to the VPDB scale using a within-run laboratory standard calibrated against NBS standards.

3.3.3 *N*-ALKANES: DETERMINATION OF CARBON PREFERENCE INDEX (CPI), ODD-OVER-EVEN PREDOMINANCE (OEP), AVERAGE CHAIN LENGTH (ACL) AND $\delta^{13}C_{ALKANE}$

The total lipid extract (TLE) was extracted from pre-weighed (ca. 50 g) powdered samples via sonication. For each sample, approximately 12.5 g of sediment was weighed into each of four 40 mL vials and each vial spiked with 0.25 µg 5α-androstane

and 0.5 µg deuterated triacontane ($C_{30}D_{62}$). Samples were sonicated for 15 minutes with DCM/acetone (2:1 v/v) and then centrifuged (2500 rpm, 2 min) to separate the supernatant from the sediment. The supernatant was transferred to a round bottom flask (combining extracts) and the extraction process repeated twice more per sample, ensuring the sediment and organic solvent was thoroughly mixed each time. The total extract was reduced to a minimal volume by rotary evaporation and the resultant TLE transferred to a pre-weighed 7 mL vial. Residual solvent was removed under a stream of nitrogen assisted by gentle heating (40°C). TLEs were air dried (2 hours) and re-weighed to obtain TLE masses. Separation of *n*-alkanes from the TLE was conducted using a proprietary technique used for the isolation of waxes from crude oil (T-SEP™; http://www.kat-lab.com/t-sep) to produce a de-waxed TLE and an *n*-alkane fraction (see method development and Table 6.2.4 of appendix 2 for further information).

The *n*-alkane fractions were analysed using gas chromatography-flame ionisation detection (GC-FID) to determine the relative peak areas of *n*-$C_{25\text{-}33}$. GC-FID was conducted using an Agilent 6890 gas chromatograph fitted with an autosampler (1 µL injection, splitless, inlet 300°C; constant flow mode, 1 mL min^{-1}, helium carrier gas), a HP-5 column (25 m x 0.2 mm x 0.33 µm; Agilent Technologies UK Ltd., Cheshire, UK), the FID at 300°C and the oven programmed from 40 – 300°C at 10°C min^{-1}, 10 min hold. An alternative oven programme was sometimes used (e.g., if screening a sample for compound specific isotope analysis) with the oven programmed from 40 – 300°C at 20°C min^{-1}, 10 min hold. Solvent blanks and a C_{25} – C_{33} *n*-alkane standard were analysed daily to ensure satisfactory performance of the GC system (i.e., no contamination and acceptable chromatography). The *n*-alkanes in sample extracts

were identified by retention time matching with peaks in the external standard. Carbon preference index (CPI = 2 x (C_{27} + C_{29} + C_{31})/ [C_{26} + 2 x (C_{28} + C_{30}) + C_{32}]; Eglinton and Hamilton 1967), odd-over-even predominance (OEP = (C_{n-2} + 6 x C_n + C_{n+2})/(4 x C_{n-1} + C_n x C_{n+1}), with n being an odd integer; Scalan and Smith 1970) and average chain length (ACL = (27 x C_{27} + ... + 33 x C_{33})/ (C_{27} + ... + C_{33}); Eglinton and Hamilton, 1967) values for *n*-alkanes within each sample were calculated using integrated peak data from the gas chromatograms.

$\delta^{13}C_{alkane}$ measurements were conducted at the Bristol NERC Life Sciences Mass Spectrometry Facility using two gas chromatograph-combustion-isotope ratio mass spectrometers (GC-C-IRMS): an Agilent 6890 gas chromatograph with a CTC A200S autosampler coupled to a ThermoQuest DeltaPlusXL mass spectrometer via a Finnigan MAT GCCIII interface, and a ThermoElectron Trace 2000 gas chromatograph with a CTC GC Pal autosampler, coupled to a ThermoElectron Delta XP via a ThermoElectron GCCIII interface. In each case the gas chromatograph was fitted with an HP-1 capillary column (50 m x 0.32 mm x 0.17 µm; Agilent Technologies UK Ltd., Cheshire, UK) with helium as the carrier gas (constant flow). The oven was programmed from 40 – 130°C at 10°C min^{-1}, 130°C – 300°C at 4°C min^{-1}, 20 min hold. Dependent upon sample concentration, 0.5 to 2 µL of sample was manually injected (inlet 300°C). Samples were analysed in either duplicate or triplicate relative to a reference gas and analytical precision was < ±0.5‰ as measured by replicate analysis of a standard fatty acid methyl ester (FAME) mixture. All values were quoted in standard ‰ notation relative to Vienna Pee Dee Belemnite (VPDB).

3.3.4 PALYNOLOGICAL ANALYSIS

Palynological preparation of 25 samples was undertaken at the British Geological Survey, Keyworth. Silicates were first dissolved by adding approximately 75 mL hydrofluoric acid to each sample and leaving the samples to stand for one week in a fume hood. Where necessary, samples were sieved at 10 µm (with the < 10 µm fraction removed) and placed in warm hydrochloric acid to dissolve carbonate material. All samples were then sieved at 500 µm and the >500 µm fraction was removed. Where minerals still remained, a heavy liquid separation was carried out to remove these. Samples were then washed in distilled or deionised water, dried, and mounted onto cover slips using PVA glue and cover slips mounted onto the slides with Elvacite. Pollen and spores were counted from prepared slides by scanning transects across the slide (Phillip Jardine: P.J., School of Geography, Earth and Environmental Sciences, University of Birmingham). Where possible, 300 palynomorphs were counted per sample unless, (a) <300 palynomorphs were evident on the slide, or (b) one pollen type entirely dominated the sample, in which case counting was continued until 200 palynomorphs of the non-dominant types had been counted (usually resulting in counts >300).

3.4 RESULTS

Experimental data are presented in Tables 3.1 and 3.2, and Tables 6.2.4 – 6.2.8 of Appendix 2 and results are presented in Figures 3.4 – 3.7.

3.4.1 BULK SEDIMENTARY PARAMETERS: TOC, TN, $\delta^{13}C_{TOC}$, $\delta^{13}C_{CARB}$ AND $\delta^{18}O_{CARB}$

Total organic carbon (wt% TOC) and nitrogen (wt% N) content are low throughout the section, ranging from 0.1 to 0.6 wt% TOC, and 0.03 to 0.09 % N, respectively (Table 6.2.4 of Appendix 6.2). Carbon/nitrogen (C/N) ratios ranged from 1.5 – 6.5 throughout the section, indicating a predominantly algal source of total organic material (Meyers 1994), although *n*-alkanes appear to show a higher-plant derived signal. Notably, both wt% TOC and the C/N ratio increase suddenly between 9.6 – 10.3 m, coincident with the recorded increase in CPI and OEP (Figure 3.5).

Wt% CaO was measured throughout the section (Figure 3.6); prior to the CIE onset indicated by carbonate isotopes, wt% CaO is variable, ranging from ca. 15 – 40%. Coincident with the CIE onset, wt% CaO decreases to ca. 0 – 5% and remains low (ca. 5 – 10%) until 13.6 m where it recovers to 30 – 60%. The decrease in wt% CaO is coincident with a deviation to positive $\delta^{13}C_{CARB}$ and $\delta^{18}O_{CARB}$ values in the middle of the CIE (Figure 3.6, Table 6.2.5), and could be interpreted in different ways. Whilst this could be a dilution signal due to Siliciclastic Unit deposition, this would not explain the positive shift in the isotopes (Figure 3.6). Alternatively, dissolution may be affecting the carbonate record, resulting in a decrease in wt% CaO. This second explanation could also explain the deviation in carbonate isotope values, as $\delta^{13}C_{CARB}$ and $\delta^{18}O_{CARB}$ values may not be recording the primary carbonate signal, but instead a secondary

diagenetic overprint (figure 3.6 and Table 6.2.5 of Appendix 2). $\delta^{13}C_{CARB}$ values below 7.1 m fluctuate between -1.1 and +1.5 ‰, at which point they shift toward more depleted values, reaching a minimum of -6‰ at 7.7 m ($\delta^{13}C_{CARB}$ PETM CIE 6‰), slightly earlier than the most ^{13}C-depleted values in the organic records. Values then recover slightly to a maximum of -1.2‰, coincident with the return to more positive $\delta^{13}C_{n\text{-alkane}}$ values, before returning to more negative values at 10.5 m. At 12.3 m, $\delta^{13}C_{CARB}$ and $\delta^{18}O_{CARB}$ values begin to return to pre-CIE values (ranging from -0.3 to +1.1‰).

$\delta^{18}O_{CARB}$ values record a similar CIE onset to $\delta^{13}C_{CARB}$ values (Figure 3.6). Below 7.1 m values range from -3.0 to -5.0‰, above which they become more ^{18}O-depleted to a minimum of -5.6‰. A shift to more positive values occurs between 7.6 – 10 m, after which a return to more negative values occurs. Like the $\delta^{13}C_{CARB}$ measurements, $\delta^{18}O_{CARB}$ values also return to pre-PETM values at 12.3 m (ranging from -2.7 to -3.6‰). Sea surface temperatures were not calculated due to the $\delta^{18}O$ data deriving from bulk rock samples; caution is necessary when interpreting bulk rock temperatures as there are unknowns in respect to source, isotopic composition of seawater and the likely influence of diagenesis.

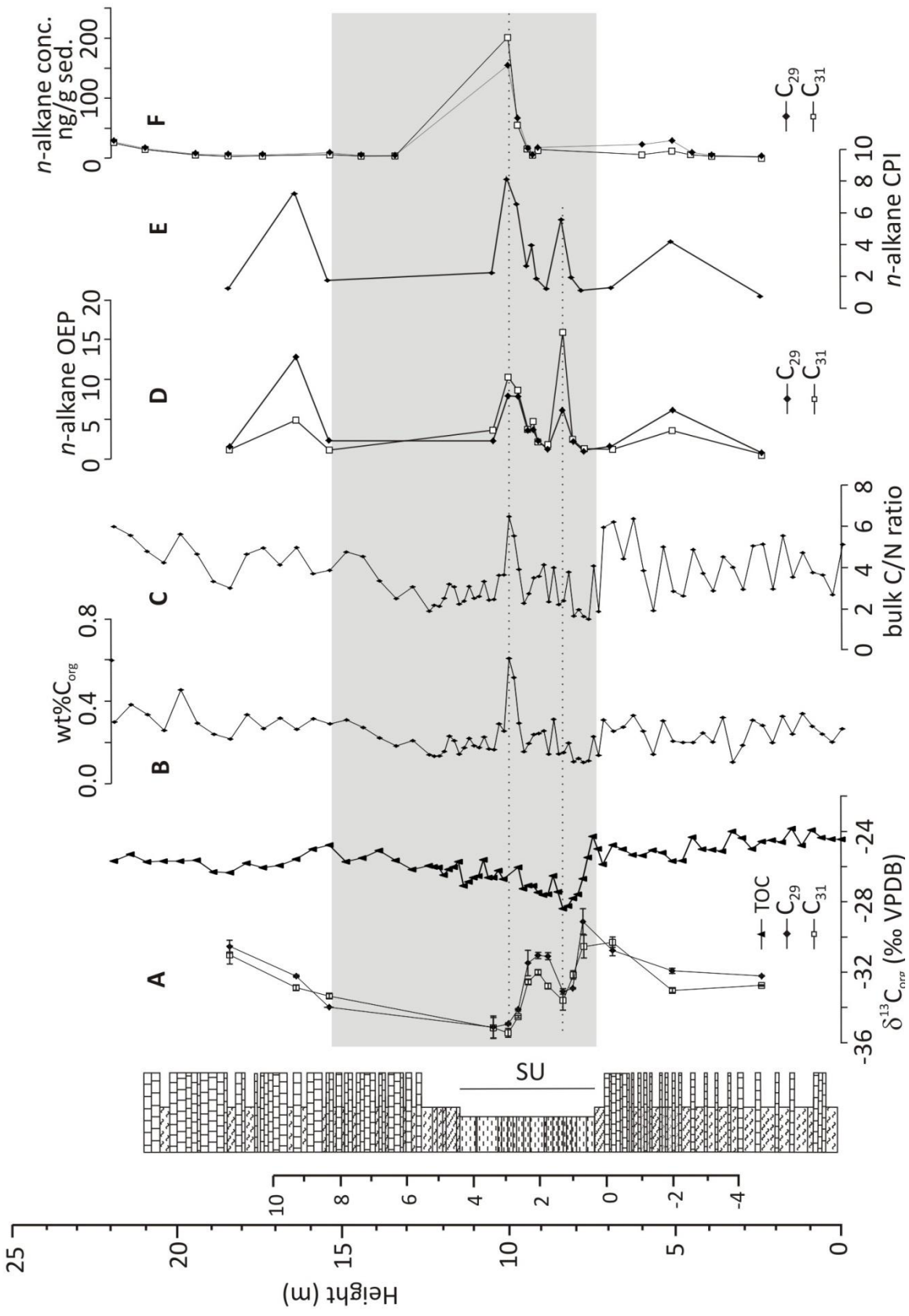

Figure 3.5. Geochemical parameters measured throughout the Zumaia section. A) $\delta^{13}C_{n\text{-alkane}}$ and bulk $\delta^{13}C_{TOC}$ values, B) wt% TOC C) bulk C/N ratios, D) odd over even predominance (OEP) calculated as described in Section 3.3.3., E) carbon preference index (CPI) calculated as described in Section 3.3.3, F) *n*-alkane concentrations (ng g^{-1} dry sediment). Grey box indicates the CIE and dotted lines illustrate peaks in OEP and CPI discussed in the text.

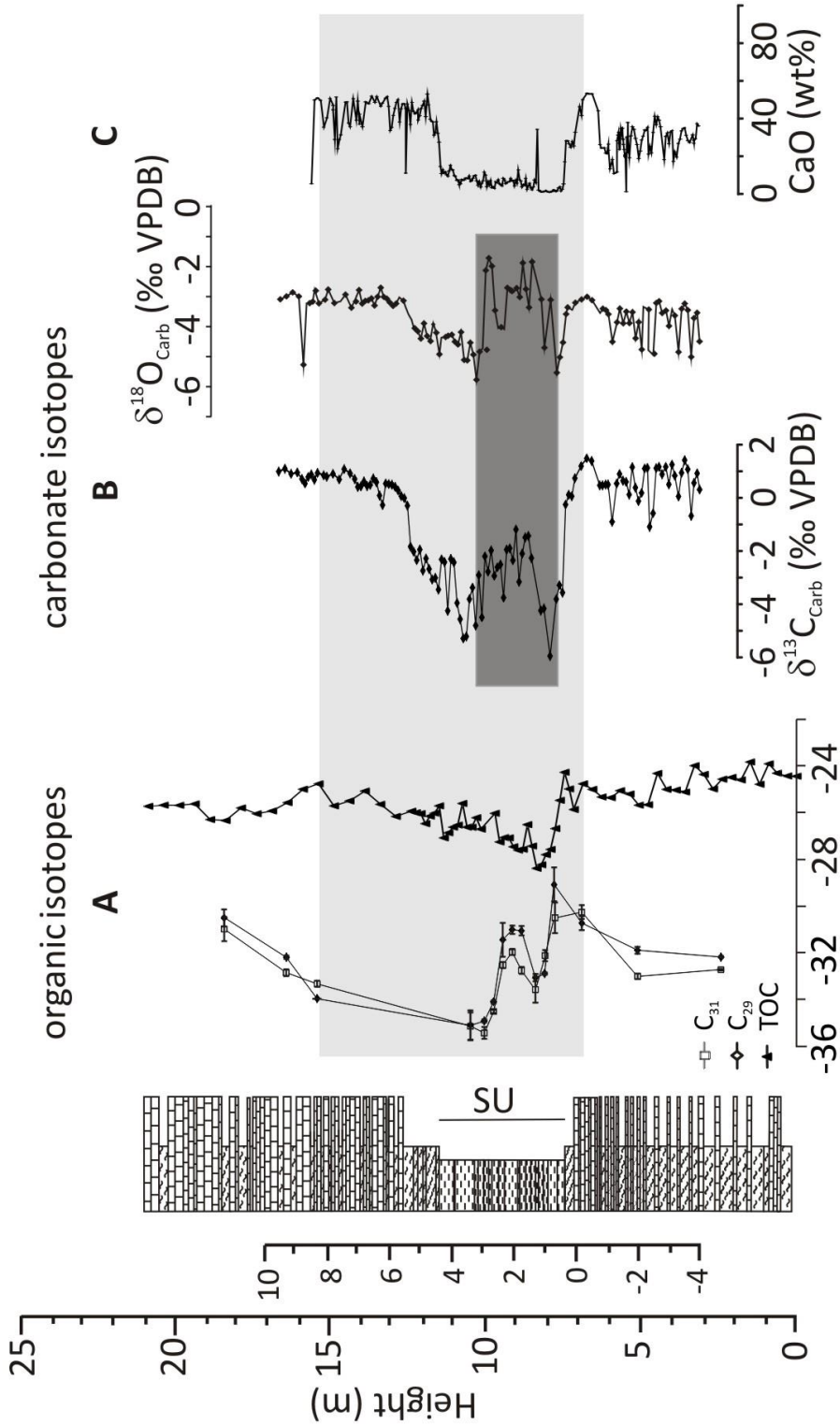

Figure 3.6. A) $\delta^{13}C$ isotope values of higher plant derived *n*-alkanes (*n*-C_{29} and *n*-C_{31}) and bulk $\delta^{13}C_{TOC}$ B) carbonate isotope values ($\delta^{13}C_{CARB}$ and $\delta^{18}O_{CARB}$) measured through the Zumaia section, C) estimated wt% CaO throughout the section. Light grey box indicates all recorded CIEs and dark grey box illustrates possible extent of dissolution of carbonate material, as evidenced by the carbonate isotope record, and the wt% CaO.

3.4.2 *N*-ALKANE ABUNDANCES AND DISTRIBUTIONS

The *n*-alkane fractions of all samples were characterised by a homologous series of *n*-alkanes, ranging from C_{25} to C_{33}, with some samples having measurable quantities of *n*-C_{22} to *n*-C_{35}. Concentrations of *n*-alkanes throughout the section were generally low, ranging from 2 – 806 ng g^{-1} dry sediment (Tables 6.2.6 and 6.2.7 of Appendix 2). However, *n*-alkane concentrations increase at the peak of the CIE, coincident with the increases recorded in OEP and CPI (Figure 3.5). Increases in OEP and CPI were also measured at the onset of the CIE. These increases at the CIE onset may further suggest enhanced terrestrial runoff during this period. Conversely, where increases are recorded in OEP and CPI in the recovery phase of the CIE, no increase in *n*-alkane concentrations occurred (Figure 3.5).

All sediments are dominated by odd-carbon numbered homologues (e.g., *n*-C_{29}, *n*-C_{31} and *n*-$C_{33;}$ Figure 3.7), a signature attributable to higher plant leaf wax *n*-alkanes (Eglinton and Hamilton 1967). CPIs and OEPs (Section 3.3.3.; Table 3.1) were used to assess the preference of odd-carbon numbered *n*-alkanes in all samples and to evaluate sources and preservation of these compounds. CPI and OEP values (*n*-C_{29} and *n*-C_{31}) range from 0.9 – 8 (CPI) and 0.5 – 16 (OEP) throughout the section and the two parameters exhibit similar trends (Figure 3.5). OEP values for *n*-C_{29} and *n*-C_{31} are generally > 1 and are fairly consistent throughout the section, apart from three horizons at 8.4, 10 and 16.4 m, where dramatic increases in OEPs are observed (OEP = 16.0, 10.3 and 4.9, respectively for *n*-C_{31}). The first horizon coincides with the onset of the CIE at this section, and the increase in OEP values at 16.4 m is coincident with the recovery from the CIE at 16.4 m. The increase in OEP at 10 m is coincident with the

maximum negative $\delta^{13}C_{TOC}$ and $\delta^{13}C_{n\text{-alkane}}$ values, during the body of the CIE. CPI trends match those of OEPs, with most CPI values throughout the section ranging from 1 – 2, however at the CIE onset, during the body (at the maximum negative $\delta^{13}C_{TOC}$ and $\delta^{13}C_{n\text{-alkane}}$ values) and at the recovery of the CIE, the CPI values increase significantly to 5.6, 8.1 and 7.2, respectively.

Table 3.1. Compound specific $\delta^{13}C$ measurements for *n*-C_{29} and *n*-C_{31} isolated from sediments at Zumaia, Northern Spain. ACL, OEP, and CPI were calculated as described in Section 3.3.3. and are plotted against the section log in Figure 3.5 and Figure 3.8.

Sample	Height (m)	$\delta^{13}C_{n\text{-alkane}}$(‰ VPDB)		ACL	OEP			CPI
		C_{29}	C_{31}		C_{27}	C_{29}	C_{31}	
ZUM-BSU+8	2.40	-32.2	-32.8	29.7	0.8	0.8	0.7	0.8
ZUM-BSU+17	5.10	-31.9	-33.0	29.6	2.3	6.2	3.6	4.2
ZUM-BSU+23	6.90	-30.8	-30.3	29.1	1.1	1.5	1.2	1.3
ZUM-SU+3	7.80	-29.1	-30.6	29.4	1.0	1.1	1.4	1.2
ZUM-SU+5	8.10	-32.9	-32.3	29.6	1.2	2.4	2.5	1.9
ZUM-SU+7	8.40	-33.1	-33.6	29.2	1.9	6.3	16.0	4.9
ZUM-SU+10	8.85	-31.1	-32.8	29.0	1.0	1.2	1.5	1.2
ZUM-SU+12	9.15	-31.1	-32.0	29.9	1.0	2.3	2.2	1.9
ZUM-SU+14	9.45	-31.5	-32.6	29.6	1.0	3.7	3.6	2.4
ZUM-SU+16	9.75	-34.1	-34.5	29.8	2.8	7.9	8.7	6.5
ZUM-SU+18	10.05	-34.9	-35.5	30.1	3.8	8.0	10.3	8.1
ZUM-SU+21	10.50	-35.1	-35.2	29.6	1.3	2.3	3.7	2.2
ZUM-ASU+5	15.45	-34.0	-33.4	29.8	2.0	2.3	1.1	1.8
ZUM-ASU+7	16.45	-32.2	-32.9	29.0	3.3	12.7	4.9	7.1
ZUM-ASU+11	18.45	-30.5	-31.0	29.5	0.9	1.6	1.2	1.3

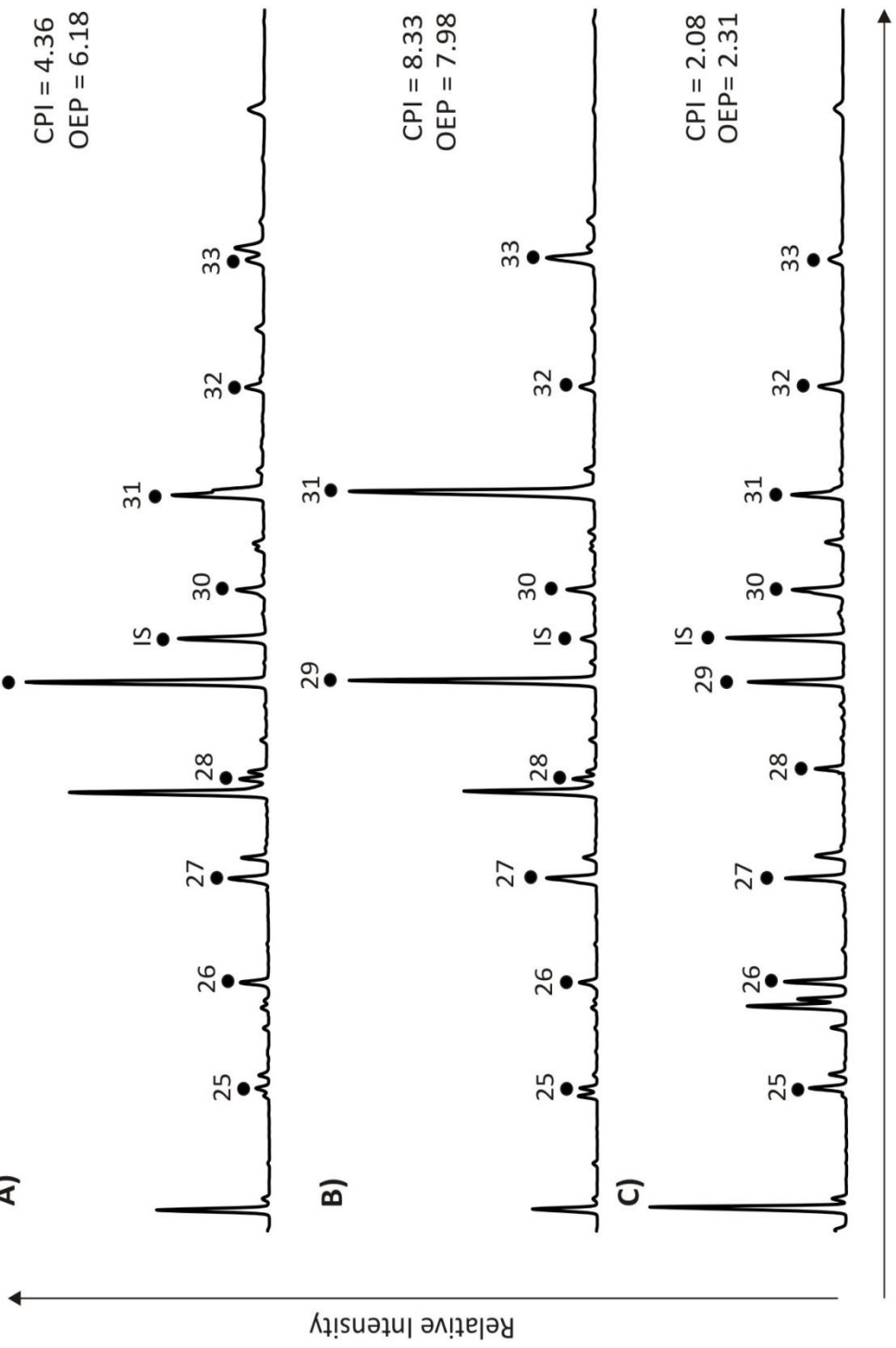

Figure 3.7. Partial gas-chromatograms of the *n*-alkane fractions for representative Zumaia sediments, demonstrating odd-over-even predominance. (A) pre-PETM (ZUM-BSU+17), (B) during-PETM (ZUM-SU+18), (C) post-PETM (ZUM-ASU+5): ● *n*-alkanes, with numbers indicating the number of carbon atoms. CPI and OEP values for each sample are displayed; OEP = C29 values.

3.4.3 *N*-ALKANE $\delta^{13}C$ VALUES

Compound specific $\delta^{13}C$ values were measured for *n*-C_{29} and *n*-C_{31} *n*-alkanes which are interpreted to primarily derive from higher plant leaf waxes (CPI ranges from 0.9 to 8.3; Table 3.1), although other potential sources are discussed in Section 3.5.1. Throughout most of the section, a slight offset in $\delta^{13}C$ values is recorded with *n*-C_{31} recording more negative $\delta^{13}C$ values than *n*-C_{29} (Figure 3.6). However, this trend is reversed for three samples (at 6.9 m, 8.1 m and 15.45 m, respectively), an observation that has also been reported by Handley *et al.* (2011). Overall however, both records display similar trends throughout the section. Values for $\delta^{13}C_{n\text{-alkane}}$ range from -29.1 to -35.1‰ for *n*-C_{29}, and from -30.3 to -35.5‰ for *n*-C_{31} throughout the section, recording more negative $\delta^{13}C$ values from 7.8 m to 10.05 m. This is interpreted to represent the onset of the CIE associated with the PETM, as confirmed by bulk $\delta^{13}C_{TOC}$ (Figure 3.6). Below 7.8 m, values range from -29.1 to -32.2‰ for *n*-C_{29}, and -30.6 to -32.8‰ for *n*-C_{31}. At 7.8 m, all values start to shift toward more negative ^{13}C values, reaching an initial minimum of -33.1‰ (*n*-C_{29}), and -33.6‰ (*n*-C_{31}) at 8.4 m; values then increase to -31.1‰ (*n*-C_{29}), and -32.0‰ (*n*-C_{31}) at 9.15 m, before becoming further depleted to -34.9‰ (*n*-C_{29}), and -35.5‰ (*n*-C_{31}) at 10.05 m. This negative excursion is interpreted as a two-step excursion into the PETM CIE (discussed further below) and the magnitude of the excursion is calculated to range between 5.8‰ (4‰ to first inflection for *n*-C_{29}) and 5.2‰ (3‰ to first inflection for *n*-C_{31}; see Manners *et al.* (2013) and Chapter 2 for magnitude calculation method). This averages to a PETM CIE magnitude value of 5.5‰ as recorded by *n*-alkanes. Above 10.05 m, values remain ^{13}C-depleted, and appear to recover from 16.45 – 18.45 m back to pre-CIE values (-30.5‰, *n*-C_{29} and -31.0‰, *n*-C_{31}).

3.4.4 PALYNOLOGY

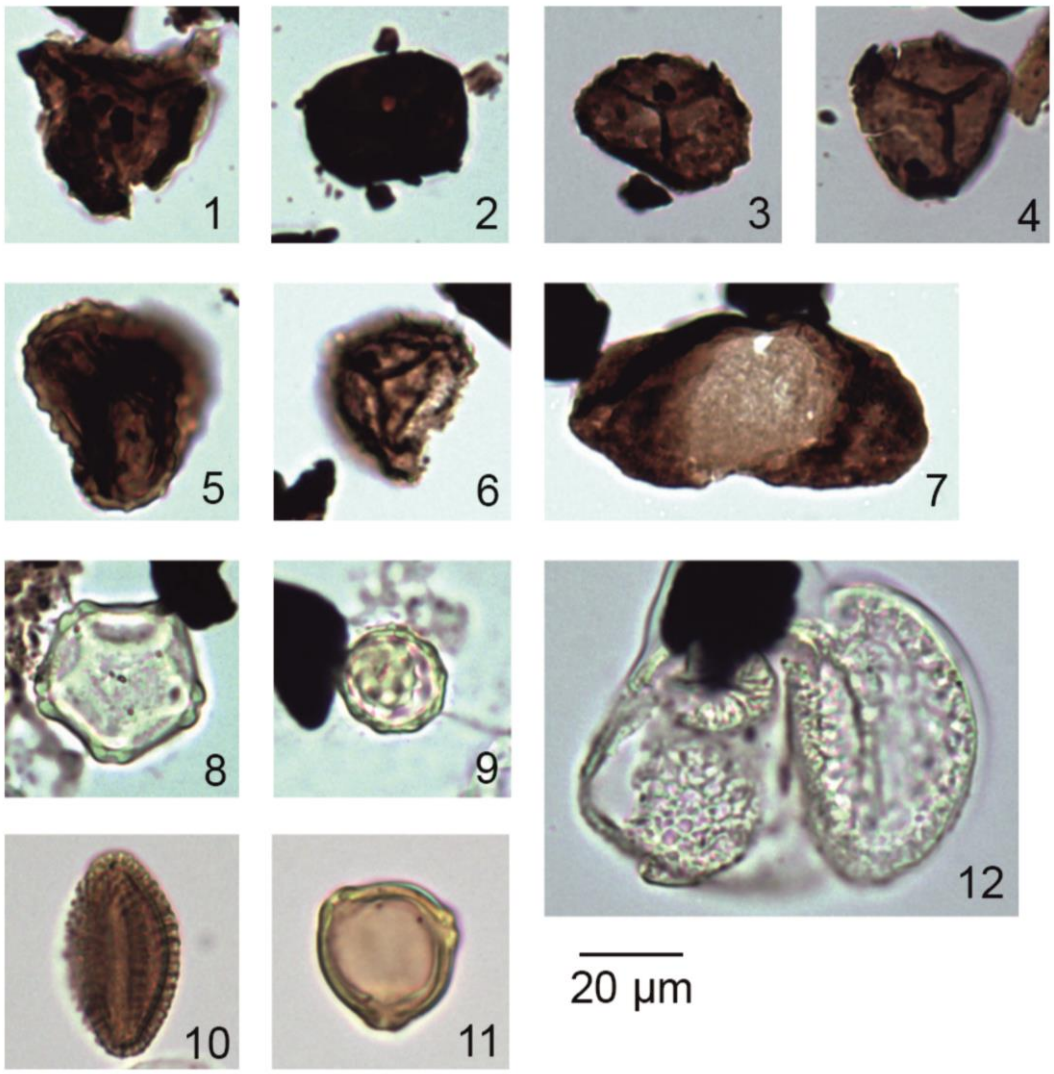

Plate 1. Reworked (1-7) and primary (8-11) sporomorphs from the Zumaia section. **(1-4)**, trilete spores from sample ZUM-SU+3; **(5 and 6)**, trilete spores from sample ZUM-SU+5; **7**, bisaccate pollen from sample ZUM-SU+6; **(8 and 9)**, *Alnipollenites* and *Periporopollenites* pollen types from sample ZUM-SU+32; **(10)**, *Tricolpopollenites* pollen from sample ZUMASU+3; **(11)**, *Triatriopollenites* pollen from sample ZUM-BSU-9; **(12)**, bisaccate pollen from sample ZUM-ASU+7. The trilete spores (1-6) were produced by pteridophytes (ferns and mosses), the bisaccate pollen (7 and 12) by gymnosperms, and the remaining pollen types (8-11) by angiosperms.

Plate 1 includes some examples of sporomorphs identified as part of this study. Palynomorph assemblages vary in preservation throughout the section, with reworking and degradation evident from 7.5 to 8.5 m based on the dominance of dark and degraded sporopmorhs and dinoflagellates cysts (lower Siliciclastic Unit; Plate 1). Throughout the rest of the section assemblages vary in abundance, with some samples

containing only very limited numbers of palynomorphs (<50; Table 6.2.8 of appendix 2). Palynomorphs, where present, comprise both terrestrial and marine groups in the form of terrestrial angiosperm, gymnosperm, and pteridophyte pollen and spores, and marine dinoflagellate cysts (Figure 3.8). Below the Siliciclastic Unit, angiosperm species proportions remain relatively constant, ranging from 57 – 66% of total plant pollen and spores. Gymnosperm species are more variable, ranging from 25 – 44%, whereas pteridophytes are consistently the lowest in abundance (0 – 8%). During the Siliciclastic Unit, angiosperm abundance is more variable, ranging from 20 – 88%, with the peak abundance occurring at 8.7 m, just after the initial carbon isotope excursion recorded in both bulk and *n*-alkane $\delta^{13}C$ records (Figure 3.8). Gymnosperm relative abundance ranges from 0 – 76%, and pteridophytes are again the lowest (0 – 13%). Above the Siliciclastic Unit, angiosperm relative abundance ranges from 8 – 58%, with a maximum occurring roughly coincident with recovery from the *n*-alkane CIE. Gymnosperm species relative abundance ranges from 42 – 92%, and pteridophytes are almost entirely absent (0 – 1% relative abundance). Dinoflagellate cyst relative abundance also varies throughout the section, ranging from 0 – 81% of total marine and terrestrial palynomorphs, with peak dinoflagellate cyst abundances occurring just after the start of the Siliciclastic Unit, and slowly declining throughout the duration of the CIE. Angiosperm ratios relative to total summed angiosperm and gymnosperm groups were calculated (Appendix 2, Table 6.2.8) to determine if any change in the dominant taxa was observed throughout the section. Maximum angiosperm abundance was recorded coincident with the CIE onset at 8.7 m (Figure 3.8), although the total sporomorph count was just eight for this sample, meaning this result should be treated with caution.

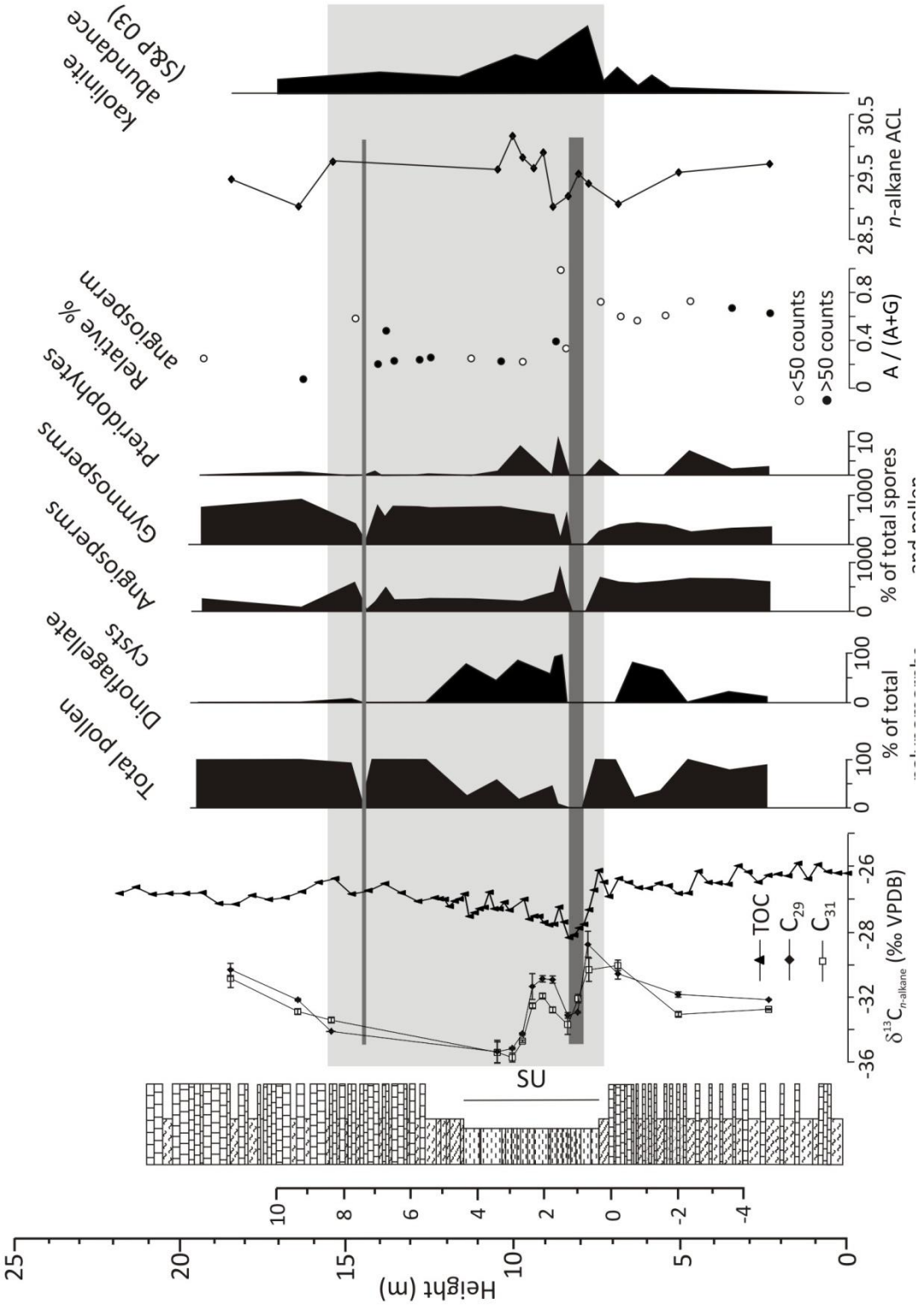

Figure 3.8. Relative abundance of groups of major palynomorphs (angiosperms, gymnosperms, and pteridophytes) expressed as percentages of the total spore and pollen counts. Terrestrial palynomorph groups are reported as a percentage relative to total plant pollen and spores, whereas marine palynomorphs (dinoflagellates cysts) are reported relative to total palynomorphs. Light grey box indicates all recorded CIEs and dark grey boxes indicate corroded (7.9 – 8.4 m) or barren samples (14.5 m). Kaolinite abundance is taken from Schmitz and Pujalte (2003) to demonstrate increased clay input into the section.

3.5 DISCUSSION

3.5.1 DEPOSITIONAL SETTING AND SOURCE INPUTS

Biomarker proxy measurements (i.e., C/N ratios, *n*-alkane concentrations, OEPs and CPIs) and palynological evidence are used to assess source inputs of supposed terrigenous material to the section. Typically, OEPs and CPIs > 4 are associated with fresh leaf waxes (Collister *et al.* 1994; McDuffee *et al.* 2004) whilst values < 4 indicate potential contributions from either marine or petroleum sources (Huang *et al.* 2000), or that the leaf waxes have been altered during burial (Kennicutt *et al.* 1987; Handley *et al.* 2011). However, very low values (<1) are typically associated with thermally mature organic matter (Kennicutt *et al.* 1987). The very high values at depths of 8.4, 10 and 16.4 m (Figure 3.5), therefore, likely reflect a strong input of relatively fresh higher plant material. These horizons are associated with elevated concentrations of *n*-alkanes, TOC contents and higher C/N ratios (Figure 3.5), all suggesting that there is an input of additional terrigenous organic matter into Zumaia sediments. By extension, lower concentrations of *n*-alkanes with lower CPIs (and lower TOC contents and C/N ratios) throughout the rest of the section apparently represent a background contribution of *n*-alkanes from a different source. This could be diagenetically altered terrestrial organic matter; i.e., plant material that has experienced more pronounced diagenetic alteration in soils via prolonged transport (e.g., Kennicutt *et al.* 1987; Handley *et al.* 2011). Alternatively, given the very low CPIs (~1) in some sediments, the *n*-alkanes could even arise from reworked, thermally mature organic matter or marine organic matter. However, whilst CPI and OEP are variable throughout the section, all samples are dominated by the *n*-alkanes C_{29} and C_{31}, indicating that whilst OEP is variable, this is still a predominantly terrigenous signal, with lower molecular weight *n*-

alkanes affecting the CPI and OEP to varying extents. Also, by extension, the similar isotope profiles for C_{29} and C_{31} suggest that there is not a complex isotopic mixing biasing their profiles.

Palynological data record an increase in abundance of terrestrial palynomorphs throughout the Siliciclastic Unit (Figure 3.8) in agreement with Schmitz *et al.* (2001), suggesting an influx of terrigenous material to the section throughout the event. The grey boxes in Figure 3.8 illustrate corroded (7.9 – 8.4 m) or barren samples (14.5 m); some of these samples also showed evidence of reworking and degradation of the palynomorphs (7.9 – 8.4 m; Plate 1). These reworked and degraded samples occur coincident with the onset of the CIE and an increase in kaolinite to the section (Schmitz and Pujalte 2003). This kaolinite flux is interpreted to represent Mesozoic material and is suggested to reflect deeper continental erosion brought about by increased seasonality. Schmitz and Pujalte (2003) suggested that this increased seasonality may have resulted in hotter and drier summers, preventing development of vegetation cover, followed by more intense rainy seasons, providing the necessary water for continental erosion. Therefore, the impoverished vegetation and degraded soils may both have contributed to the shortage or lack of palynomorphs.

There are, therefore, potentially multiple sources of organic matter deposited throughout this section. CPI and OEP values indicate a mixture of fresh and potentially diagenetically altered terrigenous material, thermally mature organic matter and/or marine organic matter. C/N ratios suggest a background of algal material within the sediments, and palynological data suggest an increase in terrestrial material

throughout the CIE, but that some samples may comprise reworked and degraded material. A previous study (Schmitz and Pujalte 2003) also suggested a contribution of reworked Mesozoic material throughout the Siliciclastic Unit. Interpretation of results is, therefore, tentative, although as previously discussed the high abundance of C_{29} and C_{31} *n*-alkanes, combined with the similarity of their isotopic profiles throughout the section may suggest a continuous fresh terrigenous input throughout.

3.5.2 ISOTOPE PROFILES AND ENVIRONMENTAL CHANGE

All isotope proxy records ($\delta^{13}C_{TOC}$, $\delta^{13}C_{CARB}$, and $\delta^{13}C_{n\text{-alkane}}$) document a rapid onset to the CIE at Zumaia, northern Spain. However, profile shape varies between isotope records (Figure 3.6), with $\delta^{13}C_{CARB}$ (and potentially $\delta^{13}C_{n\text{-alkane}}$, although this is less clear) illustrating a box-shaped profile (rapid onset, stable state, rapid recovery; Manners *et al.,* (2013) and Chapter 2). The $\delta^{13}C_{TOC}$ profile records a triangular shape indicative of a slower recovery phase or possibly a change in the dominant organic matter source, whilst all other records appear to record a more box-shaped profile. Factors such as re-working, mixing of sources, and potentially dissolution and dilution (carbonate records only) may be affecting records however, so profile shapes are compared tentatively. Dissolution and/or dilution may be affecting the carbonate records between 7.8 – 10.5 m as a result of declining ocean pH during the PETM interval (Zachos *et al.* 2005; McCarren *et al.* 2008; McInerney and Wing, 2011). This has been previously suggested by Alegret *et al*. (2009), who suggested a rapid shoaling of the carbonate compensation depth (CCD) is evidenced throughout the Siliciclastic Unit by partially corroded calcareous foraminiferal tests and decreased wt%CARB. However, Alegret *et al.* (2009) also suggested that dilution is probably affecting wt%CARB in

combination with dissolution due to an increased influx of terrigenous material throughout the Siliciclastic Unit. This is supported by the wt% CaO record produced in this study and also by Storme *et al.* (2012) who reported a dramatic decrease in the wt% $CaCO_3$ throughout the PETM interval (Figure 3.6). Variability in the carbonate carbon and oxygen isotope values prior to the onset of the CIE is interpreted to be due to noticeable lithological variability between background marl deposition and thin bands of glauconitic more cemented layers ca. 1-3cm thick. In any case, isotopic values yielded by bulk rock analysis must be treated with caution whilst no petrographical, chemical and/or cathodoluminiscence studies are available for this study, since it has been proven that diagenesis may have obscured and even reset original isotopic values (Veizer, 1992; Mitchell *et al.,* 1997; Stoll and Schrag, 2000; Rosales *et al.,* 2001). In this respect, oxygen, and to a lesser extent carbon, isotopic signals are prone to differential diagenetic alteration related to changes in the lithology as already observed in the Zumaia section (Schmitz *et al.,* 1997).

The profile of the *n*-alkane CIE records a shift to more positive $\delta^{13}C$ values shortly after the onset of the CIE (Figure 3.6). This could suggest that pulses of carbon to the atmosphere may have occurred throughout the onset and duration of the CIE, which is also potentially seen in the Southern Ocean (ODP Site 690, Bains *et al.* 1999), Polecat Bench, (Bowen *et al.* 2001, 2006; Bains *et al.* 2003), and in the South Atlantic (IODP site 1263, Zachos *et al.* 2005), but more likely this is a result of a local environmental perturbation. Garel *et al.* (2013) reported a return to more positive values as recorded by $\delta^{13}C_{n\text{-alkane}}$ data at the Vasterival Section, France, after the onset of the CIE associated with the PETM. They explained this in combination with their palynological

data as a potential reflection of a change in vegetation to more gymnosperm-dominated vegetation at this point. However, this mechanism cannot be used to explain the return to more positive values recorded here as there is no dramatic change recorded in the relative abundance of gymnosperm pollen associated with the more positive $\delta^{13}C_{n\text{-alkane}}$ values. Furthermore, Diefendorf *et al*. (2011) reported that, in modern plants, angiosperms produce on average ca. 200 times more *n*-alkanes than gymnosperms, with the latter sometimes synthesising no *n*-alkanes at all, indicating that the *n*-alkane record would almost entirely comprise an angiosperm $\delta^{13}C$ signal. This suggests that even if a change in plant community was observed, it would be unlikely to significantly affect recorded $\delta^{13}C$ values. However this study only implicates modern plants, and in areas where gymnosperms were the dominant species you would still expect to see *n*-alkanes in the sediment, potentially suggesting that PETM flora did not exhibit such a differential between species.

Kraus *et al*. (2013) suggest that major drying occurred throughout the body of the PETM interval in Wyoming, as evidenced by yellow-brown palaeosols. Other evidence for this drying throughout the body of the PETM has been identified in Wyoming, Tanzania, and the Arctic using deuterium isotopes, biomarkers, and mineralogy (Pagani *et al.* 2006; Smith *et al.* 2007; Handley *et al.* 2012). Potential evidence for this is also seen in northern Spain, where yellow palaeosols have been logged at the Claret section just above the Claret Conglomerate (Schmitz and Pujalte 2007; Domingo *et al.* 2009), which has been suggested to have been deposited <15 kyr after the CIE onset (Manners *et al.* 2013 and Chapter 2). Increased humidity has previously been linked to more depleted $\delta^{13}C$ values (ca. 2‰), and it has been suggested that this could

potentially amplify the magnitude of the CIE (Bowen *et al*. 2004; Smith and Freeman 2006). Conversely, reduced water availability associated with low precipitation has been correlated with higher $\delta^{13}C$ values (e.g., Meinzer *et al.* 1992). It follows therefore, that aridity, which has been documented later in the body of the CIE in both the USA (Wing *et al.* 2005; Kraus and Riggins 2007; Secord *et al.* 2010) and (potentially) at terrestrial sections in Spain (Domingo *et al.* 2009) could affect $\delta^{13}C_{n\text{-alkane}}$ values. This would result in a shift to more positive $\delta^{13}C_{n\text{-alkane}}$ values, and could therefore indicate that the positive shift recorded directly after the CIE onset at Zumaia is in fact a response to increased aridity during this period, and is a reflection of changes in the terrestrial palaeohydrological regime. However, Schmitz and Pujalte (2003) suggest that PETM soils reflect seasonally wetter, but generally drier conditions, and that the development of vast braid plains or megafans at the P-E boundary in the Pyrenees is consistent with model predictions of increased intra-annual humidity gradients and associated seasonal flash floods in the subtropics in a strengthened greenhouse situation (Houghton *et al.* 2001). Therefore, δD analyses would be needed to further elucidate the palaeohydrology during this period. Finally, Tipple *et al.* (2011) also documented a positive shift in *n*-alkane, TOC and carbonate $\delta^{13}C$ records just after the CIE onset, which was attributed to a subtle enrichment of surface and deep-ocean carbon pools, associated with the initial input of ^{13}C-depleted CO_2 (Zeebe *et al*. 2009).

Reworking is most likely playing a role in the structure of the *n*-alkane CIE profile. If reworked organic matter, including *n*-alkanes, was washed into the basin, this could cause a return to more positive $\delta^{13}C$ values, reflecting the reworked $\delta^{13}C$ pool. As discussed in Section 3.5.1, Schmitz and Pujalte (2003) suggested that reworked

Mesozoic material was washed into the basin coincident with the beginning of siliciclastic deposition. However, the positive shift in $\delta^{13}C_{n\text{-alkane}}$ values coincides with a gradual decrease in kaolinite abundance, indicating less physical erosion and less influence of terrestrial material. This also coincides with a drop in CPI and OEP values (to < 4) which may in turn signify a greater marine influence. This may suggest that the positive shift in $\delta^{13}C_{n\text{-alkane}}$ values is actually related to changes in the palaeohydrological regime rather than to reworking. Again, therefore, δD analyses may be crucial in resolving these questions.

Table 3.2. CIE magnitudes calculated from the different records in this study, and previous studies at Zumaia ([1] Storme *et al.* 2012, [2] Schmitz *et al.* 1997).

Data	CIE magnitude (‰ VPDB)	
	This Study	Other studies
$\delta^{13}C_{TOC}$	4.1	5.0[1]
$\delta^{13}C_{n\text{-alkane}}$	5.5	N/A
$\delta^{13}C_{carbonate}$	6.0	2.0[2]

The magnitude of the $\delta^{13}C$ CIE recorded in the three isotope records presented ($\delta^{13}C_{TOC}$, $\delta^{13}C_{n\text{-alkane}}$, $\delta^{13}C_{CARB}$) is variable, ranging from 4 – 6‰ between records (Table 3.2). Reworking and mixed sources are potentially contributing to all three records however, and as such the comparisons made here are only tentative. The mixed source $\delta^{13}C_{TOC}$ records a magnitude of 4.1 ‰, whilst the terrestrial $\delta^{13}C_{n\text{-alkane}}$ record suggests a magnitude of 5.5‰ and the marine bulk carbonate records a CIE of ca. 6‰. Previous studies for this section have yielded a magnitude of 5‰ from $\delta^{13}C_{TOC}$ (Storme *et al.* 2012), and 2‰ from bulk carbonates (Schmitz *et al*. 1997). The former is consistent with the results presented here but the latter is not and the much lower $\delta^{13}C_{CARB}$ excursion reported by Schmitz *et al.* (1997) is thought to be an artefact of the

much lower resolution of that study. According to the results presented here, both terrestrial and marine proxies show large CIEs, which indicates that for the Zumaia section, no offset between the terrestrial and marine CIEs is recorded, in contrast to comparisons at other settings (Bowen *et al.* 2004; Pagani *et al.* 2006; Smith *et al.* 2007; Zachos *et al.* 2007; Handley *et al.* 2008; Bowen and Zachos 2010; McInerney and Wing 2011; Tipple *et al.* 2011). The mean terrestrial CIE reported globally is -4.7 ± 1.5‰, whilst the mean marine CIE reported globally is -2.8 ± 1.3‰ (McInerney and Wing 2011), making both the terrestrial and marine CIE magnitudes reported here at the higher end of previous estimates (Table 3.2). This previous work also indicates that continental sections record larger CIE magnitudes than marine sections; however those data predominantly compare sections from different global localities (Koch *et al*. 1992; Bowen *et al*. 2004; Wing *et al.* 2005; Pagani *et al.* 2006; Schouten *et al.* 2007; Smith *et al.* 2007; Handley *et al.* 2008; Bowen and Zachos 2010; McInerney and Wing 2011; Tipple *et al.* 2011). Manners *et al.* (2013) suggested that differences between marine and terrestrial CIE magnitudes could, in fact, be minimal within a single sediment routing system (see also Chapter 2). This study tentatively builds upon this interpretation, as at the current resolution of the data, whilst taking into account that mixed sources and reworking may be affecting the recorded CIE magnitudes, no obvious difference in the $\delta^{13}C_{n\text{-alkane}}$ and $\delta^{13}C_{CARB}$ records is observed at the Zumaia section. This may suggest that the northern Spanish sections do not exhibit the same continental to marine magnitude differences recorded at other, more widespread, localities (Koch *et al.* 1992; Bowen and Zachos 2010; Tipple *et al.* 2011), and that the difference in marine and terrestrial magnitudes recorded elsewhere might be a local, rather than global phenomenon, especially when a range as varied as 2 to 7‰ is

recorded globally for CIE magnitude (Kennett and Stott 1991; Koch *et al.* 1992; Zachos *et al.* 2003, 2005, 2008; Magioncalda *et al.* 2004; Schouten *et al.* 2007; Smith *et al.* 2007; Handley *et al*. 2008, 2011; Bowen and Zachos 2010; McInerney and Wing 2011).

The size of CIE magnitudes recorded in this study has implications regarding carbon source and mechanisms of release. When estimating the mass of carbon released, the need for an estimate of the magnitude of the CIE is implicit. McInerney and Wing (2011), estimated that the release of carbon necessary to cause a 4.6‰ CIE would be 4,300 Pg C for methane Clathrates, 10,000 Pg C for thermogenic methane or permafrost, and 15,400 Pg C for wildfires or epicontinental seas. Whilst the need to be cautious of reworking and changing source inputs throughout the section is accepted, the fact that all three CIE magnitudes measured here are large (average 5.2‰), may indicate that greater amounts of carbon release would be required to account for the observed CIE. Dickens *et al.* (2003, 2011), suggest that methane clathrate release from slope failure or venting could account for the release of 2,000 to 3,000 Gt C during the PETM interval. As this estimate is lower than that required to explain a 4.6‰ CIE, this mechanism could not be entirely responsible for the carbon release associated with the event. This conclusion was also reached by Zeebe *et al.* (2009), who suggested that methane clathrates accounted for some of the carbon release observed, but other mechanisms “hithero unknown” had to be invoked to account for larger recorded CIE magnitudes.

3.5.3 TIMING OF EXCURSIONS

The onset of the CIE recorded in the $\delta^{13}C_{TOC}$, $\delta^{13}C_{CARB}$ and $\delta^{13}C_{n\text{-alkane}}$ records appear to be temporally offset, with the $\delta^{13}C_{CARB}$ profile recording the earliest onset, and the $\delta^{13}C_{n\text{-alkane}}$ profile recording the latest onset. This apparent lag between *n*-alkane and bulk records was also documented by Tipple *et al.* (2011) who suggested it reflected the long residence time of soil organic carbon. They argue that the time taken for leaf-wax production, transportation, and deposition in marine settings is variable between days and years (Conte and Weber, 2002), and that *n*-alkanes can be anywhere between 500 – 4000 yr older than the marine sediments in which they are deposited (Smittenberg *et al.* 2004). A sedimentary mixture incorporating *n*-alkanes deposited synchronously with the PETM and later-sourced *n*-alkanes would therefore represent the mean reservoir storage time of *n*-alkanes in soils, leading to a lag time before *n*-alkanes record the CIE associated with the PETM. This provides a plausible explanation for the lag in $\delta^{13}C_{n\text{-alkanes}}$ following CIE onset compared to CIE onset measured using $\delta^{13}C_{TOC}$ and $\delta^{13}C_{CARB}$. Furthermore, the $\delta^{13}C_{CARB}$ record reflects a marine signal, and as such is being deposited in-situ, whilst the $\delta^{13}C_{TOC}$ profile reflects a mixed terrestrial and marine signal. The temporal offset between the three records therefore likely reflects the transport time of terrestrial material deposition, with the carbonate profile recording the actual onset of the PETM CIE.

The $\delta^{13}C_{TOC}$ onset at the Zumaia section has been discussed previously in terms of sedimentology and inferred hydrological change associated with the PETM (Manners *et al*. 2013 and also Chapter 2). Schmitz *et al.* (2001) placed the onset of the CIE associated with the PETM at Zumaia as occurring simultaneously with the lithological

change to siliciclastic deposits, thus inferring the change in lithology to be related to the PETM. All three records presented in this study suggest a later CIE onset, providing further evidence that the sedimentological changes observed may have occurred prior to the onset of the CIE. Pujalte *et al.* (2014) suggest that evidence for an increased hydrological cycle is seen at the Claret section and in the surrounding terrestrial region just prior to the deposition of the Claret Conglomerate in the form of an incised valley. If this is the case, then the onset of the siliciclastic unit at Zumaia may be a reflection of sediment deposition from this incision, rather than directly linked to the Claret Conglomerate deposition. Kaolinite concentrations begin to increase dramatically coincident with the start of the siliciclastic Unit (Figure 3.8), and prior to the onset of the CIE in all $\delta^{13}C$ records, suggesting deeper continental erosion, potentially caused by an increased hydrological cycle prior to the onset of the CIE. This precursor event to the CIE may be linked to similar events found at New Jersey and Wyoming, where evidence for warming and environmental change prior to the PETM has been found (Sluijs *et al.* 2007; Secord *et al*.2010). Sluijs *et al.* (2007) report that environmental change and surface-ocean warming preceded the PETM, evidenced by the high occurrence of the dinoflagellate cyst *Apectodinium* and the TEX_{86} palaeothermometer, respectively. Secord *et al.* (2010) recorded a similar warming of about 5 °C prior to the PETM in the continental realm based on oxygen isotopes in mammal teeth.

Palynological data were used to determine reworking and reliability of the data throughout the section, and also to assess whether a change in the dominant vegetation was recorded here, as previously observed (Smith *et al*. 2007). Abundances of the different groups of palynomorphs remains fairly constant throughout the PETM

interval, with gymnosperm pollen (in particular, bisaccate pollen) dominating the species identified. However, bisaccate pollen is known to be dispersed more widely than other pollen groups due to the structure of the pollen grains containing air-sacs, making them more susceptible to aeolian and fluvial transport. Therefore, the inferred dominance of gymnosperm species may be an artefact (Heusser 1988; Traverse 1988). To assess if a shift in the dominant flora occurred coincident with the PETM, the ratio of angiosperm pollen relative to total angiosperm and gymnosperm palynomorphs was calculated throughout the section. These data suggest that a shift to a more angiosperm-dominated population may be observed coincident with the onset of the CIE at 8.7 m. However, only one data point suggests this, and the pollen count for this sample was low (eight grains). Consequently, it is tentatively inferred that no shift in the dominant group of pollen is recorded throughout the CIE at Zumaia. This would lead us to conclude that the plant community change that has been previously suggested to have occurred coincident with the onset of the PETM (Smith *et al*. 2007) does not appear to be recorded at this locality during the PETM, potentially due to poor preservation.

3.6 CONCLUSIONS

Marine bulk carbonate and higher-plant derived *n*-alkane $\delta^{13}C$ data are presented in a high resolution isotope study of the Zumaia section in Northern Spain, and compared with $\delta^{13}C_{TOC}$ data. This data represents the first organic geochemical data for the Zumaia section, and is one of only a limited number of comparisons of marine and terrestrial CIEs within the same section. The CIE magnitude between terrestrial and marine records is similar, suggesting that previously reported differences in magnitude

between the two environments is not expressed at this locality. Profile shape is assessed, and the potential for the *n*-alkane $\delta^{13}C$ record reflecting changes in the palaeohydrological regime is presented. The onset of the CIE appears to occur after the start of deposition of the Siliciclastic Unit, possibly suggesting that evidence for an increased hydrological cycle during the period preceding the PETM may have brought about sedimentological changes through deeper continental erosion. No palynological evidence was found to support the plant community change hypothesis affecting $\delta^{13}C$ values, and thereby an offset between the continental and marine records at this locality.

CHAPTER 4

4 EVALUATION OF CIES WITHIN A LINKED SEDIMENT ROUTING SYSTEM: COMPARISON OF THE CLARET AND ZUMAIA SECTIONS

ABSTRACT

The Palaeocene – Eocene Thermal Maximum (PETM), a hyperthermal event that occurred ca. 56 Ma, is associated with the release of substantial amounts of isotopically light carbon into the atmosphere and oceans, with questions as to the rate, rapidity, and amount of carbon released to cause the climatic perturbation debated. Here, total organic carbon and *n*-alkane $\delta^{13}C$ profiles across the PETM boundary at the terrestrial section of Claret, northern Spain are presented. This represents the first $\delta^{13}C_{n\text{-alkane}}$ record for this section, allowing examination of both the profile and magnitude of the CIE as expressed by leaf waxes at this locality. The $\delta^{13}C$ bulk total organic carbon (TOC) profile records a CIE magnitude of 3.5‰, whilst the $\delta^{13}C_{n\text{-alkane}}$ profile records a CIE of 4.1‰. A larger excursion expressed by *n*-alkanes than terrestrial TOC is apparent in global compilations, although this is one of the first studies where this is examined in the same section. The CIE onset as recorded by $\delta^{13}C_{29}$ and $\delta^{13}C_{31}$ appear to be temporally offset, with $\delta^{13}C_{31}$ recording an earlier onset than that of $\delta^{13}C_{29}$ data. This suggests a different, slow-responding source of organic matter recorded by the $\delta^{13}C_{29}$ data, as evidenced by OEP and CPI data. Profile shape is similar for both *n*-alkane records, although TOC data record a different profile, suggesting a longer body to the CIE. This has been interpreted to correspond to reworked organic matter affecting the profile shape. Palynological data suggest there may have been a change from a predominantly gymnosperm to an angiosperm flora coincident with the onset of the CIE, but the magnitude of the CIE here (4.1‰) compared with the global terrestrial average (4.7 ± 1.5‰) and the marine CIE recorded

at the nearby section of Zumaia (6‰, $\delta^{13}C_{CARB}$; within the same sediment routing system), suggests that this did not affect the magnitude of the terrestrial CIE. Stratigraphic differences between the onset of the CIE and sedimentological features, including the Claret Conglomerate, indicate that a time-lag is present between the onset of climatic change and sediment response within this system.

4.1 INTRODUCTION

The Palaeocene-Eocene Thermal Maximum (PETM) is a hyperthermal event that commenced at the Palaeocene-Eocene boundary (ca. 56 Ma). It has been described as the most prominent global warming event of the Cenozoic (Thomas *et al*. 2002). Temperature increases of 5 – 9 °C have been modelled within the first 10 kyr of the onset of the event, which is characterised by a near-synchronous negative carbon isotope excursion (CIE) of between 2.5 to 7 ‰, recorded in both marine and continental environments (Pagani *et al.* 2006; Smith *et al.* 2007; Zachos *et al.* 2007; Handley *et al.* 2008; Bowen and Zachos 2010; Manners *et al.* 2013). The variation in CIE magnitude is most dramatic when comparing marine (2.5 to 5.5‰) and continental (3 to 7‰) CIEs, which is suggested to reflect environmental bias between the different realms (Bowen *et al.* 2004; Zachos *et al.* 2005; Smith *et al.* 2007; McInerney and Wing 2011). Typically, continental *n*-alkane CIEs are argued to be larger than marine CIE magnitudes (McInerney and Wing 2011). Previous attempts to explain this apparent discrepancy have included potential reduction of the CIE magnitude in marine environments by carbonate dissolution or poor preservation (Zachos *et al.* 2005; McCarren *et al.* 2008), or amplification of the CIE in continental environments attributed to changes in higher plant carbon isotope fractionation (Bowen *et al.* 2004;

Smith *et al.* 2007; Handley *et al.* 2011). Specifically, it has been suggested that changes in plant assemblage from a mixed angiosperm/gymnosperm to a purely angiosperm flora could have affected continental CIE magnitudes (Smith *et al.* 2007). Angiosperms generally exhibit greater ^{13}C-discrimination during photosynthetic uptake than gymnosperms by 2.5 – 6 ‰ (Chikaraishi and Naraoka 2003; Smith *et al.* 2007; Diefendorf *et al.* 2010). This idea has recently been challenged, because deciduous angiosperms are now known to produce up to 200 times more *n*-alkanes than deciduous gymnosperms, indicating that the biomarker record would largely reflect an angiosperm signal (Diefendorf *et al.* 2011). Furthermore, whilst a plant community change may be applicable to the Bighorn Basin, it is less likely to affect areas with probable minimal gymnosperm contributions prior to the CIE (e.g., Tanzania; Handley *et al.* 2011). To assess whether a plant community change could have affected continental CIE magnitudes, further continental sections need to be studied. Currently this has only been investigated in Wyoming (Smith *et al.* 2007) and the Arctic (Schouten *et al.* 2007). Comparison of local terrestrial and marine CIE magnitudes should also help to elucidate differences recorded in CIE magnitude between continental and marine records.

The Claret section (Figure 4.1) is a continental section spanning the P/E boundary that is located in the Catalonia Region of northern Spain. A previous low-resolution study has identified the PETM CIE using soil carbonate nodules (Schmitz and Pujalte 2007) and at higher resolution using $\delta^{13}C_{TOC}$ (Domingo *et al.* 2009; Manners *et al.* 2013). An extensive conglomeratic unit, the Claret Conglomerate, is present throughout the northern Spanish terrestrial PETM sites. Previously this was interpreted to have

formed during the onset of the PETM and was thought to reflect a dramatic change in the hydrological cycle coincident with the CIE onset (Schmitz and Pujalte 2007). Based on this evidence, it was thought that the hydrological response to the PETM was extremely rapid, with an almost equally instantaneous sedimentological response, providing some insight into both climate and sediment dynamics at the beginning of the event. Domingo *et al.* (2009), and then Manners *et al.* (2013), challenged this hypothesis, suggesting that based on sedimentation rates estimated for the body of the organic CIE there was a time-lag of <15 kyr between CIE onset and conglomerate deposition (see also Chapter 2). They inferred that a time-lag must have occurred – either between climate change and sedimentological response, or between CIE onset and climatic change (with the sedimentological response being near-instantaneous). However, this time-lag between CIE onset and conglomerate deposition has previously only been recorded by $\delta^{13}C_{TOC}$ records, which may be biased by organic matter source mixing. Compound specific carbon isotope analysis allows evaluation of the recorded lag-time from a single-source (e.g. higher plant-derived $\delta^{13}C_{n\text{-alkane}}$ data), removing the bias associated with the $\delta^{13}C_{TOC}$ record.

This study presents high resolution $\delta^{13}C$ profiles of TOC and *n*-alkane data spanning the PETM interval from the continental section of Claret, building upon the earlier work of Manners *et al.* (2013) and Chapter 2. Onset of the CIE, in relation to the Claret Conglomerate, is assessed and compared to previous interpretations (Schmitz and Pujalte 2007; Manners *et al.* 2013). Profile shape of the $\delta^{13}C_{TOC}$ and $\delta^{13}C_{n\text{-alkane}}$ records are evaluated in terms of potential reworking, extent of degradation of samples, and source changes using palynological and other *n*-alkane-specific proxy data such as

average chain length (ACL; nC_{27-33}), carbon preference index (CPI; nC_{27-33}), and odd-over-even predominance (OEP; nC_{27}, n-C_{29} and n-C_{31}). Palynological data are also assessed in relation to the changes in plant community linked to the event, in the context of comparing CIE magnitudes and the profiles obtained for the different isotopic datasets. The magnitude of the CIE recorded is also compared to TOC ($\delta^{13}C_{TOC}$), *n*-alkane ($\delta^{13}C_{n\text{-alkane}}$) and carbonate ($\delta^{13}C_{CARB}$) data from the marine section of Zumaia (300 km distance), which is within the same sediment routing system, allowing variations between marine and continental CIEs to be assessed.

4.2 SAMPLE LOCATIONS AND METHODOLOGY

4.2.1 GEOLOGICAL SETTING

The Claret section (N 042°09´14.1", E 000°51´58.4") is located in the Tremp Basin in south central Pyreneés, ca. 5 km from the town of Tremp (Figure 4.1). One of several terrestrial PETM sections in this region, it is widely known for its marine Ilerdian deposits, associated with a marine transgression in the early Eocene (Schmitz and Pujalte 2003). PETM deposits in this region belong to the Tremp Group and have been dated using litho-, bio-, and chemostratigraphic techniques (Lopez-Martinez and Pelaez-Campomanes 1999; Schmitz and Pujalte 2003, 2007; Lopez-Martinez *et al.* 2006; Domingo *et al.* 2009). A conglomeratic unit in the middle of the section, known as the Claret Conglomerate, has previously been linked to the PETM using $\delta^{13}C_{TOC}$ and $\delta^{13}C_{CARB}$ data (Schmitz and Pujalte 2007; Domingo *et al.* 2009; Manners *et al.* 2013) and is considered to have formed <15 kyr after the CIE onset associated with the PETM, as defined by sedimentation rates estimated for the body of the CIE (Manners *et al.* 2013 and also Chapter 2). Deposits in the region comprise mainly yellow, grey, and red clays

containing microfossils and palynomorphs (Galbrun *et al.* 1993; Schmitz and Pujalte 2003; Domingo *et al.* 2009) indicative of a transitional environment, although the section was entirely terrestrial throughout the PETM interval (Schmitz and Pujalte 2007).

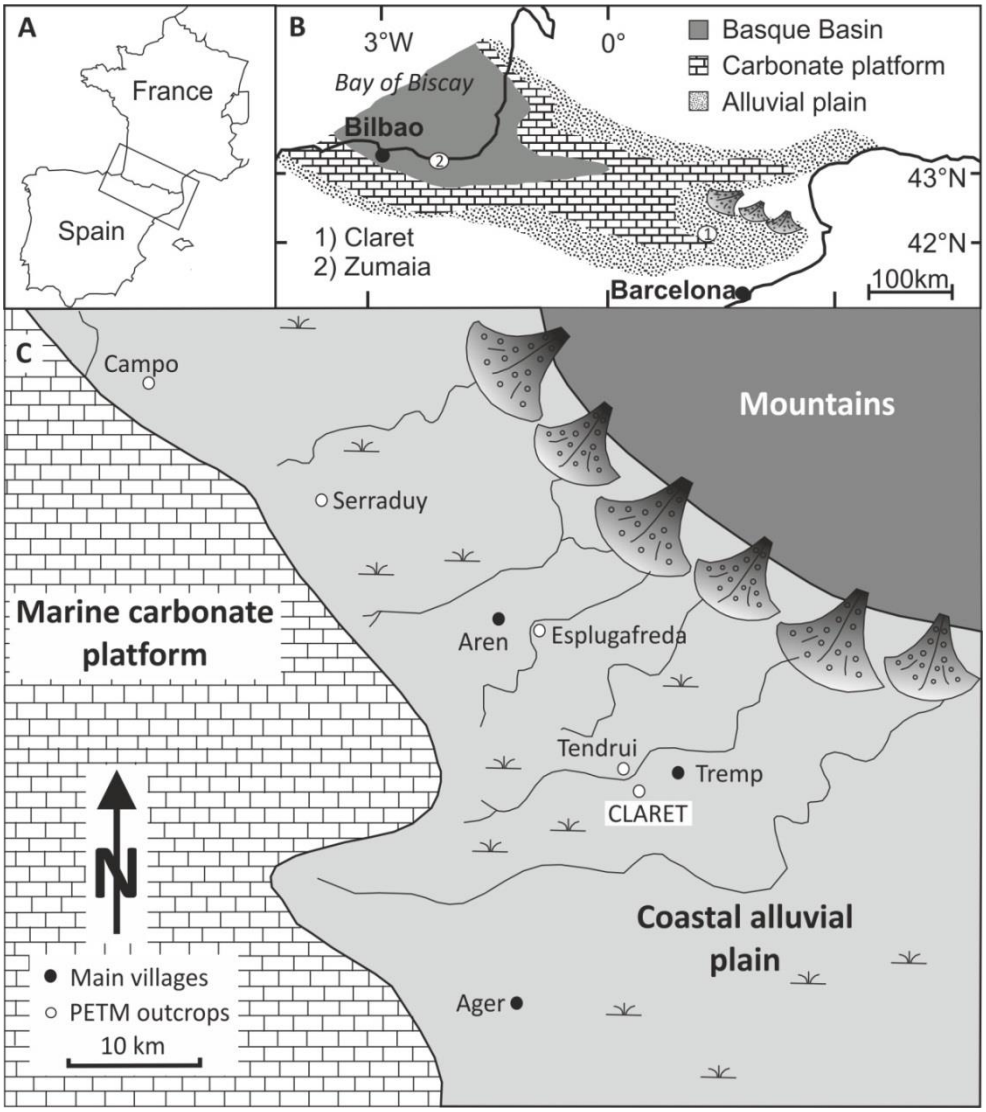

Figure 4.1. A) Geographic study area, B) General study area, highlighting the terrestrial section of Claret, and the marine section of Zumaia, C) Palaeogeographical map of the study region. showing the most important Palaeocene outcrops and the location of the Claret section. Modified from Schmitz and Pujalte (2007).

4.3 METHODS

In total, 165 samples were collected from the Claret section over several field seasons. Two logs were created over the field seasons which were correlated to each other in

order to place samples in the correct stratigraphic order (see Appendix 3, Table 6.3.1, Figures 6.3.1 and 6.3.2). Sampling frequency varied between the field seasons, with a mean sampling resolution of 70 cm for L.D. and 110 cm for R.D (see Appendix 3 for lithological correlation of the logs), which is corrected for and considered in the analysis. Prior to any chemical treatment all of the whole rock samples were oven dried (30°C, 24 hours).

4.3.1 TOTAL ORGANIC CARBON (TOC): DETERMINATION OF WT% TOC AND $\delta^{13}C_{TOC}$

Ninety-eight samples were powdered using a granite pestle and mortar. Decarbonation was conducted following the methodology of Domingo *et al.* (2009) using excess hydrochloric acid (10%, v/v) until any visible sign of reaction had ceased. Samples were neutralised by repeated washing with deionised water and oven dried (30°C, 24 hours). Total organic carbon (TOC), total nitrogen (TN) and stable isotope analyses were conducted at the NERC Isotope Geosciences Laboratory (NIGL). A full description of the methodology can be found in Manners *et al.* (2013) and Chapter 2, Section 2.2.2.

4.3.2 *N*-ALKANES: DETERMINATION OF CARBON PREFERENCE INDEX (CPI), ODD-OVER-EVEN PREDOMINANCE (OEP), AVERAGE CHAIN LENGTH (ACL) AND $\delta^{13}C_{ALKANE}$

The total lipid extract (TLE) was extracted from pre-weighed (ca. 50 g), powdered samples via sonication. *n*-alkanes were then separated from the TLE using a proprietary technique used for the isolation of waxes from crude oil (T-SEP™; http://www.kat-lab.com/t-sep) to produce a de-waxed TLE and an *n*-alkane fraction (see Chapter 3, Section 3.3.3 for full method).

Fractions containing *n*-alkanes were initially analysed using gas chromatography-flame ionisation detection (GC-FID) to determine the relative peak areas of *n*-C_{25-33}. Carbon preference index (CPI = 2 x (C_{27} + C_{29} + C_{31})/ [C_{26} + 2 x (C_{28} + C_{30}) + C_{32}]; Eglinton and Hamilton 1967), odd-over-even predominance (OEP = (C_{n-2} + 6 x C_n + C_{n+2})/(4 x C_{n-1} + C_n x C_{n+1}), with n being an odd integer; Scalan and Smith 1970) and average chain length (ACL = (27 x C_{27} + ... + 33 x C_{33})/ (C_{27} + ... + C_{33}); Eglinton and Hamilton, 1967) for *n*-alkanes were calculated.

$\delta^{13}C_{n\text{-alkane}}$ measurements were conducted at the Natural Environmental Research Council (NERC) Bristol Life Sciences Mass Spectrometry Facility using gas chromatography-combustion-isotope ratio mass spectrometry (GC-C-IRMS). Samples were analysed in either duplicate or triplicate relative to a reference gas, and analytical precision was < ±0.5‰ as measured by replicate analysis of a standard fatty acid methyl ester (FAME) mixture. All values are quoted in standard ‰ notation relative to Vienna Pee Dee Belemnite (VPDB).

4.3.3 PALYNOLOGICAL ANALYSIS

Palynological samples (25) were prepared at the British Geological Survey, Keyworth. Silicates were first dissolved by adding approximately 75 mL hydrofluoric acid to each sample and leaving the samples to stand for one week in a fume hood. Where necessary, samples were sieved at 10 µm (with the < 10 µm fraction removed) and placed in warm hydrochloric acid to dissolve carbonate material. All samples were then sieved at 500 µm and the >500 µm fraction was removed. Where minerals still remained, a heavy liquid separation was carried out to remove them. Samples were

then washed in distilled and deionised water, dried, and mounted onto cover slips using PVA glue and cover slips mounted onto the slides with Elvacite®. Pollen and spores were counted from prepared slides by Dr Phil Jardine (P.J., School of Geography, Earth and Environmental Sciences, University of Birmingham) by scanning transects across the slide. Where possible, 300 palynomorphs were counted per sample unless, (a) <300 palynomorphs were evident on the slide, or (b) one pollen type entirely dominated the sample, in which case counting was continued until 200 palynomorphs of the non-dominant types had been counted (usually resulting in counts >300).

4.4 RESULTS

Experimental data are presented in Table 4.1, and Tables 6.3.2 – 6.3.5 of Appendix 3. Results are summarised in Figures 4.2 – 4.5.

4.4.1 BULK SEDIMENTARY PARAMETERS

Total organic carbon (wt% TOC) and nitrogen content (wt% N; where quantifiable) are low throughout the section, ranging from 0.1 – 2.1 wt% TOC, and 0.07 – 0.2 % wt% N, respectively (Table 6.3.2 of Appendix 3). Wt% TOC and $\delta^{13}C_{TOC}$ results for the Claret section were first published in Manners *et al.* (2013) and are discussed below with the additional data from this current study (see also Chapter 2).

4.4.2 *N*-ALKANE ABUNDANCES AND DISTRIBUTIONS

The *n*-alkane fractions obtained from all samples were characterised by a homologous series of *n*-alkanes typically ranging from *n*-C_{25} to *n*-C_{33}, with some samples having measurable quantities of *n*-alkanes up to *n*-C_{36}. Concentrations of *n*-alkanes

throughout the section were generally low, ranging from 0.5 – 30 ng g^{-1} sediment (Tables 6.3.3 and 6.3.4 of Appendix 3). However, *n*-alkane concentrations increase at the onset of the CIE by a factor of two (Figure 4.2e). Increases in *n*-alkane concentration are also recorded in the recovery phase of the CIE.

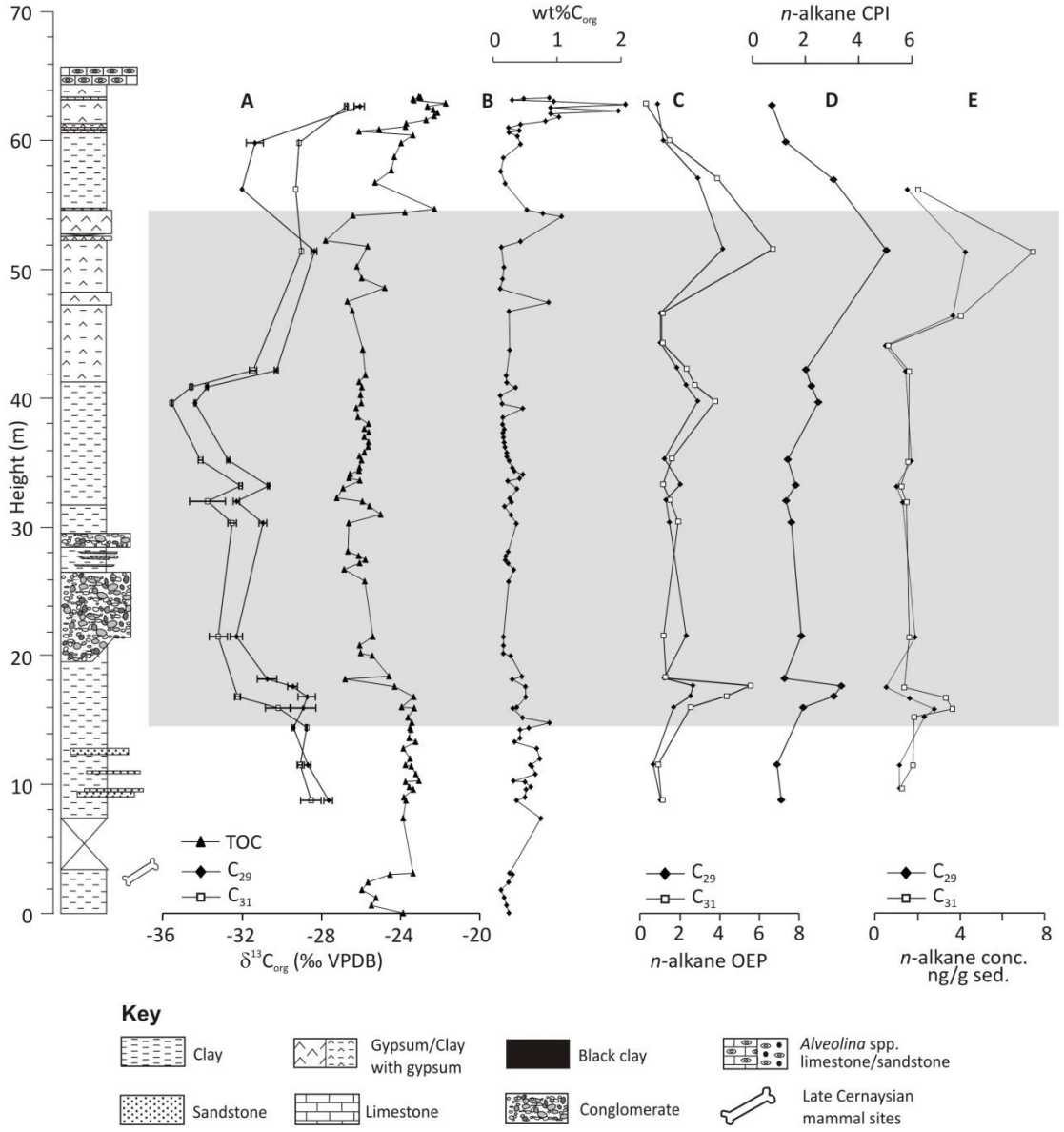

Figure 4.2. Geochemical parameters measured throughout the Claret section. A) $\delta^{13}C_{n\text{-alkane}}$ and $\delta^{13}C_{TOC}$ values, B) wt% TOC, C) odd-over-even predominance (OEP), D) carbon preference index (CPI), E) *n*-alkane concentrations (ng g^{-1} dry sediment). The grey box indicates the PETM CIE interval.

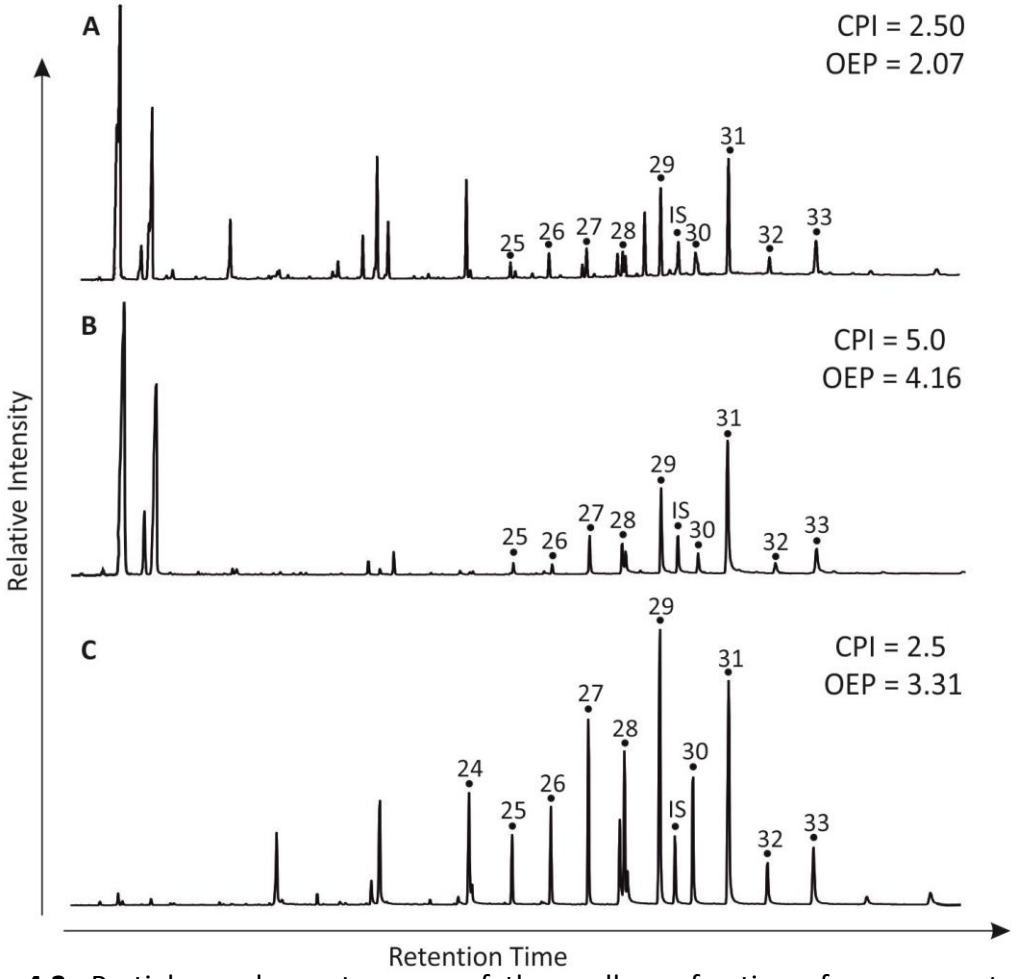

Figure 4.3. Partial gas-chromatograms of the *n*-alkane fractions for representative sediments demonstrating the odd-over-even predominance displayed. (A) pre-PETM, (B) during-PETM, (C) post-PETM: ● *n*-alkanes, with numbers indicating the number of carbon atoms.

All sediment *n*-alkane distributions are dominated by odd-carbon numbered homologues (e.g. *n*-C_{29}, *n*-C_{31} and *n*-C_{33}; Figure 4.3), a signature attributable to higher plant leaf wax *n*-alkanes (Eglinton and Hamilton 1967). OEPs and CPIs (Section 3.3.3.; Table 4.1) were used to assess the preference of odd-carbon numbered *n*-alkanes in all samples and to evaluate sources of these compounds. OEP and CPI values (C_n = 29 and 31) range from 0.3 – 6.7 (OEP) and 0.7 – 5.0 (CPI), throughout the section and the two parameters exhibit similar trends (Figure 4.2). OEP values for *n*-C_{29} and *n*-C_{31} are generally > 1, although they remain consistently low (ranging from 1 – 2) throughout the section apart from at key points described below. Coincident with the onset of the

CIE and the aforementioned increase in *n*-alkane concentrations, a dramatic increase in OEP is observed at 16.8 to 17.6m (*n*-C_{31} OEP = 5.5). Another increase in OEPs is coincident with the recovery from the CIE at 51.4 m (*n*-C_{31} OEP = 6.7), and again corresponds to an increase in *n*-alkane concentrations. CPI trends match those of the OEP, and most values throughout the section ranged from 1 – 2; however at the CIE onset and recovery the CPIs increased to 3.3 and 5, respectively.

Table 4.1. Isotope data and associated proxy measurements for the *n*-alkanes. Compound specific $\delta^{13}C$ was measured using *n*-C_{29} and *n*-C_{31}. ACL, OEP, and CPI were calculated using the methodologies described in Section 3.3.3. Hyphenated boxes in isotope data indicate uncertainty regarding isotope measurement due to obvious coelution of the measured *n*-alkane using GC-C-IRMS, so no measurement is reported.

Sample	Height (m)	$\delta^{13}C_{n\text{-alkane}}$ (‰ VPDB)		ACL	OEP			CPI	CIE
		n-C_{29}	*n*-C_{31}		*n*-C_{27}	*n*-C_{29}	*n*-C_{31}		
CLA-I-12	62.7	-26.1	-26.7	29.5	2.7	0.9	0.3	0.7	Post-
CLA-I-22	59.8	-31.4	-29.1	28.5	1.0	1.2	1.5	1.2	
CLA-5,-8	56.9	-32.0	-29.3	29.2	2.0	2.9	3.9	3.0	
CLA-5,-13	51.4	-28.4	-29.0	30.0	2.8	4.2	6.7	5.0	During-
CLA-6,+12	42.1	-30.3	-31.4	29.4	1.6	1.9	2.3	2.0	
CLA-I-39	40.9	-33.8	-34.6	29.0	1.4	2.3	2.8	2.2	
CLA-I-41	39.6	-34.4	-35.6	28.7	1.2	2.9	3.8	2.5	
CLA-6,+5	35.2	-32.7	-34.1	29.3	1.1	1.2	1.6	1.3	
CLA-6,+3	33.2	-30.7	-32.1	29.3	2.1	2.0	1.2	1.6	
CLA-I-60	32.0	-32.3	-33.8	28.8	0.9	1.3	1.5	1.3	
CLA-I-64	30.3	-30.9	-32.5	28.4	1.0	1.5	1.9	1.4	
CLA-I-70	21.5	-32.3	-33.2	28.5	2.1	2.3	1.2	1.8	
CLA-I-73	18.2	-30.7	-	28.2	1.0	1.2	1.3	1.2	
CLA-MAR´10-13	17.6	-29.4	-	29.9	1.4	2.7	5.5	3.3	
CLA-MAR´10-12	16.8	-28.7	-32.2	30.2	1.4	2.5	4.3	3.0	
CLA-I-74	15.9	-28.9	-30.2	28.7	1.5	1.7	2.5	1.9	
CLA-MAR'10-9	14.4	-29.4	-28.7	-	-	-	-	-	Pre-
CLA-I-78	11.5	-28.7	-29.1	28.7	1.0	0.7	0.9	0.9	
CLA-I-81	8.8	-27.6	-28.5	28.1	1.0	1.0	1.1	1.1	

4.4.3 *N*-ALKANE $\delta^{13}C$ VALUES

The $\delta^{13}C$ values were determined for *n*-C_{29} and *n*-C_{31} *n*-alkanes, which are interpreted based on CPI values ranging from 0.9 – 8.1 (Table 4.1) to be primarily derived from higher plant leaf waxes (other potential sources are recognised and discussed in Section 4.5.1). Throughout most of the section, *n*-C_{31} is depleted in ^{13}C by approximately 1.2‰ relative to *n*-C_{29}. However, this trend is reversed for three samples (at 14.4, 56.9 and 59.8 m); this reversal in the depletion of some samples has also been reported in Tanzania by Handley *et al.* (2011), and is also recorded at the Zumaia section (Chapter 3, Section 3.4.3). Overall, however, both records display similar trends throughout the section. The $\delta^{13}C_{n\text{-alkane}}$ values range from -26.1 to -34.4‰ for *n*-C_{29}, and -26.7 to -35.6‰ for *n*-C_{31} with the most depleted $\delta^{13}C$ values occurring at 14.4 m (*n*-C_{31}) and 16.8 m (*n*-C_{29}). This negative shift in *n*-C_{29} and *n*-C_{31} $\delta^{13}C$ values is interpreted to represent the onset of the CIE associated with the PETM and is also recorded by bulk $\delta^{13}C_{TOC}$ (Figure 4.2). The CIE onset recorded by $\delta^{13}C_{29}$ and $\delta^{13}C_{31}$, however, appears to be temporally offset, with *n*-C_{31} recording an earlier CIE onset, and *n*-C_{29} and $\delta^{13}C_{TOC}$ data recording a coincident later onset. Prior to the CIE onset, values range from -27.6 to -29.4‰ for *n*-C_{29}, and -28.5 to -29.1‰ for *n*-C_{31}. At the CIE onset (16.8 m for *n*-C_{29} and 14.4 m for *n*-C_{31}), all values start to shift toward more ^{13}C-depleted values, reaching a minimum of -30.7‰ for *n*-C_{29}, and -32.2‰ for *n*-C_{31}. The magnitude of the excursion is calculated as 3.6‰ for *n*-C_{29}, and 4.5‰ for *n*-C_{31} (see Manners *et al.* 2013 and Chapter 2 for magnitude calculation method). Above this, $\delta^{13}C$ values remain low, recovering back to near pre-CIE values between 42.1 – 51.4 m.

4.4.4 PALYNOLOGY

Palynomorph assemblages (Plate 1) vary in their degree of preservation throughout the section, with reworking and degradation evident from 31 – 36 m based on the dominance of dark and degraded sporomorphs and dinoflagellate cysts.

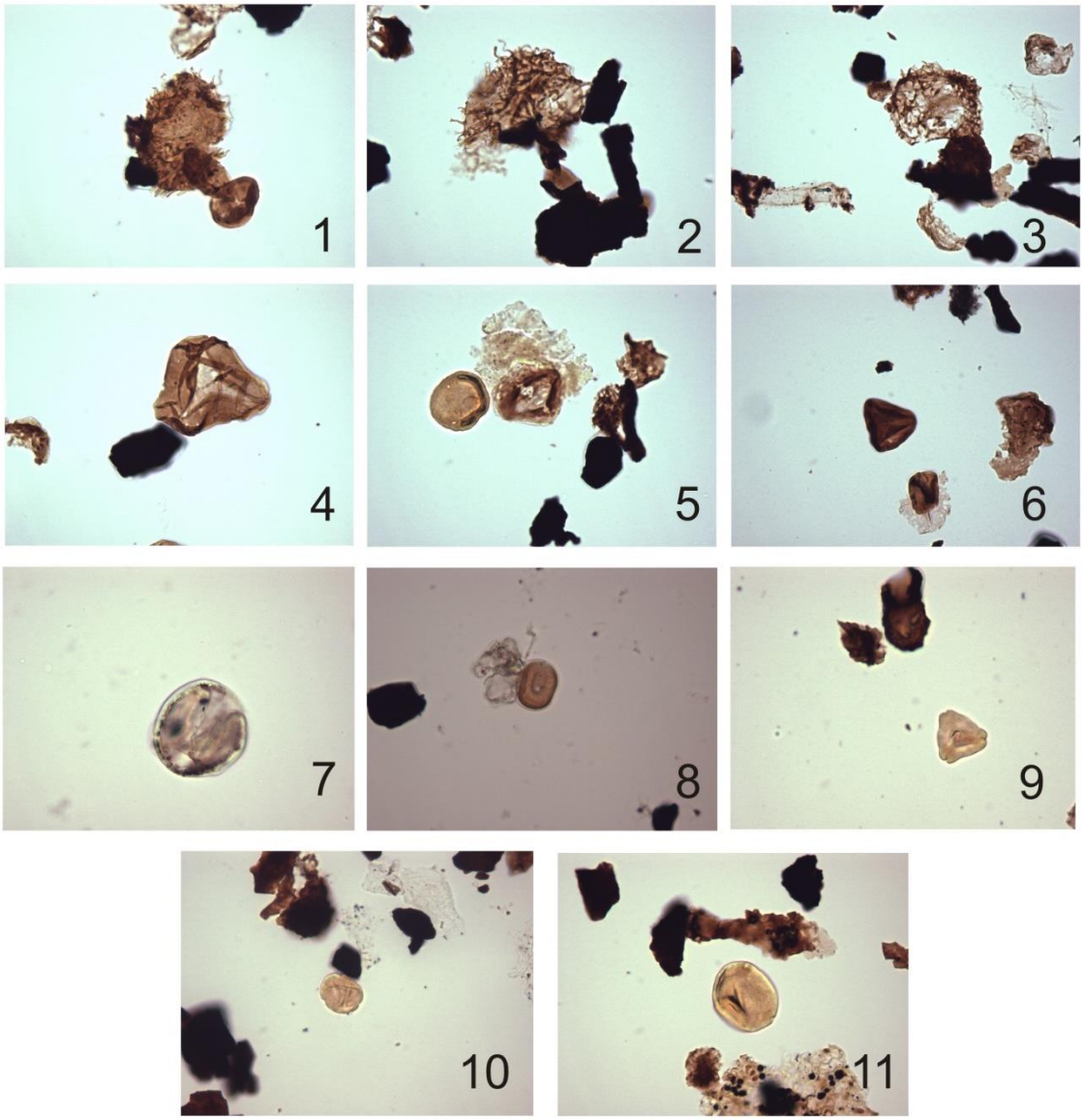

Plate 1. Reworked (1-6) and primary (7-11) palynomorphs from the Claret section. **1 – 3,** dinoflagellate cysts from samples CLA-6+1 and CLA-6+3; **4 – 6,** reworked spores from samples CLA-6+1, CLA-6+3 and CLA-6+6; **7,** bisaccate pollen from sample CLA-3-8; **8,** *Tetracolporopollenites* pollen type from sample CLA-3-8; **9,** Plicapollis pollen from sample CLA-5-5; **10, 11,** *Platycaryapollenites* and *Subtriporopollenites* pollen types from sample CLA-5-15. The biaccate pollen was produced by Gymnosperms (7) and the remaining pollen types (8 – 11) by Angiosperms.

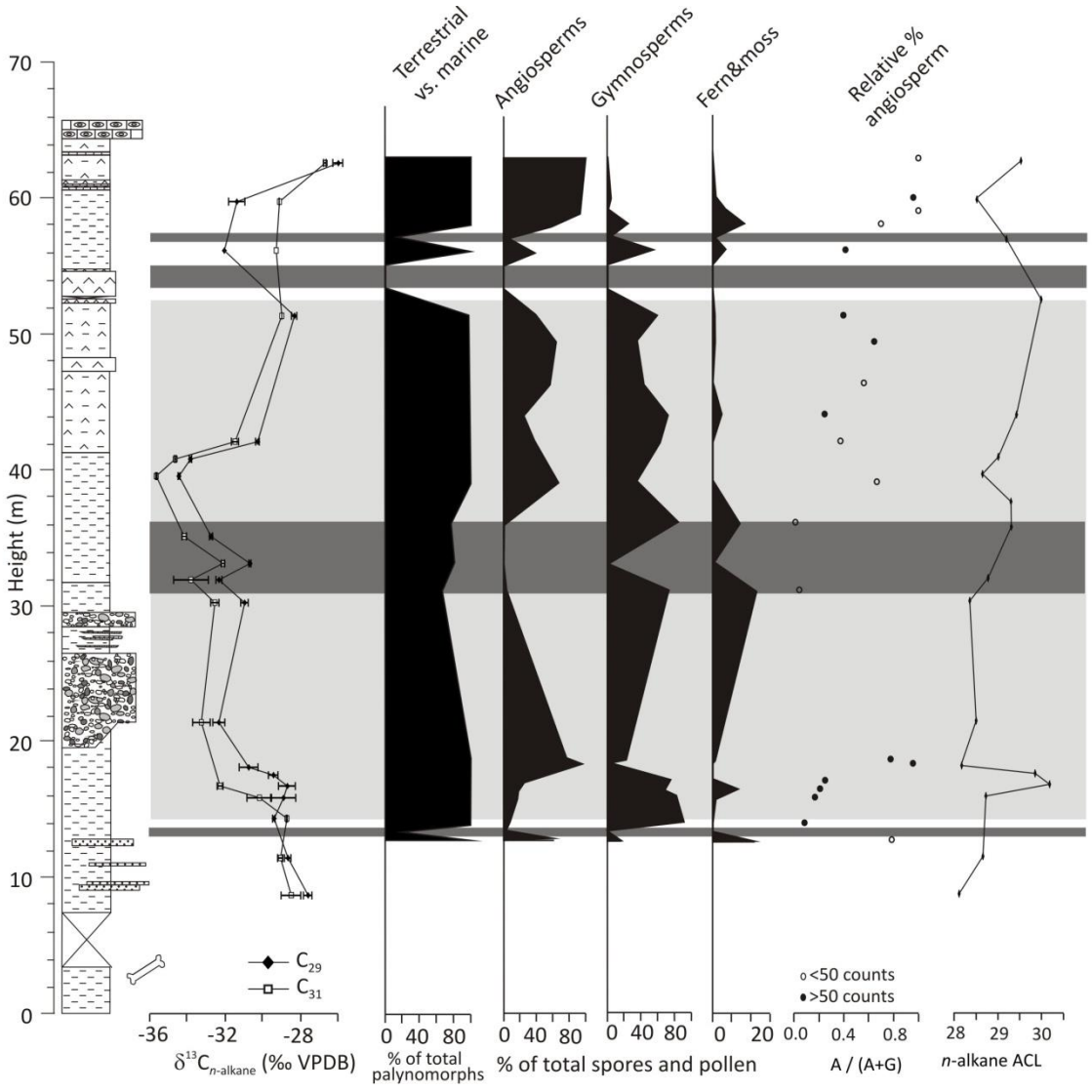

Figure 4.4. Relative abundance of groups of major palynomorphs (angiosperms, gymnosperms, and pteridophytes), expressed as percentages of the total spore and pollen counts. Total pollen is expressed as a percentage of the total palynomorphs (plant pollen + dinoflagellate cysts), giving % terrestrial relative to marine palynomorphs. The light grey box indicates the recorded CIE and the dark grey boxes illustrate barren (13.4, 53.3 – 55.3, and 57.2 m) or reworked samples (31.2 – 36.2 m); some of these samples also showed evidence of degradation of the palynomorphs (31.2 – 36.2 m). The key for the lithological log can be found in Figure 4.2.

Throughout the rest of the section assemblages vary in abundance with some samples containing only very limited numbers of palynomorphs (<50; Table 6.3.5 of Appendix 3). Angiosperm, gymnosperm, and pteridophyte pollen and spores were recorded throughout the section (Figure 4.4) with dinoflagellate cysts also found in the

reworked interval. At the base of the section (13.4 – 16.6m) gymnosperm species are the dominant pollen (ranging from 82 – 91% of the sample), whilst angiosperm proportions constitute only 9 – 16% of the total plant pollen and pteridophytes are consistently the lowest in abundance (0 – 2%). Coincident with the CIE onset (17.2 – 18.7m), angiosperm and gymnosperm proportions reverse, with angiosperm species reaching 96% of the total palynomorphs counted (gymnosperms, 4%). Throughout the body of the CIE (18.7 – 51.4m) the angiosperm proportion gradually decreases, albeit with high variability from 24 – 77%. Gymnosperm proportions are also variable, ranging from 22 – 72%, whilst pteridophyte proportion is consistently low (0 – 4.7%). After the CIE, angiosperm proportions gradually increase again (maximum 94%), whilst gymnosperm species decrease in abundance (minimum 4 %). The shaded boxes in Figure 4.4 illustrate barren (13.4, 53.3 – 55.3, and 57.2 m) or reworked samples (31.2 – 36.2 m); some of these samples also showed evidence of degradation of the palynomorphs (31.2 – 36.2 m; Plate 1). Dinoflagellate cysts were also found in some samples (31.2 – 36.2 and 49.5 – 51.4 m) indicating reworking of older, marine material.

4.5 DISCUSSION

4.5.1 DEPOSITIONAL SETTING AND SOURCE INPUTS

Source inputs of terrigenous material at Claret were assessed using biomarker proxy measurements and palynological evidence. Contributions from either fresh leaf waxes or those altered during burial, petroleum sources, and thermally mature organic matter can be elucidated via CPI and OEP measurements (Kennicutt *et al.* 1987; Collister *et al.* 1994; Huang *et al.* 2000; McDuffee *et al.* 2004; Handley *et al.* 2011). Fresh leaf waxes typically have OEPs and CPIs > 4 (Collister *et al.* 1994; McDuffee *et al.*

2004) whilst values < 4 may indicate potential contributions from either marine or petroleum sources (Huang *et al.* 2000), or that the leaf waxes have been altered during burial (Kennicutt *et al.* 1987; Handley *et al.* 2011) and very low values (<1) are typically associated with thermally mature organic matter (Kennicutt *et al.* 1987). Throughout the section relatively low CPI and OEP values are recorded, although high CPI and OEP values are recorded at depths of 15.9 – 16.8 m, and 51.4 m, which likely reflect a strong input of relatively fresh higher plant material. These horizons are associated with elevated concentrations of *n*-alkanes suggesting that there is an input of additional terrigenous organic matter into the Claret sediments. By extension, therefore, lower concentrations of *n*-alkanes with lower CPIs throughout the rest of the section likely represent a background contribution of *n*-alkanes from diagenetically altered or reworked, thermally mature organic matter. Whilst a mix of sources may be contributing to the *n*-alkane signal at Claret, all samples are dominated by *n*-C_{29} and *n*-C_{31} *n*-alkanes, indicating that whilst OEP is variable, this is still a predominantly terrigenous signal, with lower molecular weight *n*-alkanes always being subordinate. As such, the change in CPI values is interpreted as predominantly a switch between degraded soil-associated terrestrial organic matter and relative fresh organic matter derived directly from plants.

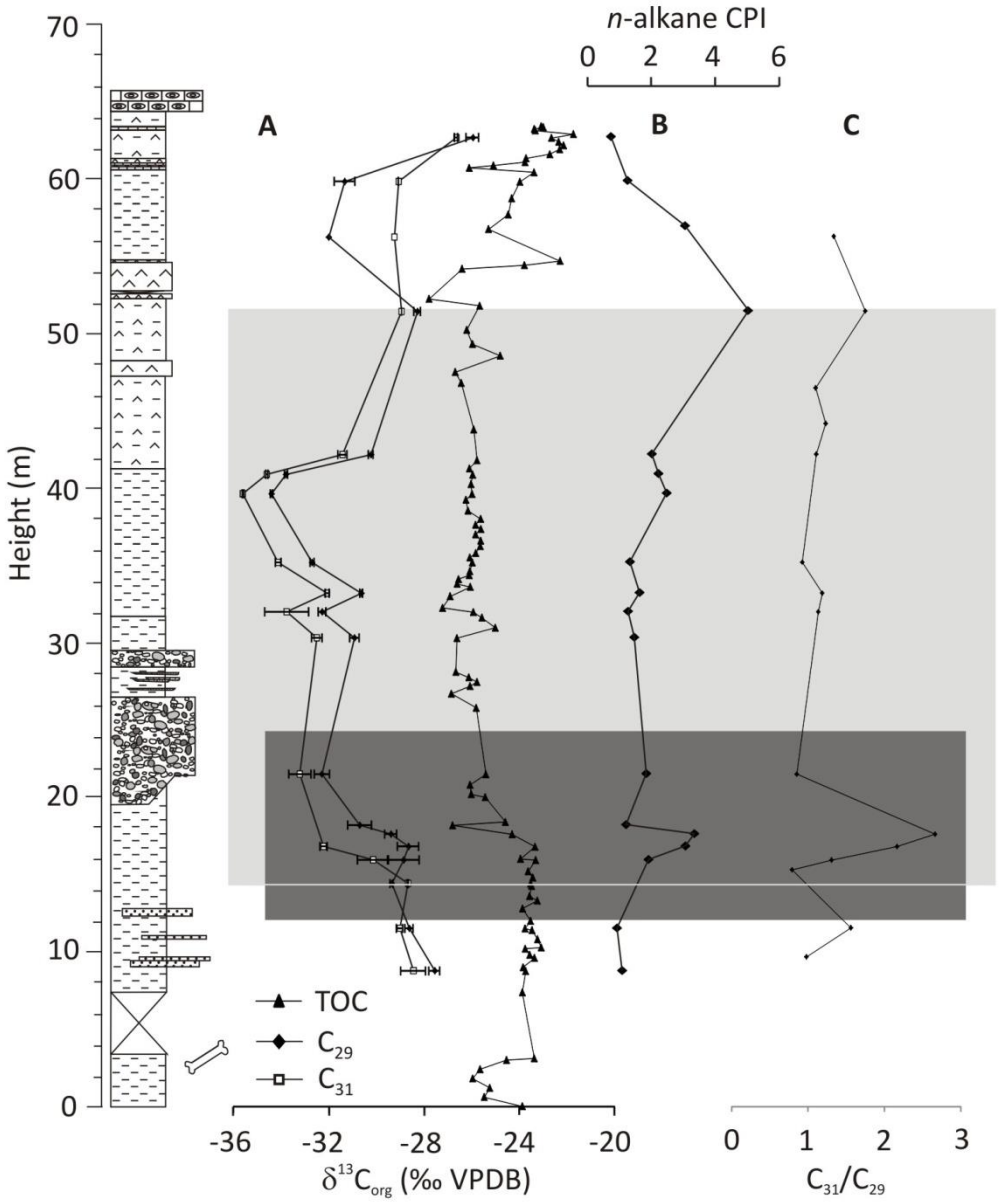

Figure 4.5. $\delta^{13}C_{TOC}$, $\delta^{13}C_{29}$ and $\delta^{13}C_{31}$ data (A) compared to CPI (B) and relative proportions of *n*-C_{31} and *n*-C_{29} concentration throughout the Claret section (C), illustrating the dramatic increase in *n*-C_{31} (deemed indicative of contemporaneous vegetation) coincident with the onset of the CIE as recorded by $\delta^{13}C_{29}$ and $\delta^{13}C_{TOC}$. The light grey indicates the recorded CIE whilst the dark grey box highlights the onset of the CIE, which is discussed in Section 4.5.1 (this section).

Likely source inputs were also assessed by comparing the isotope ($\delta^{13}C_{29}$, $\delta^{13}C_{31}$ and $\delta^{13}C_{TOC}$) profiles. The onset of the CIE as recorded by $\delta^{13}C_{31}$ occurs earlier and is of greater magnitude than that of the $\delta^{13}C_{29}$ and bulk TOC profiles. By comparing the relative concentration of *n*-C_{31} to *n*-C_{29}, ACL, CPI and OEP parameters, an evaluation of

source inputs was made (Figure 4.5). The *n*-alkane signature prior to the CIE onset, reflected in the C_{31}/C_{29} ratio, likely reflects a mixture of contemporaneous (high CPI) and reworked material (low CPI). Then, coincident with the CIE as recorded by *n*-C_{29} and bulk TOC, a pulse of fresh organic matter (potentially plants) results in increased *n*-alkane concentrations and OEPs, with a distribution shift to a more *n*-C_{31} dominated source. This shift from *n*-C_{29} to *n*-C_{31} dominance is proposed not to be a shift in vegetation (as it does not match the pollen record) but is instead driven by this change in the source of organic matter. During the transition interval between the *n*-C_{31} and *n*-C_{29} CIE onset, a brief mixing of old (lots *n*-C_{29} and bulk TOC with pre-CIE $\delta^{13}C$ values) and contemporaneous soil (*n*-C_{31} that is ^{13}C-depleted) occurs. This would therefore suggest that *n*-C_{31} is recording the true onset to the PETM CIE, with the other records delayed by mixing of older organic matter.

The marked increase in OEP and CPI values at 15.9 – 16.8 m coincides with the onset of the CIE at Claret, and possibly reflects a change of sediment source or increased deposition of fresh leaf waxes at this point, prior to deposition of the Claret Conglomerate. Similar profiles have been recorded at the Zumaia section in a completely marine environment, where OEP, CPI, and *n*-alkane concentration all increase coincident with CIE onset (Chapter 3, Section 3.4.2). This may suggest that the change in sediment source or increased deposition of fresh material at this time was seen across the region, spanning both terrestrial and marine realms. A similar increase in CPI, OEP and TOC content is recorded coincident with recovery from the CIE, again similar to Zumaia (Chapter 3, Section 3.4.2).

4.5.2 TIMING OF EXCURSIONS

Due to the terrigenous nature of this section, all organic matter should be terrestrial in origin. However, CPI and OEP values indicate a mixture of fresh and potentially diagenetically altered terrigenous material. Palynological data suggest input of terrestrial material throughout the CIE remains fairly constant, but that some samples may contain reworked and degraded material (31.2 – 36.2 m). Interpretation of results is therefore tentative, although as previously discussed the high abundance of C_{29} and C_{31} *n*-alkanes may suggest a contemporaneous terrigenous input throughout.

Increases in CPI, OEP and *n*-alkane concentrations, interpreted to represent a change in sediment source/increased input of fresh organic matter, are recorded coincident with CIE onset and recovery, both of which occur relatively rapidly at this section. However, the onset of the CIE as recorded by $\delta^{13}C_{TOC}$ and $\delta^{13}C_{29}$ records appear to be temporally offset from that of the $\delta^{13}C_{31}$ record, with CIE onset occurring earlier in the *n*-C_{31} record. It is suggested that the *n*-C_{31} profile documents the true onset of the CIE as recorded by fresh vegetation, whilst the bulk TOC and *n*-C_{29} records are biased by incorporation of a slow-responding source of organic matter, such as soil material gradually incorporating CIE-associated vegetation (Section 4.5.1). This has been reported before, suggesting that *n*-alkanes may record a time-lag relative to other isotope records due to a long residence time of soil organic carbon (Tipple *et al.* 2011). The TOC record may also be affected by older reworked organic matter; a smaller magnitude of CIE is recorded for the $\delta^{13}C_{TOC}$ data, and within the reworked interval $\delta^{13}C$ values shift to more positive values. Incorporation of reworked organic matter into the $\delta^{13}C_{TOC}$ record could also explain the later recovery recorded in the $\delta^{13}C_{TOC}$ profile than that of the $\delta^{13}C_{n\text{-alkane}}$ profile. If the $\delta^{13}C_{29}$ record represents a time-lag due

to soil organic matter, then as this record eventually incorporates CIE-associated vegetation it should match the $\delta^{13}C_{31}$ profile, both in terms of profile shape and recovery. This is apparent in the *n*-alkane records (Figure 4.2), with recovery occurring earlier than that of the $\delta^{13}C_{TOC}$ record. It is suggested, therefore, that these records document how different pools of organic matter are being mobilised in response to the major changes at the PETM.

The $\delta^{13}C_{TOC}$ onset at the Claret section has been discussed previously (Manners *et al*. 2013 and Chapter 2) in terms of sedimentology and inferred hydrological change associated with the PETM. Schmitz and Pujalte (2007) placed the onset of the CIE associated with the PETM at Claret as occurring almost simultaneously with deposition of the base of the Claret Conglomerate. This was inferred to reflect the dramatic near-instantaneous response of the sediment routing system to climate and hydrological change associated with the PETM. Domingo *et al.* (2009) and Manners *et al.* (2013) suggested that a time-lag (<15 kyr) between CIE onset and conglomeratic deposition occurred. Due to the short timescales involved, this lag-time was deemed likely to comprise components of two mechanisms that could have occurred. First, there was a genuine lag between the input of light carbon to the atmosphere and the expression of its full forcing effect on the climate system in terms of warming and hydrological change (Pagani *et al.* 2006; Secord *et al.* 2010; Rohling *et al.* 2012). This lag between carbon injection and hydrological change would suggest that the sedimentological response to changing hydrological regimes is near-instantaneous due to the relatively short timescale between CIE onset and Claret Conglomerate deposition. Second, carbon injection and hydrological change are near-instantaneous, and the observed

time-lag is largely due to the timescales of response of the eroding hinterland and sediment transport to a shift in the hydrological regime. This study suggests that there was an immediate sedimentological response to the PETM, reflected in the isotope records and biomarker ratios discussed previously. The Claret Conglomerate must therefore represent a more slowly developing sedimentological response. This is remarkably similar to observations at the nearby marine Zumaia section, where increases in OEP and CPI also occur coincidentally with the onset and, potentially, recovery of the CIE associated with the PETM (Chapter 3, Section 3.5.1). This is important because it suggests that changes in fresh soil versus degraded terrestrial organic matter inputs in response to the PETM appear to be consistent over an entire routing system (continental to marine).

Evaluation of the sedimentology at the Claret section with respect to the body of the CIE demonstrates that peak negative values are recorded long after deposition of the Claret Conglomerate. Normal or background sedimentation resumes before the CIE recovery, suggesting that the sedimentological change is not linearly correlated to the CIE (i.e., CO_2 or higher temperature). Instead, this may suggest that at least some of the sedimentological change is a non-linear geomorphological response to the climate perturbation. The warming represents a deviation from steady state which brings about a dramatic change in the erosional/sedimentological regime. However, equilibrium between climate and geomorphology is then restored, as erosion in the absence of tectonic uplift is a finite process within the timeframe discussed. This absence of tectonic uplift is demonstrated by Pujalte *et al.* (2014), who suggest that

the Palaeocene – Eocene interval is a period of tectonic quiescence, as illustrated by the absence of angular unconformities and growth structures within the succession.

4.5.3 ISOTOPE PROFILES AND ENVIRONMENTAL CHANGE

All isotope records ($\delta^{13}C_{TOC}$ and $\delta^{13}C_{n\text{-alkane}}$) document rapid depletion of $\delta^{13}C$ values between 14.4 – 16.8 m, suggesting a rapid onset to the PETM CIE at Claret. In all instances a box-shaped profile is observed, as originally suggested by Bowen and Zachos (2010) to indicate a rapid onset and recovery from the event (Figure 4.2). However, factors such as re-working, changing source input and compaction have likely occurred, dictating caution in interpretation of profile shapes (e.g., Manners *et al.* 2013 and Chapter 2).

Bowen *et al.* (2010) suggested that, for a box-shaped profile, the rapid recovery from the CIE associated with the PETM may be explained by the rapid re-growth of biospheric carbon stocks (i.e. living biomass, soils and peats) that may have been released at the onset of the event. If this theory is invoked here, palynological evidence and ACL may be reflecting a transient change in vegetation at the onset of the event (whilst taking caution with ACL, other authors have demonstrated its use in plant community identification e.g., Eglinton and Hamilton 1967; Collister *et al.* 1994; Chikaraishi and Naraoka 2003; Jeng 2006; Sachse *et al.* 2006). However, this cannot be unequivocally demonstrated at the end of the event due to barren palynological samples at these horizons. Comparison of the isotopic profile shapes of $\delta^{13}C_{TOC}$ and $\delta^{13}C_{n\text{-alkane}}$ at the Claret section to that recorded at Zumaia provides additional evidence for the box-shaped profile in northern Spain (Chapter 3, Section 3.5.2).

Whilst factors such as reworking must be considered in the interpretation of profile shape in this region, $\delta^{13}C_{TOC}$ and $\delta^{13}C_{n\text{-alkane}}$ at Claret, and $\delta^{13}C_{n\text{-alkane}}$ and $\delta^{13}C_{CARB}$ at Zumaia all record a more box-shaped profile, adding substantial evidence to the argument of Bowen and Zachos (2010), that a rapid onset and recovery from the PETM occurred.

Table 4.2. CIE magnitudes calculated from the different records in this study, and compared with those from the Zumaia section (marine).

Section	Data	CIE magnitude (‰ VPDB)
Claret	$\delta^{13}C_{TOC}$	3.5
	$\delta^{13}C_{n\text{-alkane}}$	3.6 - 4.5
Zumaia	$\delta^{13}C_{TOC}$	4.1
	$\delta^{13}C_{n\text{-alkane}}$	5.5
	$\delta^{13}C_{carbonate}$	6.0

The magnitude of the CIE recorded by all three isotope records presented for the Claret section is similar, ranging from 3.5 – 4.5 ‰ (Table 4.2). However, as discussed previously, the smaller CIE magnitude recorded by $\delta^{13}C_{TOC}$ data (3.5 ‰) may be reflecting incorporation of older or more thermally mature organic matter. Furthermore, whilst the $\delta^{13}C_{29}$ data initially records a smaller CIE magnitude than that of the $\delta^{13}C_{31}$ data, ($\delta^{13}C_{29}$: 3.6‰, $\delta^{13}C_{31}$: 4.5‰), eventually these records converge, suggesting the gradual incorporation of CIE-associated vegetation in the *n*-C_{29} record. A study by Schmitz and Pujalte (2007) yielded a larger CIE magnitude of 6 – 7 ‰ from soil carbonate nodules for this section. Similar differences in magnitude have previously been recorded between TOC and carbonate profiles (e.g., Smith *et al.* 2007), which has been attributed to soil carbonates incorporating carbon isotopic signatures of a mixture of atmospheric and respired CO_2, resulting in amplification of the CIE

using soil carbonates due to the greater contribution of organic carbon to nodule formation during the PETM (Cerling 1984; Bowen *et al*. 2004; Domingo *et al.* 2009). Furthermore, the low resolution of the study by Schmitz and Pujalte (2007) may have hindered effective interpretation of their measured CIE magnitude.

Comparing the magnitude of the CIE recorded in $\delta^{13}C_{TOC}$ and $\delta^{13}C_{n\text{-alkane}}$ at Claret to that measured in $\delta^{13}C_{TOC}$, $\delta^{13}C_{n\text{-alkane}}$, and $\delta^{13}C_{CARB}$ data from Zumaia (Chapter 3, Section 3.5.2) illustrates that the CIE magnitude appears similar between different depositional environments. Both the terrestrial organic and marine carbonate CIEs are large, indicating that no offset in CIE magnitude is recorded when comparing the terrestrial Claret and marine Zumaia records, in contrast to comparisons in other settings across the globe (Bowen *et al.* 2004; Pagani *et al.* 2006; Smith *et al.* 2007; Zachos *et al.* 2007; Handley *et al.* 2008; Bowen and Zachos 2010; McInerney and Wing 2011; Tipple *et al.* 2011). Previous work indicates that continental sections record larger CIE magnitudes than marine sections; however these datasets predominantly compare sections from different global localities, using analysis of different proxies (Koch *et al.* 1992; Bowen *et al.* 2004; Wing *et al.* 2005; Pagani *et al.* 2006; Schouten *et al.* 2007; Smith *et al.* 2007; Handley *et al.* 2008; Bowen and Zachos 2010; McInerney and Wing 2011; Tipple *et al.* 2011). Manners *et al.* (2013) suggested that differences between marine and terrestrial CIE magnitudes could, in fact, be minimal within a single sediment routing system (see also Chapter 2). Comparing the magnitudes of CIE at both Claret and Zumaia builds upon this interpretation. At the current resolution of the data, no obvious difference in the $\delta^{13}C_{TOC}$, $\delta^{13}C_{n\text{-alkane}}$ and $\delta^{13}C_{CARB}$ records is observed. This may suggest that the northern Spanish sections do not exhibit the same continental to

marine magnitude differences recorded at other global localities (Koch *et al.* 1992; Bowen and Zachos 2010; Tipple *et al.* 2011). Furthermore, the use of different proxies to measure the PETM CIE makes direct comparison of the CIE magnitude from global marine and terrestrial records challenging. Here, for the first time, records derived from organic matter are used to compare the CIE magnitude within the same sediment routing system.

In studies where a difference in magnitude between terrestrial and marine CIEs has been recorded, a change in the plant community from mixed gymnosperm/angiosperm to purely angiosperm flora has been invoked as a potential mechanism for causing an artificially high CIE magnitude in terrestrial records (Smith *et al.* 2007). This has been disputed by Diefendorf *et al*. (2011), who reported that angiosperms produce, on average, ca. 200 times more *n*-alkanes than gymnosperms, with the latter sometimes synthesising no *n*-alkanes at all. In such cases the *n*-alkane record should almost entirely comprise an angiosperm $\delta^{13}C$ signal. However this study only implicates modern plants, and in areas where gymnosperms were the dominant species you would still expect to see *n*-alkanes in the sediment, potentially suggesting that PETM flora did not exhibit such a differential between species. In this study, a peak in angiosperm pollen abundance is recorded coincident with the onset of the CIE. This peak also coincides with an increase in the ACL of the *n*-alkanes, which has previously been inferred to reflect a change in the dominant vegetation present, specifically from gymnosperm to angiosperm flora, in agreement with the palynological data (Smith *et al.* 2007). An increase in ACL has also been measured across the PETM in sediments from across the world (Arctic, Schouten *et al*. 2007; New

Zealand, Kaiho *et al.* 1996; South Atlantic, Hasegawa *et al.* 2006). However, ACL data must be treated with caution as it is known that in modern systems ACL can also increase with increasing temperature and precipitation (Sachse *et al.* 2006), and that values vary widely for different taxa (Collister *et al.,* 1994; Chikaraishi and Naraoka, 2003; Bi *et al.,* 2005; Sachse *et al.,* 2006). Therefore, whilst cautiously interpreting ACL data independent of other parameters, in combination with palynological data this would suggest that a change in the plant community occurred coincident with the onset of the PETM at this location. The magnitude of the terrestrial CIE (4.1 ‰) is in line with the global average (4.7 ± 1.5‰; McInerney and Wing 2011) and does not appear to be affected by the change in dominant vegetation at this locality.

4.6 CONCLUSIONS

The data presented in this study illustrate how different pools of organic matter are being mobilised in response to the major changes at the PETM, suggesting a complex mix of reworking of older material, input of relatively fresh terrigenous material, and soil organic matter incorporation causing lags in recording the PETM CIE onset. Furthermore, this study suggests that there was an immediate sedimentological response to the PETM, reflected in the isotope profiles and biomarker ratios, but that a time-lag between CIE onset and deposition of a massive conglomeratic unit (Claret Conglomerate) occurred. This unit has previously been suggested to reflect dramatic changes in the hydrological cycle associated with the PETM, but is now thought to represent a more slowly developing sedimentological response. More evidence to support the box-shaped profile suggested by Bowen and Zachos (2010) is presented, which could in turn have implications for interpretations of how recovery from the

PETM occurred. Evidence for a change in vegetation from predominantly gymnosperm to angiosperm flora is recorded coincident with the onset of the CIE by both palynological and ACL data. However, the terrestrial CIE (4.1‰) does not record a larger magnitude CIE than the marine CIE magnitudes recorded by $\delta^{13}C_{TOC}$ (4.1‰), $\delta^{13}C_{n\text{-alkane}}$ (5.5‰) and $\delta^{13}C_{CARB}$ (6‰) at the nearby marine section of Zumaia, suggesting that if a change in plant community did occur in northern Spain, it does not bias the magnitude of the recorded CIE. Furthermore, this may suggest that differences between marine and terrestrial CIE magnitudes could in fact be minimal within a single sediment routing system.

CHAPTER 5

5 SYNOPSIS

5.1 OVERVIEW

The aims of this research were to:

- Evaluate the magnitude of the recorded PETM CIE in both continental and marine settings within a linked routing system, to determine if a difference in magnitude was recorded between the two realms. (WP1)
- Evaluate the magnitude of the CIE as recorded by marine and terrestrial proxies at a single marine section (i.e., Zumaia; WP2).
- Assess likely controls on both magnitude and profile shape of the CIE associated with the PETM (WP2 and WP3).
- Review how the sediment system responds locally and regionally to such climatic perturbations (WP1 and WP3).
- Determine whether a change in the plant community was observed coincident with the onset of the PETM in northern Spain (WP3).

To achieve these aims, $\delta^{13}C_{TOC}$ was measured at six sections (Claret, Tendrui, Esplugafreda, Campo, Ermua and Zumaia), with further work conducted on the two end-member sections (Claret; terrestrial and Zumaia; marine). Statistical *t*-tests were used to determine whether a significant shift in $\delta^{13}C_{TOC}$ values was recorded, and thus the CIE associated with the PETM rather than, for example, a change in lithology or source input. This investigation suggests that no systematic variation between magnitude and depositional environment was recorded for the northern Spanish sections. This potentially indicates that globally recorded differences in CIE magnitude between marine and terrestrial environments may not be expressed within a linked

sediment routing system. However, due to the complicated nature of bulk TOC records and the mixed organic matter pool they reflect, this hypothesis needs further verification. Compound specific isotope analysis was conducted on higher plant-derived long chain *n*-alkanes (C_{25}-C_{33}) in order to minimise the effects of multiple organic matter sources on the recorded CIE. The continental section of Claret and the marine section of Zumaia were chosen for this work to assess the magnitude of the CIE in terrestrial and marine settings. Bulk carbonate analysis was also conducted at Zumaia, to provide a marine CIE record. The *n*-alkane record for Zumaia produced a greater CIE magnitude (5.5 ‰) than that for Claret (4.1 ‰), whilst the bulk carbonate profile recorded a greater CIE magnitude (6.0 ‰) than both *n*-alkane records. The terrestrial-sourced CIE magnitudes were within the range reported globally for terrestrial sections (4.7 ± 1.5 ‰; McInerney and Wing 2011), whilst the marine-sourced CIE was much greater than the average reported for marine successions (2.8 ± 1.3‰; McInerney and Wing 2011). Whilst limitations of the bulk carbonate record must be accepted, this suggests that the difference previously observed in CIE magnitude between the marine and terrestrial realm is not recorded in northern Spain. This data may imply that the wide range of CIE magnitudes recorded globally are in fact limited by local variations. However, to further confirm this interpretation ideally all sites would be compared using one proxy, a single method of calculating CIE magnitude and error bars accounted for (both instrumental and environmental).

Palynological data (Claret and Zumaia only) were used to determine source inputs of material to these sections, assess potential reworking, and determine whether a change in the plant community occurred coincident with the onset of the CIE (Smith *et*

al. 2007). These data were accompanied by *n*-alkane proxy data such as OEP, CPI, *n*-alkane concentrations and ACL. It is concluded that a continuous source of relatively-fresh higher plant material was deposited at both sections throughout the event, although other potential sources of organic matter may also be contributing to the record. This other material could be diagenetically altered terrigenous material, thermally mature organic matter, or marine organic matter (Zumaia only). The potential for mixing of differentially sourced organic matter in northern Spain complicates inferences on the magnitude and profile shape of the CIE.

To assess whether a change in the plant community occurred coincident with the onset of the PETM, the relative abundance of gymnosperm, angiosperm and pteridophyte pollen was compared throughout both sections. In the Zumaia section, no clear evidence for a switch from a mixed angiosperm/gymnosperm to a predominantly angiosperm population was recorded. However, the dominant gymnosperm pollen in the samples was bisaccate pollen, which disperses more widely than other pollen groups due to air sacs within their structure. This makes them predisposed to aeolian and fluvial transport (Heusser 1988; Traverse 1988). Therefore, the recorded dominance of gymnosperm pollen at the Zumaia section may be an artefact of transport bias, thus affecting the pollen record at this location. This potential bias of the marine record may be confirmed by comparison with the Claret section, where a vegetation change is recorded. A vegetation change coincident with the CIE has previously been suggested to affect continental CIE magnitude (Smith *et al.* 2007), recording a greater CIE due to increased plant δ^{13}C fractionation. Here, a shift in the dominant vegetation occurs coincident with the CIE onset, but CIE magnitude

does not appear to be affected. This suggests that, for this region, whilst a change in the plant community occurred, it does not influence the magnitude of the CIE.

CIE profile shape was investigated for $\delta^{13}C_{TOC}$, $\delta^{13}C_{CARB}$ and $\delta^{13}C_{n\text{-alkane}}$ records, to assess likely mechanisms of carbon release and drawdown at both the onset and termination of the event. Bulk TOC profiles recorded both triangular and box-shaped profiles, suggesting that mixing organic matter sources, reworking and sedimentation rates may be controlling the profile shape in northern Spain, as it is unlikely that different mechanisms of carbon release are operating within a single sediment routing system. At Claret, both the bulk TOC and *n*-alkane isotope data suggest a box shaped profile, whilst at Zumaia, carbonate and (potentially) *n*-alkane data suggest a box shaped profile, whilst TOC data record a triangular shaped profile. Ultimately, most records suggest a box-shaped profile, providing some support for the hypothesis of Bowen and Zachos (2010) that both onset and recovery from the PETM period were rapid. The profile shape of the *n*-alkane record at Zumaia documents a shift to more positive $\delta^{13}C$ values just after the onset of the CIE. This has also been reported in Italy (Tipple *et al.* 2011), France (Garel *et al.* 2013), and Wyoming (Kraus *et al.* 2013), and is attributed to aridity, vegetation change and subtle enrichment in surface- and deep-ocean carbon pools associated with the initial input of ^{13}C-depleted CO_2 (Tipple *et al.* 2011; Garel *et al.* 2013; Kraus *et al.* 2013). In the Zumaia section, however, it is suggested that this may reflect changes in the palaeohydrological regime, as the positive shift coincides with a gradual decrease in kaolinite abundance (Schmitz and Pujalte 2003), indicating less physical erosion and less influence of terrestrial material. Synchronously, a drop in CPI and OEP values may reflect a stronger marine influence to the signal.

Finally, the onset of the CIE and its relationship with the sedimentological response of the landscape was assessed. Comparing the onset of the CIE, as recorded by bulk TOC, suggested that there may be a time-lag between the onset of the PETM and changes in the weathering/erosional regime. This is similar to the findings of Handley *et al*. (2012). The Claret Conglomerate, a prominent marker bed in the terrestrial successions in northern Spain, has been suggested to have been deposited as a result of extreme hydrological changes related to the onset of the PETM (Schmitz and Pujalte 2007). Bulk TOC and *n*-alkane data from this study suggest that a small time-lag (< 15 kyr) between the response of the landscape and depositional system to the climate perturbation may have occurred. This is contrary to the interpretation of the bulk TOC and *n*-alkane data recorded in the Zumaia section, where sedimentological change appears to occur prior to the CIE onset. A change to siliciclastic deposition at Zumaia has previously been suggested to be coincident with CIE onset, reflecting the same dramatic hydrological change as in the terrestrial realm. Deposition of the Claret Conglomerate and the Siliciclastic Unit were, therefore, suggested to occur synchronously. Pujalte *et al.* (2014) suggest that an incised valley is seen at the Claret section directly below the Claret Conglomerate. If this is the case, then the onset of the siliciclastic unit at Zumaia may be a reflection of sediment deposition from this incision, rather than directly linked to the Claret Conglomerate deposition. This would suggest, therefore, that deposition of the Claret Conglomerate (which occurred after CIE onset) and the Siliciclastic Unit was not synchronous and, in fact, that sedimentological change in relation to dramatic climatic events may be more complicated than previously thought in this region.

5.2 FURTHER WORK

This research has identified several key topics that warrant further investigation.

1) Terrestrial plant biomarker δD analysis to determine palaeohydrological changes. An area of significant interest is the determination of the changes in the hydrological cycle in this region. This work could help to constrain the timing of hydrological response to climatic upheaval, and subsequently could be linked to proposed time-lags in the response of the sediment routing system. The hydrogen isotopic composition (δD) of lipid biomarkers derived from terrestrial plants can be used to examine both global and local hydrological patterns. Global latitudinal moisture transport and localised relative humidity changes can be evaluated. The PETM sections studied in this research represent an ideal setting from which to generate further δD records as, so far, only five PETM δD records have been established (the Arctic – Pagani *et al*., 2006; Wyoming – Smith *et al*., 2007; Tanzania – Handley *et al*., 2008, 2012; Italy – Tipple *et al*., 2011; New Zealand – Handley *et al*., 2011). This work would, therefore, provide further insight into both regional and global hydrological cycle patterns. The sections studied throughout this research comprise multiple sites from a single depositional system; this would therefore allow the first evaluation of the integrity of δD records, as most previous records derive from marginal settings, where lipid biomarkers have been transported, and thus potentially altered before burial. Furthermore, this would add a suite of new PETM δD records, to compare global changes in hydrology throughout the PETM interval.

2) Evaluation of sea surface temperature (SST), mean annual air temperature (MAT), and organic matter input to the marine realm using glycerol dialkyl glycerol tetraethers (GDGTs). Whilst a number of studies detailing the sedimentology, palaeontology, and inorganic chemostratigraphy (e.g., Schmitz *et al.* 1997, 2001; Schmitz and Pujalte 2003, 2007) have been conducted at all the sections described in this research, the present study was the first to investigate any organic geochemical parameters for these sections. Extending the organic geochemical investigation of these sections would enable assessment of palaeoenvironmental parameters such as SST, MAT, input of soil organic matter to marine environments, and soil pH during the PETM. All of these parameters can be explored using a group of biomarker proxy compounds; GDGTS (Schouten *et al.* 2013). The palaeothermometer, TEX_{86} (tetraether index of 86 carbon atoms), has been used to reconstruct Palaeogene SST globally (Brinkhuis *et al.* 2006; Sluijs *et al.* 2006, 2007, 2008a; Zachos *et al.* 2006; Pearson *et al*. 2007; Sangiorgi *et al.* 2008a; Bijl *et al.* 2009) and should be used, specifically for the Zumaia section, to reconstruct SST changes within the northeast Atlantic Ocean. This would be the first study of its kind in this region and would allow further understanding of oceanic change during the PETM interval. The input of soil organic matter to the marine environment could also be evaluated at the Zumaia section using the branched isoprenoid tetraether (BIT) index. The BIT index has been used previously to suggest elevated sea levels during the PETM (Sluijs *et al.* 2008b) and reconstruct changes in soil organic matter input to the Arctic Ocean (Brinkhuis *et al*. 2006; Sluijs *et al.* 2006, 2008a; Sangiorgi *et al.* 2008a,b). Data obtained from such studies might constrain what is controlling the shape and magnitude of the CIE at the Zumaia section, and may shed light on the positive shift in *n*-alkane isotope values just

after the onset of the CIE. Finally, methylation of branched tetraethers)/cyclisation of branched tetraethers (MBT/CBT) indices could be used to reconstruct MAT and soil pH, respectively at the Claret section. This proxy is considered to reflect soil temperature better than air temperature, but a correlation has been demonstrated for these two parameters (Schouten *et al.* 2013). MBT/CBT has been used to reconstruct MAT throughout geological time (e.g., Weijers *et al.* 2007a,b; Schouten *et al.* 2008) and could be attempted at Zumaia to provide the first organic geochemical record of palaeotemperature throughout the PETM interval at this section.

3) Biomarker analysis to assess plant community change, mixing ratios of organic matter sources, and thermal maturity of the sediments. Palynological evidence suggests that a shift in the dominant vegetation occurred coincident with the onset of the PETM at the Claret section. However, transport biases can affect relative palynomorph proportions, distorting the record. The relative proportion of biomarker compounds specific to angiosperms and gymnosperms could be assessed throughout the section to evaluate the vegetational shift as recorded by palynomorphs. This could be extended to Zumaia, where palynomorph transport biases would most greatly affect the record, whilst biomarker proportions should remain relatively unaffected. Specifically, compounds such as simonellite and dehyroabietane (specific to gymnosperm taxa) and triterpenoids such as oleanane (specific to angiosperm taxa) could be used, and have previously been used to test the plant community change hypothesis previously (Schouten *et al.* 2007).

The distribution of hydrocarbon biomarkers can reflect thermal maturity, depositional environment, and lithology (Peters *et al.* 2005). The thermal maturity of sediments could be assessed using the homohopane isomerisation ratio (22R to 22S) for the C_{31} homohopane. This could be useful in determining source inputs to the section, as CPI and OEP values indicate that some of the Zumaia section may have a thermally mature input of organic matter. These mixing ratios could be used to further evaluate the likely controls on CIE profile and magnitude.

4) Species specific $\delta^{13}C$ at Zumaia to further assess the marine CIE and compare with terrestrial records. This and previous studies (Schmitz *et al.* 1997) have generated bulk carbonate carbon isotope records for the Zumaia section, identifying the CIE associated with the PETM at this location. However, bulk records are known to be difficult to deconvolute and single-source records are preferred. Currently, as far as can be ascertained, no species specific $\delta^{13}C$ marine records, from analysis of either foraminifera or planktonic species, have been attempted at the Zumaia section. Schmitz *et al.* (1997) suggested that, due to poor preservation of foraminifera throughout the Palaeocene, bulk samples may give more meaningful $\delta^{13}C$ values than a species specific record at this site. However, recent and on-going developmental work is leading towards the capability to analyse $\delta^{13}C$ of dinoflagellate cysts (Appy Sluijs, pers. comm., 07/13). The palynological data produced in this study has shown dinoflagellate cysts to be well preserved throughout the PETM interval. Therefore, perhaps in the near-future, the $\delta^{13}C$ of dinoflagellate cysts could be measured to generate a more accurate marine CIE. This would aid comparison to terrestrial records both at the Zumaia section, and throughout the region.

5) Increased resolution of $\delta^{13}C_{n\text{-alkane}}$ data. To evaluate changes in profile shape more accurately throughout both Zumaia and Claret, the resolution of the *n*-alkane isotope data could be increased. Furthermore, $\delta^{13}C_{n\text{-alkane}}$ records could be established for the four intermediate sections of Tendrui, Esplugafreda, Campo and Ermua, in order to assess CIE magnitude differences across the region, and evaluate sedimentological response to climatic upheaval.

5.3 PUBLICATIONS

This study has already led to the publication of preliminary $\delta^{13}C_{TOC}$ data comparing the magnitude, profile shape and onset of the CIE throughout a linked sediment routing system in the journal Earth and Planetary Science Letters (Manners *et al.* 2013). Further publications are planned continuing this work with evaluation of the terrestrial (Claret) and marine (Zumaia) end-member sections. The Zumaia section is one of the first studies where the marine and terrestrial CIE have been measured using different proxies at one location, allowing direct comparison of CIE magnitude between the realms and assessment of controls on the CIE profiles. Following on from this a paper on the Claret data will compare the terrestrial CIE magnitude as measured by *n*-alkanes across the sediment routing system between Claret and Zumaia, and will evaluate whether a plant community change occurred in northern Spain, along with its effects on CIE magnitude.

6 APPENDICES

6.1 APPENDIX 1: ADDITIONAL DATA FOR CHAPTER 2

This appendix provides supplementary information for Chapter 2. Further information regarding geological setting, methods, and field localities is presented. Results tables for the statistical analysis of lithology and wt%TOC, and absolute $\delta^{13}C_{TOC}$ values measured via isotope ratio mass spectrometry are provided for all sections discussed.

PALAEOGEOGRAPHICAL RECONSTRUCTION

The Pyrénées

The Pyrénées are an E-W oriented mountain belt situated between Spain and France, largely controlled through the Cenozoic by the interaction between the European and Iberian plates (Baceta *et al.* 2011). At the beginning of the Cenozoic, the Pyrénéan embayment mostly comprised (hemi)pelagic and turbidite sediments, surrounded predominantly by shallow marine carbonate platform systems, which in turn were bordered by continental alluvial plains (Pujalte *et al.* 2000a; Schmitz and Pujalte 2003). The early Palaeogene was part of a longer-term relatively quiet phase with respect to tectonism in the area and this, combined with rising sea levels globally, reduced terrigenous supply, and favourable climates led to an overall transgression, resulting in enhanced carbonate sedimentation across the shallow areas bordering the Pyrénéan embayment (Pujalte *et al.* 2000a; 2000b; Baceta *et al.* 2011). The sections studied in this area are all within the Tremp-Graus Basin, which developed as a piggy-back basin of the Ebro Basin and is characterised by upper Palaeocene-lower Eocene continental

and platform deposits (Gibbons *et al.* 2002). These deposits are well exposed across the region.

The Basque region

The Basque Basin, situated in the western Pyrénées, extends from the city of Bilbao to near the border between Spain and France. Initially the basin was created in early Triassic times (ca. 250 Ma) as a result of the break-up of Pangaea, when the northern margin of the Iberian Peninsula was stretched and began to sink (Pujalte 2003). Throughout the next 200 Myr the basin was in-filled and during the Cretaceous to lower Palaeogene became uplifted and inverted forming the Pyrénéan mountain belt (Gibbons *et al.* 2002; Pujalte 2003). During the Palaeogene the Basque Basin had become an area of intermediate water depth of E-W orientation which opened westwards into the Bay of Biscay. A wide variety of Palaeogene-Neogene sedimentary rocks are found in the region, ranging from alluvial conglomerates to deep water marine hemipelagites (Pujalte *et al.* 2000b; Schmitz and Pujalte 2003, 2007; Baceta *et al.* 2011). The outer part of the basin comprised shallow carbonate platform-shelves, whilst the central part received sediments from density flows and hemipelagic material (Bernaola *et al.* 2006). The sections studied in this area are both within the Basque Basin, and represent some of the most expanded and continuous marine PETM sections now uplifted and exposed (Schmitz *et al.* 2001).

APPENDIX 1

INDIVIDUAL LOGS, DESCRIPTIONS AND FIELD PHOTOGRAPHS FOR CHAPTER 2

This section provides individual logs, desrciptions and field photographs for each section studied throughout this research.

TERRESTRIAL AND MIXED SECTION DESCRIPTIONS

Claret

The Claret Section is a composite section located in the Catalonia province, near the city of Tremp, south-central Pyrénées, Spain. The dip of the beds in this region is variable between 30 - 40°, in a south-easterly direction (145° SE), and accessibility is easy due to its proximity to the road C-1311. This section belongs to the upper part of the Tremp Formation (Unit 4 as proposed by Galbrun *et al.* 1993), ending with the marine Ilerdian *Alveolina* Beds. It comprises mainly yellow, grey, and red clays containing microfossils and palynomorphs (Galbrun *et al.* 1993; Schmitz and Pujalte 2003; Domingo *et al.* 2009), indicating a transitional environment, although the section was entirely terrestrial throughout the PETM interval. Exposure of the section is good, and digging back to fresh material is easy due to low (if any) vegetation cover.

Tendrui

The Tendrui section is located in Catalonia Province, ca. 3 km from the Claret section. The beds dip in a north-westerly direction (10° dip, 320° NW), and accessibility to the section is again easy, although due to the site being situated on private land, permissions must be sought prior to sampling. Vegetation covers more of this section, but can be easily removed to dig back to fresh material. This section is thicker than that of Claret, but again comprises mostly yellow, grey, and red clays, with the Claret Conglomerate and *Alveolina* Beds exposed.

APPENDIX 1

Esplugafreda

The Esplugafreda section is located ca. 12 km from the Claret and Tendrui sections in the province of Aragón, is the last of the continental sections studied. The dip of the beds here is 28 - 32°, in a southerly direction (166° SSE -196° SSW). Sedimentologically it is similar to both Claret and Tendrui, in that both the *Alveolina* Beds and the Claret Conglomerate are recorded, and the succession comprises red, yellow and grey clays with abundant palaeosol horizons. These palaeosol horizons contain abundant centimetre-sized soil carbonate nodules and gypsum indicating a semi-arid to arid palaeoenvironment. Accessibility to the section is relatively easy from a side road off the N-230. Exposure is varied, with parts of the section being more densely covered in vegetation. It is, however, still possible to sample fresh material by composing a composite section.

Campo

The Campo section is located ca. 30 km from Esplugafreda, just outside the town of Campo in the province of Aragón. The dip of the beds is 35-45°, in a southwesterly direction (225°). Accessibility to this section is easy from a side road off the N-260. Exposure is good with little or no vegetation cover. The campo section consists of yellow and grey clays and marls, topped by the *Alveolina* Beds observed at all continental sections associate with an Ilerdian transgression. During the early Palaeogene, Campo was a continental shoreline section, and as such alternated between subaerial exposure and submergence by shallow seas; although over the Paleocene/Eocene boundary Campo was entirely continental (Molina *et al.* 2000; Orue-Etxebarria *et al.* 2001; Pujalte *et al.* 2009a).

Figure A6.1.1. The Claret Conglomerate, a prominent marker bed linked to the onset of the CIE associated with the PETM (Schmitz and Pujalte 2007). This unit has been interpreted to form from a series of alluvial megafans induced by extreme hydrological changes related to the onset of the PETM over a period of 10 kyr or less (Schmitz and Pujalte 2007).

Figure A6.1.2. The gypsum layers found at all three continental sections, above the Claret Conglomerate (unit "d" in Figure A6.1.6.). At Claret and Tendrui these horizons are more prominent (ca. 1 – 2 m). These horizons have previously been suggested to be the result of a more arid palaeoenvironment and therefore intense evaporation rates (Domingo *et al.* 2009).

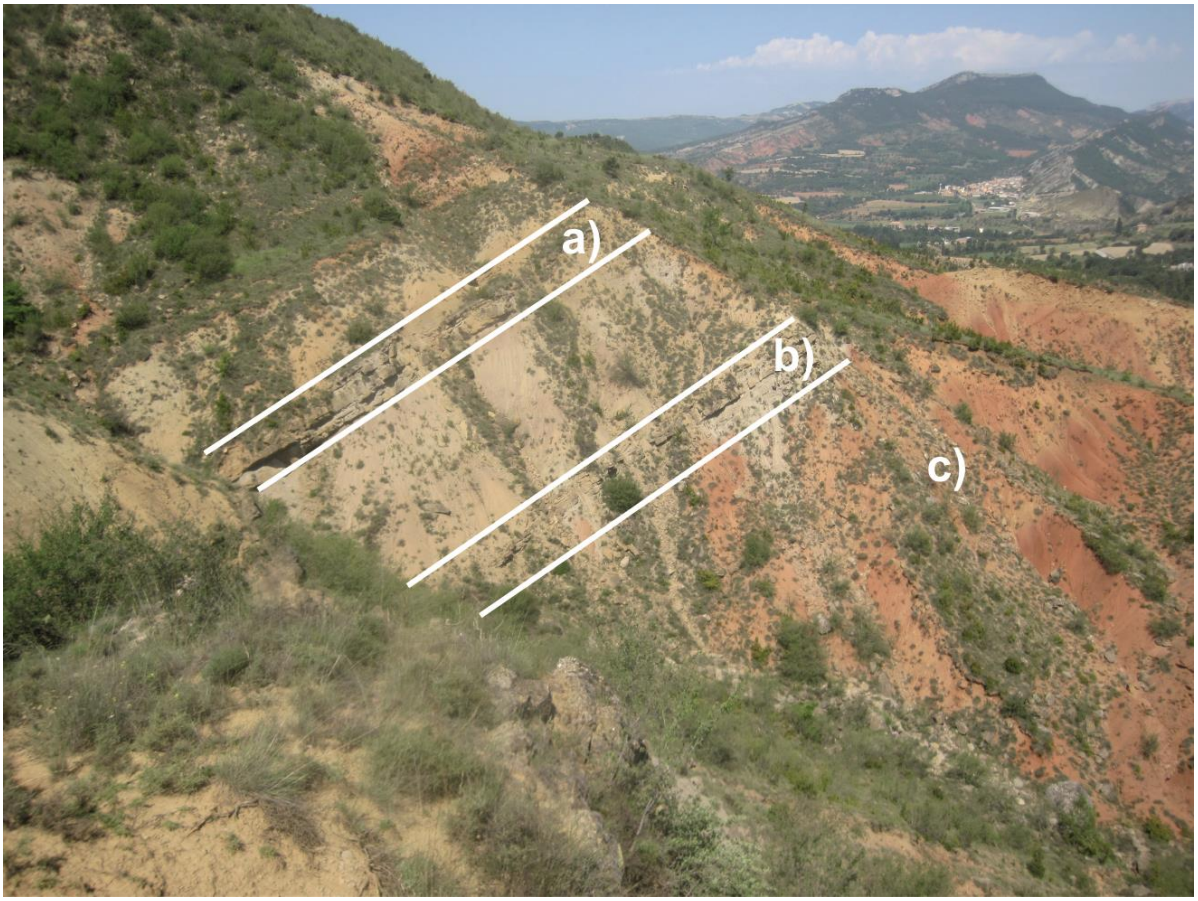

Figure A6.1.3. The Esplugafreda section. a) Claret Conglomerate, b) lower sandstone bed, c) Paleocene red clays.

Figure A6.1.4. The sandstone bed (unit "d", Figure A6.1.8.) interpreted to be the distal equivalent of the Claret Conglomerate (Pujalte *et al.* 2009b).

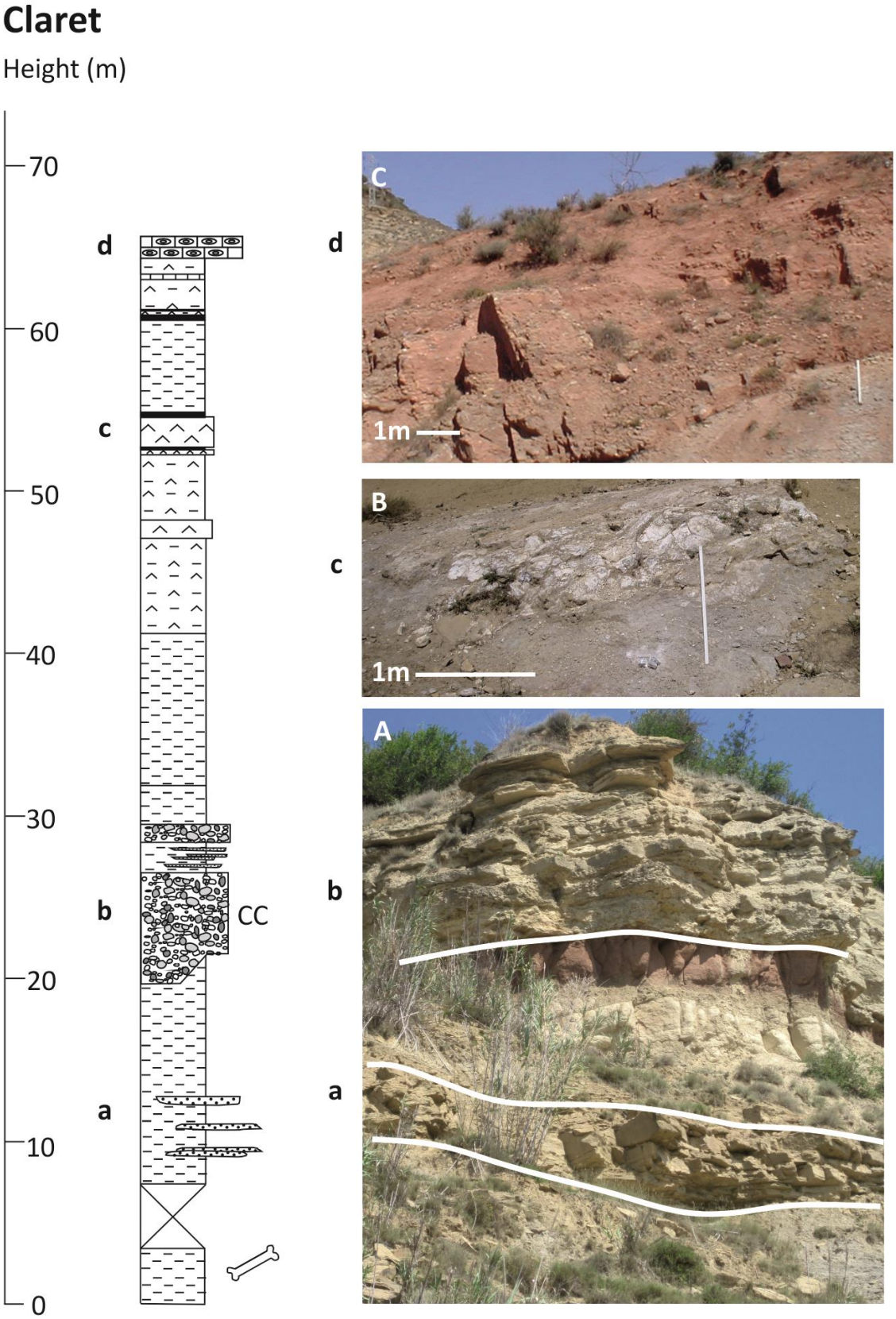

Figure A6.1.5. The Claret section: A) The Claret section up to and including the Claret Conglomerate including a) the sandstone channel below the Claret Conglomerate and b) the Claret Conglomerate, B) image showing gypsum and the surrounding sediment c) gypsum beds associated with the recovery of the CIE at this section, C) the top of the section, including d) the *Alveolina* Beds (limestone). The bone represents the location of fossil mammal sites found by Domingo *et al.* (2009).

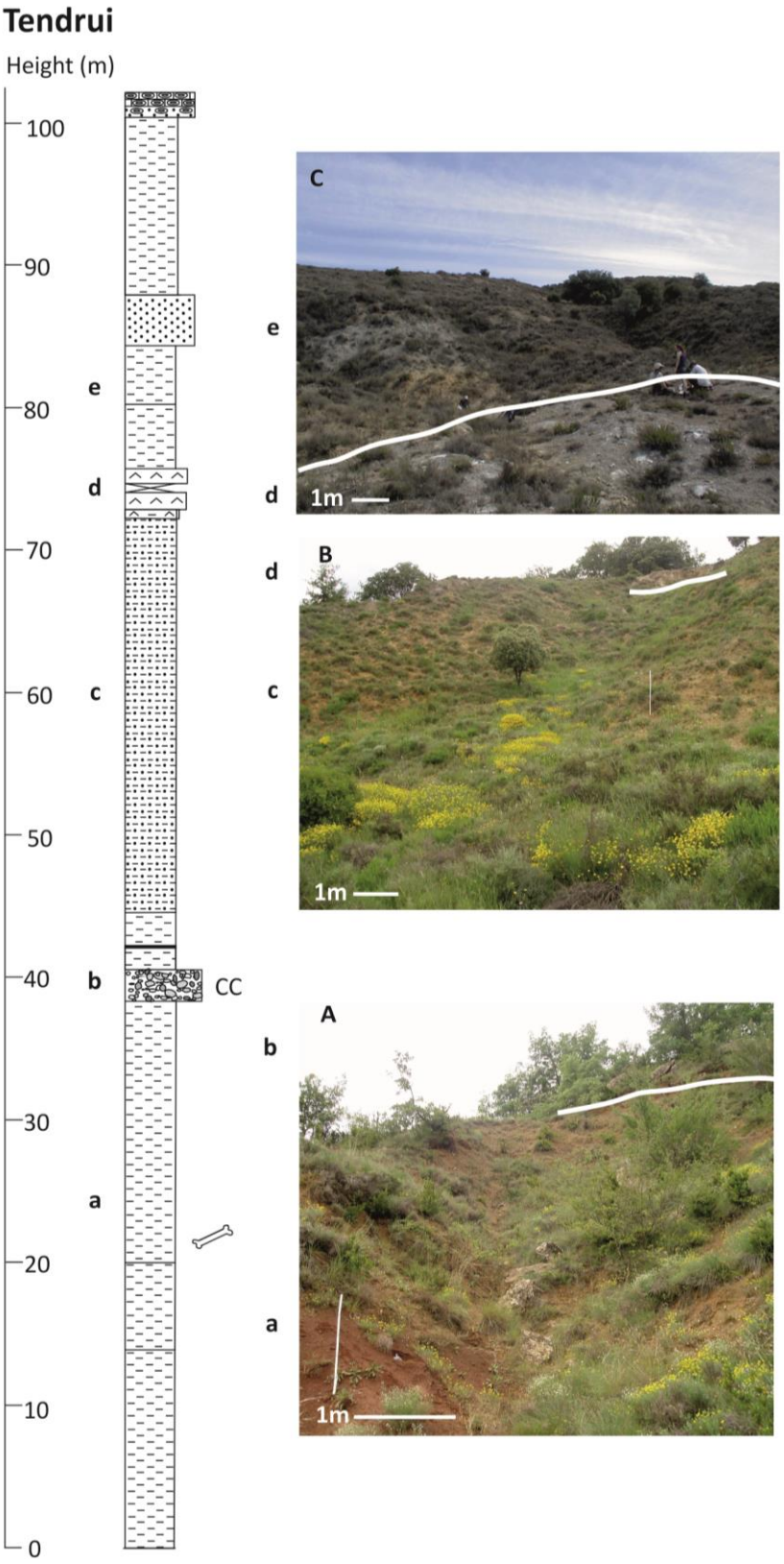

Figure A6.1.6. The Tendrui section: A) The bottom of the section, up to the Claret Conglomerate including a) Clays below the Claret Conglomerate and b) the Claret conglomerate, B) the middle of the section including c) sandy clays above the Claret Conglomerate and d) gypsum beds associated with the recovery of the CIE at this section, C) the top of the section including the gypsum beds from d) and e) clays above the gypsum beds. The bone represents the location of fossil mammal sites found by Domingo *et al.* (2009).

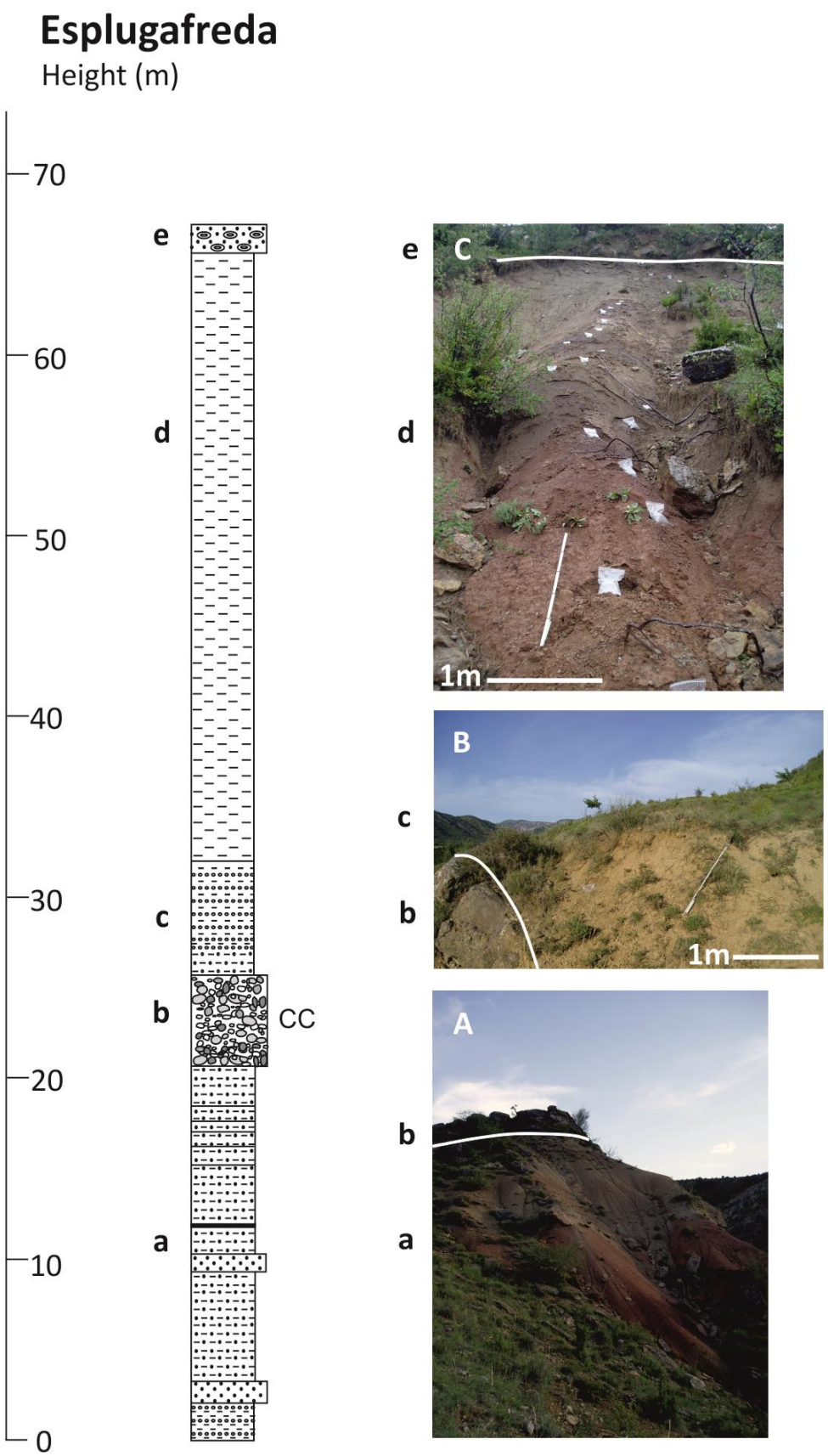

Figure A6.1.7. The Esplugafreda section: A) The bottom of the section, up to the Claret Conglomerate, including a) red clays below the Claret Conglomerate and b) the Claret Conglomerate, B) the middle of the section including the Claret Conglomerate and c) clay containing carbonate nodules above the Claret Conglomerate, C) The top of the section including d) red clays and e) the *Alveolina* Beds (sandstone).

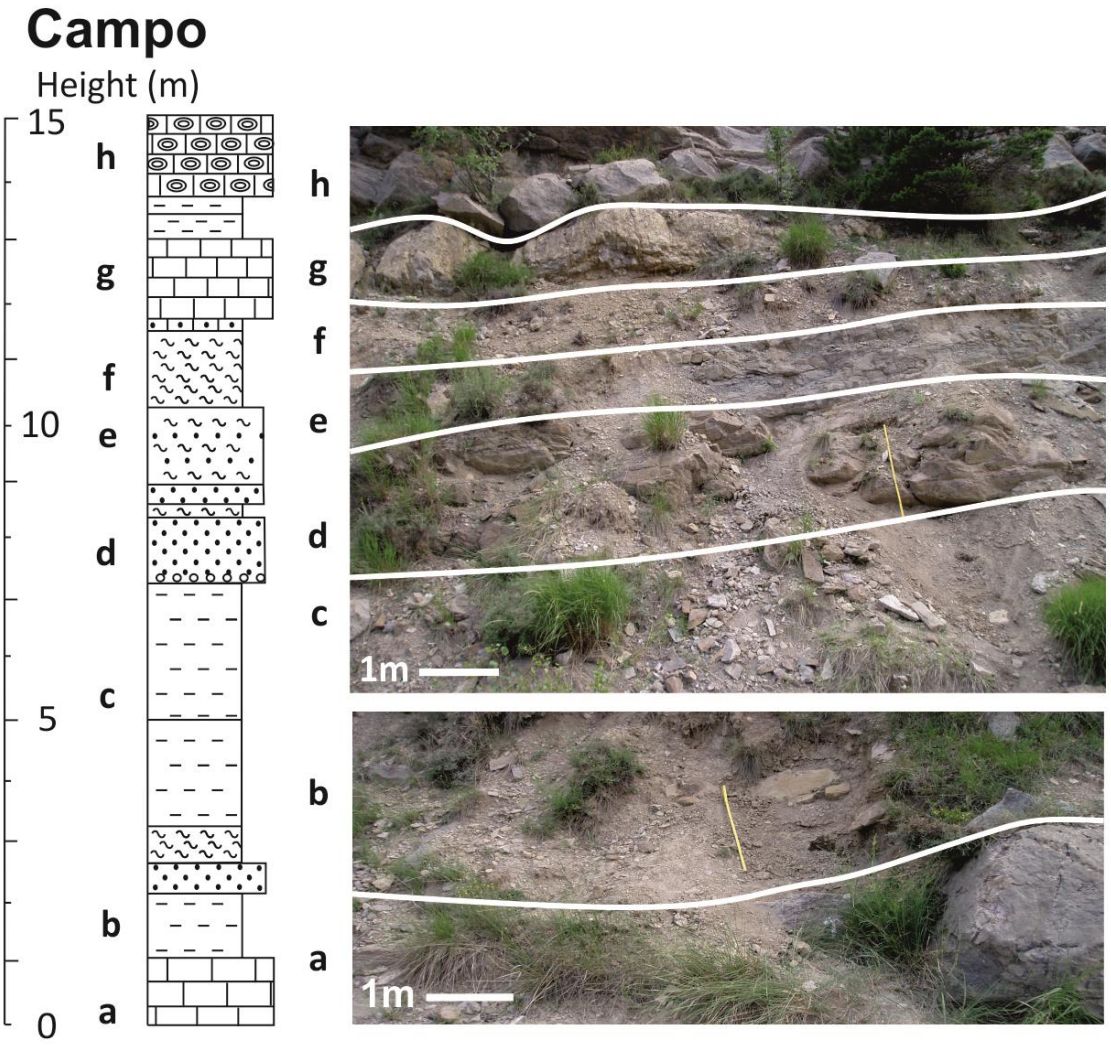

Figure A6.1.8. The Campo section: a) thick limestone bed at the bottom of the section, b&c) continental clays associated with a sea-level lowstand (Molina *et al.* 2000; Schmitz and Pujalte 2003; Pujalte *et al.* 2009a), d) sandstone beds interpreted to be the distal equivalent of the Claret Conglomerate (Schmitz and Pujalte 2007), e) marly sandstone above the distal equivalent of the Claret Conglomerate, f) marl beds, g) thick limestone bed below the *Alveolina* Beds, h) the *Alveolina* Beds (limestone).

MARINE SECTION DESCRIPTIONS

Ermua

The Ermua section is located in the Basque country in the northwestern part of the Pyrénées. This is a road section very close to the AP-8 road, so accessibility is easy. Part of the section is, however, covered with dense vegetation (ca. 11 – 21 m) making sampling extremely challenging. The dip of the beds is 56°, in a south-easterly direction (112° ESE). During the late Cretaceous to early Eocene, the Basque Basin was

at intermediate water depth, with the Ermua section located at the base of the slope. The section comprises limestone and marl couplets in the lower part of the section, which progresses to sandstones and marls with interbedded turbidites (referred to as the Siliciclastic Unit; Schmitz *et al.* 2001). The top of the section comprises massive limestone and marl beds, with a characteristic black limestone bed capping where sampling was finished (ca. 1 m thick; unit "c").

Zumaia

The Zumaia section is located in the Basque country, ca. 25 km from Ermua, on the modern-day shoreline of Itzurun beach. This is the most renowned of all the sections, and was considered for the global stratotype section and point for the Paleocene/Eocene boundary (Aubry *et al.* 2007). The dip of the beds is 70°, in a south-easterly direction (100° ESE). Essentially continuous sea-cliff outcrop deposits from lower Santonian to lower Eocene can be found along the coast of the Gipuzkoa Province halfway between Bilbao and Santander. During the early Palaeogene, the section of Zumaia was bathyal in nature, with a palaeo-depth of ca. 1000m (Baceta *et al.* 2000). Later compression led to uplift of these deep-water deposits, resulting in their present exposure on Itzurun Beach. Accessibility to the section is good, and vegetation cover low, resulting in good exposure and ease of sampling. Specifically, the part of the section studied outcrops adjacently to the pedestrian road leading from the town to the beach. The section studied comprises hemipelagic limestones and marls, followed by thicker limestone and marl units just below the contact with the Siliciclastic Unit, which in this case comprises entirely marls. Above this, the section contains more massive limestone deposits with the occasional marl beds.

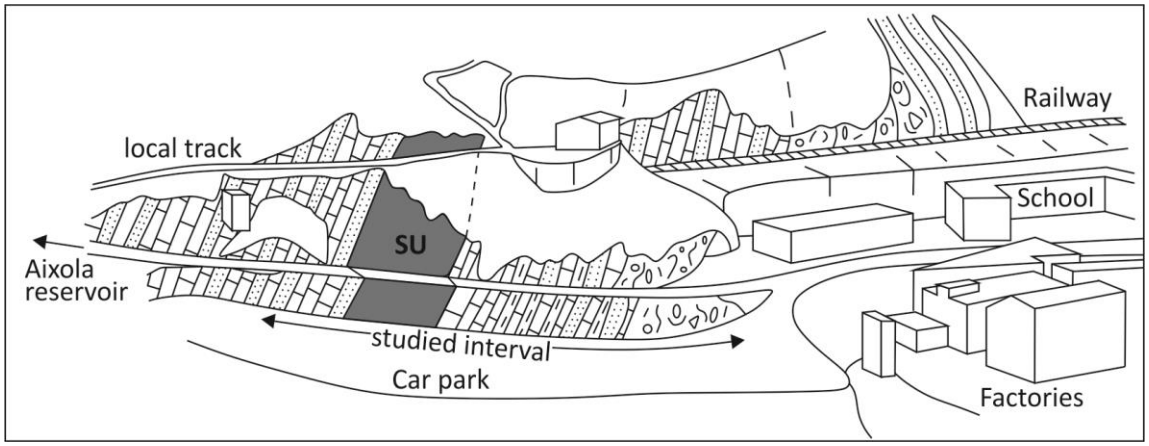

Figure A6.1.9. Location map of the Ermua section modified from Schmitz *et al.* (2001) highlighting the Siliciclastic Unit. The Ermua section is easily accessible from the town of Ermua.

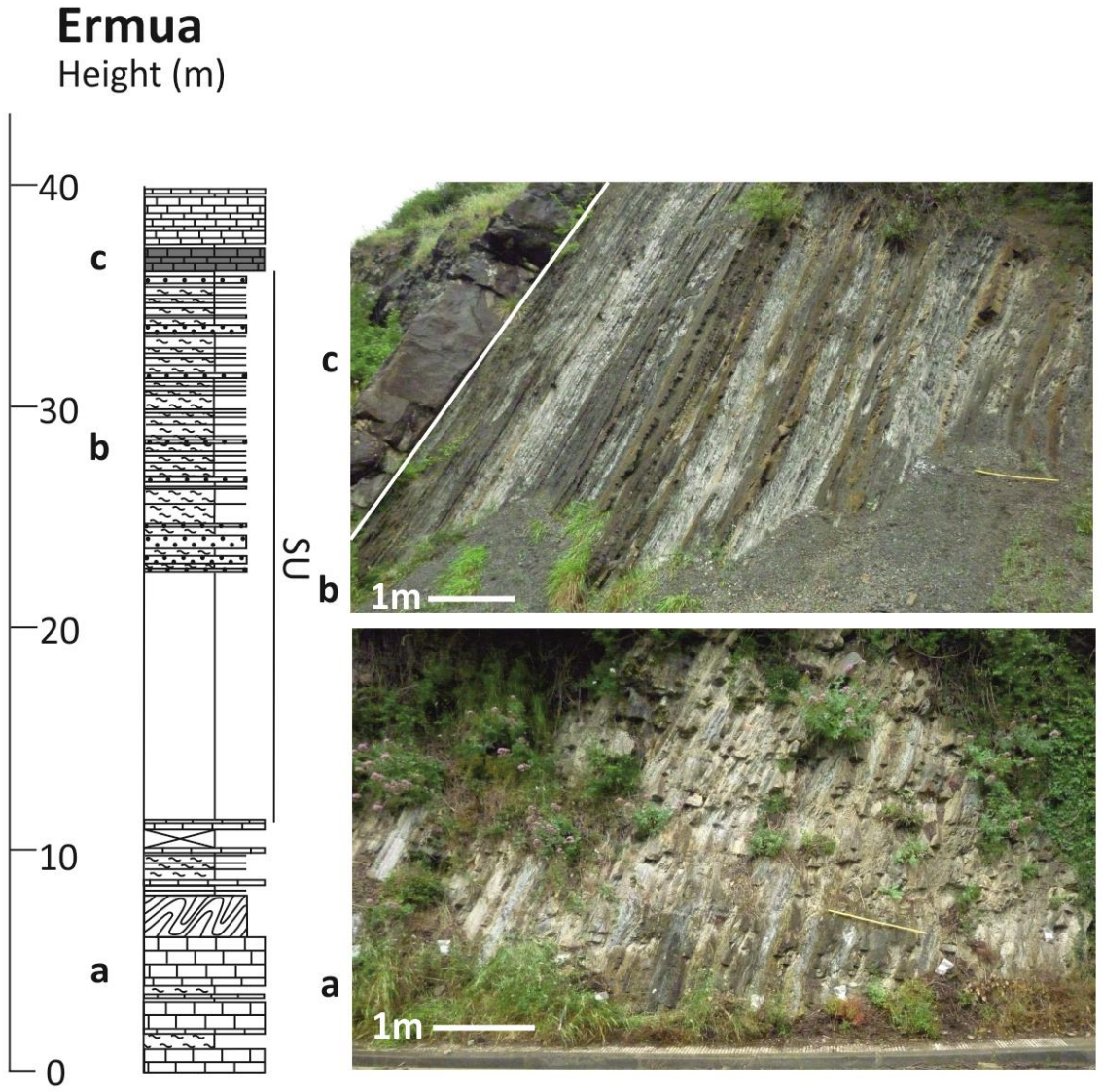

Figure A6.1.10. The Ermua section: A) limestone and marl beds below the Siliciclastic Unit, b) upper exposed portion of the Siliciclastic Unit, c) massive black limestone bed at the top of the Siliciclastic unit.

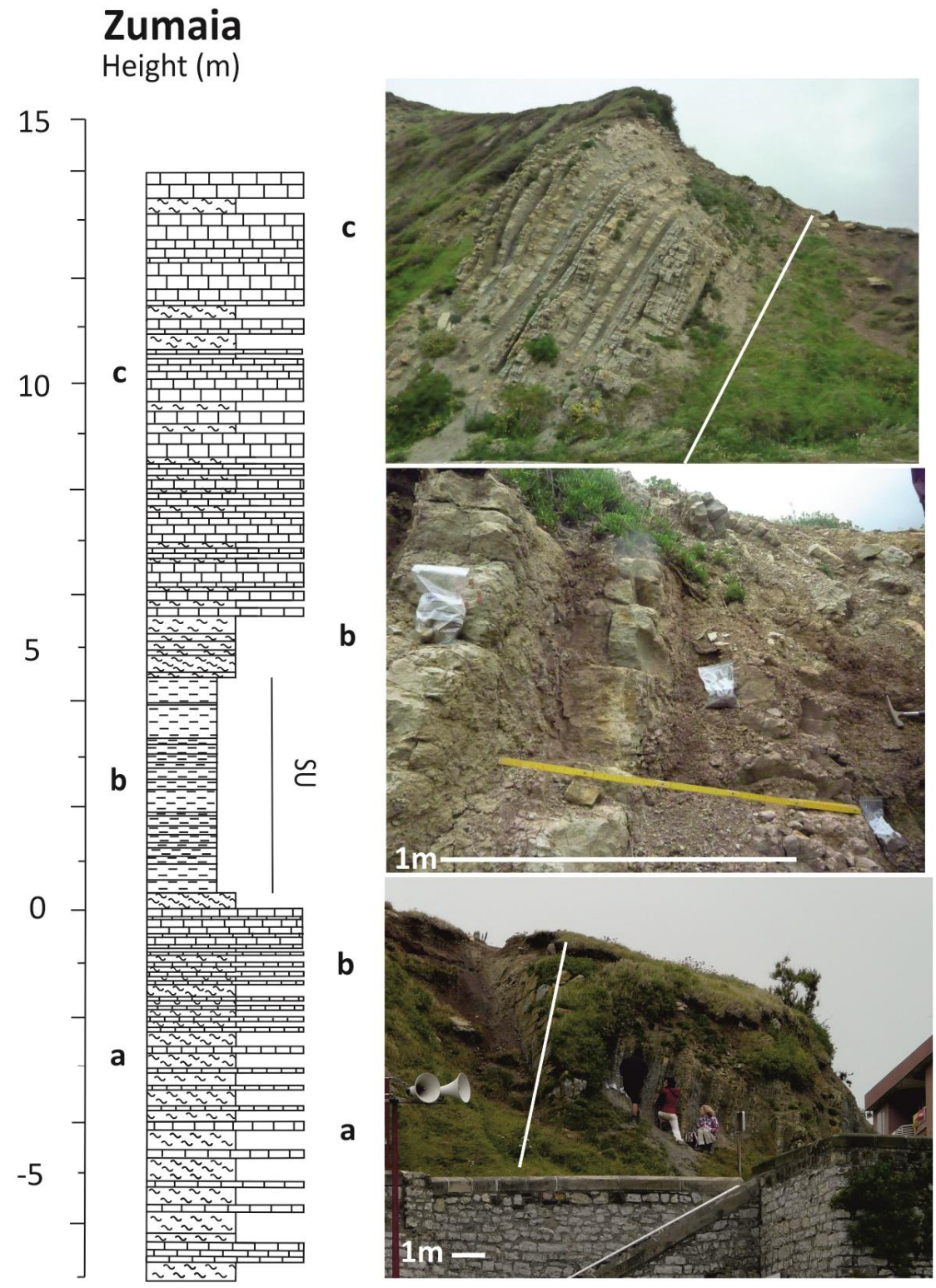

Figure A6.1.11. The Zumaia section: A) limestone and marl beds below the Siliciclastic Unit, b) the Siliciclastic Unit, c) limestone and marl beds above the Siliciclastic Unit.

APPENDIX 1

ANALYTICAL AND STATISTICAL RESULTS FOR CHAPTER 2

This section provides statistical and analytical data discussed in chapter 2.

Statistical data tables

Table A6.1.1. Statistical comparison of lithology and wt%TOC for the section to Claret determine whether wt%TOC is influenced by lithological change. Where $p < 0.05$, a significant difference between wt%TOC and lithology may be observed (highlighted in grey).

Lithology	Range wt%TOC	Mean wt%TOC	Clay	Clay with gypsum	Gypsum	Conglomerate
Clay	0.1 to 0.9	0.4	-	t = -1.8	t = -5.1	t = 0.55
				p = 0.09	p = 0.00	p = 0.58
Clay with gypsum	0.1 to 2.1	0.6	-	-	t = -0.75	t = 0.89
					p = 0.46	p = 0.39
Gypsum	0.3 to 1.1	0.8	-	-	-	t = 2.7
						p = 0.035
Conglomerate	0.2 to 0.5	0.3	-	-	-	-

Table A6.1.2. Statistical comparison of lithology and wt%TOC for the Tendrui section to determine whether wt%TOC is influenced by lithological change. Where $p < 0.05$, a significant difference between wt%TOC and lithology may be observed (highlighted in grey).

Lithology	Range wt% TOC	Mean wt% TOC	Clay	Clay with gypsum	Gypsum	Conglomerate	Limestone
Clay	0.1 to 1.7	0.2	-	t = 1.2	t = -0.87	t = -1.6	t = -3.5
				p = 0.25	p = 0.54	p = 0.12	p = 0.001
Clay with gypsum	0.06 to 0.3	0.2	-	-	t = -1.0	t = -6.8	t = -2.2
					p = 0.49	p = 0.000	p = 0.28
Gypsum	0.2 to 0.9	0.5	-	-	-	t = 0.3	t = -0.4
						p = 0.83	p = 0.75
Conglomerate	0.4 to 0.5	0.4	-	-	-	-	t = -1.1
							p = 0.47
Limestone	0.4 to 0.9	0.7	-	-	-	-	-

Table A6.1.3. Statistical comparison of lithology and wt%TOC for the Esplugafreda section to determine whether wt%TOC is influenced by lithological change. Where $p < 0.05$, a significant difference between wt%TOC and lithology may be observed (highlighted in grey).

Lithology	Range wt%TOC	Mean wt%TOC	Clay	Conglomerate	Sandstone
Clay	0.06 to 0.4	0.2	-	t = -2.2	t = -1.9
				p = 0.28	p = 0.06
Conglomerate	0.5 to 1.0	0.7	-	-	t = 2.3
					p = 0.09
Sandstone	0.1 to 0.5	0.2	-	-	-

Table A6.1.4. Statistical comparison of lithology and wt%TOC for the Campo section to determine whether wt%TOC is influenced by lithological change. Where $p < 0.05$, a significant difference between wt%TOC and lithology may be observed (highlighted in grey).

Lithology	Range wt%TOC	Mean wt%TOC	Clay	Limestone	Sandstone	Marl
Clay	0.1 to 1.4	0.5	-	t = -2.8	t = 0.45	t = 1.8
				p = 0.012	p = 0.66	p = 0.079
Limestone	0.3 to 2.3	1.3	-	-	t = 2.2	t = 2.6
					p = 0.062	p = 0.084
Sandstone	0.3 to 1.3	0.4	-	-	-	t = 1.2
						p = 0.26
Marl	0.1 to 0.4	0.2	-	-	-	-

Table A6.1.5. Statistical comparison of lithology and wt%TOC for the Ermua section to determine whether wt%TOC is influenced by lithological change. Where $p < 0.05$, a significant difference between wt%TOC and lithology may be observed (highlighted in grey).

Lithology	Range wt%TOC	Mean wt%TOC	Limestone	Marl	Siliciclastics
Limestone	0.2	0.2	-	t = -0.34	t = -0.91
				p = 0.79	p = 0.37
Marl	0.1 to 0.2	0.2	-	-	t = -0.83
					p = 0.41
Siliciclastics	0.1 to 1.4	0.4	-	-	-

Table A6.1.6. Statistical comparison of lithology and wt%TOC for the Zumaia section to determine whether wt%TOC is influenced by lithological change. Where $p < 0.05$, a significant difference between wt%TOC and lithology may be observed (highlighted in grey).

Lithology	Range wt%TOC	Mean wt%TOC	Limestone	Marl	Siliciclastics
Limestone	0.1 to 0.5	0.3	-	t = 1.62	t = 4.1
				p = 0.11	p = 0.000
Marl	0.1 to 0.3	0.2	-	-	t = 2.2
					p = 0.036
Siliciclastics	0.1 to 0.3	0.2	-	-	-

Table captions and tables for analytical data

Table A6.1.7. The $\delta^{13}C_{TOC}$ results for the Claret section, produced from the analysis of TOC in sediment samples. Thicker lines above or below rows indicate interpreted CIE for the section, and the cells highlighted in grey are maximum and minimum values used to calculate CIE magnitude.

Table A6.1.8. The $\delta^{13}C_{TOC}$ results for the Tendrui section, produced from the analysis of TOC in sediment samples. Thicker lines above or below rows indicate interpreted CIE for the section, and the cells highlighted in grey are maximum and minimum values used to calculate CIE magnitude.

Table A6.1.9. The $\delta^{13}C_{TOC}$ results for the Esplugafreda section, produced from the analysis of TOC in sediment samples. Thicker lines above or below rows indicate interpreted CIE for the section, and the cells highlighted in grey are maximum and minimum values used to calculate CIE magnitude. Superscripted numbers indicate range of values used to calculate CIE magnitude.

Table A6.1.10. The $\delta^{13}C_{TOC}$ results for the Campo section, produced from the analysis of TOC in sediment samples. Thicker lines above or below rows indicate interpreted CIE for the section, and the cells highlighted in grey are maximum and minimum values used to calculate CIE magnitude.

Table A6.1.11. The $\delta^{13}C_{TOC}$ results for the Ermua section, produced from the analysis of TOC in sediment samples. Thicker lines above or below rows indicate interpreted CIE for the section, and the cells highlighted in grey are maximum and minimum values used to calculate CIE magnitude.

Table A6.1.12. The $\delta^{13}C_{TOC}$ results for the Zumaia section, produced from the analysis of TOC in sediment samples. Thicker lines above or below rows indicate interpreted CIE for the section, and the cells highlighted in grey are maximum and minimum values used to calculate CIE magnitude.

Table A6.1.7.

Sample	Height (m)	$\delta^{13}C_{TOC}$ (‰ VPDB)	wt%C	Sample	Depth (m)	$\delta^{13}C_{TOC}$ (‰ VPDB)	wt%C
CLA-I+30	63.41	-23.1	0.9	CLA-I-56	33.80	-26.6	0.4
CLA-I+15	63.34	-23.0	0.5	CLA-I-57	33.61	-26.1	0.2
CLA-I-0	63.23	-23.4	0.3	CLA-I-58	33.00	-26.9	0.4
CLA-I-10	63.13	-23.3	1.0	CLA-I-59	32.25	-27.2	0.3
CLA-I-11	62.89	-21.7	2.1	CLA-I-60	31.97	-25.9	0.3
CLA-I-12	62.65	-22.7	0.9	CLA-I-62	31.62	-25.6	0.2
CLA-I-13	62.40	-22.3	2.0	CLA-I-63	30.97	-25.0	0.3
CLA-I-14	62.18	-22.1	0.9	CLA-I-64	30.29	-26.6	0.4
CLA-I-15	61.92	-22.3	1.0	CLA-I-65	28.10	-26.7	0.3
CLA-I-16	61.60	-22.7	0.8	CLA-I-66	27.75	-26.1	0.2
CLA-I-17	61.34	-23.7	0.4	CLA-I-69	27.45	-25.8	0.2
CLA-I-18	61.09	-23.8	0.3	CLA-I-67	27.19	-26.1	0.3
CLA-I-19	60.87	-25.1	0.4	CLA-I-68	26.70	-26.9	0.3
CLA-I-20	60.72	-26.1	0.3	CLA-I-61	25.78	-25.8	0.3
CLA-I-21	60.43	-23.4	0.4	CLA-I-70	21.48	-25.4	0.2
CLA-I-22	59.81	-24.0	0.4	CLA-I-71	20.80	-26.1	0.2
CLA-I-23	58.74	-24.3	0.2	CLA-I-72	20.19	-26.0	0.2
CLA-I-24	57.70	-24.5	0.1	CLA-MAR´10-15	20.0	-25.4	0.3
CLA-I-25	56.75	-25.3	0.2	CLA-MAR´10-14	18.4	-24.6	0.5
CLA-I-26	54.69	-22.3	0.5	CLA-I-73	18.18	-26.8	0.3
CLA-I-27	54.42	-23.8	0.8	CLA-MAR´10-13	17.6	-24.3	0.5
CLA-I-28	54.18	-26.4	1.1	CLA-MAR´10-12	16.8	-23.3	0.5
CLA-I-29	52.24	-27.8	0.4	CLA-MAR´10-11	16	-24.0	0.4
CLA-I-30	51.80	-25.7	0.1	CLA-I-74	15.93	-23.3	0.3
CLA-I-31	50.23	-26.2	0.2	CLA-MAR´10-10	15.2	-23.6	0.5
CLA-I-32	49.32	-26.0	0.2	CLA-I-75	14.80	-23.4	0.9
CLA-I-33	48.56	-24.8	0.1	CLA-MAR´10-9	14.4	-23.5	0.6
CLA-I-34	47.50	-26.7	0.9	CLA-I-76	14.25	-23.5	0.4
CLA-I-35	46.80	-26.4	0.3	CLA-MAR´10-8	13.6	-23.6	0.4
CLA-I-36	43.79	-25.9	0.3	CLA-I-77	13.31	-23.2	0.4
CLA-I-37	41.80	-25.8	0.2	CLA-MAR´10-7	12.8	-23.9	0.7
CLA-I-38	41.27	-26.1	0.2	CLA-MAR´10-6	12	-23.5	0.7
CLA-I-39	40.87	-26.0	0.4	CLA-I-78	11.50	-23.8	0.6
CLA-I-40	40.25	-26.0	0.1	CLA-MAR´10-5	11.4	-23.5	0.6
CLA-I-41	39.61	-26.0	0.2	CLA-MAR´10-4	10.8	-23.2	0.7
CLA-I-42	39.25	-26.2	0.5	CLA-I-79	10.27	-23.1	0.3
CLA-I-43	38.54	-26.2	0.2	CLA-MAR´10-3	10.2	-23.8	0.5
CLA-I-44	38.00	-25.6	0.2	CLA-I-80	9.80	-23.6	0.6
CLA-I-45	37.62	-25.8	0.2	CLA-MAR´10-2	9.6	-23.4	0.5
CLA-I-46	37.35	-25.6	0.2	CLA-MAR´10-1	9	-23.8	0.5
CLA-I-47	37.00	-25.8	0.2	CLA-I-81	8.75	-23.7	0.4
CLA-I-48	36.60	-25.6	0.2	CLA-I-82	7.37	-23.9	0.8
CLA-I-49	36.25	-25.6	0.2	CLA-I-83	3.10	-23.4	0.3
CLA-I-50	35.80	-25.8	0.2	CLA-MAR´10 YAC-0	3	-24.5	0.3
CLA-I-51	35.50	-26.1	0.2	CLA-MAR´10 YAC-1	2.4	-25.6	0.3
CLA-I-52	35.18	-26.0	0.3	CLA-MAR´10 YAC-2	1.8	-26.0	0.1
CLA-I-53	34.62	-26.1	0.3	CLA-MAR´10 YAC-3	1.2	-25.2	0.2
CLA-I-54	34.37	-26.1	0.3	CLA-MAR´10 YAC-4	0.6	-25.5	0.2
CLA-I-55	34.11	-26.6	0.5	CLA-I-84	0.00	-23.9	0.3

Table A6.1.8.

Sample	Height (m)	$\delta^{13}C_{TOC}$ (‰ VPDB)	wt%C	Sample	Height (m)	$\delta^{13}C_{TOC}$ (‰ VPDB)	wt%C
TEN-V+9	92.20	-23.9	0.9	TEN-V-34	12.52	-25.5	0.1
TEN-V+8	90.33	-23.3	1.7	TEN-V-35	12.19	-24.8	0.1
TEN-V+7	89.11	-23.6	0.4	TEN-V-36	11.55	-25.5	0.1
TEN-V+6	77.89	-24.1	0.4	TEN-V-37	11.00	-23.9	0.2
TEN-V+5	74.10	-23.0	0.6	TEN-V-38	10.89	-25.4	0.2
TEN-V+4	70.98	-25.0	0.2	TEN-V-39	10.02	-25.0	0.2
TEN-V+3	66.80	-24.7	0.2	TEN-V-40	9.85	-25.7	0.2
TEN-V+2	65.80	-23.9	0.2	TEN-MAR´10+5	9.815	-24.2	0.2
TEN-V+1	63.98	-26.1	0.9	TEN-V-41	9.11	-24.3	0.1
TEN-V-0	63.19	-26.5	0.1	TEN-V-42	8.90	-24.8	0.1
TEN-V-1	62.72	-26.7	0.2	TEN-MAR´10+4	8.666	-24.3	0.2
TEN-V-2	61.53	-26.6	0.1	TEN-V-43	8.51	-24.0	0.1
TEN-V-3	59.48	-25.9	0.1	TEN-V-44	8.00	-24.3	0.1
TEN-V-4	56.77	-26.6	0.1	TEN-V-45	7.77	-25.0	0.1
TEN-V-5a	53.61	-26.1	0.2	TEN-MAR´10+3	7.517	-23.4	0.2
TEN-V-5b	52.75	-26.2	0.1	TEN-V-46	6.83	-24.7	0.1
TEN-V-6a	51.70	-26.4	0.1	TEN-MAR´10+2	6.368	-24.1	0.2
TEN-V-6b	49.11	-26.6	0.1	TEN-V-47	5.43	-24.3	0.1
TEN-V-7	45.36	-25.9	0.1	TEN-MAR´10+1	5.219	-24.6	0.2
TEN-V-7b	45.36	-26.6	0.1	TEN-V-48	4.63	-24.3	0.1
TEN-V-8	43.48	-26.3	0.1	TEN-MAR´10-1	4.07	-24.4	0.2
TEN-V-9	39.61	-26.2	0.1	TEN-V-49	3.71	-24.0	0.1
TEN-V-10	35.18	-26.1	0.2	TEN-MAR´10-2	3.67	-25.5	0.2
TEN-V-11	32.00	-26.0	0.3	TEN-MAR´10-3	3.27	-24.8	0.2
TEN-V-12b	30.81	-26.3	0.1	TEN-MAR´10-4	2.87	-25.2	0.2
TEN-V-12a	30.81	-26.5	0.2	TEN-MAR´10-5	2.47	-25.0	0.2
TEN-V-13	29.36	-26.1	0.4	TEN-V-50	2.29	-23.6	0.1
TEN-V-14	28.47	-25.6	0.5	TEN-MAR´10-6	2.07	-24.9	0.1
TEN-V-15	25.57	-25.7	0.2	TEN-MAR´10-7	1.67	-25.4	0.2
TEN-V-16	24.00	-26.4	0.2	TEN-V-51	1.35	-23.0	0.1
TEN-V-17	22.80	-25.5	0.2	TEN-MAR´10-8	1.27	-24.6	0.1
TEN-V-18	22.09	-25.2	0.2	TEN-MAR´10-9	0.87	-24.6	0.2
TEN-V-19	21.47	-24.7	0.1	TEN-V-52	0.50	-23.7	0.1
TEN-V-20	20.88	-25.0	0.2	TEN-MAR´10-10	0.47	-25.1	0.2
TEN-V-21	20.25	-24.6	0.2	TEN-MAR´10-11	0.07	-22.9	0.2
TEN-V-22	19.80	-24.6	0.2	TEN-MAR´10-12	-0.33	-23.9	0.2
TEN-V-23	19.57	-24.7	0.2	TEN-MAR´10-13	-0.93	-24.2	0.2
TEN-V-24	19.06	-25.1	0.2	TEN-MAR´10-14	-1.53	-23.8	0.2
TEN-V-25	18.48	-24.4	0.2	TEN-MAR´10-15	-2.13	-23.4	0.3
TEN-V-26	17.90	-26.0	0.3	TEN-MAR´10-16	-2.73	-23.3	0.2
TEN-V-27	17.20	-25.5	0.2	TEN-MAR´10-17	-3.33	-24.7	0.1
TEN-V-28	16.41	-25.0	0.2	TEN-MAR´10-18	-3.93	-24.9	0.2
TEN-V-29	15.70	-24.4	0.2	TEN-MAR´10-19	-4.53	-24.3	0.2
TEN-V-30	15.00	-25.3	0.2	TEN-MAR´10-20	-5.13	-25.3	0.2
TEN-V-31	14.25	-24.6	0.1	TEN-MAR´10-21	-6.93	-26.1	0.3
TEN-V-32	13.78	-24.8	0.2	TEN-MAR´10-22	-7.73	-25.1	0.2
TEN-V-33	13.16	-24.9	0.2	TEN-MAR´10-23	-8.53	-25.1	0.3

Table A6.1.9.

Sample	Height (m)	$\delta^{13}C_{TOC}$ (‰ VPDB)	wt%C	Sample	Height (m)	$\delta^{13}C_{TOC}$ (‰ VPDB)	wt%C
ESP-IL-0	66.21	-22.3	0.5	ESP-MAR´10-5	19.37	-23.6	0.3
ESP-IL-1	65.50	-22.0	0.4	ESP-MAR´10-6	19.07	-23.4	0.3
ESP-IL-2	64.71	-22.3	0.1	ESP-3	18.86	-24.8	0.2
ESP-IL-3	63.93	-22.3	0.1	ESP-MAR´10-7	18.77	-22.9	0.2
ESP-IL-4	63.14	-22.3	0.1	ESP-MAR´10-8	18.47	-23.9	0.3
ESP-IL-5	62.29	-21.1	0.2	ESP-MAR´10-9	18.17	-24.5	0.2
ESP-IL-6	61.57	-21.6	0.1	ESP-4	18.14	-22.1	0.2
ESP-IL-7	60.71	-22.1	0.1	ESP-MAR´10-10	17.87	-23.5	0.2
ESP-IL-8	59.93	-21.7	0.1	ESP-MAR´10-11	17.57	-23.3	0.2
ESP-IL-9	59.14	-21.8	0.1	ESP-5	17.29	-22.2	0.2
ESP-IL-10	58.29	-21.1	0.1	ESP-MAR´10-12	17.27	-23.6	0.2
ESP-IL-11	57.50	-21.5	0.1	ESP-MAR´10-13	16.97	-24.0	0.2
ESP-IL-12	56.64	-21.5	0.1	ESP-MAR´10-14	16.67	-24.6	0.2
ESP-IL-13	55.86	-21.1	0.1	ESP-6	16.43	-21.2	0.2
ESP-IL-14	55.00	-21.4	0.1	ESP-MAR´10-15	16.27	-25.0	0.2
ESP-IL-15	54.14	-21.4	0.1	ESP-MAR´10-16	15.87	-24.5	0.2
ESP-IL-16	53.36	-21.6	0.1	ESP-7	15.71	-21.2	0.1
ESP-IL-17	52.57	-21.4	0.1	ESP-MAR´10-17	15.47	-24.4	0.2
ESP-IL-18	51.68	-21.6	0.1	ESP-8	14.86	-21.9	0.1
ESP-IL-19	50.75	-21.3	0.1	ESP-9	14.07	-21.9	0.1
ESP-IL-20	50.00	-21.0	0.1	ESP-10	13.29	-22.2	0.1
ESP-IL-21	49.07	-21.0	0.1	ESP-11	12.57	-21.9	0.1
ESP-IL-22	48.28	-21.5	0.1	ESP-12	11.86	-21.9	0.1
ESP-IL-23	47.57	-21.9	0.1	ESP-13	11.00	-21.7	0.1
ESP-IL-24	46.71	-21.9	0.1	ESP-14	10.29	-21.6	0.2
ESP-IL-25	45.93	-22.4	0.1	ESP-15	9.43	-21.8	0.2
ESP-IL-26	45.14	-22.0	0.1	ESP-16	8.86	-21.7	0.3
ESP-IL-27	44.57	-22.3	0.1	ESP-17	7.71	-21.9	0.2
ROJO+2	39.00	-24.2	0.2	ESP-18	6.86	-21.7	0.2
ROJO+1	37.43	-23.4	0.1	ESP-19	6.11	-21.9	0.2
ESP+9	32.14	-26.3	0.2	ESP-20	5.29	-21.8	0.2
ESP+8	31.36	-26.5	0.1	ESP-21	2.00	-22.7	0.1
ESP+7	30.50	-26.2	0.1	ESP-22	1.14	-22.7	0.1
ESP+6	29.71	-26.2	0.1				
ESP+5	29.04	-25.9	0.1				
ESP+4	28.07	-25.1	0.1				
ESP+3	27.43	-25.8	0.1				
ESP+2	26.57	-25.4	0.1				
ESP+1	25.71	-25.7	0.2				
CC+2	24.50	-24.7	0.5				
CC+1	22.71	-26.0	1.0				
ESP-1	20.57	-23.2	0.3				
ESP-MAR´10-1	20.57	-24.2	0.3				
ESP-MAR´10-2	20.27	-23.4	0.3				
ESP-MAR´10-3	19.97	-23.4	0.3				
ESP-2	19.86	-21.9	0.2				
ESP-MAR´10-4	19.67	-23.9	0.3				

Table A6.1.10.

Sample	Height (m)	$\delta^{13}C_{TOC}$ (‰ VPDB)	wt%C
CPE+20	13.08	-23.6	2.2
CPE+19	12.47	-21.3	1.4
CPE-MAR´10+11	12.2	-24.9	0.2
CPE+18	11.81	-25.0	0.1
CPE+17	11.21	-25.9	0.3
CPE+16	10.63	-25.5	0.2
CPE-MAR´10+10	10.33	-26.7	0.2
CPE+15	10.02	-26.0	0.1
CPE-MAR´10+9	9.73	-26.4	0.2
CPE+14	9.42	-26.2	0.1
CPE-MAR´10+8	9.23	-26.6	0.2
CPE+13	8.92	-26.4	0.3
CPE-MAR´10+7	8.63	-26.5	0.2
CPE+12	8.34	-27.3	0.4
CPE+11	7.75	-26.5	0.4
CPE+10	6.94	-28.0	1.3
CPE+9	6.66	-27.9	0.6
CPE-MAR´10+6	6.36	-28.9	1.1
CPE+8	5.94	-28.5	0.9
CPE-MAR´10+5	5.76	-28.7	0.8
CPE+7	5.31	-28.3	0.8
CPE-MAR´10+4	5.06	-26.4	0.2
CPE+6	4.69	-26.2	0.1
CPE-MAR´10+3	4.51	-26.4	0.2
CPE+5	3.94	-26.4	0.1
CPE+4	3.33	-26.4	0.1
CPE+3	2.78	-27.9	0.4
CPE+2	2.23	-25.1	0.2
CPE-MAR´10+2	1.75	-25.2	0.3
CPE+1	1.60	-24.9	0.2
CPE-MAR´10+1	1.25	-26.6	0.5
CPE-A	1.09	-25.4	0.9
CPE-0	0.94	-23.5	1.4
CPE-3	0.55	-23.4	1.1

Table A6.1.11.

Sample Name	Height (m)	$\delta^{13}C_{TOC}$ (‰ VPDB)	wt%C
ERM-ASU+12	45	-22.6	0.6
ERM-ASU+11	44	-26.7	0.2
ERM-ASU+10	43	-26.6	0.4
ERM-ASU+9	42	-27.5	0.5
ERM-ASU+8	41	-27.7	0.2
ERM-ASU+7	40	-28.7	0.3
ERM-ASU+6	39	-28.7	0.3
ERM-ASU+5	38	-29.0	0.2
ERM-ASU+4	37	-29.2	0.3
ERM-ASU+3	36	-29.2	0.2
ERM-ASU+2	35	-29.3	0.2
ERM-ASU+1	34	-29.0	0.4
ERM-ASU+0	33	-28.8	0.3
ERM-SU+18	32	-28.3	0.3
ERM-SU+17	31	-28.2	0.2
ERM-SU+16	30	-28.9	0.3
ERM-SU+15	29	-28.5	1.1
ERM-SU+14	28	-29.1	0.2
ERM-SU+13	27	-28.7	0.2
ERM-SU+12	26	-29.5	0.2
ERM-SU+11	25	-28.6	0.2
ERM-SU+10	24	-28.8	0.2
ERM-SU+9	23	-28.0	0.3
ERM-SU+8	22	-27.0	0.59
ERM-SU+7	21	-27.9	0.1
ERM-SU+6	20	-27.5	0.7
ERM-SU+5	19	-27.9	0.4
ERM-SU+4	18	-27.1	0.2
ERM-SU+3	17	-24.5	0.2
ERM-SU+2	16	-26.9	1.4
ERM-SU+1	15	-27.2	1.4
ERM-SU+0	14	-22.4	0.1
ERM-BSU+15	13	-24.2	0.2
ERM-BSU+14	12	-24.2	0.1
ERM-BSU+13	11	-24.2	0.2
ERM-BSU+12	10	-24.0	0.2
ERM-BSU+11	9	-24.8	0.2
ERM-BSU+10	8	-24.3	0.3
ERM-BSU+9	7	-23.7	0.3
ERM-BSU+8	6	-23.5	0.2
ERM-BSU+7	5	-24.1	0.3
ERM-BSU+6	4	-23.8	0.1
ERM-BSU+5	3	-24.1	0.2
ERM-BSU+4	2	-23.4	0.1
ERM-BSU+3	1	-23.6	0.1
ERM-BSU+2	0	-22.8	0.1

Table A6.1.12.

Sample	Height (m)	$\delta^{13}C_{TOC}$ (‰ VPDB)	wt%C	Sample	Height (m)	$\delta^{13}C_{TOC}$ (‰ VPDB)	wt%C
ZUM-ASU+18	21.95	-25.7	0.3	ZUM-SU+9	8.70	-26.5	0.3
ZUM-ASU+17	21.45	-25.3	0.4	ZUM-SU+8	8.55	-27.4	0.1
ZUM-ASU+16	20.95	-25.7	0.3	ZUM-SU+7	8.40	-28.4	0.2
ZUM-ASU+15	20.45	-25.7	0.3	ZUM-SU+6	8.25	-28.2	0.2
ZUM-ASU+14	19.95	-25.7	0.5	ZUM-SU+5	8.10	-27.8	0.1
ZUM-ASU+13	19.45	-25.6	0.3	ZUM-SU+4	7.95	-27.6	0.1
ZUM-ASU+12	18.95	-26.3	0.2	ZUM-SU+3	7.80	-26.7	0.1
ZUM-ASU+11	18.45	-26.3	0.2	ZUM-SU+2	7.65	-25.5	0.1
ZUM-ASU+10	17.95	-25.8	0.3	ZUM-SU+1	7.50	-24.3	0.2
ZUM-ASU+9	17.45	-26.1	0.3	ZUM-SU+0	7.35	-25.0	0.1
ZUM-ASU+8	16.95	-25.9	0.3	ZUM-BSU+24	7.20	-25.9	0.3
ZUM-ASU+7	16.45	-25.6	0.3	ZUM-BSU+23	6.90	-24.8	0.3
ZUM-ASU+6	15.95	-25.0	0.3	ZUM-BSU+22	6.60	-25.0	0.3
ZUM-ASU+5	15.45	-24.8	0.3	ZUM-BSU+21	6.30	-25.3	0.3
ZUM-ASU+4	14.95	-25.7	0.3	ZUM-BSU+20	6.00	-25.4	0.3
ZUM-ASU+3	14.45	-25.5	0.3	ZUM-BSU+19	5.70	-25.1	0.1
ZUM-ASU+2	13.95	-25.1	0.2	ZUM-BSU+18	5.40	-25.2	0.3
ZUM-ASU+1	13.45	-25.7	0.2	ZUM-BSU+17	5.10	-25.7	0.2
ZUM-ASU+0	12.95	-26.2	0.2	ZUM-BSU+16	4.80	-25.7	0.2
ZUM-SU+34	12.45	-26.0	0.1	ZUM-BSU+15	4.50	-24.3	0.2
ZUM-SU+33	12.30	-26.0	0.1	ZUM-BSU+14	4.20	-25.0	0.2
ZUM-SU+32	12.15	-26.1	0.1	ZUM-BSU+13	3.90	-25.0	0.2
ZUM-SU+31	12.00	-26.5	0.2	ZUM-BSU+12	3.60	-25.1	0.3
ZUM-SU+30	11.85	-26.2	0.2	ZUM-BSU+11	3.30	-24.0	0.1
ZUM-SU+29	11.70	-26.0	0.2	ZUM-BSU+10	3.00	-24.4	0.2
ZUM-SU+28	11.55	-25.7	0.1	ZUM-BSU+9	2.70	-25.0	0.3
ZUM-SU+27	11.40	-27.1	0.2	ZUM-BSU+8	2.40	-24.6	0.3
ZUM-SU+26	11.25	-26.9	0.2	ZUM-BSU+7	2.10	-24.5	0.2
ZUM-SU+25	11.10	-26.6	0.2	ZUM-BSU+6	1.80	-24.6	0.3
ZUM-SU+24	10.95	-26.5	0.2	ZUM-BSU+5	1.50	-23.8	0.2
ZUM-SU+23	10.80	-25.6	0.2	ZUM-BSU+4	1.20	-24.8	0.3
ZUM-SU+22	10.65	-26.6	0.2	ZUM-BSU+3	0.90	-23.9	0.3
ZUM-SU+21	10.50	-26.6	0.2	ZUM-BSU+2	0.60	-24.4	0.2
ZUM-SU+20	10.35	-26.2	0.3	ZUM-BSU+1	0.30	-24.4	0.2
ZUM-SU+19	10.20	-26.7	0.3	ZUM-BSU+0	0.00	-24.5	0.3
ZUM-SU+16	9.75	-26.0	0.3				
ZUM-SU+15	9.60	-27.3	0.2				
ZUM-SU+14	9.45	-27.1	0.2				
ZUM-SU+13	9.30	-27.1	0.2				
ZUM-SU+12	9.15	-27.5	0.2				
ZUM-SU+11	9.00	-27.6	0.3				
ZUM-SU+10	8.85	-27.6	0.1				

6.2 APPENDIX 2: ADDITIONAL DATA FOR CHAPTER 3

This appendix provides supplementary information for Chapter 3. Method development and result tables for *n*-alkane isolation method development, *n*-alkane concentrations, carbonate isotopes, and palynological assemblages are provided for all data discussed.

METHOD DEVELOPMENT

Prior to extraction of the TLE and subsequent separation of *n*-alkanes using T-SEP™, several methods were investigated to ensure efficient and effective methods were employed.

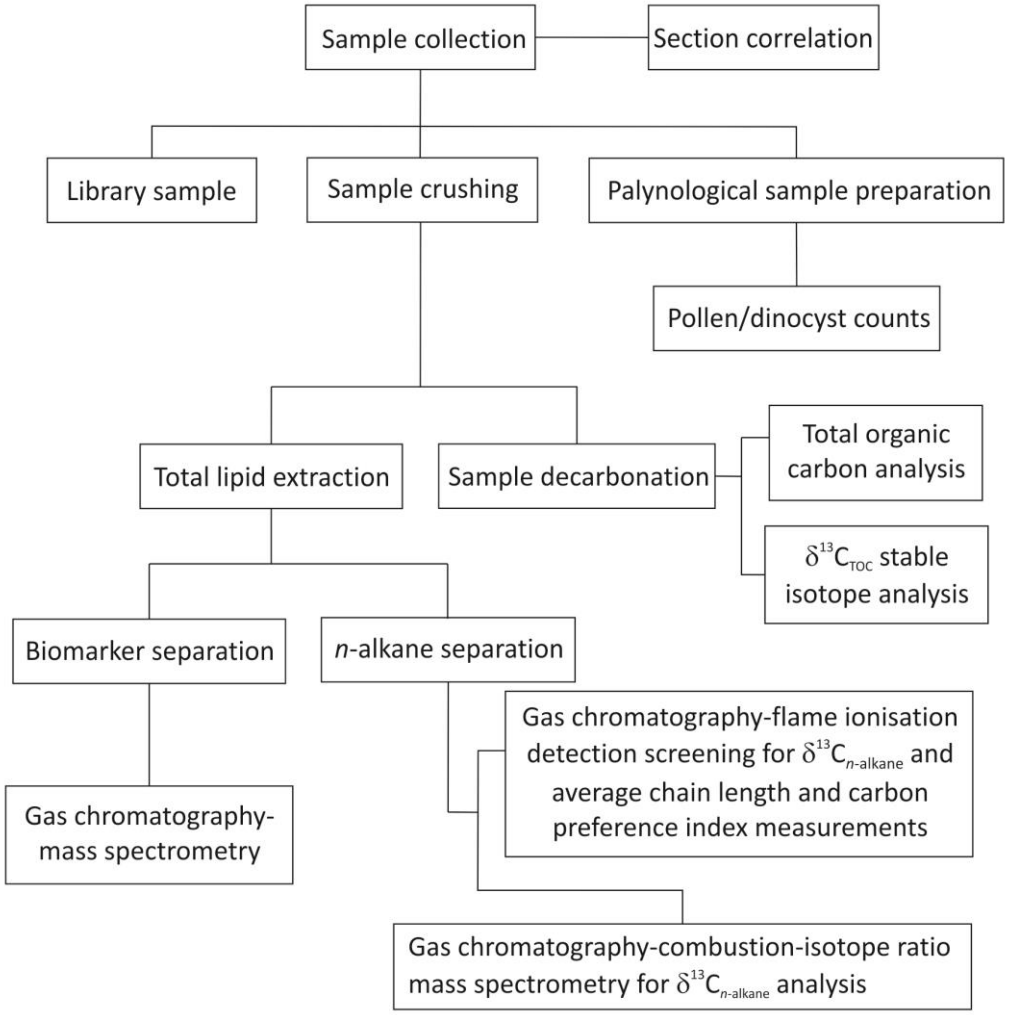

Figure 6.2.1. Flow chart detailing all the geological and geochemical methods used during this research, from sample collection to compound identification.

6.2.1.1 Reference Sediment (CLA-4)

Operator reproducibility, analytical precision, and method efficiency were all investigated prior to extraction and analysis of collected samples. In order to do this a reference sediment (referred to as CLA-4) was used. This was prepared by crushing and homogenising a bulk quantity of sediment from the Claret section. An equimolar C_{25} to C_{33} *n*-alkane standard was spiked into the reference sediment each time it was used to check that *n*-alkanes could be adequately recovered from the sample. To make the equimolar C_{25-33} *n*-alkane standard, individual *n*-alkanes were each weighed into separate vials and diluted to 0.1 mg mL^{-1}. The equimolar standard was then prepared by dispensing appropriate volumes of each individual *n*-alkane based on the ratio of their relative molecular mass (RMM) to that of tritriacontane (Table 6.2.1.). The final number of moles of each *n*-alkane ($2.16x10^{-7}$) was calculated using Equation 6.2.1.

Quantification of analytes was achieved by integrating the peak areas of the analytes and the internal standard in either the gas chromatogram from the GC-FID, or the total ion chromatogram (TIC) obtained using GC-MS, and dividing the analyte peak area by the peak area of the internal standard, and multiplying by the mass of internal standard (Equation 6.2.2.).

Table 6.2.1. Data for preparation of the equimolar *n*-alkane standard.

***n*-alkane**	**RMM**	**relative volume of 0.1 mg mL^{-1} solution (mL)**	**Mass of *n*-alkane added (mg)**	**number of moles of *n*-alkane**
C25	352	0.759	0.0759	2.16E-07
C26	366	0.789	0.0789	2.16E-07
C27	380	0.819	0.0819	2.16E-07
C28	394	0.849	0.0849	2.16E-07
C29	408	0.879	0.0879	2.16E-07
C30	422	0.909	0.0909	2.16E-07
C31	436	0.940	0.0940	2.16E-07
C32	450	0.970	0.0970	2.16E-07
C33	464	1.000	0.1000	2.16E-07
Total volume (mL)		7.914		

$$\boldsymbol{Number\ of\ moles} = \frac{\boldsymbol{mass\ (g)}}{\boldsymbol{relative\ molecular\ mass\ (g\ mol^{-1})}}$$

Equation 6.2.1.

$$\boldsymbol{M_{analyte}} = \frac{\boldsymbol{A_{analyte}}}{\boldsymbol{A_{standard}}} \times \boldsymbol{M_{standard}}$$

Equation 6.2.2.

Where M = mass (µg), A= peak area integral

6.2.1.2 Lipid extraction procedures

Soxhlet and sonication extraction were investigated for extracting the total lipid extract (TLE). For the Soxhlet method, pre-weighed powdered samples were placed in pre-extracted cellulose thimbles and extracted under reflux using a Soxhlet apparatus (Figure 6.2.2.) for 8 hours with dichloromethane/acetone (DCM/acetone, 2:1 v/v). After extraction the solvent was reduced to a minimal volume by rotary evaporation and the resultant TLE transferred to a pre-weighed 7 mL vial. Residual

solvent was removed under a stream of nitrogen, assisted by gentle heating (40°C; blow-down). TLEs were air dried (2 hours) and re-weighed to obtain TLE masses. Lipids were also extracted from pre-weighed (ca. 50 g) powdered samples via sonication. For each sample, approximately 12.5 g of sediment was weighed into each of four 40 mL labelled vials and each vial spiked with 50 µL 0.005 mg mL^{-1} 5α-androstane and 50 µL 0.01 mg mL^{-1} deuterated triacontane ($C_{30}D_{62}$). Samples were sonicated for 15 minutes with DCM/acetone (2:1 v/v) and then centrifuged (2500 rpm, 2 min) to separate the supernatant from the sediment. The supernatant was transferred to a round bottom flask (combining extracts) and the extraction process repeated twice more per sample, ensuring the sediment and organic solvent was thoroughly mixed each time. The total extract was reduced to a minimal volume by rotary evaporation and the resultant TLE transferred to a pre-weighed 7 mL vial. Residual solvent was removed under a stream of nitrogen assisted by gentle heating (40°C; blow-down). TLEs were air dried (2 hours) and re-weighed to obtain TLE masses.

Initially, a procedural blank and the reference sediment (CLA-4, spiked with the equimolar *n*-alkane standard) were extracted using the Soxhlet apparatus. This resulted in efficient extraction of *n*-alkanes from CLA-4, although a procedural blank indicated that contamination was being introduced (Figure 6.2.3.). Introduction of contaminants could have occurred in a number of ways and a series of tests to check methods and equipment used to extract the TLE from a sample were investigated in order to determine the source of contamination (Table 6.2.2.).

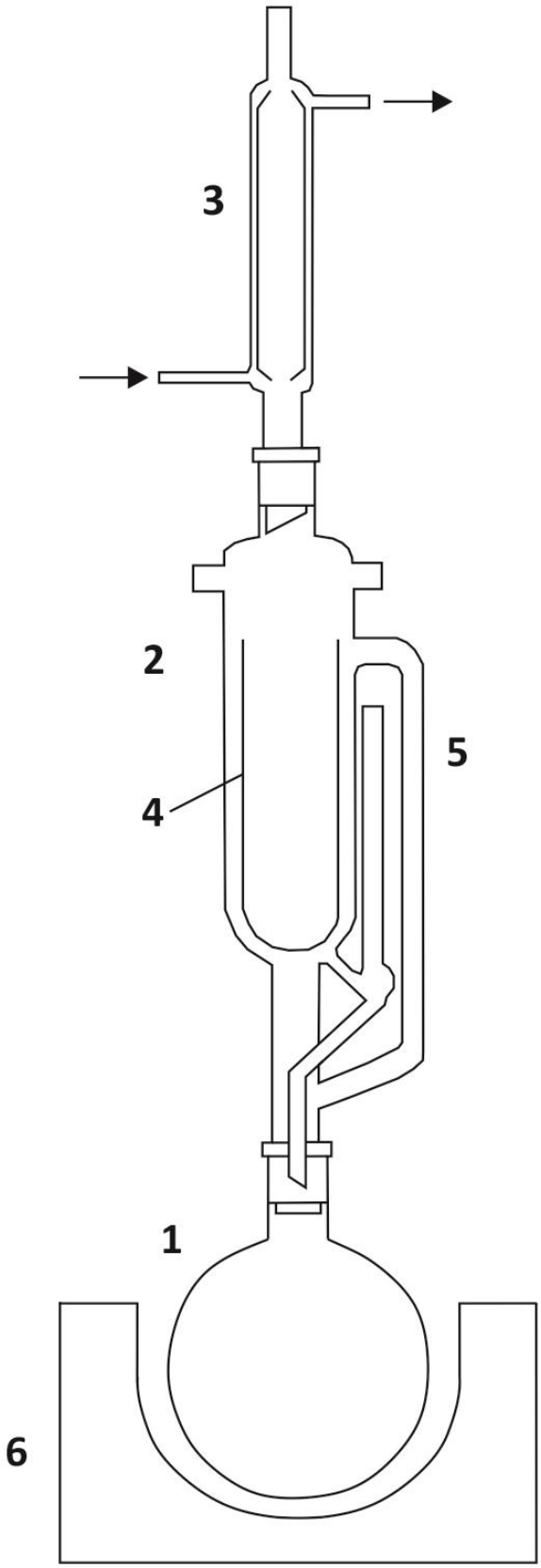

Figure 6.2.2. Schematic of Soxhlet extraction 1) round bottom flask, 2) soxhlet apparatus, 3) condenser (arrows indicate water direction, 4) cellulose thimble, 5) siphon tube, 6) heating mantle.

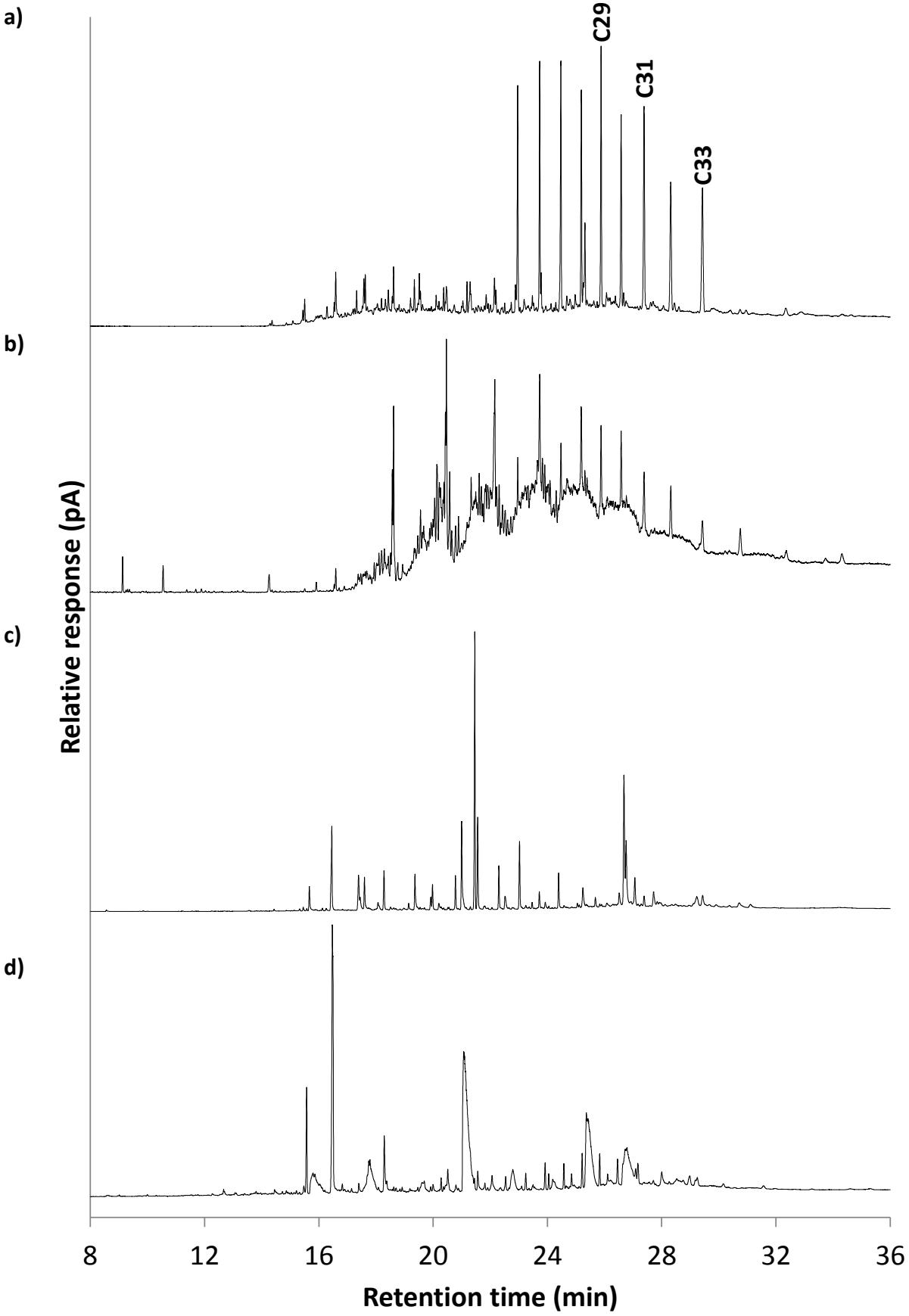

Figure 6.2.3. Gas chromatograms comparing TLEs of Soxhlet extraction a) CLA-4 spiked reference sediment, b) procedural blank, c) Whatman thimble, d) FisherBrand thimble.

APPENDIX 2

Table 6.2.2. Methodological and equipment tests investigated to determine the source of contamination in the procedural blanks.

Test	Potential contamination source	Method employed	Result	Action taken
Solvent	Solvent	Solvent blanks analysed	Solvents clean	None
Micro-syringe	Cross contamination from previous use	Solvent rinses collected into different vials and analysed	Syringes clean	None
Glassware	Cross contamination from previous use	Solvent rinses collected into different vials and analysed	Glassware had low level contamination	Solvent rinsing until clean
Large Solvent volume	Solvent at low levels	ca. 150 mL of solvents rotary evaporated and analysed	Solvents clean	None
Pipettes	De-fatted cotton wool	Solvents drawn up at different speeds	Some methods introduced contamination	Method of pipette use evaluated
Blow-down needles	Contact with vials	Needles sonicated and solvent analysed	Contamination observed	Routine cleaning of needles employed
Soxhlet thimbles	Thimble	Soxhlet extraction of thimble, solvent analysed	Contamination observed	Sonication used instead

All tests were conducted in the order listed in Table 6.2.2., so that contamination issues could be eliminated in a methodical fashion. After ruling out all other equipment as the source of contamination, the thimbles used for Soxhlet extraction were investigated. Two different brands of soxhlet thimble (double thickness cellulose, 41 mm x 123 mm, Whatman Ltd., London, UK, and single thickness cellulose, 41 mm x 123 mm, Thermo Fisher Scientific Inc. Loughborough, UK) were tested. Contamination was found to leach from both thimbles (Figure 6.2.3.) after pre-extraction (8 hours), and it was, therefore, decided to proceed with sonication

extraction. The Soxhlet and sonication methods produced comparable results for extraction efficiency, as evidenced by the CLA-4 sediment, but sonication appeared to produce no contamination from the outset (Figure 6.2.4.) and was quicker as thimbles would need to be pre-extracted prior to use for sample extraction for an extended period of time (>8 hours) to ensure no contamination was introduced to the samples.

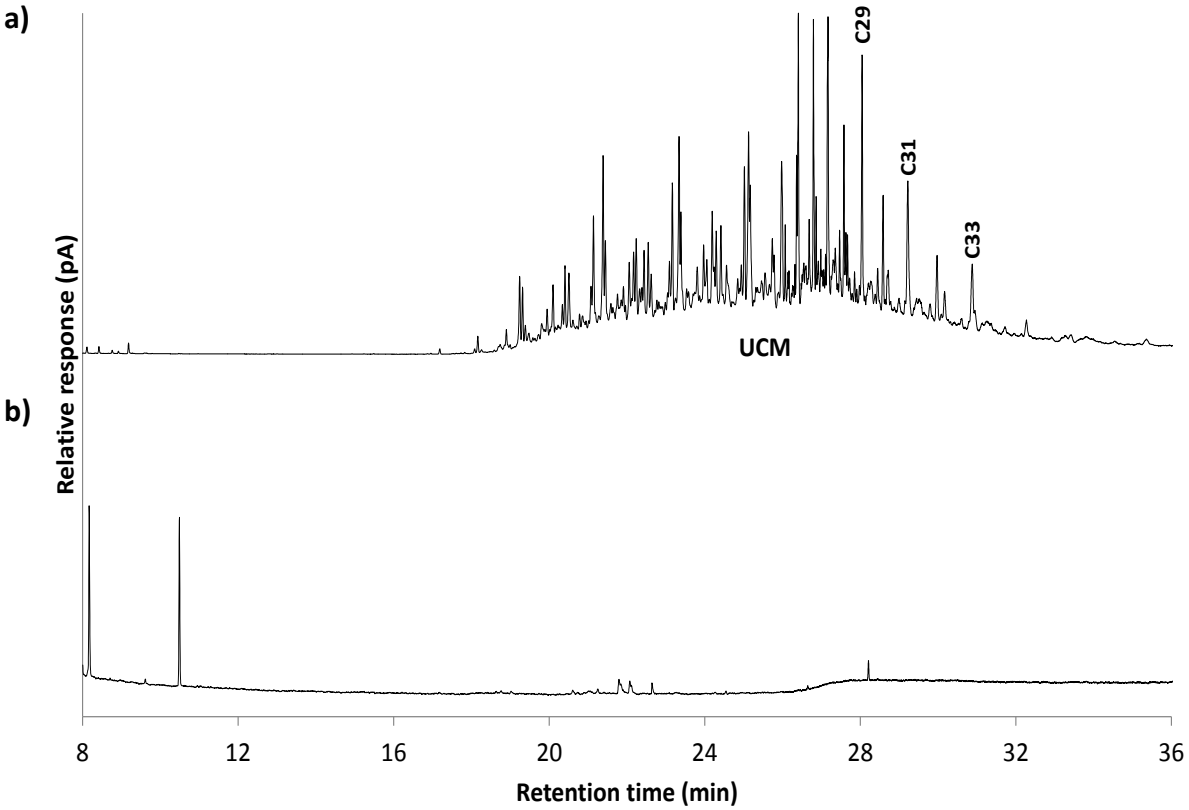

Figure 6.2.4. Gas chromatograms for TLEs obtained using sonication extraction a) CLA-4 spiked reference sediment, b) procedural blank. UCM = unresolved complex mixture.

6.2.1.3 *n*-alkane separation procedures

Six different separation techniques were investigated for the purification of *n*-alkanes from the TLE for compound specific isotope analysis (Table 6.2.3.). These included adsorption chromatography using silica, alumina, argentatious silica, urea adduction, a proprietary T-SEP™ technique and urea adduction combined with T-SEP™.

APPENDIX 2

Table 6.2.3. Methods investigated for *n*-alkane separation from the TLE.

Method	Sample used	Result
Silica chromatography	CLA-4 reference sediment	Poor *n*-alkane separation from apolar unresolved complex mixture (UCM)
	Procedural blank	No contamination
Alumina chromatography	CLA-4 reference sediment	Poor *n*-alkane separation from apolar UCM
	Procedural blank	No contamination
Silver ion SPE	CLA-4 reference sediment	Good *n*-alkane separation from apolar UCM
	Procedural blank	No contamination
	ZUM-ASU+4 sample	Poor *n*-alkane separation from apolar UCM
Urea adduction	CLA-4 reference sediment	Good *n*-alkane separation from apolar UCM, but overlap with DCM fraction
	Procedural blank	No contamination
T-SEP™	CLA-4 reference sediment	Good *n*-alkane separation from apolar UCM for CLA-4
	Procedural blank	No contamination
	ZUM-ASU+4 sample	Good *n*-alkane separation from apolar UCM ZUM-ASU+4
Urea adduction-TSEP™	CLA-4 reference sediment	Good *n*-alkane separation from apolar UCM
	Procedural blank	No contamination

In each case a reference sediment spiked with C_{25} to C_{33} *n*-alkane standards was used to determine if; a) the *n*-alkane standards were recovered in a single fraction to eliminate chromatographic isotope fractionation; and b) the *n*-alkane fraction was sufficiently pure by GC-FID (i.e., co-eluting non-*n*-alkanes were adequately removed) for compound specific isotope analysis (CSIA) to be conducted. Prior to any column chromatography, the column to be used was conditioned to remove any contamination

by eluting with solvents in reverse order; e.g., 3 column volumes of DCM followed by 3 column volumes of *n*-hexane (used in most cases). After each technique had been investigated using the reference sediment, a sample was then separated using this technique (if separation of the reference sediment was good). In each case the same sample from the Zumaia section (ZUM-ASU+4) was used. The results of this sample were then compared before proceeding with any separation procedure. All the methods described were investigated due to the nature of the samples to extract and separate; total organic carbon content was low (generally < 1%), making separation of sufficient material for $\delta^{13}C_{n\text{-alkane}}$ and biomarker analysis of paramount importance. Therefore rigorous testing of each method was conducted.

6.2.1.3.1 Silica column chromatography

Initially silica column separation was attempted using a short glass pipette column packed with pre-extracted cotton wool (DCM, 24 hours) and activated (110°C) silica gel (SiO_4). Samples were transferred onto the silica column in minimal *n*-hexane with brief sonication (<2 min). Apolar fractions (expected to contain *n*-alkanes) were eluted with 3 column volumes of *n*-hexane and polar fractions eluted with 3 column volumes of DCM, each collected in separate 7mL vials, dried under blow-down (N_2, 40°C), and derivatised where necessary (all polar fractions) prior to analysis. GC analysis of samples from this separation showed that *n*-alkanes were eluted entirely in the hexane fraction, but that an unresolved complex mixture (UCM) of other apolar compounds were also present that would interfere with compound specific isotope analysis, making this method unsuitable for *n*-alkane purification on its own (Figure 6.2.5.).

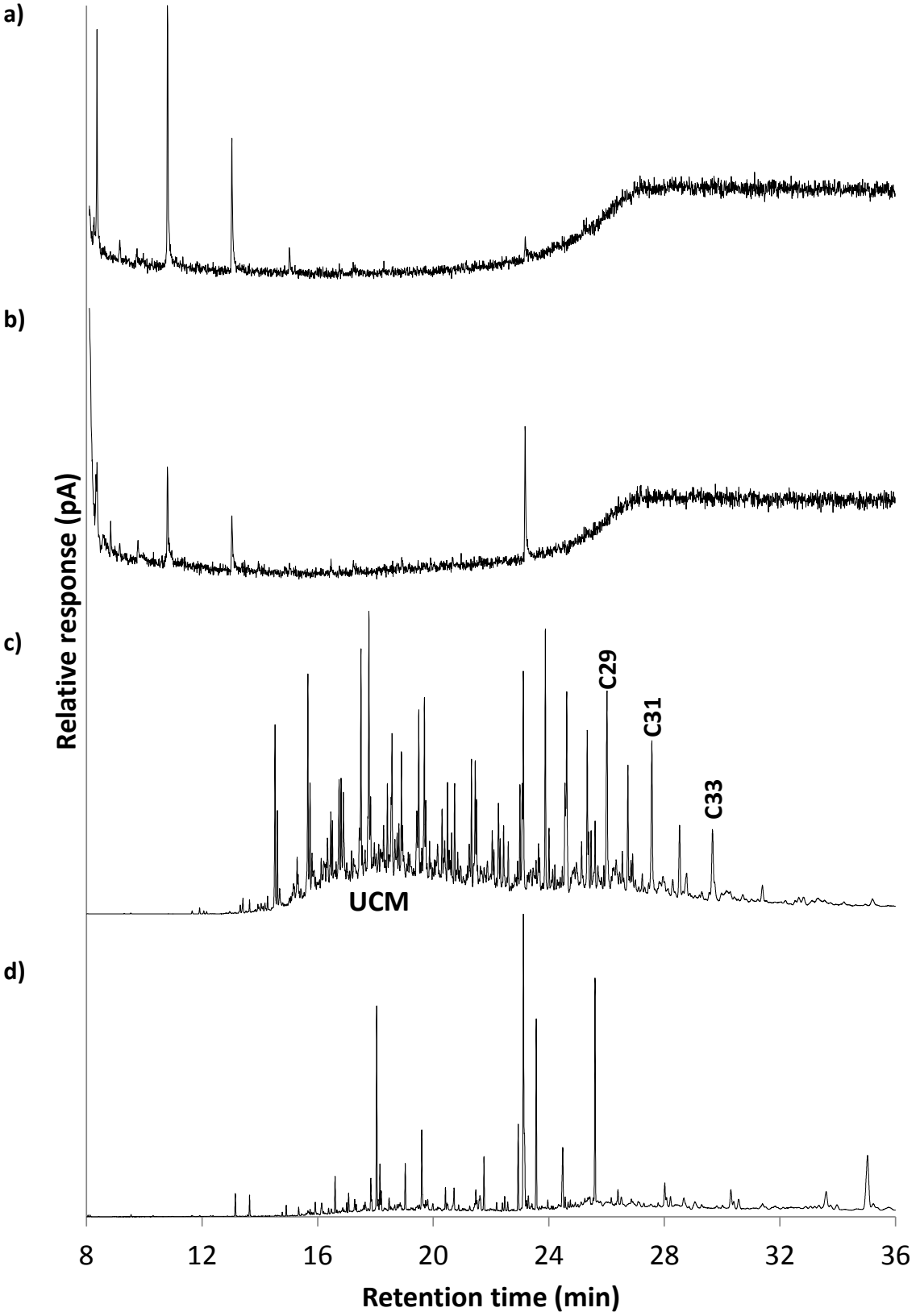

Figure 6.2.5. Gas chromatograms of fractions isolated from the TLE using silica column chromatography during method development a) procedural blank from silica column separation hexane fraction, b) DCM fraction, c) CLA-4 spiked reference sediment hexane fraction demonstrating *n*-alkane separation was not adequate for CSIA, d) DCM fraction (*n*-alkanes not present). UCM = unresolved complex mixture.

6.2.1.3.2 Alumina column chromatography

Further separation of the UCM apolar compounds was then attempted via alumina column chromatography, using a short glass pipette column packed with pre-extracted cotton wool (DCM, 24 hours) and activated (110°C) alumina (Al_2O_3). Samples were transferred onto the alumina column in minimal *n*-hexane with brief sonication (<2 min). Apolar fractions (expected to contain *n*-alkanes) were eluted with 3 column volumes of *n*-hexane and polar fractions eluted with 3 column volumes of DCM, each collected in separate 7mL vials, dried under blow-down (N_2, 40°C), and derivatised where necessary (all polar fractions) prior to analysis. GC analysis of samples from this separation showed that *n*-alkanes were eluted entirely in the hexane fraction, but that the UCM of other apolar compounds was still present, making this method also unsuitable for *n*-alkane purification on its own (Figure 6.2.7.).

6.2.1.3.3 Silver ion solid phase extraction

Argentatious or silver ion (Ag^+) solid phase extraction (SPE) was investigated for the further purification of *n*-alkanes from the hexane extract obtained using alumina chromatography. Ag^+ SPE, under normal phase conditions, separates compounds based upon their double bond equivalents (DBE; Equation 6.2.3). DBE is a measure of hydrogen deficiency; the higher the degree of unsaturation, the greater a compound's affinity for the stationary phase (Ag^+; Figure 6.2.6.).

$$\boldsymbol{DBE = \#C - \frac{\#H}{2} + 1} \qquad \textbf{Equation 6.2.3.}$$

Where #C = the number of carbon atoms, and #H = the number of hydrogen atoms

Samples were transferred onto a Discovery® Ag-Ion SPE cartridge (750 mg/6 mL; Supelco (Sigma-Aldrich Co., Dorset, UK) in *n*-hexane with brief sonication (<2 min) and eluted with 3 column volumes of *n*-hexane (*n*-alkanes), and DCM (other apolar material). This appeared to produce reasonable results for the CLA-4 standard sediment, although when applied to the Zumaia test-sample (ZUM-ASU+4) the separation was not satisfactory for CSIA. Because *n*-alkanes have DBE = 0, no retention to the stationary phase should occur. This led to an investigation of the effect of using smaller solvent volumes to elute the different fractions, for example one column volume of each solvent. This did not, however, improve resolution of *n*-alkanes from the UCM of other apolar compounds (Figure 6.2.8.).

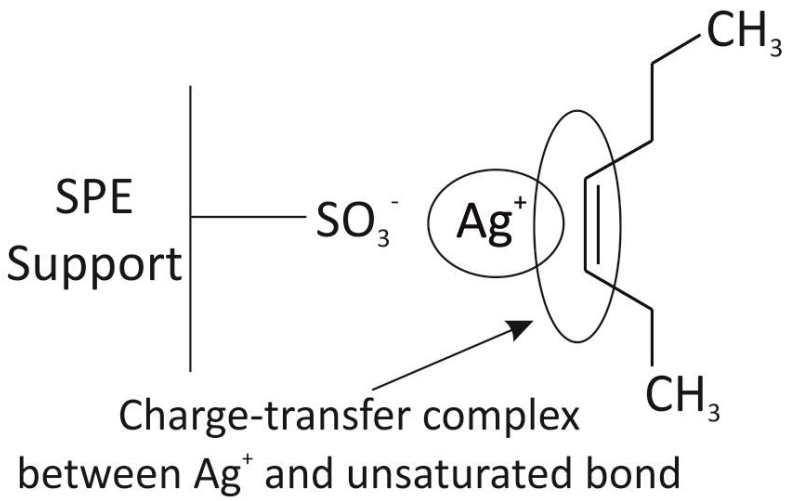

Figure 6.2.6. Schematic representation of the interaction mechanism of silver ion stationary phase with the double bond of an alkene.

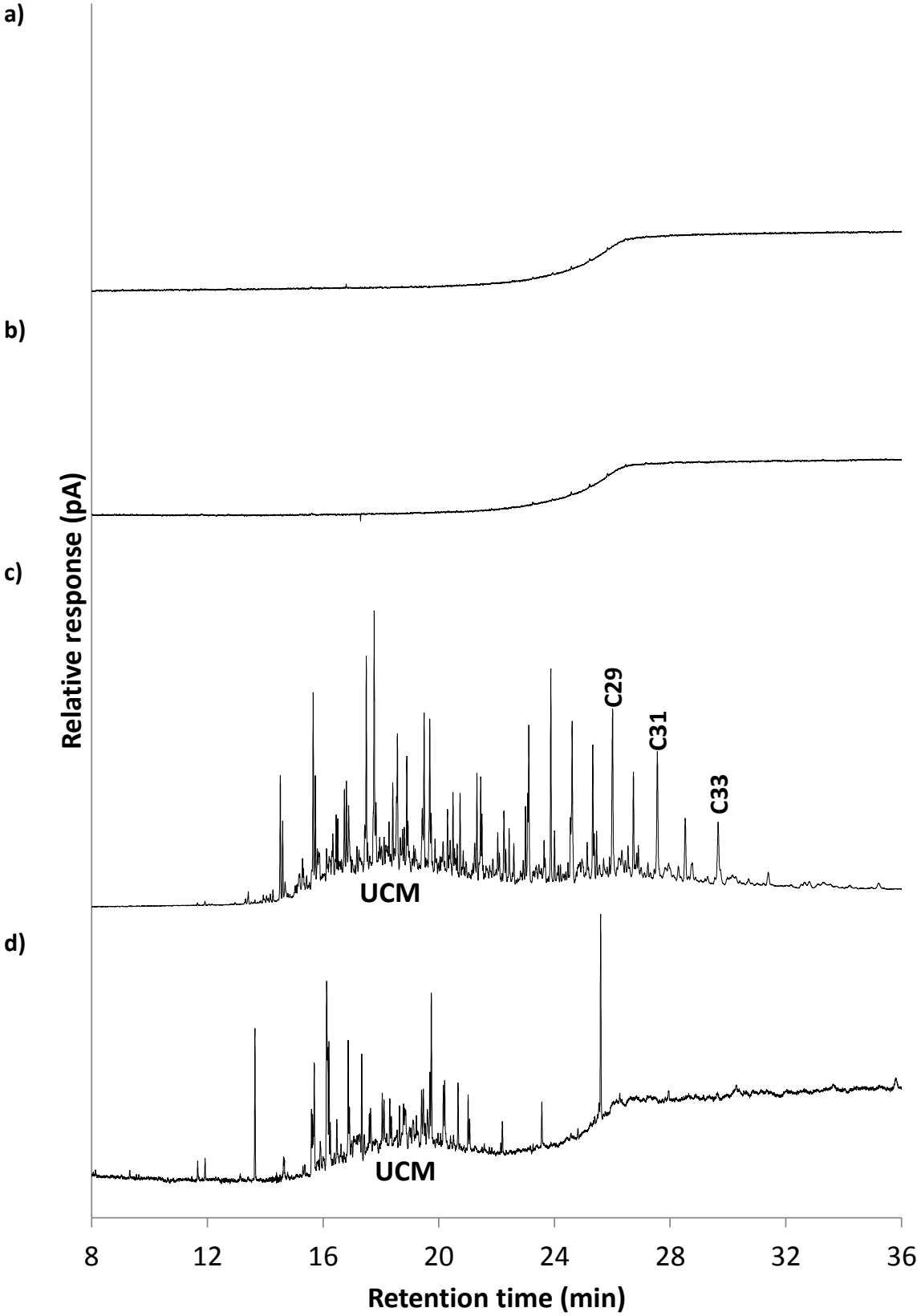

Figure 6.2.7. Gas chromatograms of fractions isolated from the TLE using alumina column chromatography during method development a) Procedural blank produced from alumina column separation hexane fraction, b) DCM fraction, c) CLA-4 spiked reference sediment hexane fraction, d) DCM fraction. UCM = unresolved complex mixture.

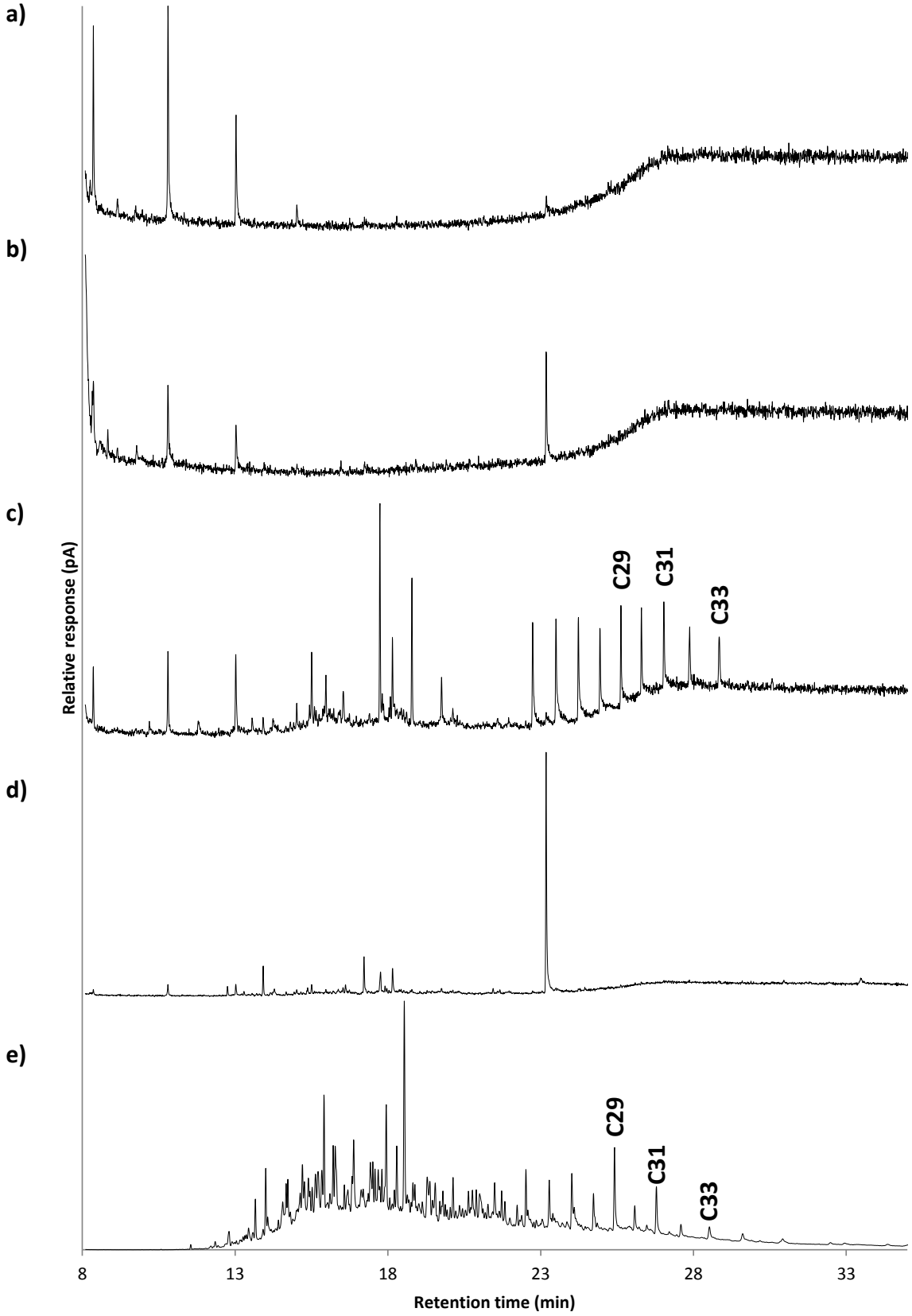

Figure 6.2.8. Total ion chromatograms of fractions obtained during Ag^+ SPE method development; a) Procedural blank from Ag^+ SPE separation hexane fraction, b) DCM fraction c) CLA-4 spiked reference sediment hexane fraction demonstrating good *n*-alkane separation, d) DCM fraction, e) Zumaia sample (ZUM-ASU+4) hexane fraction from Ag^+ SPE separation, demonstrating poor *n*-alkane separation.

6.2.1.3.4 Urea adduction

Urea adduction is commonly employed for *n*-alkane isolation (e.g., Ellis *et al.* 1998; Pearson and Eglinton 2000; Handley *et al.* 2008, 2011, 2012). However, it is time consuming to prepare the reagents and the method does not always produce sufficiently clean *n*-alkane fractions (Pearson and Eglinton 2000; Xu *et al.* 2005). Use of urea adduction was investigated to determine if suitable *n*-alkane separation could be achieved. Urea forms crystalline complexes with straight-chain compounds (e.g., *n*-alkanes), allowing separation from the TLE which comprises branched, cyclic, and aromatic compounds.

Initially the urea was purified using recrystallisation. Recrystallisation involved dissolving a sample in a solvent chosen specifically for its miscibility with respect to the product; the product will be insoluble at room temperature, but soluble upon heating in a suitable recrystallisation solvent. After heating and dissolving of the sample, the solution was left to cool, forming purified crystals of the desired compound with the impurities remaining in solution. Ether was chosen as the recrystallisation solvent; an aliquot of urea was added to a conical flask, and small amounts of hot ether were decanted into the conical flask over a hot water bath until the urea and any impurities were dissolved in a minimal volume of solvent. Once the urea had dissolved, the conical flask was left to cool, forming purified urea crystals. The crystals were removed from the solvent using Büchner vacuum filtration, and left to air dry before storage in a glass container. For urea adduction to occur the urea has to be in liquid form, so urea saturated methanol was prepared. Solubility of urea in methanol at room temperature is 0.2g g^{-1} urea/methanol, and amount of urea required per sample

for efficient separation is 5:1 v/v urea/sample. The amount of urea required to separate a large batch of samples was determined by calculation of the average weight of a TLE (ca. 0.5 mg), determining a number of samples for separation (60) and calculating the amount of urea saturated methanol needed for processing. To process ca. 60 samples, 150 mg of purified, dry, urea was transferred to a pre-weighed 7 mL vial. The weight of methanol required to produce a saturated solution was calculated by dividing the weight of urea by the saturation weight of urea in methanol at room temperature, resulting in addition of 750 mg methanol.

After reagent preparation, samples were weighed to determine the appropriate volume of urea saturated methanol required per sample to obtain a 5:1 v/v urea/sample mixture. The urea solution was measured into a 7 mL vial, and the sample was introduced to the solution. This mixture was left to stand (24 hours) for straight-chain compounds to bind to the urea, after which the sample was dried under blow-down (N_2, 40°C) to remove excess methanol and produce the urea-complex crystals. The crystals were rinsed with ether (3 mL) to remove any surface impurities, and dissolved in water (2 mL) to release the *n*-alkanes from the complex. Liquid-liquid extraction was then conducted via addition of cyclohexane (2 mL), mixing the sample via shaking followed by vortex-mixing, and removing the cyclohexane (upper) layer containing the *n*-alkanes. This process was repeated twice more to ensure maximum recovery. Liquid extraction was then performed with DCM to extract compounds remaining in the water phase, and both fractions were analysed. The urea adduction method was first investigated with the CLA-4 spiked reference sediment. Good separation of *n*-alkanes from the apolar UCM was achieved, although *n*-alkane

abundance was low. Analysis of the DCM fraction revealed *n*-alkanes in this fraction (Figure 6.2.9.), indicating that *n*-alkanes were poorly resolved from the urea-crystal complex.

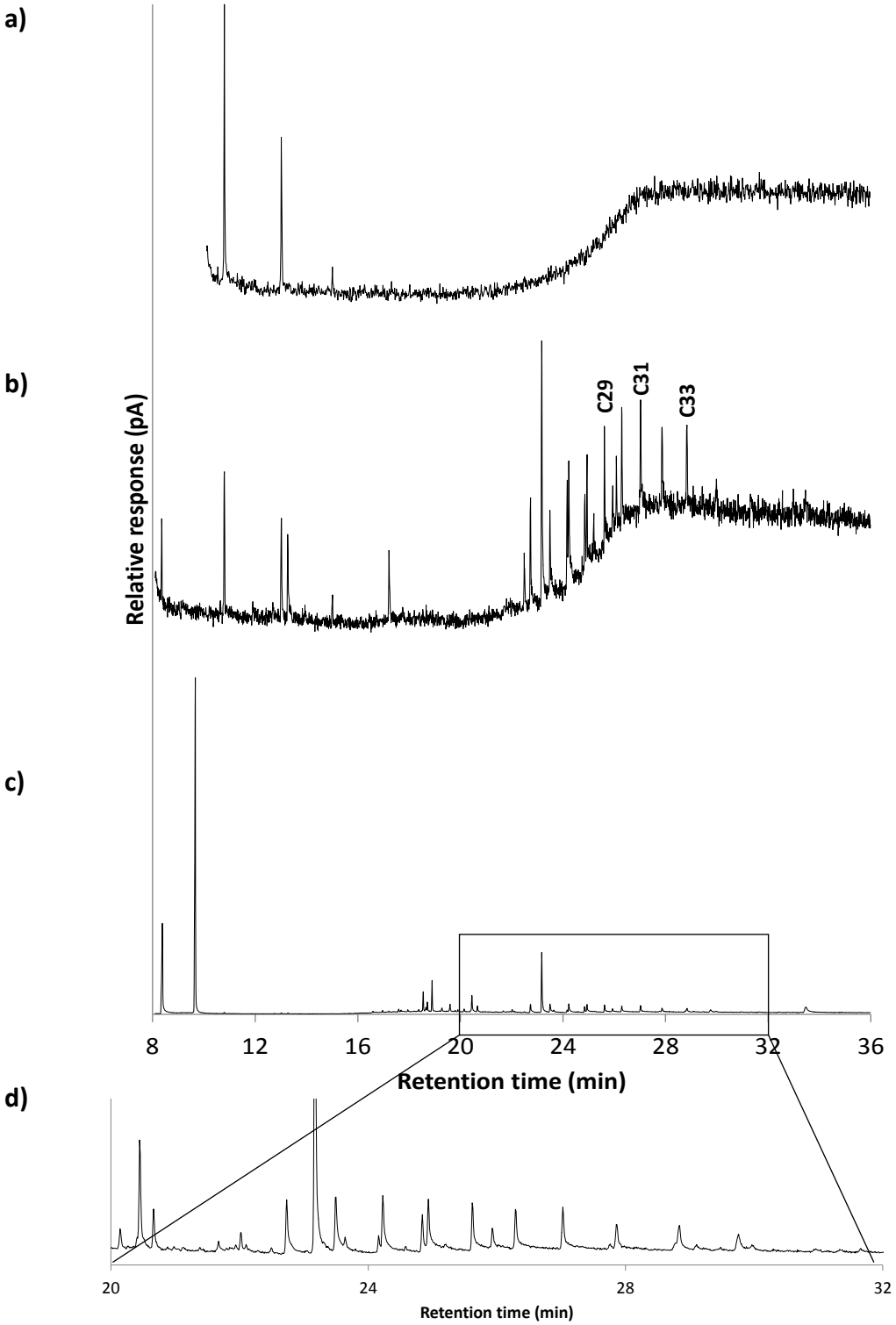

Figure 6.2.9. Total ion chromatograms from urea adduction method development a) procedural blank from urea adduction b) CLA-4 = spiked reference sediment hexane fraction demonstrating good *n*-alkane separation, c) DCM fraction, d) zoomed portion of c) demonstrating *n*-alkanes in DCM fraction.

6.2.1.3.5 T-SEP

All of the above separation procedures for *n*-alkane isolation were attempted on their own and in combination, but none could provide completely satisfactory *n*-alkane separation. For this reason, T-SEP™ was investigated for separation of *n*-alkanes from the TLE. The T-SEP™ technique was tested to determine its suitability to purify *n*-alkanes from a TLE with little or no other compounds present and elute all *n*-alkanes into a single fraction to minimise carbon isotope fractionation. The $\delta^{13}C$ values of *n*-alkanes obtained in this manner were measured to determine whether the T-SEP™ process introduced any isotope bias. Results from tests using a C_{25} – C_{33} *n*-alkane standard demonstrated that all *n*-alkanes were eluted in one fraction, and that whilst carbon isotope ratio was affected slightly it was always within the analytical error of the instrument (±0.5‰; Figure 6.2.10., Table 6.2.4.).

Table 6.2.4. Compound Specific $\delta^{13}C$ isotope values as measured for a pure *n*-alkane standard sample and post T-SEP™ separation, demonstrating all values lie within instrumental error.

C#	$\delta^{13}C$ (‰ VPDB) pre T-SEP™	$\delta^{13}C$ (‰ VPDB) post T-SEP™	$\Delta\ \delta^{13}C$
27	-25.8	-25.3	0.5
28	-26.9	-26.4	0.5
29	-30.1	-29.9	0.2
30	-32.8	-32.3	0.5
31	-32.1	-31.7	0.4
32	-28.9	-28.4	0.5
33	-30.6	-30.5	0.1

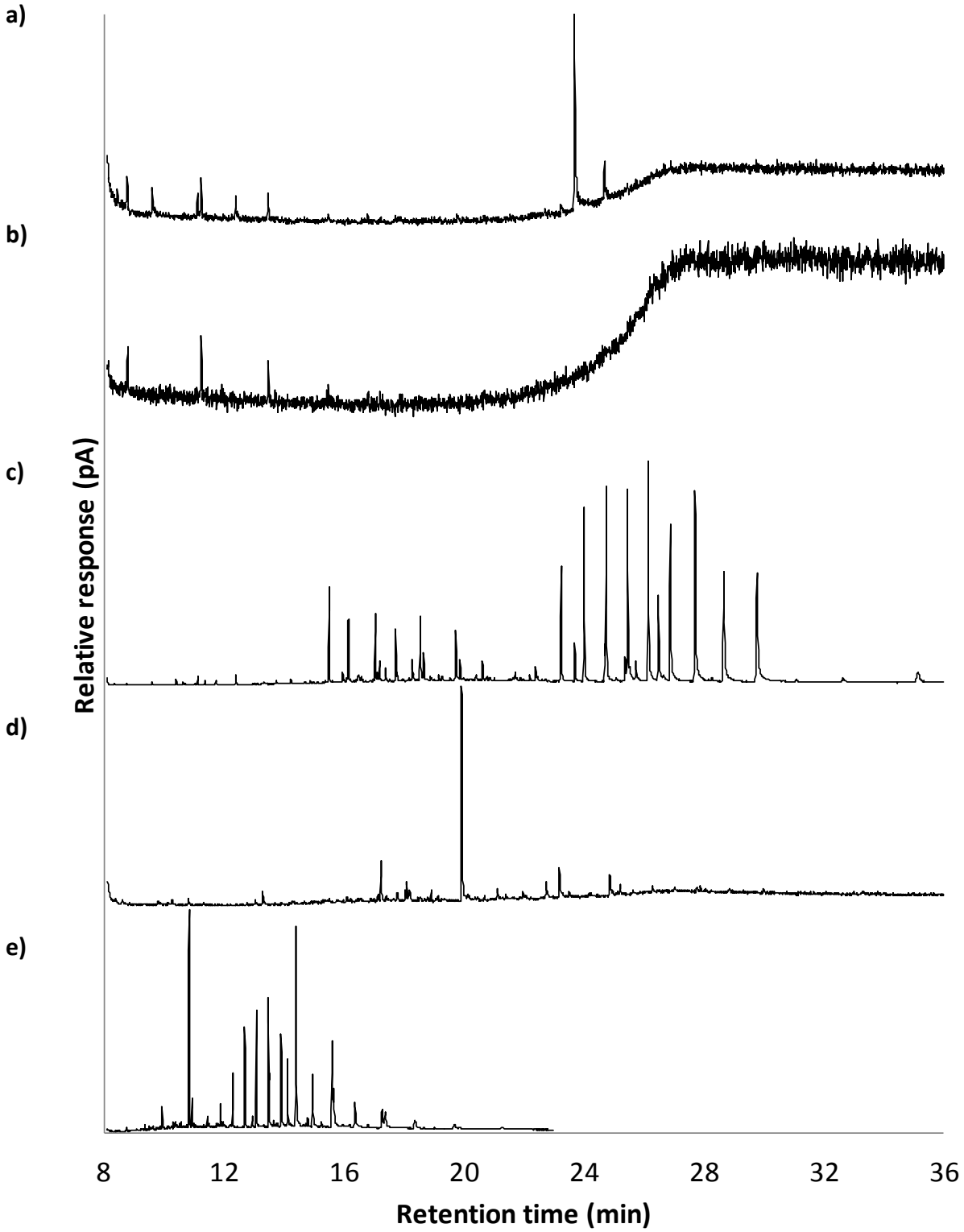

Figure 6.2.10. Total ion chromatograms from T-SEP™ method development; a) Procedural blank from T-SEP™ separation hexane fraction, b) DCM fraction, c) CLA-4 spiked reference sediment hexane fraction after T-SEP™ separation, demonstrating good *n*-alkane separation, d) DCM fraction, e) Zumaia sample (ZUM-ASU+4) after T-SEP™ separation, demonstrating good *n*-alkane separation. Note the different GC oven programme used for 3).

6.2.1.3.6 Urea adduction combined with T-SEP

An additional investigation was conducted combining urea adduction with the T-SEP™ procedure. Samples were transferred onto a cartridge packed with urea saturated methanol in a matrix of cellulose. T-SEP™ was then conducted to produce a de-waxed TLE and an *n*-alkane fraction. Separation was comparable to using T-SEP™ independently, but T-SEP™ without urea adduction resulted in better recovery of the *n*-alkanes so it was decided to continue with T-SEP™ independent of urea adduction (Figure 6.2.11.).

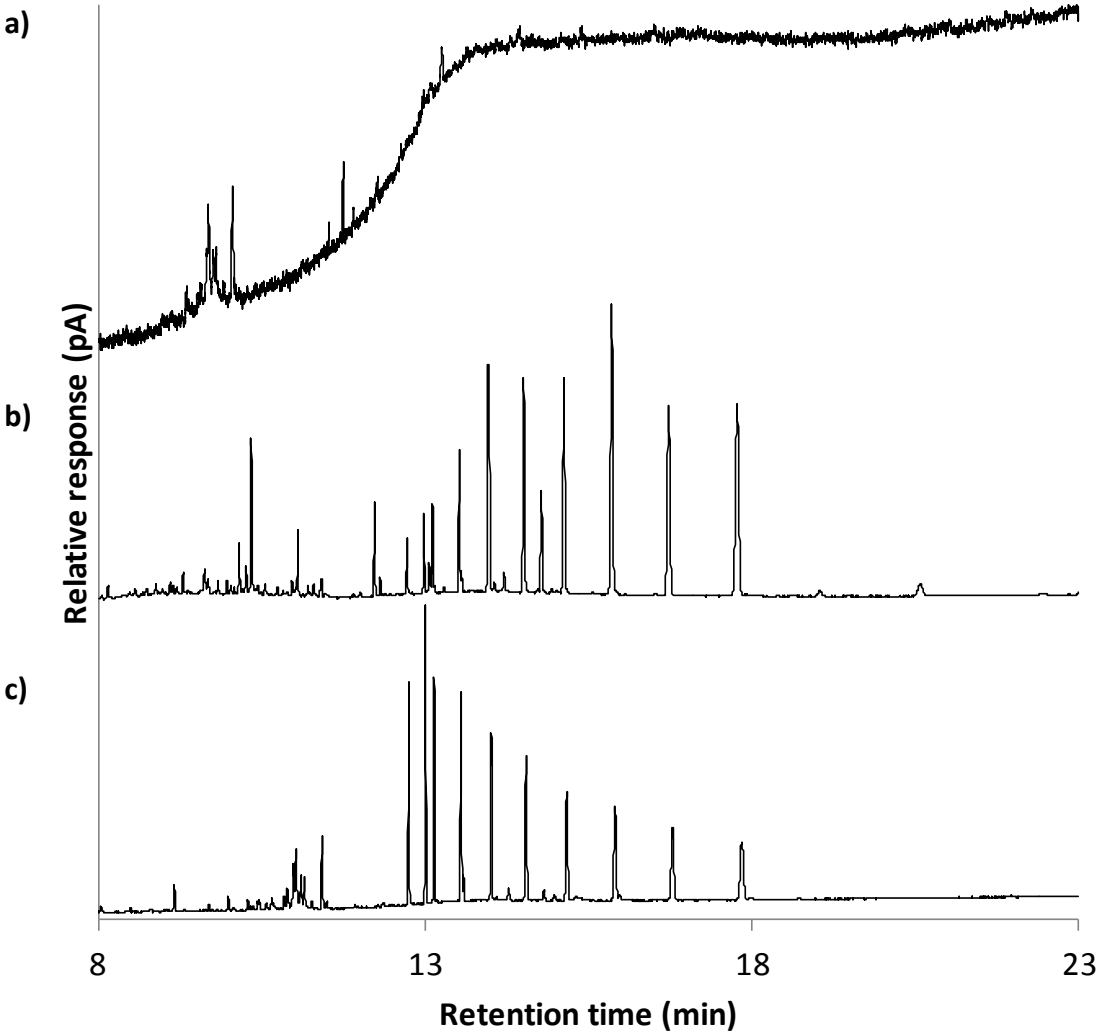

Figure 6.2.11. Gas chromatograms comparing T-SEP™ and urea adduction combined with T-SEP method development; a) Procedural blank from urea adduction-T-SEP™ separation, b) CLA-4 spiked reference sediment hexane fraction after T-SEP™ demonstrating good *n*-alkane separation, c) CLA-4 spiked reference sediment hexane fraction after T-SEP™ combined with urea adduction hexane fraction demonstrating reduced recovery in comparison with T-SEP™.

6.2.1.4 Internal standards

Internal standards (deuterated triacontane and 5α-androstane) were added to all samples prior to extraction for quantification purposes. A calibration series was produced to determine a suitable concentration to spike into samples (Figure 6.2.12.), and certain concentrations were generated in triplicate to determine operator reproducibility. Relative standard deviations (RSD; Equation 6.2.4.), calculated to estimate error associated with the measurements, were acceptable (<4%). A linear response for the standards was recorded over at least two orders of magnitude (0.001 to 0.1 mg mL^{-1}). Deuterated triacontane ($C_{30}D_{62}$) was added in known quantity (0.5 µg) for compound specific isotope analyses and was recovered in the T-SEP™ *n*-alkane fraction.

$$\boldsymbol{RSD} = \left(\frac{\boldsymbol{\sigma}}{\bar{\boldsymbol{x}}}\right) \qquad \textbf{Equation 6.2.4.}$$

Where σ = standard deviation and $\bar{x}$ = mean of the samples

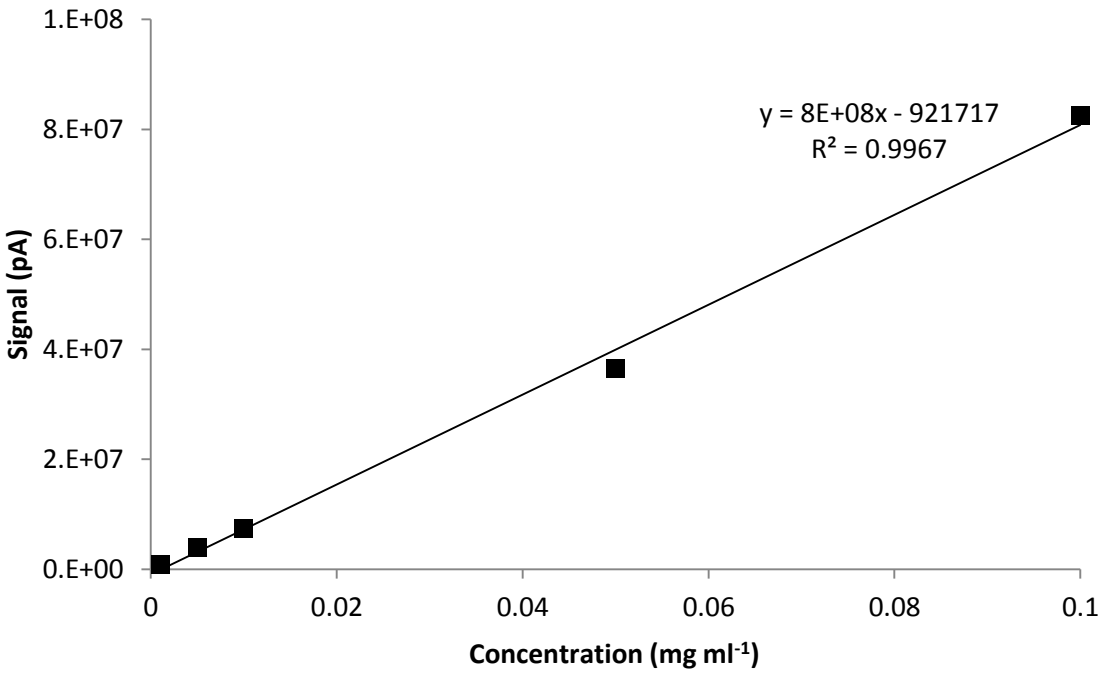

Figure 6.2.12. Calibration graph produced using GC-MS for the internal standard 5α-androstane, added for biomarker quantification (n = 3 at 0.001 mg mL^{-1}, and n = 1 at 0.005 and 0.1 mgmL^{-1}).

5α-androstane was added for biomarker quantification (Figure 6.2.13.). A calibration series was produced to determine a suitable concentration to spike into samples (Figure 6.2.14.), and certain concentrations were generated in triplicate. RSD calculated to estimate error associated with the measurement, was acceptable (<4%). 5α-androstane was added in known quantity (0.25 µg) and was recovered in the T-SEP™ de-waxed TLE fraction. Semi-quantification of analytes was achieved by calculating response factors relative to the internal standard (Equation 6.2.2).

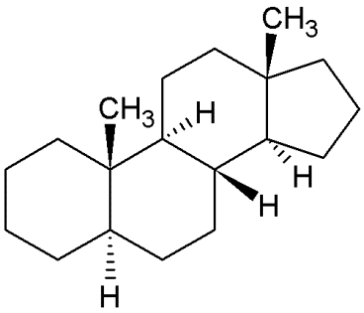

Figure 6.2.13. Structure of 5α-androstane internal standard spiked into samples prior to extraction for quantification purposes.

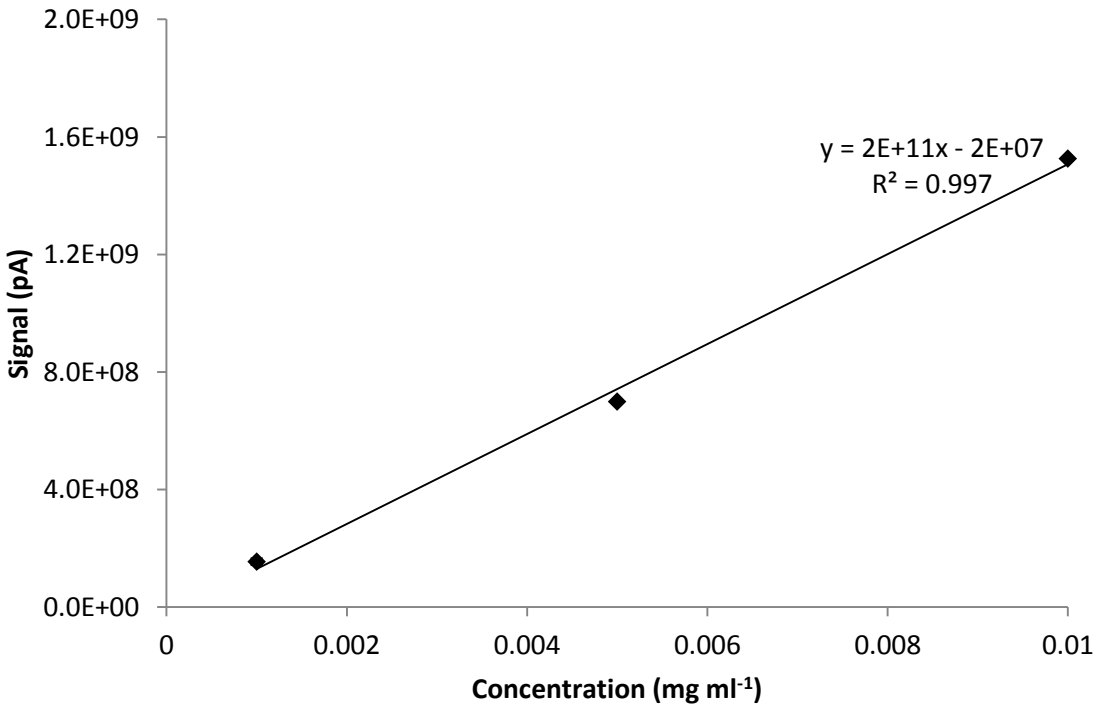

Figure 6.2.14. Calibration graph produced using GC-MS for the internal standard 5α-androstane, added for biomarker quantification (n = 3 at 0.001 mg mL^{-1}, and n = 1 at 0.005 and 0.1 $mgmL^{-1}$).

APPENDIX 2

ANALYTICAL RESULTS TABLES FOR CHAPTER 3

Table 6.2.4. Weight percent carbon (wt% C) and nitrogen (wt% N) determined in Zumaia sediment samples and calculated C/N ratios. Further data relating to $\delta^{13}C_{TOC}$ measurements can be found in the supplementary material of Manners *et al.* (2013) and Appendix 6.1. Cells highlighted in grey represent samples within the CIE.

Sample	Height (m)	%C	%N	C/N
ZUM-BSU+0	0.00	0.3	0.05	5.2
ZUM-BSU+1	0.30	0.2	0.08	2.7
ZUM-BSU+2	0.60	0.2	0.07	3.7
ZUM-BSU+3	0.90	0.3	0.07	3.8
ZUM-BSU+4	1.20	0.3	0.07	4.8
ZUM-BSU+5	1.50	0.2	0.07	3.6
ZUM-BSU+6	1.80	0.3	0.06	5.6
ZUM-BSU+7	2.10	0.2	0.07	3.0
ZUM-BSU+8	2.40	0.3	0.06	5.2
ZUM-BSU+9	2.70	0.3	0.06	5.1
ZUM-BSU+10	3.00	0.2	0.06	3.0
ZUM-BSU+11	3.30	0.1	0.03	4.0
ZUM-BSU+12	3.60	0.3	0.07	4.5
ZUM-BSU+13	3.90	0.2	0.07	2.9
ZUM-BSU+14	4.20	0.2	0.07	3.7
ZUM-BSU+15	4.50	0.2	0.04	4.9
ZUM-BSU+16	4.80	0.2	0.08	2.6
ZUM-BSU+17	5.10	0.2	0.07	2.9
ZUM-BSU+18	5.40	0.3	0.06	5.0
ZUM-BSU+19	5.70	0.1	0.07	1.9
ZUM-BSU+20	6.00	0.3	0.07	3.9
ZUM-BSU+21	6.30	0.3	0.05	6.4
ZUM-BSU+22	6.60	0.3	0.06	4.5
ZUM-BSU+23	6.90	0.3	0.04	6.2
ZUM-BSU+24	7.20	0.3	0.05	6.0
ZUM-SU+0	7.35	0.1	0.07	1.9
ZUM-SU+1	7.50	0.2	0.06	4.1
ZUM-SU+2	7.65	0.1	0.07	1.5
ZUM-SU+3	7.80	0.1	0.06	1.7
ZUM-SU+4	7.95	0.1	0.06	2.0
ZUM-SU+5	8.10	0.1	0.06	1.7
ZUM-SU+6	8.25	0.2	0.05	3.8
ZUM-SU+7	8.40	0.2	0.06	2.4
ZUM-SU+8	8.55	0.1	0.07	2.2
ZUM-SU+9	8.70	0.3	0.08	4.0
ZUM-SU+10	8.85	0.1	0.06	2.4
ZUM-SU+11	9.00	0.3	0.06	4.2
ZUM-SU+12	9.15	0.2	0.07	3.6
ZUM-SU+13	9.30	0.2	0.07	3.5
ZUM-SU+14	9.45	0.2	0.07	2.8

Sample	Height (m)	%C	%N	C/N
ZUM-SU+15	9.60	0.2	0.07	2.3
ZUM-SU+16	9.75	0.3	0.08	3.9
ZUM-SU+17	9.90	0.5	0.09	5.6
ZUM-SU+18	10.05	0.6	0.09	6.5
ZUM-SU+19	10.20	0.3	0.07	3.7
ZUM-SU+20	10.35	0.3	0.08	3.7
ZUM-SU+21	10.50	0.2	0.07	2.5
ZUM-SU+22	10.65	0.2	0.07	2.4
ZUM-SU+23	10.80	0.2	0.07	3.4
ZUM-SU+24	10.95	0.2	0.07	2.6
ZUM-SU+25	11.10	0.2	0.07	2.5
ZUM-SU+26	11.25	0.2	0.07	3.1
ZUM-SU+27	11.40	0.2	0.07	2.4
ZUM-SU+28	11.55	0.1	0.06	2.3
ZUM-SU+29	11.70	0.2	0.07	3.1
ZUM-SU+30	11.85	0.2	0.07	3.2
ZUM-SU+31	12.00	0.2	0.06	2.5
ZUM-SU+32	12.15	0.1	0.06	2.1
ZUM-SU+33	12.30	0.1	0.06	2.2
ZUM-SU+34	12.45	0.1	0.07	1.9
ZUM-ASU+0	12.95	0.2	0.07	3.1
ZUM-ASU+1	13.45	0.2	0.07	2.5
ZUM-ASU+2	13.95	0.2	0.07	3.4
ZUM-ASU+3	14.45	0.3	0.06	4.6
ZUM-ASU+4	14.95	0.3	0.07	4.8
ZUM-ASU+5	15.45	0.3	0.08	3.9
ZUM-ASU+6	15.95	0.3	0.09	3.7
ZUM-ASU+7	16.45	0.3	0.05	5.0
ZUM-ASU+8	16.95	0.3	0.08	4.2
ZUM-ASU+9	17.45	0.3	0.05	5.0
ZUM-ASU+10	17.95	0.3	0.07	4.7
ZUM-ASU+11	18.45	0.2	0.07	3.0
ZUM-ASU+12	18.95	0.2	0.07	3.3
ZUM-ASU+13	19.45	0.3	0.06	4.7
ZUM-ASU+14	19.95	0.5	0.08	5.7
ZUM-ASU+15	20.45	0.3	0.06	4.3
ZUM-ASU+16	20.95	0.3	0.07	4.8
ZUM-ASU+17	21.45	0.4	0.07	5.6
ZUM-ASU+18	21.95	0.3	0.05	6.0

Table 6.2.5. $\delta^{13}C_{CARB}$ and $\delta^{18}O_{CARB}$ isotope results from the Zumaia section. Cells highlighted in light grey represent samples within the CIE, whilst cells highlighted in dark grey are maximum and minimum values used to calculate CIE magnitude. Blank cells represent samples where insufficient carbonate was present for analysis. Height is in metres relative to the base of the Siliciclastic Unit.

Sample	Height (m)	$\delta^{13}C$	$\delta^{18}O$	wt% CaO
Zum-HR, -72	3.00	+0.3	-4.5	-
Zum-HR, -70	3.08	+0.9	-3.6	36.8
Zum-HR, -68	3.18	+0.5	-3.7	28.0
Zum-HR, -66	3.27	-0.7	-5.0	-
Zum-HR, -64	3.38	+1.1	-3.5	27.9
Zum-HR, -62	3.48	+1.4	-3.3	34.6
Zum-HR, -60	3.58	+0.9	-3.4	33.0
Zum-HR, -58	3.68	+0.0	-4.9	26.3
Zum-HR, -56	3.80	+0.8	-3.7	21.9
Zum-HR, -54	3.89	+1.2	-3.5	33.1
Zum-HR, -52	3.99	+0.5	-4.0	26.2
Zum-HR, -50	4.09	+1.1	-3.5	30.1
Zum-HR, -48	4.21	+0.9	-3.6	-
Zum-HR, -46	4.31	+1.1	-3.2	38.7
Zum-HR, -44	4.40	+1.1	-3.2	36.3
Zum-HR, -42	4.50	-0.6	-4.9	32.2
Zum-HR, -40	4.61	-1.1	-4.8	24.8
Zum-HR, -38	4.68	+1.1	-3.4	34.9
Zum-HR, -36	4.77	+1.1	-3.4	33.5
Zum-HR, -34	4.87	+0.2	-4.8	28.1
Zum-HR, -32	4.97	-0.1	-3.9	18.3
Zum-HR, -30	5.07	+0.4	-4.4	29.0
Zum-HR, -28	5.17	+1.1	-3.5	35.2
Zum-HR, -26	5.27	+0.1	-3.9	18.7
Zum-HR, -24	5.37	+0.6	-3.5	20.2
Zum-HR, -22	5.47	+0.6	-3.9	28.5
Zum-HR, -20	5.58	+0.9	-3.4	29.8
Zum-HR, -18	5.67	+0.5	-3.9	27.8
Zum-HR, -16	5.82	-0.9	-4.5	17.7
Zum-HR, -14	5.95	+0.5	-3.6	22.7
Zum-HR, -12	6.03	+0.5	-3.5	21.2
Zum-HR, -10	6.13	+0.5	-3.4	-
Zum-HR, -8	6.22	+0.4	-3.6	25.7
Zum-HR, -6	6.48	+1.4	-3.1	52.7
Zum-HR, -4	6.64	+1.5	-3.0	53.0
Zum-HR, -2	6.82	+1.2	-3.1	41.2
Zum-HR, 0	7.02	+0.7	-3.2	32.3
Zum-HR, 2	7.12	+0.0	-3.5	27.3
Zum-HR, 4	7.22	+0.1	-3.5	26.1
Zum-HR, 6	7.32	-0.3	-3.6	27.7
Zum-HR, 8	7.40	-3.6	-4.6	4.78

Table 6.2.5 continued

Sample	Height (m)	$\delta^{13}C$	$\delta^{18}O$	wt% CaO
Zum-HR, 10	7.48	-3.3	-5.0	1.0
Zum-HR, 12	7.56	-3.8	-5.6	2.6
Zum-HR, 14	7.65			0.8
Zum-HR, 16	7.73	-6.0	-3.1	1.6
Zum-HR, 18	7.81			0.7
Zum-HR, 20	7.89	-4.2	-4.7	0.6
Zum-HR, 22	7.97	-4.3	-3.1	1.1
Zum-HR, 24	8.05			0.7
Zum-HR, 26	8.13			0.6
Zum-HR, 28	8.22	-2.3	-1.9	1.5
Zum-HR, 30	8.30	-1.5	-3.4	5.5
Zum-HR, 32	8.38	-1.5	-2.8	3.2
Zum-HR, 34	8.46	-2.1	-1.9	2.6
Zum-HR, 36	8.54	-3.2	-3.0	3.7
Zum-HR, 38	8.62	-1.2	-2.7	7.7
Zum-HR, 40	8.70	-2.4	-2.9	4.5
Zum-HR, 42	8.79	-1.9	-2.8	6.4
Zum-HR, 44	8.87	-2.0	-2.7	12.2
Zum-HR, 46	8.95	-3.8	-4.1	6.8
Zum-HR, 48	9.03	-2.5	-4.0	6.6
Zum-HR, 50	9.11	-2.6	-4.1	7.6
Zum-HR, 52	9.19	-3.0	-3.5	5.8
Zum-HR, 54	9.27	-2.0	-2.0	5.0
Zum-HR, 56	9.36	-2.8	-1.7	7.8
Zum-HR, 58	9.44	-2.2	-2.2	4.3
Zum-HR, 60	9.52	-4.5	-4.8	7.0
Zum-HR, 62	9.60	-2.9	-4.9	5.9
Zum-HR, 64	9.68	-4.8	-5.8	3.3
Zum-HR, 66	9.76	-3.4	-5.0	6.6
Zum-HR, 68	9.84	-3.8	-4.6	6.0
Zum-HR, 70	9.92	-5.2	-5.2	9.5
Zum-HR, 72	10.01	-5.3	-5.1	6.5
Zum-HR, 74	10.09	-4.6	-4.2	3.1
Zum-HR, 76	10.17	-4.0	-4.6	4.1
Zum-HR, 78	10.25	-2.5	-4.5	9.4
Zum-HR, 80	10.33	-2.3	-4.3	7.8
Zum-HR, 82	10.41	-4.3	-4.3	6.2
Zum-HR, 84	10.49	-2.4	-4.4	7.7
Zum-HR, 86	10.58	-2.3	-4.4	7.9
Zum-HR, 88	10.66	-3.5	-5.0	6.8
Zum-HR, 90	10.74	-3.0	-4.2	4.9

Table 6.2.5 continued

Sample	Height (m)	$\delta^{13}C$	$\delta^{18}O$	wt% CaO
Zum-HR, 92	10.82	-3.1	-4.0	6.9
Zum-HR, 94	10.90	-2.7	-4.5	8.9
Zum-HR, 96	10.98	-2.3	-4.3	12.2
Zum-HR, 98	11.06	-2.8	-3.9	14.7
Zum-HR, 100	11.15	-2.0	-4.4	8.9
Zum-HR, 102	11.23	-2.4	-4.2	11.2
Zum-HR, 104	11.31	-2.0	-4.1	12.4
Zum-HR, 106	11.39	-1.9	-3.8	14.1
Zum-HR, 108	11.47	-0.3	-3.6	31.7
Zum-HR, 110	11.55	0.0	-3.4	32.2
Zum-HR, 112	11.63	0.0	-3.2	37.8
Zum-HR, 114	11.72	0.3	-3.1	39.2
Zum-HR, 116	11.80	0.4	-3.3	52.6
Zum-HR, 118	11.88	0.5	-3.3	48.8
Zum-HR, 120	11.96	0.5	-3.2	44.9
Zum-HR, 122	12.04	0.5	-3.1	44.2
Zum-HR, 124	12.12	-0.3	-3.0	42.1
Zum-HR, 126	12.20	0.1	-2.7	48.2
Zum-HR, 128	12.29	0.6	-3.0	43.8
Zum-HR, 130	12.37	0.7	-3.3	45.0
Zum-HR, 132	12.45	0.5	-3.1	47.3
Zum-HR, 134	12.53	0.4	-3.2	37.8
Zum-HR, 136	12.61	0.6	-3.2	48.2
Zum-HR, 138	12.69	0.4	-3.3	41.2
Zum-HR, 140	12.77	0.4	-2.8	33.2
Zum-HR, 142	12.86	0.7	-3.2	51.2
Zum-HR, 144	12.98	0.9	-3.4	47.8
Zum-HR, 146	13.13	1.1	-3.0	51.2
Zum-HR, 148	13.26	0.7	-3.2	51.4
Zum-HR, 150	13.43	0.9	-3.2	48.4
Zum-HR, 152	13.59	0.8	-2.8	41.9
Zum-HR, 154	13.67	0.8	-3.1	38.7
Zum-HR, 156	13.83	0.9	-3.3	35.2
Zum-HR, 158	13.91	0.7	-2.8	48.4
Zum-HR, 160	13.99	0.9	-3.2	-
Zum-HR, 162	14.08	0.8	-3.2	30.9
Zum-HR, 164	14.16	0.5	-3.3	23.5
Zum-HR, 166	14.24	0.7	-5.3	28.4
Zum-HR, 168	14.36	0.9	-3.0	50.2
Zum-HR, 170	14.52	0.9	-2.9	35.0
Zum-HR, 172	14.69	1.1	-3.0	50.5
Zum-HR, 174	14.85	1.0	-3.1	4.9

Table 6.2.6. Peak integral and *n*-alkane mass data normalised to the internal standard (ng) for all Zumaia samples. IS = internal standard, deuterated triacontane ($C_{30}D_{62}$). Cells highlighted in grey represent samples within the CIE.

Sample	Height (m)	Sediment weight (g)	C25			C26			C27		
			RT (min)	Area (pA)	Mass (ng)	RT (min)	Area (pA)	Mass (ng)	RT (min)	Area (pA)	Mass (ng)
ZUM-ASU+18	21.95	42.73	22.751	1280060	1920.2	23.518	1026385	1539.7	24.258	582128	873.3
ZUM-ASU+16	20.95	42.45	22.755	4692322	1441.5	23.522	4662031	1432.2	24.263	4129370	1268.6
ZUM-ASU+13	19.45	45.76	22.305	5457080	824.8	23.07	1.5E+07	2266.7	23.805	6975322	1054.2
ZUM-ASU+11	18.45	45.98	22.299	1422193	361.2	23.058	2635623	669.4	23.799	1893596	480.9
ZUM-ASU+9	17.45	46.24	22.303	3878812	473.6	23.065	8997419	1098.5	23.804	5016872	612.5
ZUM-ASU+5	15.45	46.01	22.302	5449597	667.6	23.062	8582254	1051.3	23.801	8290720	1015.6
ZUM-ASU+3	14.45	45.92	22.298	2159045	486.3	23.059	5899477	1328.9	23.798	2979169	671.1
ZUM-ASU+1	13.45	45.82	22.301	2325180	322.4	23.061	5463755	757.5	23.802	3998163	554.3
ZUM-SU+18	10.05	45.45	22.302	3296608	1849.5	23.056	3758867	2108.9	23.802	1.3E+07	7563.8
ZUM-SU+16	9.75	46.90	22.302	2996193	1059.7	23.055	4988422	1764.3	23.799	1E+07	3619.4
ZUM-SU+14	9.45	37.59	22.396	2700196	1057.3	23.055	5013517	1963.1	23.793	2844239	1113.7
ZUM-SU+13	9.30	34.41	-	-	-	-	-	-	23.937	6.5E+07	105.1
ZUM-SU+12	9.15	45.62	22.303	3397189	772.1	23.063	5298355	1204.2	23.8	4069736	925.0
ZUM-BSU+20	6.00	45.56	22.3	1445206	456.4	23.055	3206086	1012.6	23.796	2208642	697.6
ZUM-BSU+17	5.10	45.62	22.301	918564	308.0	23.055	1992335	668.0	23.799	3115408	1044.6
ZUM-BSU+15	4.50	46.17	22.302	672204	410.7	23.06	1283479	784.2	23.798	1054365	644.2
ZUM-BSU+13	3.90	45.97	22.3	1711179	580.8	23.058	3378788	1146.8	23.797	1904215	646.3
ZUM-BSU+8	2.40	44.49	22.314	362835	121.5	23.071	1261761	422.5	23.812	705290	236.2

Table 6.2.6 continued

Sample	C28			C29			C30		
	RT (min)	Area (pA)	Mass (ng)	RT (min)	Area (pA)	Mass (ng)	RT (min)	Area (pA)	Mass (ng)
ZUM-ASU+18	24.972	308445	462.7	25.666	3E+06	4610.9	0.0270	26.332	1792.1
ZUM-ASU+16	25.051	2654653	815.5	25.669	9E+06	2612.7	26.335	5905262	1814.2
ZUM-ASU+13	24.618	9041693	1366.5	25.206	7E+06	1126.9	25.863	1.8E+07	2724.8
ZUM-ASU+11	24.51	1670932	424.4	25.196	3E+06	876.7	25.856	2267831	576.0
ZUM-ASU+9	-	-	-	25.204	8E+06	932.3	25.864	7413029	905.1
ZUM-ASU+5	-	-	-	25.203	1E+07	1586.5	25.861	1E+07	1247.0
ZUM-ASU+3	24.575	2888849	650.7	25.197	3E+06	736.4	25.852	3331291	750.4
ZUM-ASU+1	24.514	4314639	598.2	25.199	6E+06	768.1	25.861	7334796	1016.9
ZUM-SU+18	24.509	5027629	2820.7	25.213	5E+07	28123.9	25.862	6864312	3851.1
ZUM-SU+16	24.509	3916165	1385.0	25.207	4E+07	12487.1	25.859	4025505	1423.7
ZUM-SU+14	24.505	1310884	513.3	25.197	6E+06	2431.0	25.857	1723661	674.9
ZUM-SU+13	24.646	9.8E+07	159.1	25.332	4E+08	626.5	25.996	9.2E+07	149.0
ZUM-SU+12	24.512	5059975	1150.0	25.204	1E+07	3215.5	25.861	5998933	1363.4
ZUM-BSU+20	24.508	1386275	437.8	25.2	1E+07	4097.9	25.854	2217564	700.4
ZUM-BSU+17	24.509	1924460	645.3	25.201	2E+07	5272.8	25.859	2274621	762.7
ZUM-BSU+15	24.509	1038359	634.5	25.196	3E+06	1705.8	25.857	1194994	730.2
ZUM-BSU+13	24.508	1613705	547.7	25.196	2E+06	776.6	25.855	1906047	647.0
ZUM-BSU+8	24.52	624343	209.0	25.21	1E+06	401.7	25.874	2135918	715.2

Table 6.2.6. continued

Sample	C31			C32			C33			IS	
	RT (min)	Area (pA)	Mass (ng)	RT (min)	Area (pA)	Mass (ng)	RT (min)	Area (pA)	Mass (ng)	RT (min)	Area (pA)
ZUM-ASU+18	27.096	2811612	4217.7	27.975	235395	353.1	29.008	410118	615.2	25.975	1333230
ZUM-ASU+16	27.101	7560518	2322.7	27.978	1636301	502.7	29.012	2472695	759.6	25.979	6510154
ZUM-ASU+13	26.539	5949704	899.2	27.315	4558559	689.0	28.225	3114027	470.6	25.521	13233210
ZUM-ASU+11	26.533	1761332	447.3	27.307	869280	220.8	28.216	727237	184.7	25.512	7875051
ZUM-ASU+9	26.541	5502872	671.9	27.313	3314162	404.6	28.224	2596703	317.0	25.522	16381105
ZUM-ASU+5	26.539	8102101	992.5	27.312	4502922	551.6	28.219	3061560	375.0	25.518	16326182
ZUM-ASU+3	26.533	2426518	546.6	27.309	1982997	446.7	28.215	1341703	302.2	25.511	8878637
ZUM-ASU+1	26.537	4352034	603.4	27.312	3599228	499.0	28.22	2273260	315.2	25.516	14425846
ZUM-SU+18	26.564	6.5E+07	36654.2	27.31	4221260	2368.3	28.231	1.7E+07	9292.4	25.509	3564848
ZUM-SU+16	26.548	2.9E+07	10173.3	27.309	2142784	757.8	28.222	7355759	2601.5	25.51	5654989
ZUM-SU+14	26.534	4879472	1910.6	27.307	799509	313.1	28.217	1245305	487.6	25.511	5107720
ZUM-SU+13	26.686	4.2E+08	674.5	27.463	6.4E+07	104.0	28.366	7.9E+07	127.2	25.648	1.24E+09
ZUM-SU+12	26.54	1.1E+07	2577.7	27.311	3991802	907.3	28.222	3875787	880.9	25.512	8799714
ZUM-BSU+20	26.535	3277532	1035.2	27.306	748143	236.3	28.304	1778707	561.8	25.51	6332408
ZUM-BSU+17	26.536	6330203	2122.5	27.305	1583804	531.0	28.216	1830851	613.9	25.511	5964890
ZUM-BSU+15	26.531	1525262	932.0	27.308	773227	472.5	28.216	569896	348.2	25.509	3273207
ZUM-BSU+13	26.532	1582934	537.3	27.307	947170	321.5	28.218	613536	208.2	25.511	5892350
ZUM-BSU+8	26.551	872847	292.3	27.329	460657	154.2	28.244	300838	100.7	25.526	5973237

Table 6.2.7. Concentrations (ng g^{-1}) of extracted *n*-alkanes C_{25} – C_{33} throughout the Zumaia section determined using gas chromatography flame ionisation detection. Cells highlighted in grey represent samples within the CIE.

Sample	Height	*n*-alkane mass (ng g^{-1} dry sediment)								
		C25	C26	C27	C28	C29	C30	C31	C32	C33
ZUM-BSU+8	2.40	2.7	9.5	5.3	4.7	9.0	16.1	6.6	3.5	2.3
ZUM-BSU+13	3.90	12.6	24.9	14.1	11.9	16.9	14.1	11.7	7.0	4.5
ZUM-BSU+15	4.50	8.9	17.0	14.0	13.7	36.9	15.8	20.2	10.2	7.5
ZUM-BSU+17	5.10	6.8	14.6	22.9	14.1	115.6	16.7	46.5	11.6	13.5
ZUM-BSU+20	6.00	10.0	22.2	15.3	9.6	89.9	15.4	22.7	5.2	12.3
ZUM-SU+12	9.15	16.9	26.4	20.3	25.2	70.5	29.9	56.5	19.9	19.3
ZUM-SU+13	9.30	-	-	3.1	4.6	18.2	4.3	19.6	3.0	3.7
ZUM-SU+14	9.45	28.1	52.2	29.6	13.7	64.7	18.0	50.8	8.3	13.0
ZUM-SU+16	9.75	22.6	37.6	77.2	29.5	266.3	30.4	216.9	16.2	55.5
ZUM-SU+18	10.05	40.7	46.4	166.4	62.1	618.8	84.7	806.5	52.1	204.5
ZUM-ASU+1	13.45	7.0	16.5	12.1	13.1	16.8	22.2	13.2	10.9	6.9
ZUM-ASU+3	14.45	10.6	28.9	14.6	14.2	16.0	16.3	11.9	9.7	6.6
ZUM-ASU+5	15.45	14.5	22.9	22.1	-	34.5	27.1	21.6	12.0	8.2
ZUM-ASU+9	17.45	10.2	23.8	13.2	-	20.2	19.6	14.5	8.8	6.9
ZUM-ASU+11	18.45	7.9	14.6	10.5	9.2	19.1	12.5	9.7	4.8	4.0
ZUM-ASU+13	19.45	18.0	49.5	23.0	29.9	24.6	59.5	19.7	15.1	10.3
ZUM-ASU+16	20.95	34.0	33.7	29.9	19.2	61.5	42.7	54.7	11.8	17.9
ZUM-ASU+18	21.95	44.9	36.0	20.4	10.8	107.9	41.9	98.7	8.3	14.4

Table 6.2.8. Total angiosperm, gymnosperm, pteridophyte, and dinoflagellate cyst assemblage counts in samples throughout the Zumaia section. Ratios calculated are for comparison of marine and terrestrial and relative palynomorph assemblages throughout the section. Cells highlighted in grey represent samples within the CIE, and those marked with "N/A" represent barren or reworked samples.

												Above SU		
Sample name	Height (m)	Angiosperms	Gymnosperms	Pteridophytes	Sporomorph total	Dinoflagellate cysts	Angiosperm % of total plant pollen	Gymnosperm % of total plant pollen	Pteridophyte % of total plant pollen	Angiosperm % of total palynomorphs	Gymnosperm % of total palynomorphs	Pteridophyte% of total palynomorphs	Dinoflagellate cysts % of total of palynomorphs (marine v terr)	
ZUM-ASU+13	19.45	1	3	0	4	0	25	75	0	25	75	0	0	
ZUM-ASU+7	16.45	49	586	7	642	0	8	91	1	8	91	1	0	
ZUM-ASU+6	14.88	7	5	0	12	1	58	42	0	54	39	0	8	
ZUM-ASU+5	14.53	N/A	N/A	N/A	N/A	N/A	N/A	N/A	N/A	N/A	N/A	N/A	N/A	
ZUM-ASU+4	14.20	15	59	1	75	0	20	79	1	20	79	1	0	
ZUM-ASU+3	13.96	25	27	0	52	0	48	52	0	48	52	0	0	
ZUM-ASU+2	13.71	110	369	0	479	0	23	77	0	23	77	0	0	
ZUM-ASU+0	12.95	33	105	0	138	0	24	76	0	24	76	0	0	
ZUM-SU+32	12.62	126	363	2	491	2	26	74	0.4	26	74	0.4	0.4	SU
ZUM-SU+27	11.40	3	9	0	12	41	25	75	0	6	17	0	77	
ZUM-SU+21	10.50	33	113	2	148	111	22	76	1	13	44	1	43	
ZUM-SU+15	9.85	2	7	1	10	55	20	70	10	3	11	2	85	
ZUM-SU+10	8.85	20	31	0	51	64	39	61	0	17	27	0	56	

Table 6.2.8. continued

Sample name	Height (m)	Angiosperms	Gymnosperms	Pteridophytes	Sporomorph total	Dinoflagellate cysts	Angiosperm % of total plant pollen	Gymnosperm % of total plant pollen	Fern/moss % of total plant pollen	Angiosperm % of total palynomorphs	Gymnosperm % of total palynomorphs	Fern/moss % of total palynomorphs	Dinoflagellates cysts % of total of palynomorphs (marine v terr)
ZUM-SU+8	8.71	7	0	1	8	98	87.5	0.0	12.5	6.6	0.0	0.9	92.5
ZUM-SU+7	8.55	4	8	1	13	301	30.8	61.5	7.7	1.3	2.5	0.3	95.9
ZUM-SU+6	8.38	N/A	N/A	N/A	N/A	N/A	N/A	N/A	N/A	N/A	N/A	N/A	N/A
ZUM-SU+5	8.22	N/A	N/A	N/A	N/A	N/A	N/A	N/A	N/A	N/A	N/A	N/A	N/A
ZUM-SU+3	7.89	N/A	N/A	N/A	N/A	N/A	N/A	N/A	N/A	N/A	N/A	N/A	N/A
ZUM-SU+1	7.50	13	5	1	19	0	68.4	26.3	5.3	68.4	26.3	5.3	0.0
ZUM-BSU+23	6.90	3	2	0	5	0	60.0	40.0	0.0	60.0	40.0	0.0	0.0
ZUM-BSU-4	6.40	13	10	0	23	96	56.5	43.5	0.0	10.9	8.4	0.0	80.7
ZUM-BSU-9	5.55	14	9	0	23	42	60.9	39.1	0.0	21.5	13.8	0.0	64.6
ZUM-BSU+16	4.80	16	6	2	24	0	66.7	25.0	8.3	66.7	25.0	8.3	0.0
ZUM-BSU-14	3.55	61	30	2	93	26	65.6	32.3	2.2	51.3	25.2	1.7	21.8
ZUM-BSU+8	2.40	42	25	2	69	9	60.9	36.2	2.9	53.8	32.1	2.6	11.5

6.3 APPENDIX 3: ADDITIONAL DATA FOR CHAPTER 4

This appendix provides supplementary information for Chapter 4. Results tables for C/N values, *n*-alkane concentrations, and palynological assemblages are provided for all data discussed.

LITHOLOGICAL CORRELATION

For this lithological correlation, the height of the base of each marker bed was measured and the gradient and intercept between these points calculated. For example, the base of bed "1" (Figure 6.3.1) would be measured on both logs, relative to zero. These values would then be plotted as xy co-ordinates, where y = data tied to the first log (Claret: L.D., July 2005), and x = data tied to the second log (Claret: R.D., June 2011). The gradient and intercept were then calculated between the base of one marker bed and the next using the linear equation ($y = mx + c$). These data were used to normalise heights from Log 2 to Log 1 (Figure 6.3.1). In total, 165 samples were collected for the Claret section over four field seasons (29 in July 2005 by Laura Domingo, L.D.; 51 in June 2007 by L.D.; 18 in March 2010 by L.D.; and 67 in June 2011 by Hayley R. Manners, H.R.M., Tom Dunkley Jones, T.D.J. and Rob Duller, R.D.), with two logs created (June 2005 by L.D. and June 2011 by R.D.). All samples collected prior to June 2011 were included on the log of L.D., and those collected in June 2011 were included on the log produced by R.D. Samples were collected by L.D. (< June 2010), H.R.M. and L.D. (June 2010), and H.R.M. and T.D.J. (June 2011). Dotted lines indicate same horizons on both logs. Letters in Figure 6.2.3 indicate correlative beds as described in Table 6.3.1. The marker beds used for the Claret section were the base of the *Alveolina* Beds, the Claret Conglomerate, and the top of a conglomerate further

down the section (Table 6.3.1). Below the lower conglomerate (letter "a"; Figure 6.3.2) no tie points were recorded so samples were correlated to the lower conglomerate. In addition to using marker beds, where information on sample heights relative to a marker bed was known, these were also incorporated. For example, when a sample was known to have been taken 0.2 m below a marker bed, all heights were adjusted so that samples started at the stated height.

ANALYTICAL DATA TABLES FOR CHAPTER 4

Table 6.3.1. Lithological correlation data for the Claret section. Tie point height 1 = original log created in July 2005, tie point height 2 = most recent log created in June 2011. FAH = First Appearance Height (base) of the marker bed; LAH = Last Appearance Height (top) of the marker bed. CC = Claret Conglomerate; A. Limestone = *Alveolina* Limestone. Where no marker beds were present for correlation, the stratigraphically closest tie point was used instead.

Lithology/ correlative beds used	Tie point height 1 (m)	"FAH" 1	"LAH" 1	Tie point height 2 (m)	"FAH" 2	"LAH" 2	Gradient and intercept	Letter on Figure 6.3.2.
CC upper to A. Limestone	35	20.5	55.5	35	26.2	61.2	m = -1.00 c = -5.70	c
CC thickness	9.5	11	20.5	12	14.2	26.2	m = 0.45 c = 8.71	b
Lower conglomerate to CC lower base	7	4	11	11.2	3	14.2	m = 0.63 c = 2.13	a
Lower conglomerate thickness	4	0	4	3	0	3		
Clay to lower conglomerate	Different sampling heights, no tie point							

APPENDIX 3

Table 6.3.2. Weight percent carbon (wt% C) and nitrogen (wt% N) determined in Claret sediment samples. C/N ratios were calculated throughout the section where possible. Where %N was below the instrumental limit of detection, in around half the samples, the C/N ratio could not be calculated and is not shown here. $\delta^{13}C_{TOC}$ data, and wt% C for the whole section can be found in the supplementary material of Manners *et al.* (2013) and Appendix 6.1.

Sample	Height (m)	%C	%N	C/N	Sample	Height (m)	%C	%N	C/N
CLA-I-38	41.3	0.2	0.1	2.8	CLA-I-63	31.0	0.3	0.1	3.6
CLA-I-39	40.9	0.4	0.1	3.6	CLA-I-64	30.3	0.4	0.1	3.4
CLA-I-40	40.3	0.1	0.1	1.4	CLA-I-65	28.1	0.2	0.1	2.7
CLA-I-41	39.6	0.2	0.1	1.7	CLA-I-66	27.8	0.2	0.1	2.6
CLA-I-42	39.3	0.5	0.1	4.0	CLA-I-69	27.5	0.2	0.1	2.9
CLA-I-43	38.5	0.2	0.1	2.0	CLA-I-67	27.2	0.2	0.1	3.1
CLA-I-44	38.0	0.2	0.1	1.8	CLA-I-68	26.7	0.3	0.1	3.7
CLA-I-45	37.6	0.2	0.1	1.9	CLA-I-61	25.8	0.3	0.1	3.2
CLA-I-46	37.4	0.2	0.1	2.1	CLA-I-70	21.5	0.2	0.1	2.5
CLA-I-47	37.0	0.2	0.1	2.2	CLA-I-71	20.8	0.2	0.1	2.2
CLA-I-48	36.6	0.2	0.1	2.3	CLA-I-72	20.2	0.2	0.1	2.1
CLA-I-49	36.3	0.2	0.1	2.5	CLA-I-73	18.2	0.3	0.1	4.4
CLA-I-50	35.8	0.2	0.1	2.8	CLA-I-74	15.9	0.3	0.1	3.2
CLA-I-51	35.5	0.2	0.1	2.8	CLA-I-75	14.8	0.9	0.1	11.1
CLA-I-52	35.2	0.3	0.1	3.3	CLA-I-76	14.3	0.4	0.2	2.2
CLA-I-53	34.6	0.3	0.1	3.9	CLA-I-77	13.3	0.3	0.2	1.5
CLA-I-54	34.4	0.3	0.1	4.3	CLA-I-78	11.5	0.6	0.2	3.7
CLA-I-55	34.1	0.5	0.1	6.0	CLA-I-79	10.3	0.3	0.2	2.1
CLA-I-56	33.8	0.4	0.1	5.3	CLA-I-80	9.8	0.6	0.2	3.5
CLA-I-57	33.6	0.2	0.1	3.0	CLA-I-81	8.8	0.4	0.2	2.4
CLA-I-58	33.0	0.4	0.1	4.8	CLA-I-82	7.4	0.8	0.2	4.2
CLA-I-59	32.3	0.3	0.1	3.4	CLA-I-83	3.1	0.3	0.2	1.5
CLA-I-60	32.0	0.3	0.1	3.7	CLA-I-84	0.0	0.3	0.2	1.5
CLA-I-62	31.6	0.2	0.1	2.4					

Table 6.3.3. Peak integral and *n*-alkane mass data normalised to the internal standard (ng) for all Claret samples. IS = internal standard, deuterated triacontane ($C_{30}D_{62}$). Cells highlighted in grey represent samples within the CIE.

Sample	Height (m)	Sediment weight (g)	C25			C26			C27		
			RT (min)	Area (pA)	Mass (ng)	RT (min)	Area (pA)	Mass (ng)	RT (min)	Area (pA)	Mass (ng)
CLA-5,-8	56.22	46.17	23.239	172081456	155.4	24.005	1.57E+08	141.8	24.733	2.25E+08	203.2
CLA-5,-13	51.40	41.01	23.235	20229188	74.9	24	20791190	76.9	24.738	83171486	307.8
CLA-6,+16	46.43	45.90	23.23	288555739	636.7	23.996	2.92E+08	643.8	24.733	2.99E+08	659.7
CLA-6,+14	44.13	45.86	23.23	286320179	271.6	23.995	2.82E+08	267.1	24.733	2.82E+08	268.0
CLA-6,+12	42.14	45.52	23.235	41338254	21.0	24	39870785	20.3	24.737	85859733	43.7
CLA-6,+5	35.17	45.47	23.239	174931819	124.8	24.005	1.72E+08	122.4	24.733	2E+08	142.8
CLA-6,+3	33.18	45.27	23.23	309042671	202.7	23.996	3.11E+08	204.3	24.733	3.26E+08	214.0
CLA-I-60	31.97	46.58	22.481	3051647	55.9	23.241	3367214	61.7	23.975	4305104	78.9
CLA-I-70	21.48	45.72	23.229	254348703	372.1	23.995	2.41E+08	352.1	24.733	2.47E+08	362.0
CLA-MAR´10-13	17.60	46.78	22.48	5063198	41.7	23.241	4627297	38.1	23.978	6591076	54.2
CLA-MAR´10-12	16.80	33.54	22.482	6429689	73.8	23.241	5735856	65.8	23.976	8680755	99.6
CLA-3,-5	15.92	40.95	22.31	631535	92.8	23.068	1910402	280.7	23.811	1550948	227.9
CLA-3,-6	15.30	41.81	22.434	13230420	122.1	23.199	21725797	200.4	23.934	22178684	204.6
CLA-2, +5	11.55	41.56	22.313	795233	78.1	23.069	2924175	287.3	23.812	1439242	141.4
CLA-2, +2	9.67	41.42	22.312	316231	89.0	23.067	1110950	312.7	23.812	607603	171.0

Table 6.3.3. continued

Sample	C28			C29			C30		
	RT (min)	Area (pA)	Mass (ng)	RT (min)	Area (pA)	Mass (ng)	RT (min)	Area (pA)	Mass (ng)
CLA-5,-8	25.452	2.03E+08	183.6	26.142	3.11E+08	280.8	26.879	1.97E+08	178.1
CLA-5,-13	25.449	42910666	158.8	26.142	1.88E+08	695.2	26.874	49509246	183.2
CLA-6,+16	25.452	3E+08	662.9	26.142	3.04E+08	671.7	26.879	3.02E+08	666.0
CLA-6,+14	25.452	2.74E+08	260.1	26.142	2.79E+08	264.6	26.879	2.82E+08	267.7
CLA-6,+12	25.451	61770615	31.4	26.142	1.05E+08	53.4	26.875	50268118	25.6
CLA-6,+5	25.452	2.06E+08	146.8	26.142	2.59E+08	184.8	26.879	2.17E+08	154.6
CLA-6,+3	-	0	-	26.142	3.6E+08	235.9	26.879	3.58E+08	234.5
CLA-I-60	24.686	4445506	81.4	25.369	7158762	131.1	26.033	4203155	77.0
CLA-I-70	-	0	-	26.142	2.36E+08	344.5	26.88	2.02E+08	294.9
CLA-MAR´10-13	24.685	5350306	44.0	25.37	11778192	96.9	26.033	4545861	37.4
CLA-MAR´10-12	24.685	7264440	83.4	25.371	17966061	206.2	26.033	7966470	91.4
CLA-3,-5	24.522	1099510	161.6	25.212	3103982	456.1	25.875	2439770	358.5
CLA-3,-6	24.645	44017066	406.1	25.328	42044886	387.9	25.99	43285537	399.3
CLA-2, +5	24.52	1124697	110.5	25.207	1929183	189.6	25.872	3031270	297.9
CLA-2, +2	24.523	405458	114.1	25.208	679069	191.2	25.879	1096871	308.8

Table 6.3.3. continued

Sample	C31			C32			C33			IS	
	RT (min)	Area (pA)	Mass (ng)	RT (min)	Area (pA)	Mass (ng)	RT (min)	Area (pA)	Mass (ng)	RT (min)	Area (pA)
CLA-5,-8	27.702	4.16E+08	375.6	28.656	1.03E+08	92.9	29.774	2.17E+08	196.3	26.483	2.21E+09
CLA-5,-13	27.702	3.29E+08	1216.5	28.652	35134849	130.0	29.766	99659773	368.8	26.474	5.4E+08
CLA-6,+16	27.702	3.35E+08	739.1	28.665	2.85E+08	629.3	29.775	2.21E+08	488.7	26.478	9.06E+08
CLA-6,+14	27.702	3.09E+08	293.2	28.664	2.61E+08	247.7	29.776	2.25E+08	213.7	26.482	2.11E+09
CLA-6,+12	27.701	1.17E+08	59.6	28.652	46070289	23.4	29.767	91992780	46.8	26.487	3.93E+09
CLA-6,+5	27.702	3.07E+08	219.3	28.659	1.57E+08	111.7	29.777	2.78E+08	198.3	26.484	2.8E+09
CLA-6,+3	27.702	4.08E+08	267.6	28.657	3.36E+08	220.4	29.782	3.75E+08	245.7	26.486	3.05E+09
CLA-I-60	26.731	7871061	144.2	27.521	3259165	59.7	28.432	4511696	82.7	25.685	1.09E+08
CLA-I-70	27.708	2.01E+08	293.8	28.66	1.27E+08	185.3	29.774	1.13E+08	164.9	26.481	1.37E+09
CLA-MAR´10-13	26.734	31362701	258.1	27.522	4102772	33.8	28.435	11958882	98.4	25.685	2.43E+08
CLA-MAR´10-12	26.732	38884939	446.3	27.52	7368434	84.6	28.433	23601478	270.9	25.685	1.74E+08
CLA-3,-5	26.55	4060701	596.7	27.327	644979	94.8	28.242	1233402	181.2	25.53	13609968
CLA-3,-6	26.679	33285899	307.1	27.46	30702567	283.2	28.362	16448912	151.7	25.643	2.17E+08
CLA-2, +5	26.552	3011752	295.9	27.331	1147018	112.7	28.244	2243725	220.5	25.531	20353903
CLA-2, +2	26.551	665130	187.2	27.327	239408	67.4	28.248	375011	105.6	25.528	7104942

Table 6.3.4. Concentrations (ng g^{-1}) of extracted *n*-alkanes C_{25} – C_{33} throughout the Claret section determined using gas chromatography flame ionisation detection. Cells highlighted in grey represent samples within the CIE.

Sample	Height (m)	*n*-alkane mass (ng g^{-1} dry sediment)								
		C25	C26	C27	C28	C29	C30	C31	C32	C33
CLA-5,-8	56.22	3.4	3.1	4.4	4.0	6.1	3.9	8.1	2.0	4.3
CLA-5,-13	51.40	1.8	1.9	7.5	3.9	17.0	4.5	29.7	3.2	9.0
CLA-6,+16	46.43	13.9	14.0	14.4	14.4	14.6	14.5	16.1	13.7	10.6
CLA-6,+14	44.13	5.9	5.8	5.8	5.7	5.8	5.8	6.4	5.4	4.7
CLA-6,+12	42.14	0.5	0.4	1.0	0.7	1.2	0.6	1.3	0.5	1.0
CLA-6,+5	35.17	2.7	2.7	3.1	3.2	4.1	3.4	4.8	2.5	4.4
CLA-6,+3	33.18	4.5	4.5	4.7	-	5.2	5.2	5.9	4.9	5.4
CLA-I-60	31.97	1.2	1.3	1.7	1.7	2.8	1.7	3.1	1.3	1.8
CLA-I-70	21.48	8.1	7.7	7.9	-	7.5	6.5	6.4	4.1	3.6
CLA-MAR´10-13	17.60	0.9	0.8	1.2	0.9	2.1	0.8	5.5	0.7	2.1
CLA-MAR´10-12	16.80	2.2	2.0	3.0	2.5	6.1	2.7	13.3	2.5	8.1
CLA-3,-5	15.92	2.3	6.9	5.6	3.9	11.1	8.8	14.6	2.3	4.4
CLA-3,-6	15.30	2.9	4.8	4.9	9.7	9.3	9.6	7.3	6.8	3.6
CLA-2, +5	11.55	1.9	6.9	3.4	2.7	4.6	7.2	7.1	2.7	5.3
CLA-2, +2	9.67	2.1	7.6	4.1	2.8	4.6	7.5	4.5	1.6	2.5

APPENDIX 3

Table 6.3.5. Total angiosperm, gymnosperm, pteridophyte, and dinoflagellate cyst assemblage counts in samples throughout the Claret section. Ratios calculated are for comparison of marine and terrestrial and relative palynomorph assemblages throughout the section. Cells highlighted in light grey represent samples within the CIE, and cells highlighted in dark grey indicate where samples were barren or showed evidence of reworking, including dinoflagellate cysts in some samples.

Sample name	Height (m)	Angiosperms	Gymnosperms	Pteridophytes	Sporomorph total	Dinoflagellate cysts	Angiosperm % of total	Gymnosperm % of total	Pteridophyte % of total	Sporomorphs % of total palynomorphs (total pollen Figure 4)
CLA-5-1	62.97	20	0	0	20	0	100	0	0	100
CLA-5-4	60.08	117	5	2	124	0	94	4	2	100
CLA-5-5	59.11	14	0	1	15	0	93	0	7	100
CLA-5-6	58.15	7	3	2	12	0	58	25	17	100
CLA-5-7	57.18	0	0	0	0	0	0	0	0	0
CLA-5-8	56.22	17	24	3	44	0	39	55	7	100
CLA-5-9	55.26	0	0	0	0	0	0	0	0	0
CLA-5-11	53.33	0	0	0	0	0	0	0	0	0
CLA-5-13	51.40	72	109	2	183	5	39	60	1	97
CLA-5-15	49.47	102	56	2	160	2	64	35	1	99
CLA-6+16	46.43	9	7	0	16	0	56	44	0	100
CLA-6+14	44.13	20	61	4	85	0	24	72	5	100
CLA-6+12	42.14	6	10	0	16	0	38	63	0	100
CLA-6+9	39.15	2	1	0	3	0	67	33	0	100
CLA-6+6	36.17	1	77	13	91	28	1	85	14	77
CLA-6+3	33.18	-	-	-	150	36	0	0	0	81
CLA-6+1	31.19	4	86	27	117	60	3	74	23	66
CLA-3-1	18.74	122	35	2	159	0	77	22	1	100
CLA-3-2	18.42	44	2	0	46	0	96	4	0	100
CLA-3-3	17.17	24	71	0	95	0	25	75	0	100
CLA-3-4	16.55	4	15	3	22	0	18	68	14	100
CLA-3-5	15.92	10	49	1	60	0	17	82	2	100
CLA-3-8	14.05	28	297	0	325	0	9	91	0	100
CLA-3-9	13.42	0	0	0	0	0	0	0	0	0
CLA-3-10	12.80	11	3	4	18	0	61	17	22	100

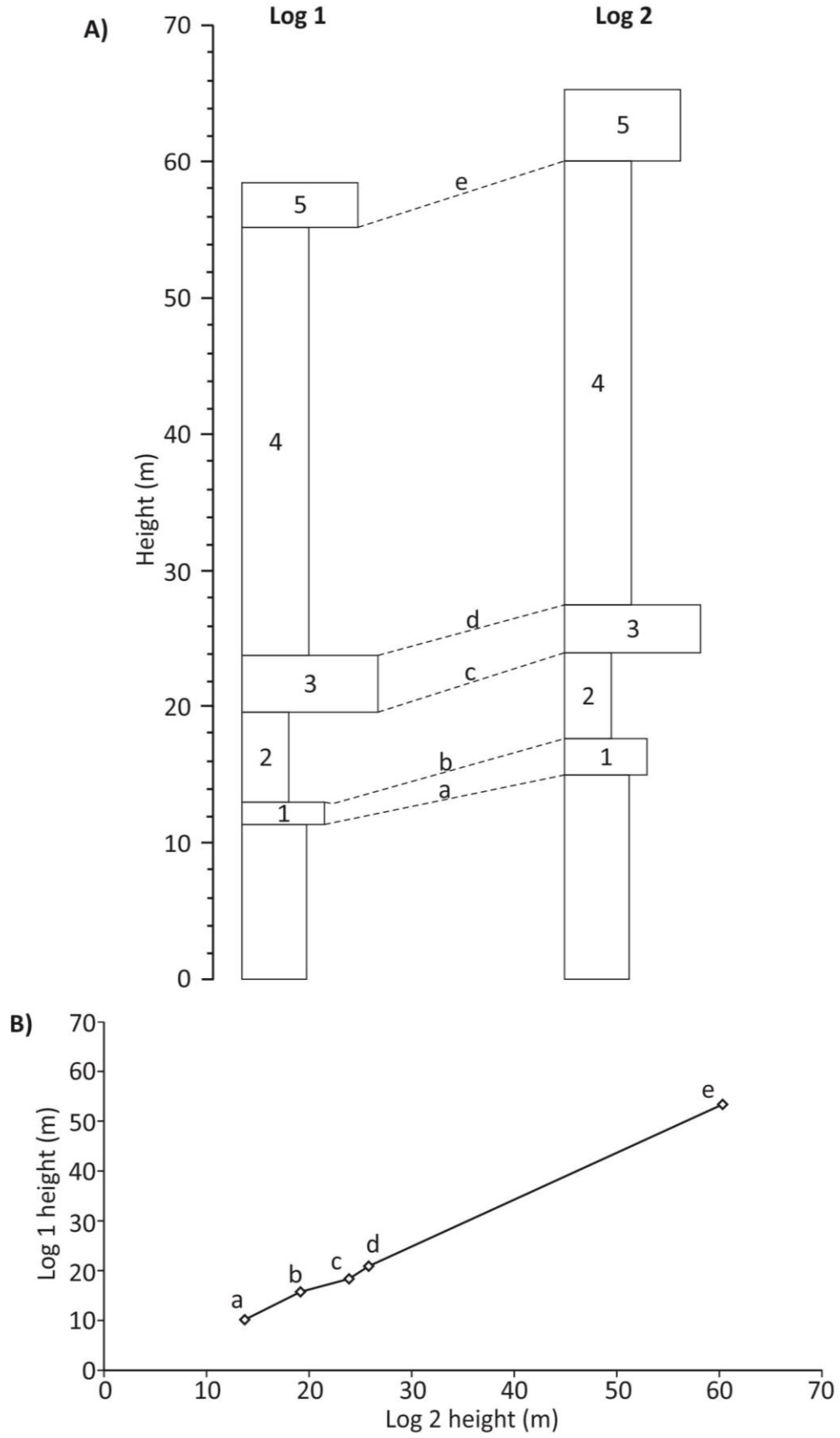

Figure 6.3.1. Schematic of graphical correlation employed. A) Exemplar logs of the same section for correlation. Numbers indicate marker beds used for correlation, with dotted lines illustrating how these beds align in independent logs of the same section. Letters indicate base of beds used for calculation of gradient and intercept. B) Graphical correlation employed using letters from A).

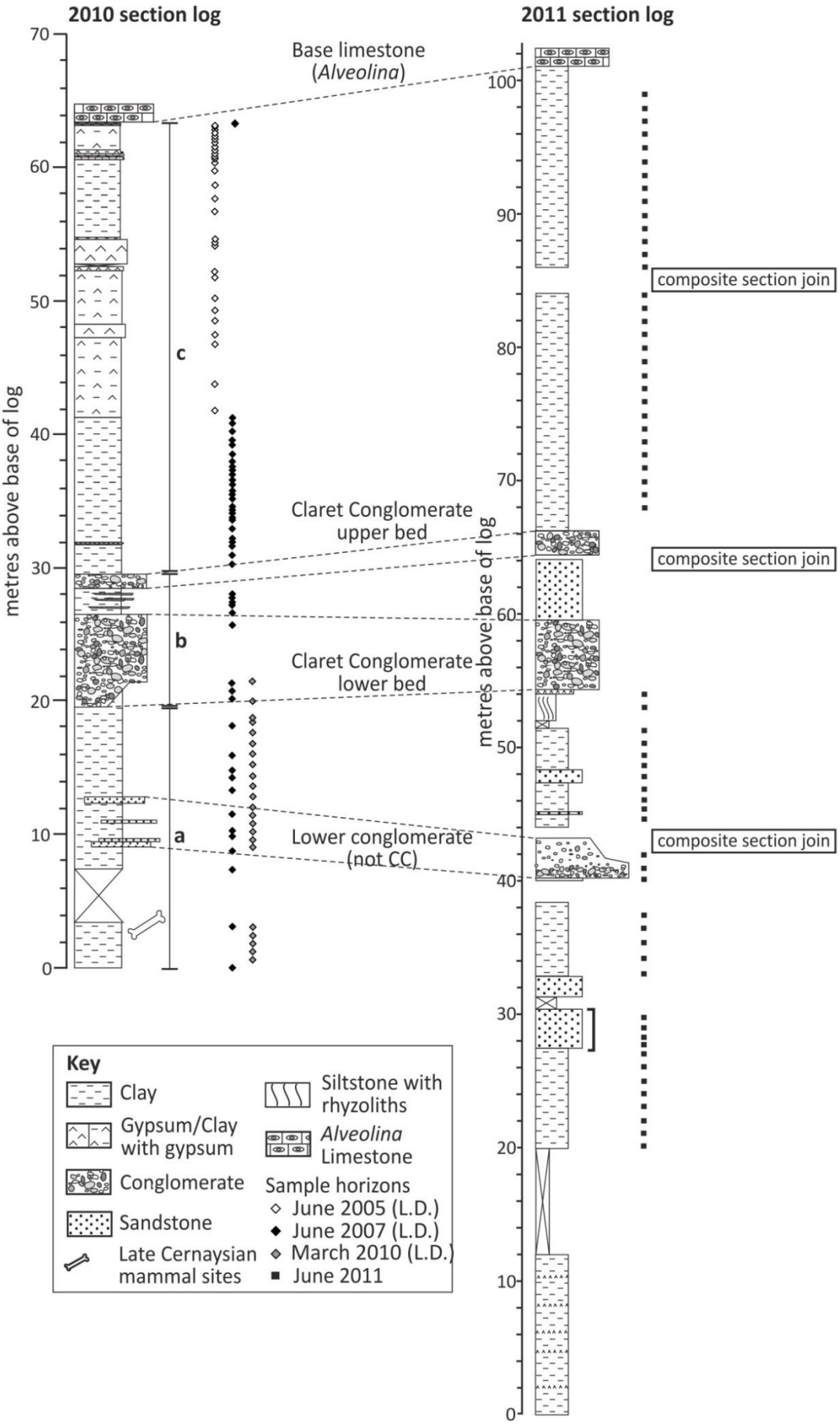

Figure 6.3.2. Lithological correlation method employed for the Claret section to correlate samples.

7 REFERENCES

Alegret, L., Ortiz, S., Orue-Etxebarria, X., Bernaola, G., Baceta, J. I., Monechi, S., Apellaniz, E., Pujalte, V., 2009. The Palaeocene-Eocene Thermal Maximum: New data on microfossil turnover at the Zumaia section, Spain. Palaios 24, 318 – 328

Aubry, M., Ouda, K., Dupuis, C., Berggren, W., Van Couvering, J., 2007. The Global Standard Stratotype-section and Point (GSSP) for the base of the Eocene Series in the Dababiya section (Egypt). Episodes 30, 271 – 286.

Aziz H.A., Hilgen F.J., van Luijk G.M., Sluijs A., Kraus M.J., Pares, J.M., Gingerich, P.D., 2008. Astronomical climate control on palaeosol stacking patterns in the upper Palaeocene-lower Eocene, Willwood Formation, Bighorn Basin, Wyoming. Geology 36, 531 – 34

Baceta, J.I., Pujalte, V., Dinares-Turell, J., Payros, A., Orue-Etxebarria, X., Bernaola, G., 2000. The Palaeocene/Eocene Boundary Interval in the Zumaia section (Gipuzkoa, Basque basin): Magnetostratigraphy and high resolution lithostratigraphy. Revista de la Sociedad Geológica de España 13, 375 – 391.

Baceta, J.I., Pujalte, V., Wright, V.P., Schmitz, B. 2011. Carbonate platform models, sea-level changes and extreme climatic events during the Palaeocene-early Eocene greenhouse interval: a basin-platform-coastal plain transect across the southern Pyrénéan basin *in* Pre-meeting field trips guidebook, 28th IAS meeting, Zaragoza. Sociedad Geológica de España, Geo-Guías 7, 151 – 198.

Bains, S., Corfield, R.M., Norris, R.D., 1999. Mechanisms of climate warming at the end of the Palaeocene. Science 285, 724 – 727

Bains, S., 2000. Termination of global warmth at the Palaeocene/Eocene boundary through productivity feedback. Nature 407, 467 – 467

Bains, S., Norris, R.D., Corfield, R.M., Bowen, G.J., Gingerich, P.D., Koch, P.L., 2003. Marine-terrestrial linkages at the Palaeocene-Eocene boundary *in* Wing, S.L., Gingerich, P.D., Schmitz, B. and Thomas, E.M., Causes and consequences of globally warm climates in the early Palaeogene: Boulder, Colorado. Geological Society of America Special Paper 369, 1-9

Beard, K. C. 2008. The oldest North American primate and mammalian biogeography during the Palaeocene-Eocene Thermal Maximum. Proceedings of the National Academy of Sciences 105, 3815 – 3818.

Beerling, D.J., 1996. Ecophysiological responses of woody plants to past CO_2 concentrations. Tree Physiology 16, 389 – 396.

Beerling, D. J., 2000. Increased terrestrial carbon storage across the palaeocene-eocene boundary. Palaeogeography Palaeoclimatology Palaeoecology 161, 395 – 405

Bernaola, G., Baceta, J. I., Payros, A., Orue-Etxebarria, X., Apellaniz, E., 2006. The Palaeocene and lower Eocene of the Zumaia section (Basque Basin). Climate and Biota of the Early Palaeogene post conference Fieldtrip Guidebook. KOPIAK, Bilbao.

REFERENCES

Bi, X., Sheng, G., Liu, X., Li, C., Fu, J., 2005. Molecular carbon and hydrogen isotopic composition of *n*-alkanes in plant leaf waxes. Organic Geochemistry 36, 1405 – 1417.

Bice, K. L. and Marotzke, J. 2002. Could changing ocean circulation have destabilised methane hydrate at the Palaeocene/Eocene boundary? Paleoceanography 17, 8.1 – 8.13.

Bijl, P.K., Schouten, S., Brinkhuis, H., Sluijs, A., Reichart, G.J., Zachos, J.C., 2009. Early Palaeogene temperature evolution of the Southwest Pacific Ocean. Nature 461, 776 – 779.

Bowen, G.J., Koch, P.L., Gingerich, P.D., Norris, R.D., Bains, S., Corfield, R.M., 2001. Refined isotope stratigraphy across the continental Palaeocene-Eocene boundary on Polecat Bench in the northern Bighorn Basin. University of Michigan Papers on Palaeontology 33, 73 – 88

Bowen, G.J., Beerling, D.J., Koch, P.L., Zachos, J.C., Quattlebaum, T., 2004. A humid climate state during the Palaeocene/Eocene thermal maximum. Nature 432, 495 – 499.

Bowen, G.J., Bralower, T.J., Delaney, M.L., Dickens, G.R., Kelly, D.C., Koch, P.L., Kump, L.R., Meng, J., Sloan, L.C., Thomas, E., Wing, S.L., Zachos, J.C., 2006. Eocene Hyperthermal Event Offers Insight Into Greenhouse Warming. Eos Transactions, American Geophysical Union 87, 165 – 169.

Bowen, G.J. and Zachos, J.C., 2010. Rapid carbon sequestration at the termination of the Palaeocene-Eocene Thermal Maximum. Nature Geoscience 3, 866 – 869.

Brinkhuis, H., Schouten, S., Collinson, M.E., Sluijs, A., Sinninghe Damsté, J.S., Dickens, G.R., Huber, M., Cronin, T.M., Onodera, J., Takahashi, K., Bujak, J.P., Stein, R., Van Der Burgh, J., Eldrett, J.S., Harding, I.C., Lotter, A.F., Sangiorgi, F., Van Konijnenburg-Van Cittert, H., De Leeuw, J.W., Matthiessen, J., Backman, J., Moran, K., The Expedition 302 Scientists, *et al.*, 2006. Episodic fresh surface waters in the Eocene Arctic Ocean. Nature 441, 606 – 609.

Canudo, J. I., Molina, E., 1992. Planktic foraminiferal faunal turnover and bio-chronostratigraphy of the Palaeocene-Eocene boundary at Zumaya (northern spain). Revista de la Sociedad Geológica de España 5, 145 – 157

Canudo, J. I., Keller, G., Molina, E., Ortiz, N., 1995. Planktic foraminiferal turnover and $\delta^{13}C$ isotopes across the Palaeocene-Eocene transition at Caravaca and Zumaya, Spain. Palaeogeography Palaeoclimatology Palaeoecology 114, 75 – 100

Cerling, T.E., 1991. Carbon-Dioxide in the Atmosphere - Evidence from Cenozoic and Mesozoic Palaeosols. American Journal of Science 291, 377 – 400.

Chikaraishi, Y., Naraoka, H., 2003. Compound-specific δD-$\delta^{13}C$ analyses of *n*-alkanes extracted from terrestrial and aquatic plants. Phytochemistry 63, 361 – 371

Clyde, W. C., Gingerich, P. D., 1998. Mammalian community response to the latest Palaeocene thermal maximum: An isotaphonomic study in the northern Bighorn Basin, Wyoming. Geology 26, 1011 – 1014.

REFERENCES

Collister, J.W., Rieley, G., Stern, B., Eglinton, G., Fry, B., 1994. Compound-specific $\delta^{13}C$ analyses of leaf lipids from plants with differing carbon-dioxide metabolisms. Organic Geochemistry 21, 619 – 627.

Conte, M.H.,Weber, J.C., 2002. Long-range atmospheric transport of terrestrial biomarkers to the western North Atlantic. Global Biogeochemical Cycles 16, 1142.

Cramer, B. S. and Kent, D. V., 2005. Bolide summer: The Palaeocene/Eocene Thermal Maximum as a response to an extraterrestrial trigger. Palaeogeography, Palaeoclimatology, Palaeoecology 224, 144 – 166.

Cui, Y., Kump, L.R., Ridgwell, A.J., Charles, A.J., Junium C.K., Diefendorf A.F., Freeman K.H., Urban N.M., Harding I.C., 2011. Slow release of fossil carbon during the Palaeocene-Eocene Thermal Maximum. Nature Geoscience 4, 481 – 485.

DeConto, R.M., Galeotti, S., Pagani, M., Tracy, D., Schaefer, K., Zhang, T.J., Pollard, D., Beerling, D.J., 2012. Past extreme warming events linked to massive carbon release from thawing permafrost. Nature 484, 87 – 92.

Dickens, G.R., 2003. Rethinking the global carbon cycle with a large, dynamic and microbially mediated gas hydrate capacitor. Earth and Planetary Science Letters 213, 169 – 183.

Dickens, G. R. 2004. Global change: Hydrocarbon-driven warming. Nature 429, 513 – 515.

Dickens, G.R., 2011. Down the Rabbit Hole: toward appropriate discussion of methane release from gas hydrate systems during the Palaeocene-Eocene Thermal Maximum and other past hyperthermal events. Climate of the Past 7, 831 – 846.

Dickens, G.R., O'Neil, J.R., Rea, D.K., Owen, R.M., 1995. Dissociation of oceanic methane hydrate as a cause of the carbon isotope excursion at the end of the Palaeocene. Palaeogeography 10, 965 – 971.

Dickens, G.R., Paull, C.K., Wallace, P., 1997. Direct measurement of in situ methane quantities in a large gas-hydrate reservoir. Nature 385, 426 – 428.

Diefendorf, A. F., Mueller, K.E., Wing, S.L., Koch, P.L., Freeman, K.H., 2010. Global patterns in leaf C-13 discrimination and implications for studies of past and future climate. Proceedings of the National Academy of Sciences 107, 5738 – 5743.

Diefendorf, A. F., Freeman, K. H., Wing, S.L., Graham, H.V., 2011. Production of n-alkyl lipids in living plants and implications for the geologic past. Geochimica et Cosmochimica Acta 75, 7472 – 7485.

Dinarès-Turell, J., Baceta, J.I., Bernaola, G., Orue-Etxebarria, X., Pujalte, V., 2007. Closing the Mid-Palaeocene gap: Toward a complete astronomically tuned Palaeocene Epoch and Selandian and Thanetian GSSPs at Zumaia (Basque Basin, W Pyrénées). Earth and Planetary Science Letters 262, 450 – 467.

Domingo, L., López-Martínez, N., Leng, M.J., Grimes, S.T., 2009. The Palaeocene-Eocene Thermal Maximum record in the organic matter of the Claret and

Tendruy continental sections (South-central Pyrénées, Lleida, Spain). Earth and Planetary Science Letters 281, 226 – 237.

Dunkley Jones, T., Ridgwell, A., Lunt, D., Maslin, M.A., Schmidt, D.N., Valdes, P.J., 2010. A Palaeogene perspective on climate sensitivity and methane hydrate instability. Philosophical Transactions of the Royal Society A: Mathematical, Physical and Engineering Sciences 368, 2395 – 2415.

Dunkley Jones, T., Lunt, D.J., Schmidt, D.N., Ridgwell, A., Sluijs, A., Valdes, P.J., Maslin, M., 2013. Climate model and proxy data contraints on ocean warming across the Paleocene – Eocene Thermal Maximum. Earth-Science Reviews 125, 123 – 145.

Edwards, T.W.D., Graf, W., Trimborn, P., Stichler, W., Lipp, J., Payer, H.D., 2000. $\delta^{13}C$ response surface resolves humidity and temperature signals in trees. Geochimica et Cosmochimica Acta 64, 161 – 167.

Eglinton, G., Hamilton, R.J., 1967. Leaf Epicuticular Waxes. Science 156, 1322 – 1335.

Farley, K. A. and S. F. Eltgroth (2003). An alternative age model for the Palaeocene-Eocene thermal maximum using extraterrestrial 3He. Earth and Planetary Science Letters 208, 135 – 148.

Handley, L., Pearson, P.N., McMillan, I.K., Pancost, R.D., 2008. Large terrestrial and marine carbon and hydrogen isotope excursions in a new Palaeocene/Eocene boundary section from Tanzania. Earth and Planetary Science Letters 275, 17 – 25.

Galbrun, B., Feist, M., Colombo, F., Rocchia, R., Tambareau, Y., 1993. Magnetostratigraphy and biostratigraphy of Cretaceous-Tertiary continental deposits, Ager Basin, Province of Lerida, Spain. Palaeogeography Palaeoclimatology Palaeoecology 102, 41 – 52.

Garel, S., Schnyder, J., Jacob, J., Dupuis, C., Boussafir, M., Le Milbeau, C., Storme, J.Y., Iakovleva, A.I., Yans, J., Baudin, F., Flehoc, C., Quesnel, F., 2013. Palaeohydrological and palaeoenvironmental changes recorded in terrestrial sediments of the Palaeocene-Eocene boundary (Normandy, France). Palaeogeography Palaeoclimatology Palaeoecology 376, 184 – 199.

Gavrilov Y.O., Shcherbinina E.A., Oberhansli H., 2003. Palaeocene-Eocene boundary events in the northeastern Peri-Tethys. Geological Society of America Special Paper 369, 147 – 168.

Gibbons, W., Moreno, T. Geological Society of London. 2002. The Geology of Spain. The Geological Society, London, UK.

Gibbs, S. J., Stoll, H. M., Bown, P. R., Bralower, T. J., 2010. Ocean acidification and surface water carbonate production across the Palaeocene – Eocene Thermal Maximum. Earth and Planetary Science Letters 295, 583 – 592

Gingerich, P. D. 2003. Mammalian responses to climate change at the Palaeocene-Eocene boundary: Polecat Bench record in the northern Bighorn Basin, Wyoming. Geological Society of America, Special Papers 369, 463 – 478.

Handley, L., Pearson, P.N., McMillan, I.K., Pancost, R.D., 2008. Large terrestrial and marine carbon and hydrogen isotope excursions in a new Palaeocene/Eocene

boundary section from Tanzania. Earth and Planetary Science Letters 275, 17 – 25.

Handley, L., Crouch, E.M., Pancost, R.D., 2011. A New Zealand record of sea level rise and environmental change during the Palaeocene-Eocene Thermal Maximum. Palaeogeography Palaeoclimatology Palaeoecology 305, 185 – 200.

Handley, L., O'Halloran, A., Pearson, P.N., Hawkins, E., Nicholas, C.J., Schouten, S., McMillan, I.K., Pancost, R.D., 2012. Changes in the hydrological cycle in tropical East Africa during the Palaeocene–Eocene Thermal Maximum. Palaeogeography, Palaeoclimatology, Palaeoecology 329, 10 – 21.

Hasegawa, T., Yamamoto, S., Pratt, L.M., 2006. Data report: stable carbon isotope fluctuation of long-chain n-alkanes from Leg 208 Hole 1263A across the Paloecene/Eocene boundary. In: Kroon, D., Zachos, J.C., Richter, C. (Eds), Proc. ODP, Sci. Results, vol. 208. Ocean Drilling Program, College Sation Texas. doi:10.2973/odp.proc.sr.208.202.2006.

Hayes, J.M., 2001. Fractionation of carbon and hydrogen isotopes in biosynthetic processes. Stable Isotope Geochemistry 43, 225 – 277.

Heusser, L. E. 1988. Pollen distribution in marine-sediments on the continental margin off northern California. Marine Geology 80, 131 – 147.

Higgins, J. A. and Schrag, D. P. 2006. Beyond methane: Towards a theory for the Palaeocene-Eocene Thermal Maximum. Earth and Planetary Science Letters 245, 523 – 537.

Houghton, J. T., Ding, Y., Griggs, D. J., Noguer, M., van der Linden, P. J., Dai, X., Maskell, K., Johnson, C. A., 2001. Climate change 2001: The scientific basis. Cambridge University Press, Cambridge.

Huang, Y.S., Dupont, L., Sarnthein, M., Hayes, J.M., Eglinton, G., 2000. Mapping of C-4 plant input from North West Africa into North East Atlantic sediments. Geochimica et Cosmochimica Acta 64, 3505 – 3513.

Kaiho, K., Arinobu, T., Ishiwatari, R., Morgans, H.E.G., Okada, H., Takeda, N., Tazaki, K., Zhou, G., Kajiwara, Y., Matsumoto, R., Hirai, A., Niitsuma, N., Wada, H., 1996. Latest Palaeocene benthic foraminiferal extinction and environmental changes at Tawanui, New Zealand. Paleoceanography 11, 447 – 465.

Katz M.E., Pak D.K., Dickens G.R., Miller K.G. 1999. The source and fate of massive carbon input during the Latest Palaeocene Thermal Maximum. Science 286, 1531 – 1533.

Kennett, J.P. and Stott, L.D., 1991. Abrupt deep-sea warming, palaeoceanographic changes and benthic extinctions at the end of the Palaeocene. Nature 353, 225 – 229.

Kennicutt, M.C., Barker, C., Brooks, J.M., DeFreitas D.A., Zhu, G.H., 1987. Selected organic matter source indicators in the Orinoco, Nile and Changjiang deltas. Organic Geochemistry 11, 41 – 51

Kelly, D. C., Zachos, J. C., Bralower, T. J., Schellenberg, S. A., 2005. Enhanced terrestrial weathering/runoff and surface ocean carbonate production during the

recovery stages of the palaeocene-eocene thermal maximum. Paleoceanography 20, PA4023

Kelly, D. C., Nielsen, T. M. J., McCarren, H. K., Zachos, J. C., Rohl, U., 2010. Spatiotemporal patterns of carbonate sedimentation in the south atlantic: Implications for carbon cycling during the Palaeocene-Eocene Thermal Maximum. Palaeogeography Palaeoclimatology Palaeoecology 293, 30 – 40

Kent, D. V., Cramer, B. S., Lanci, L., Wang, D., Wright, J. D. and Van der Voo, R., 2003. A case for a comet impact trigger for the Palaeocene/Eocene Thermal Maximum and carbon isotope excursion. Earth and Planetary Science Letters 211, 13 – 26.

Koch, P.L., Zachos, J.C., Gingerich, P.D., 1992. Correlation between Isotope Records in Marine and Continental Carbon Reservoirs near the Palaeocene Eocene Boundary. Nature 358, 319 – 322.

Komar, N. and Zeebe, R.E., 2011. Oceanic calcium changes from enhanced weathering during the Palaeocene-Eocene thermal maximum: No effect on calcium-based proxies. Paleoceanography 26, doi: 10.1029/2010PA001979.

Kopp, R. E., Raub, T. D., Schumann, D., Vali, H., Smirnov, A. V. and Kirschvink, J. L., 2007. Magnetofossil spike during the Palaeocene-Eocene thermal maximum: Ferromagnetic resonance, rock magnetic, and electron microscopy evidence from Ancora, New Jersey, United States. Paleoceanography 22, PA4103.

Kraus, M.J., Riggins, S., 2007. Transient drying during the Palaeocene-Eocene Thermal Maximum (PETM): Analysis of palaeosols in the Bighorn Basin, Wyoming. Palaeogeography Palaeoclimatology Palaeoecology 245, 444 – 461.

Kraus, M.J., McInerney, F.A., Wing, S.L., Secord, R., Baczynski, A.A., Bloch, J.I., 2013. Palaeohydrologic response to continental warming during the Palaeocene-Eocene Thermal Maximum, Bighorn Basin, Wyoming. Palaeogeography Palaeoclimatology Palaeoecology 370, 196 – 208.

Kurtz, A.C., Kump, L.R., Arthur, M.A., Zachos, J.C., Paytan, A., 2003. Early Cenozoic decoupling of the global carbon and sulfur cycles. Paleoceanography 18, 1090.

Lippert, P. C. and Zachos, J. C., 2007. A biogenic origin for anomalous fine-grained magnetic material at the Palaeocene-Eocene boundary at Wilson Lake, New Jersey. Paleoceanography 22, PA4104.

Lockheart, M.J., VanBergen, P.F., Evershed, R.P., 1997. Variations in the stable carbon isotope compositions of individual lipids from the leaves of modern angiosperms: Implications for the study of higher land plant-derived sedimentary organic matter. Organic Geochemistry 26, 137 – 153.

Lopez-Martinez, N. and Pelaez-Campomanes, P., 1999. New mammals from south-central Pyrénées (Tremp Formation, Spain) and their bearing on late Palaeocene marine-continental correlations. Bulletin de la Société Géologique de France 170, 681 – 696.

Lopez-Martinez, N., Smith, R., Pelaez-Campomanes, P., Smith, T., 2006. The acme of the micromammal *Paschatherium* across the Palaeocene-Eocene boundary in continental Europe. Micropalaeontology 52, 267 – 280.

REFERENCES

Magioncalda, R., Dupuis, C., Smith, T., Steurbaut, E., Gingerich, P.D., 2004. Palaeocene-Eocene carbon isotope excursion in organic carbon and pedogenic carbonate: Direct comparison in a continental stratigraphic section. Geology 32, 553 – 556.

Manners, H.R., Grimes, S.T., Sutton, P.A., Domingo, L., Leng, M.J., Twitchett, R.T., Hart, M.B., Dunkley Jones, T., Pancost, R.D., Duller, R., Lopez-Martinez, N. 2013. Magnitude and profile of organic carbon isotope records from the Palaeocene–Eocene Thermal Maximum: evidence from northern Spain. Earth and Planetary Science Letters 377, 220 – 230.

McCarren, H.,Thomas, E., Hasegawa, T., Röhl, U., Zachos, J.C., 2008. Depth dependency of the Palaeocene-Eocene carbon isotope excursion: Paired benthic and terrestrial biomarker records (Ocean Drilling Program Leg 208, Walvis Ridge). Geochemistry Geophysics Geosystems 9, Q10008.

McDuffee, K.E., Eglinton, T.I., Sessions, A.L., Sylva, S., Wagner, T., Hayes, J.M., 2004. Rapid analysis of 13C in plant-wax n-alkanes for reconstruction of terrestrial vegetation signals from aquatic sediments. Geochemistry Geophysics Geosystems 5, Q10004.

McInerney, F.A. and Wing, S.L., 2011. The Palaeocene-Eocene Thermal Maximum: A Perturbation of Carbon Cycle, Climate, and Biosphere with Implications for the Future. Annual Review of Earth and Planetary Sciences 39, 489 – 516.

Meinzer F.C., Rundel P.W., Goldstein G., Sharifi M.R., 1992. Carbon isotope composition in relation to leaf gas exchange and environmental conditions. Oecologia 91, 305 – 311.

Meyers, P. A., 1994. Preservation of elemental and isotopic source identification of sedimentary organic-matter. Chemical Geology 114, 289 – 302

Mitchell, S.F., Ball, J.D., Crowley, S.F., Marshall, J.D., Paul, C.R.C., Veltkamp, C.J., Samir, A., 1997. Isotope data from Cretaceous chalks and foraminifera: Environmental or diagenetic signals? Geology 25, 691 – 694.

Molina, E., Angori, E., Arenillas, I., Simonetta, M., Schmitz, B., 2000. Integrated stratigraphy across the Palaeocene/Eocene boundary at Campo, Spain. Geologiska Föreningens i Stockholm Förhandlingar (GFF) 122, 106 – 107.

Molina, E., Angori, E., Arenillas, I., Brinkhuis, H., Crouch, E.M., Luterbacher, H., Monechi, S., Scmitz, B., 2003. Correlation between the Palaeocene/Eocene boundary and the Ilerdian at Campo, Spain. Revue de Micropalèontologie 46, 95 – 109.

Moore, E. A., Kurtz, A. C., 2008. Black carbon in Palaeocene-Eocene boundary sediments: A test of biomass combustion as the PETM trigger. Palaeogeography Palaeoclimatology Palaeoecology 267, 147 – 152

Murphy, B. H., Farley, K. A., Zachos, J.C., 2010. An extraterrestrial He-3-based timescale for the Palaeocene-Eocene Thermal Maximum (PETM) from Walvis Ridge, IODP Site 1266. Geochimica et Cosmochimica Acta 74, 5098 – 5108.

Norris, R.D., Rohl, U., 1999. Carbon cycling and chronology of climate warming during the Palaeocene/Eocene transition. Nature 401, 775 – 778.

REFERENCES

Nunes, F., Norris, R. D., 2006. Abrupt reversal in ocean overturning during the Palaeocene/Eocene warm period. Nature 439, 60 – 63.

Nuñez-Betelu, K., Pujalte, V., Payros, A., Baceta, J.I., Bernaola, G., 2000. The Ilerdian parastratotype at Campo (central South Pyrénéan Basin, Spain): A palynological re-study of the uppermost Palaeocene and lowermost Eocene. Geologiska Föreningens i Stockholm Förhandlingar (GFF) 122, 119 – 120.

O'Leary, M.H., 1981. Carbon Isotopes in Photosynthesis. BioScience 38, 328 – 336.

Orue-Etxebarria, X., Apellaniz, E., Baceta, J.I., Coccioni, R., Di Leo, R., Dinares-Turell, J., Galeotti, S., Monechi, S., Nuñez-Betelu, K., Pares, J.M., Payros, A., Pujalte, V., Samso, J.M., Serra-Kiel, J., Schmitz, B., Tosquella, J., 1996. Physical and biostratigraphic analysis of two prospective Palaeocene-Eocene Boundary stratotypes in the intermediate-deep water Basque Basin, western Pyrénées: the Trabakua Pass and Ermua sections. Neues Jahrbuch für Geologie und Paläontologie Abhandlungen 201, 179 – 242.

Orue-Etxebarria, X., Pujalte, V., Bernaola, G., Apellaniz, E., Baceta, J.I., Payros, A., Nuñez-Betulu, K., Serra-Kiel, J., Tosquella, J., 2001. Did the Late Palaeocene Thermal Maximum affect the evolution of larger foraminifers? Evidence from calcareous plankton of the Campo Section (Pyrénées, Spain). Marine Micropaleontology 41, 45 – 71.

Pagani, M., Pedentchouk, N., Huber, M., Sluijs, A., Schouten, S., Brinkhuis, H., Sinninghe Damste, J., Dickens, G.R., Expedition 302 Scientists, 2006. Arctic hydrology during global warming at the Palaeocene/Eocene Thermal Maximum. Nature 442, 671 – 675.

Panchuk, K., Ridgwell, A., Kump, L.R., 2008. Sedimentary response to Palaeocene-Eocene Thermal Maximum carbon release: A model-data comparison. Geology 36, 315 – 318.

Pancost, R.D., Pagani, M. 2006. Controls on the Carbon Isotopic Compositions of Lipids in Marine Environments *in* Volkman, J.K., 2006. Marine Organic Matter: Biomarkers, Isotopes, and DNA. The Handbook of Environmental Chemistry, Volume 2N, 209 – 249.

Pearson, P.N., van Dongen, B.E., Nicholas, C.J., Pancost, R.D., Schouten, S., Singano, J.M., Wade, B.S., 2007. Stable warm tropical climate through the Eocene epoch. Geology 35, 211 – 214.

Peters, K.E., Walters, C.C., Moldowan, J.M., 2005. The Biomarker Guide. Cambridge University Press, Cambridge.

Poole, I., van Bergen, P.F., Kool, J., Schouten, S., Cantrill, D.J., 2004. Molecular isotopic heterogeneity of fossil organic matter: implications for δ^{13}C-biomass and δ^{13}C-palaeoatmosphere proxies. Organic Geochemistry 35, 1261 – 1274.

Pujalte, V., Baceta, J.I., Payros, A., Orue-Etxebarria, X., Schmitz, B. 2000a. Upper Palaeocene-lower Eocene strata of the western Pyrénées, Spain: A shelf-to-basin correlation. Geologiska Föreningens i Stockholm Förhandlingar (GFF) 122, 129 – 130.

Pujalte, V., Robles, S., Orue-Etxebarria, X., Baceta, J.I., Payros, A., Larruzea, I.F. 2000b. Uppermost Cretaceous-middle Eocene strata of the Basque-Cantabrian region

and western Pyrénées: A sequence stratigraphic perspective. Revista de la Sociedad Geológica de España 13, 191 – 211.

Pujalte, V., Orue-Etxebarria, X., Schmitz, B., Tosquella, J., Baceta, J. I., Payros, A., Bernaola, G., Caballero, F., Apellaniz, E. Basal Ilerdian (earliest Eocene) turnover of larger foraminifera: Age constraints based on calcareous plankton and d13C isotopic profiles from new southern Pyrénéann sections (Spain) *in* Wing, S.L., Gingerich, P.D., Schmitz, B., Thomas, E., eds., Causes and consequences of Globally Warm Climates in the Early Palaeogene. Boulder, Colorado, Geological Society of America Special Paper 369, 205 – 221.

Pujalte, V., Schmitz, B., Baceta, J. I., Orue-Etxebarria, X., Bernaola, G., Dinares-Turrell, J., Payros, A., Apellaniz, E., Caballero, F. 2009a. Correlation of the Thanetian-Ilerdian turnover of larger foraminifera and the Palaeocene-Eocene Thermal Maximum: confirming evidence from the Campo area (Pyrénées, Spain). Geologica Acta, 161 – 175.

Pujalte, V., Baceta, J. I., Schmitz, B., Orue-Etxebarria, X., Payros, A., Bernaola, G., Apellaniz, E., Caballero, F., Robador, A., Serra-Kiel, J., Tosquella, J. 2009b. Redefinition of the Ilerdian Stage (early Eocene). Geologica Acta 7, 177 – 194.

Pujalte, V., Scmitz, B., Baceta, J.I., 2014. Sea-level changes across the Paleocene-Eocene interval in the Spanish Pyrenees, and their possible relationship with North Atlantic magmatism. Palaeogeography, Palaeoclimatology, Palaeoecology. DOI 10.1016/j.palaeo.2013.10.016.

Rohl, U, Norris, R.D., Ogg J.G., 2003. Cyclostratigraphy of upper Palaeocene and lower Eocene sediments at Blake Nose Site 1051 (western North Atlantic). Geological Society of America, Special Papers 369, 567 – 88.

Rohl, U., Westerhold, T., Bralower, T.J., Zachos, J.C., 2007. On the duration of the Palaeocene-Eocene Thermal Maximum (PETM). Geochemistry Geophysics Geosystems 8. Q12002.

Rohling, E. J., Sluijs, A., Dijkstra, H. A., Kohler, P., de Wal, R. S. W. V., von der Heydt, A. S., Beerling, D. J., Berger, A., Bijl, P. K., Crucifix, M., DeConto, R., Drijfhout, S. S., Fedorov, A., Foster, G. L., Ganopolski, A., Hansen, J., Honisch, B., Hooghiemstra, H., Huber, M., Huybers, P., Knutti, R., Lea, D. W., Lourens, L. J., Lunt, D., Masson-Demotte, V., Medina-Elizalde, M., Otto-Bliesner, B., Pagani, M., Palike, H., Renssen, H., Royer, D. L., Siddall, M., Valdes, P., Zachos, J. C., Zeebe, R. E., Members, P. P., 2012. Making sense of palaeoclimate sensitivity. Nature 491, 683 – 691

Rosales, I., Quesada, S., Robles, S., 2001. Primary and diagenetic isotopic signals in fossils and hemipelagic carbonates: the Lower Jurassic of northern Spain. Sedimentology 48, 1149 – 1169.

Sachse, D., Radke, J., Gleixner, G., 2006. δD values of individual *n*-alkanes from terrestrial plants along a climatic gradient—implications for the sedimentary biomarker record. Organic Geochemistry 37, 469 – 483.

Sangiorgi, F., van Soelen, E.E., Spofforth, D.J.A., Pälike, H., Stickley, C.E., St. John, K., Koç, N., Schouten, S., Sinninghe Damsté, J.S., Brinkhuis, H., 2008a. Middle Eocene cyclicity in the Central Arctic Ocean sediment record: orbital forcing and palaeoenvironmental response. Paleoceanography 23, PA1S08

REFERENCES

Sangiorgi, F., Brumsack, H.J., Willard, D.A., Schouten, S., Stickley, C.E., O'Regan, M., Reichart, G.J., Sinninghe Damsté, J.S., Brinkhuis, H., 2008b. A ~25 Million years gap in the central Arctic record at the Greenhouse–Icehouse transition: looking for clues. Paleoceanography 23, PA1S04.

Scalan R.S., Smith, J.E., 1970. An improved measure of the odd-even predominance in the normal alkanes of sediment extracts and petroleum. Geochimica et Cosmochimica Acta 34, 611 – 620.

Schmitz, B., Asaro, F., Molina, E., Monechi, S., von Salis, K., Speijer, R.P., 1997. High-resolution iridium, $\delta^{13}C$, $\delta^{18}O$, foraminifera and nannofossil profiles across the latest Palaeocene benthic extinction event at Zumaya, Spain. Palaeogeography, Palaeoclimatology, Palaeoecology 133, 49 – 68.

Schmitz, B., Pujalte, V., Núñez-Betelu, K., 2001. Climate and sea-level perturbations during the Incipient Eocene Thermal Maximum: evidence from siliciclastic units in the Basque Basin (Ermua, Zumaia and Trabakua Pass), northern Spain. Palaeogeography, Palaeoclimatology, Palaeoecology 165, 299 – 320.

Schmitz, B., Pujalte, V., 2003. Sea-level, humidity, and land-erosion records across the initial Eocene thermal maximum from a continental-marine transect in northern Spain. Geology 31, 689 – 692.

Schmitz, B., Pujalte, V., 2007. Abrupt increase in seasonal extreme precipitation at the Palaeocene-Eocene boundary. Geology 35, 215 – 218.

Schmitz, B., Pujalte, V., Molina, E., Monechi, S., Orue-Etxebarria, X., Speijer, R. P., Alegret, L., Apellaniz, E., Arenillas, I., Aubry, M.-P., Baceta, J.-I., Berggren, W. A., Bernaola, G., Caballero, F., Clemmensen, A., Dinarès-Turell, J., Dupuis, C., Heilmann-Clausen, C., Orús, A. H., Knox, R., Martín-Rubio, M., Ortiz, S.,Payros, A., Petrizzo, M. R., von Salis, K., Sprong, J., Steurbaut, E., Thomsen, E., 2011. The global Stratotype Sections and Points for the bases of the Selandian (Middle Palaeocene) and Thanetian (Upper Palaeocene Palaeocene) stages at Zumaia, Spain. Episodes, 34 (4), 220 – 243.

Schouten, S., Woltering, M., Rijpstra, W.I.C., Sluijs, A., Brinkhuis, H., and Damsté, J.S.S., 2007. The Palaeocene-Eocene carbon isotope excursion in higher plant organic matter: Differential fractionation of angiosperms and conifers in the Arctic: Earth and Planetary Science Letters 258, 581 – 592.

Schouten, S., Eldrett, J.S., Greenwood, D., Harding, I., Baas, M., Sinninghe Damsté, J.S., 2008. Onset of long term cooling of Greenland near the Eocene–Oligocene boundary as revealed by branched tetraether lipids. Geology 36, 147 – 150.

Schouten, S., Hopmans, E.C., Sinninghe Damsté, J.S., 2013. The organic geochemistry of glycerol dialkyl glycerol tetraether lipids: a review. Organic Geochemistry 54, 19 – 61.

Secord, R., Gingerich, P.D., Lohmann, K.C., MacLeod, K.G., 2010. Continental warming preceding the Palaeocene-Eocene thermal maximum. Nature 467, 955 – 958.

Sluijs, A., Schouten, S., Pagani, M., Woltering, M., Brinkhuis, H., Sinninghe Damsté, J.S., Dickens, G.R., Huber, M., Reichart, G.-J., Stein, R., Matthiessen, J., Lourens, L.J., Pedentchouk, N., Backman, J., Moran, K., The Expedition 302 Scientists, *et al.*,

2006. Subtropical Arctic Ocean temperatures during the Palaeocene–Eocene Thermal Maximum. Nature 441, 610 – 613.

Sluijs, A., Brinkhuis, H., Schouten, S., Bohaty, S.M., John, C.M., Zachos, J.C., Reichart, G-J., Sinninghe Damste, J.S., Crouch, E.M., Dickens, G.R., 2007. Environmental precursors to rapid light carbon injection at the Palaeocene/Eocene boundary. Nature 450, 1218 – 1221.

Sluijs, A., Röhl, U., Schouten, S., Brumsack, H., Sangiorgi, F., Sinninghe Damsté, J.S., Brinkhuis, H., 2008a. Arctic Late Palaeocene–Early Eocene palaeoenvironments with special emphasis on the Palaeocene–Eocene Thermal Maximum (Lomonosov Ridge, IODP Expedition 302). Paleoceanography 23, PA1S11.

Sluijs, A., Brinkhuis, H., Crouch, E.M., John, C.M., Handley, L., Munsterman, D., Bohaty, S.M., Zachos, J.C., Reichart, G.-J., Schouten, S., Pancost, R.D., Sinninghe Damsté, J.S., Welters, N.L.D., Lotter, A.F., Dickens, G.R., 2008b. Eustatic variations during the Palaeocene–Eocene greenhouse world. Paleoceanography 23, PA4216.

Sluijs, A., Brinkhuis, H., 2009. A dynamic climate and ecosystem state during the Palaeocene-Eocene Thermal Maximum: Inferences from dinoflagellate cyst assemblages on the New Jersey shelf. Biogeosciences 6, 1755 – 1781

Smith, F.A., Freeman, K.H. 2006. Influence of physiology and climate on δD of leaf wax *n*-alkanes from C3 and C4 grasses. Geochimica et Cosmochimica Acta 70, 1172 – 1187.

Smith, T., Rose, K. D. and Gingerich, P. D., 2006. Rapid Asia-Europe-North America geographic dispersal of earliest Eocene primate Teilhardina during the Palaeocene-Eocene Thermal Maximum. Proceedings of the National Academy of Sciences 103, 11223 – 11227.

Smith, F.A., Wing, S.L., Freeman, K.H., 2007. Magnitude of the carbon isotope excursion at the Palaeocene-Eocene thermal maximum: The role of plant community change. Earth and Planetary Science Letters 262, 50 – 65.

Smittenberg, R.H., Hopmans, E.C., Schouten, S., Hayes, J.M., Eglinton, T.I., Sinninghe Damste, J.S. 2004. Compound-specific radiocarbon dating of the varved Holocene sedimentary record of Saanich Inlet, Canada. Paleoceanography 19, PA2012.

Stassen, P., Thomas, E., Speijer, R.P., 2012. Integrated stratigraphy of the Palaeocene-Eocene thermal maximum in the New Jersey Coastal Plain: Toward understanding the effects of global warming in a shelf environment. Paleoceanography 27, PA4210.

Stoll, H.M., Schrag, D.P., 2000. High-resolution stable isotope records from the Upper Cretaceous rocks of Italy and Spain: Glacial episodes in a greenhouse planet? Geological Society of America Bulletin 112, 308 – 319.

Storme, J. Y., Devleeschouwer, X., Schnyder, J., Cambier, G., Baceta, J.I., Pujalte, V., Di Matteo, A., Iacumin, P., Yans, J., 2012. The Palaeocene/Eocene boundary section at Zumaia (Basque-Cantabric Basin) revisited: new insights from high-resolution magnetic susceptibility and carbon isotope chemostratigraphy on organic matter (δ^{13}Corg). Terra Nova 24, 310 – 317.

REFERENCES

Svensen, H., Planke, S., Malthe-Sorenssen, A., Jamtveit, B., Myklebust, R., Rasmussen Eidem, T., Rey, S.S., 2004. Release of methane from a volcanic basin as a mechanism for initial Eocene global warming. Nature 429, 542 – 545.

Svensen, H., Planke, S., Chevallier, L., Malthe-Sørenssen, A., Corfu, F. and Jamtveit, B., 2007. Hydrothermal venting of greenhouse gases triggering Early Jurassic global warming. Earth and Planetary Science Letters 256, 554 – 566.

Svensen, H., Planke, S., Corfu, F., 2010. Zircon dating ties NE Atlantic sill emplacement to initial Eocene global warming. Journal of the Geological Society, London 167, 433 – 436.

Thomas, E., 1998, The biogeography of the late Palaeocene benthic foraminiferal extintion, in Late Palaeocene–Early Eocene Biotic and Climatic Events *in* the Marine and Terrestrial Records, edited by M. P. Aubry *et al*., 214–243, Columbia Univ. Press, New York.

Thomas, D.J., Zachos, J.C., Bralower, T.J., Thomas, E., Bohaty, S., 2002. Warming the fuel for the fire: Evidence for the thermal dissociation of methane hydrate during the Palaeocene-Eocene Thermal Maximum. Geology 30, 1067 – 1070.

Thomas, D. J., Bralower, T. J. and Jones, C. E., 2003. Neodymium isotopic reconstruction of late Palaeocene-early Eocene thermohaline circulation. Earth and Planetary Science Letters 209, 309 – 322.

Tipple, B.J., Pagani, M., Krishnan, S., Dirghangi, S.S., Galeotti, S., Agnini, C., Giusberti, L., Rio, D., 2011. Coupled high-resolution marine and terrestrial records of carbon and hydrologic cycles variations during the Palaeocene-Eocene Thermal Maximum (PETM). Earth and Planetary Science Letters 311, 82 – 92.

Torfstein, A., Winckler, G., Tripati, A., 2010. Productivity feedback did not terminate the Palaeocene-Eocene Thermal Maximum (PETM). Climates of the Past 6, 265 – 272

Traverse, A. 1988. Palaeopalynology: Second edition Springer 2007.

Tripati, A. K. and Elderfield, H., 2004. Abrupt hydrographic changes in the equatorial Pacific and subtropical Atlantic from foraminiferal Mg/Ca indicate greenhouse origin for the thermal maximum at the Palaeocene-Eocene Boundary. Geochemistry Geophysics, Geosystems 5, Q02006.

Veizer, J., 1992. Depositional and diagenetic history of limestones: Stable and radiogenic isotopes. Isotopic signatures and sedimentary records. Lecture Notes in Earth Sciences 43, 13 – 48.

Ward, J.K., Harris, J. M., Cerling, T. E., Wiedenhoeft, A., Lott, M. J., Dearing, M. D., Coltrain, J. B. and Ehleringer, J. R., 2005. Carbon starvation in glacial trees recovered from the La Brea tar pits, southern California. Proceedings of the National Academy of Sciences 102, 690 – 694.

Weijers, J.W.H., Schefuss, E., Schouten, S., Sinninghe Damsté, J.S., 2007a. Coupled thermal and hydrological evolution of tropical Africa over the last deglaciation. Science 315, 1701 – 1704.

REFERENCES

Weijers, J.W.H., Schouten, S., Sluijs, A., Brinkhuis, H., Sinninghe Damsté, J.S., 2007b. Warm Arctic continents during the Palaeocene–Eocene Thermal Maximum. Earth and Planetary Science Letters 261, 230 – 238.

Westerhold, T., Rohl, U., McCarren, H. K., Zachos, J. C., 2009. Latest on the absolute age of the Palaeocene-Eocene Thermal Maximum (PETM): New insights from exact stratigraphic position of key ash layers+19 and-17. Earth and Planetary Science Letters 287, 412 – 419

Wing, S.L., Harrington, G.J., Smith, F.A., Bloch, J.I., Boyer, D.M., Freeman, K.H., 2005. Transient Floral Change and Rapid Global Warming at the Palaeocene-Eocene Boundary. Science 310, 993 – 996.

Wynn, J.G., Bird, M.I., Wong, V.N.L., 2005. Rayleigh distillation and the depth profile of $^{13}C/^{12}C$ ratios of soil organic carbon from soils of disparate texture in Iron Range National Park, Far North Queensland, Australia. Geochimica et Cosmochimica Acta 69, 1961 – 1973.

Wynn, J. G. 2007. Carbon isotope fractionation during decomposition of organic matter in soils and palaeosols: Implications for palaeoecological interpretations of palaeosols. Palaeogeography Palaeoclimatology Palaeoecology 251, 437 – 448.

Zachos, J.C., Stott, L.D., Lohmann, K.C., 1994. Evolution of early Cenozoic marine temperatures. Paleoceanography 9, 353–387.

Zachos, J.C., Pagani, M., Sloan, L., Thomas, E., Billups K., 2001. Trends, Rhythms and Aberrations in Global Climate 65 Ma to Present. Science 292, 686 – 693.

Zachos, J. C., Wara, M. W., Bohaty, S., Delaney, M. L., Petrizzo, M. R., Brill, A., Bralower, T. J., Premoli-Silva, I., 2003. A transient rise in tropical sea surface temperature during the Palaeocene-Eocene Thermal Maximum. Science 302, 1551 – 1554

Zachos, J.C., Rohl, U., Schellenberg, S.A., Sluijs, A., Hodell, D.A., Kelly, D.C., Thomas, E., Nicolo, M., Raffi, I., Lourens, L.J., McCarren, H., Kroon, D., 2005. Rapid Acidification of the Ocean During the Palaeocene-Eocene Thermal Maximum. Science 308, 1611 – 1615.

Zachos, J. C., Schouten, S., Bohaty, S., Quattlebaum, T., Sluijs, A., Brinkhuis, H., Gibbs, S. J., Bralower, T. J., 2006. Extreme warming of mid-latitude coastal ocean during the Palaeocene-Eocene Thermal Maximum: Inferences from TEX_{86} and isotope data. Geology 34, 737 – 740

Zachos, J.C., Bohaty, S.M., John, C.M., McCarren, H., Kelly, D.C., Nielsen, T., 2007. The Palaeocene-Eocene carbon isotope excursion: constraints from individual shell planktonic foraminifer records. Philosophical Transactions of the Royal Society A: Mathematical, Physical and Engineering Sciences 365, 1829 – 1842.

Zachos, J.C., Dickens, G.R., Zeebe, R.E., 2008. An early Cenozoic perspective on greenhouse warming and carbon-cycle dynamics. Nature 451, 279 – 283.

Zeebe, R.E., Zachos, J.C., Dickens, G.R., 2009. Carbon dioxide forcing alone insufficient to explain Palaeocene-Eocene Thermal Maximum warming. Nature Geoscience 2, 576 – 580.

Zeebe, R. E., 2011. Where are you heading Earth? Nature Geoscience 4, 416 – 417.

8 PUBLICATIONS

8.1 PEER REVIEWED PUBLICATIONS

Earth and Planetary Science Letters 376 (2013) 220–230

Contents lists available at SciVerse ScienceDirect

Earth and Planetary Science Letters

www.elsevier.com/locate/epsl

Discussion

Magnitude and profile of organic carbon isotope records from the Paleocene–Eocene Thermal Maximum: Evidence from northern Spain

Hayley R. Manners [a,*], Stephen T. Grimes [a], Paul A. Sutton [a], Laura Domingo [b], Melanie J. Leng [c,d], Richard J. Twitchett [a], Malcolm B. Hart [a], Tom Dunkley Jones [e], Richard D. Pancost [f], Robert Duller [g], Nieves Lopez-Martinez [1]

[a] School of Geography, Earth & Environmental Sciences, Plymouth University, Drake Circus, Plymouth, Devon PL4 8AA, UK
[b] Earth & Planetary Sciences Department, University of California, Santa Cruz, CA 95064, USA
[c] Department of Geology, University of Leicester, Leicester LE1 7RH, UK
[d] NERC Isotope Geosciences Laboratory, British Geological Survey, Nottingham NG12 5GG, UK
[e] School of Geography, Earth and Environmental Sciences, University of Birmingham, Edgbaston, Birmingham B15 2TT, UK
[f] Organic Geochemistry Unit, The Cabot Institute, School of Chemistry, University of Bristol, Bristol BS8 1TS, UK
[g] Department of Earth, Ocean & Ecological Sciences, 4 Brownlow Street, Jane Herdman Building, University of Liverpool, Liverpool, L69 3GP, UK

ARTICLE INFO

Article history:
Received 5 April 2012
Received in revised form 6 June 2013
Accepted 11 June 2013
Available online 5 July 2013
Editor: G. Henderson

Keywords:
carbon isotopes
Paleocene–Eocene thermal maximum
CIE
Northern Spain

ABSTRACT

The Paleocene–Eocene Thermal Maximum (PETM), a hyperthermal event that occurred ca. 56 Ma, has been attributed to the release of substantial amounts of carbon, affecting the atmosphere, biosphere and the oceans. Current issues with respect to our understanding of the PETM include the amount of carbon released, the duration of carbon release, and the mechanism(s) of release, all of which are related to the magnitude and profile of the associated Carbon Isotope Excursion (CIE). High-resolution organic carbon profiles ($\delta^{13}C$) of six PETM sections in northern Spain are presented that span a transect from continental to marine environments. These data represent the highest-resolution isotope records for these sections and allow a comparison of the magnitude of the excursion, the shape of the vertical $\delta^{13}C$ profile during the PETM episode, and the relative timing of the onset of the excursion across a linked sediment routing system. Previous studies using carbonate $\delta^{13}C$ data have suggested that the continental Claret Conglomerate, found in this region, formed synchronously with a marine clay-rich siliciclastic unit, with these key lithological changes interpreted to be driven by increased seasonal rainfall-runoff in the warmer PETM climate. Our data suggest that deposition of these units did not immediately follow the CIE onset, indicating that there may be a temporal lag between the onset of the PETM warming and the response of the depositional systems in northern Spain. No systematic variation in the magnitude of the CIE between different depositional environments was found; the marine CIE magnitudes are at the higher end of those previously described (3.7 ± 1.4‰), and the continental ranges are lower (3.1 ± 1.3‰).

1. Introduction

The Paleocene–Eocene Thermal Maximum (PETM; ca. 56 Ma) is the most dramatic and rapid global warming event of the Cenozoic Era, with global surface temperatures estimated to have risen by 5–9 °C in less than 10,000 years (Dickens et al., 1995; Thomas et al., 2002; Wing et al., 2005; Zachos et al., 2005; Rohl et al., 2007; Sluijs et al., 2007; Zeebe et al., 2009; Dunkley Jones et al., 2010). Geological and geochemical evidence indicate that this warming was driven by a major perturbation to the global carbon cycle, with the release of several thousand gigatons of isotopically light carbon as methane or carbon dioxide to the ocean–atmosphere system (Dickens et al. 1995, 1997; Dickens, 2011; Panchuk et al., 2008; Zeebe et al., 2009; Cui et al., 2011).

One of the major unresolved questions surrounding the PETM is the precise magnitude of the carbon release. Current estimates range from 1500 Gt to 12,000 Gt of carbon (Dickens et al., 1995; Dickens, 2003, 2011; Panchuk et al., 2008; Zeebe et al., 2009; Cui et al., 2011), depending on the carbon source and its isotopic composition. A key constraint on estimates of the PETM carbon cycle perturbation is the magnitude of the accompanying negative Carbon Isotope Excursion (CIE), which, at the resolution of current data, is recorded simultaneously in environments as disparate as continental soils and deep ocean sediments (Koch et al., 1992; Bowen et al., 2004; Zachos et al., 2005). There is, however, a discrepancy in the magnitude of the recorded negative CIE between continental and marine sediments,

* Corresponding author.
E-mail address: hayley.manners@plymouth.ac.uk (H.R. Manners).
[1] Deceased.

0012-821X/$ – see front matter
http://dx.doi.org/10.1016/j.epsl.2013.06.016

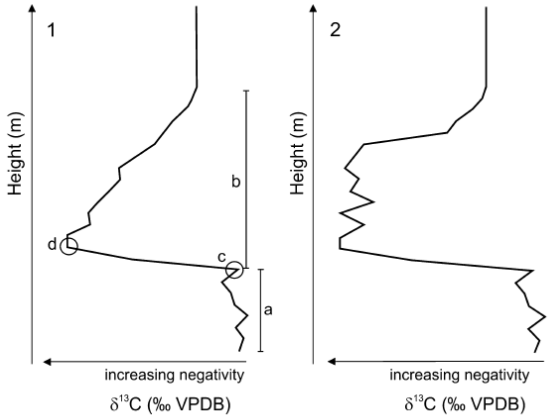

Fig. 1. Exemplar CIE profile shapes illustrating: (1) the triangular profile (Zachos et al., 2008), and (2) the box profile (Bowen and Zachos, 2010). The data used to generate the profiles is for illustrative purposes only. Methods for calculating CIE magnitude are shown on the triangular profile (1). Previous studies have subtracted the pre-CIE average (a) from the CIE average (b). This study subtracts the most positive $\delta^{13}C_{TOC}$ value immediately prior to the negative $\delta^{13}C_{TOC}$ shift (c), from the most negative $\delta^{13}C_{TOC}$ value at the base of the CIE (d).

with the continental CIE consistently recorded as around 2 to 4‰ greater than the marine CIE shift (continental CIE ~3–7‰; marine CIE ~2.5–5.5‰; Pagani et al., 2006; Smith et al., 2007; Zachos et al., 2007; Handley et al. 2008; Bowen and Zachos, 2010; McInerney and Wing, 2011). Carbonate dissolution and poor preservation may have dampened the CIE recorded in many marine sections, especially in the deep sea (Zachos et al., 2005; McCarren et al., 2008), although the most complete marine records do not record a CIE much in excess of 4‰ (Zachos et al., 2007). In contrast, amplification of the CIE in the continental realm has been attributed to increased moisture availability (Beerling, 1996; Bowen et al., 2004; Ward et al., 2005) allowing continental plants to increase $\delta^{13}C$ discrimination (Bowen et al., 2004); temperature effects on carbon isotope fractionation (Edwards et al., 2000); and possible changes in soil productivity and organic matter turnover rates (Bowen et al., 2004). An additional problem is that many previous studies comparing continental and marine sections are at a low resolution, an issue that is exacerbated when records derive from sections from different basins (Koch et al., 1992; Schmitz and Pujalte, 2003; Bowen et al., 2004; Wing et al., 2005; Pagani et al., 2006; Handley et al., 2011; Bowen and Zachos, 2010; Tipple et al., 2011). Another unresolved issue is the variability in the PETM isotopic profiles. The overall structure of (presumably) complete profiles is defined by three phases: initiation, alternate semi-stable state, and recovery (Bowen et al., 2006). However, not all sections exhibit the semi-stable state.

Differences among sites are typically interpreted with respect to how rapidly carbon was added to, and removed from, the ocean–atmosphere reservoir. For example, from studies of carbonate $\delta^{13}C$ values, Zachos et al. (2008) showed that at several South Atlantic ODP sites a rapid PETM onset occurred, followed by a gradual recovery that they attributed to silicate weathering feedback (Zachos et al. 2005, 2008). This is considered the classical model, and is exemplified by a triangular-shaped CIE profile (Fig. 1.1). In contrast, well-dated marine bulk-carbonate and terrestrial soil-nodule carbonate $\delta^{13}C$ records from ODP Site 690 and Polecat Bench respectively imply both a rapid release and drawdown of carbon at the onset and termination of the PETM (Bowen and Zachos, 2010), with an expanded alternate semi-stable state, leading to a box-shaped CIE profile (Fig. 1.2). Bowen and Zachos (2010) considered that this rapid recovery was inconsistent with the expected ~100 kyr response time of the silicate weathering feedback, and instead explained it by the rapid re-growth of biospheric carbon stocks that may have been released at the onset of the event. Furthermore, a semi-stable state may suggest continued release of ^{13}C-depleted carbon during the event; an idea also proposed by Zeebe et al. (2009), who hypothesised that to maintain the negative body of the CIE, pulsed releases of carbon throughout the CIE may be necessary. Currently there is no consensus on whether one profile is a better reflection of the CIE associated with the PETM, or whether other factors, such as sedimentation rates and/or decompaction, may be biasing all recorded shapes (McInerney and Wing, 2011).

This study presents a series of high-resolution $\delta^{13}C$ profiles from organic matter in six well-known PETM sections in northern Spain, spanning continental to marine depositional environments. This provides an opportunity to track changes in the recorded CIE across various palaeoenvironments. Previous isotope studies in northern Spain have presented either low-resolution soil nodule carbonate or bulk marine carbonate $\delta^{13}C$ excursions from the same sections (Schmitz and Pujalte 2003, 2007), or organic carbon $\delta^{13}C$ excursions from individual sections (Domingo et al., 2009; Storme et al., 2012). The CIE magnitudes and profiles across this continental to marine transect are compared, providing new insights into the depositional control on the recorded CIE and the sedimentological response to the PETM warming episode.

2. Sample locations and methodology

2.1. Geological setting

The Tremp–Graus and Basque–Cantabrian basins of northern Spain are unique in providing a series of expanded and accessible PETM sedimentary sections that span the continental to marine realms within the same depositional system (Schmitz et al., 2001). The PETM has already been located by carbonate $\delta^{13}C$ stratigraphy in most of the sections (Schmitz et al. 1997, 2001; Schmitz and Pujalte 2003, 2007), which are, from east to west (Fig. 2), the continental sections of Claret (N 042°09′14.1″, E 000°51′58.4″), Tendrui (N 042°10′07.2″, E 000°51′25.3″), and Esplugafreda (N 042°14′47.3″, E 000°45′22.7″), the transitional mixed shallow marine and continental deposits of Campo (N 042°23′24.5″, E 000°23′50.2″), and the marine sections of Ermua (N 043°10′44.1″, W 002°29′49.1″) and Zumaia (N 043°18′4.5″, W 002°15′31.2″).

The lithological logs produced in this study (Fig. 3) are similar to those published previously for all sections (Schmitz et al. 1997, 2001; Schmitz and Pujalte 2003, 2007; Domingo et al., 2009). The continental sections have been correlated predominantly using fossil mammal sites comprising, for example, dental remains of the condylarth genus *Paschatherium* found at Claret and Tendrui. These are dated as late Paleocene and occurring before the mammalian dispersal event (MDE), placing the sections close to the Paleocene–Eocene boundary (Lopez-Martinez and Pelaez-Campomanes, 1999; Lopez-Martinez et al., 2006; Domingo et al., 2009). In addition to fossil sites, chemostratigraphic features such as the CIE, and lithostratigraphic marker horizons such as the Claret Conglomerate and *Alveolina* Beds have been used in correlation (Molina et al., 2000; Pujalte et al., 2000; Schmitz and Pujalte, 2007). The *Alveolina* Beds are a prominent marker bed in the Ilerdian representing a shallow marine environment associated with a basin-wide transgression in the early Eocene (Molina et al., 2000).

The marine sections of Zumaia (bathyal) and Ermua (base-of-slope-apron; Schmitz and Pujalte, 2003) and the mixed marine/continental section at Campo, have been correlated to each other using biostratigraphic (Molina et al., 2000; Nuñez-Betelu et al., 2000; Orue-Etxebarria et al., 2001), chemostratigraphic

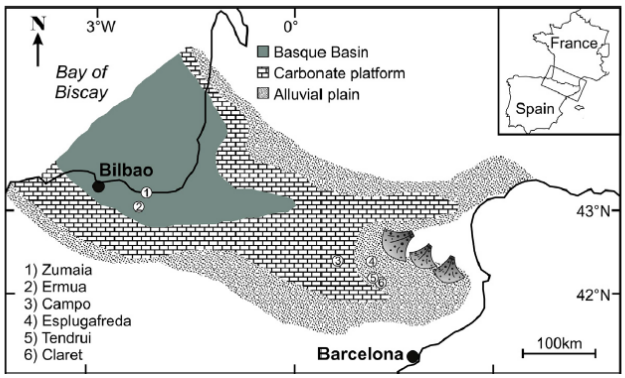

Fig. 2. Palaeogeographic reconstruction and location map (redrawn from Schmitz and Pujalte, 2003). Numbers on map represent studied sections, which are: (1) Zumaia, (2) Ermua, (3) Campo, (4) Esplugafreda, (5) Tendrui and (6) Claret.

(Schmitz and Pujalte, 2003) and lithostratigraphic (Pujalte et al., 2000; Schmitz and Pujalte, 2007) methods. Pujalte et al. (2000) constructed a shelf to basin tentative correlation in the Pyrenees using four main lithological tie points, whilst Molina et al. (2000) undertook a detailed bio- and chemostratigraphic study at Campo to identify the PETM. Orue-Etxebarria et al. (2001) used these data and data from a palynological study by Nuñez-Betelu et al. (2000) to correlate Campo to the Benthic Extinction Event (BEE), recorded at Zumaia and Ermua, respectively (Schmitz et al., 1997; Schmitz and Pujalte, 2007). Further correlative studies have also been undertaken in this region linking basin, slope and mixed marine PETM settings (Orue-Etxebarria and et al., 1996; Baceta et al., 2000; Molina et al., 2003).

Correlation between the continental and marine sections in northern Spain has been achieved by Schmitz and Pujalte (2003) using a combination of all the bio-, litho- and chemostratigraphic techniques previously discussed. The Claret Conglomerate is a continental feature propagating westwards toward the marine sections, whilst the *Alveolina* Beds are a marine unit that transgresses eastwards, both of which can be seen at the transitional section of Campo (Molina et al. 2000, 2003; Schmitz and Pujalte, 2007). Campo is, therefore, a fundamental section in this correlation, owing to its marine sediments immediately above and below the PETM, and the transition to continental deposition during the PETM (Molina et al., 2000; Orue-Etxebarria et al., 2001; Schmitz and Pujalte, 2003; Pujalte et al., 2009). Carbonate $\delta^{13}C$ profiles have been used to further confirm correlation between sections (Schmitz et al., 2001; Schmitz and Pujalte 2003, 2007).

2.2. Methods

All sections have been logged and 285 samples collected and analysed for organic carbon content and $\delta^{13}C$ (Table 1). Results for Claret and Tendrui were added to the previously published data of Domingo et al. (2009) to provide a total of 98 samples at Claret and 94 samples at Tendrui. Sampling frequency varied according to the length and exposure of each section, with shorter sections (<25 m) ideally being sampled at 30 cm resolution, whilst longer sections (>25 m) were sampled at 50 cm intervals where possible.

Whole rock samples were oven dried (30 °C, 24 hours), crushed using a granite pestle and mortar, and de-carbonated following the methodology of Domingo et al. (2009) using excess hydrochloric acid (10% v/v) until any visible sign of reaction had ceased. This was followed by repeated washing with deionised water until a neutral solution was obtained, then oven drying (30 °C, 24 hours). Stable isotope analyses were conducted at the NERC Isotope Geosciences Laboratory. Total organic carbon (TOC) content was measured using a Carlo Erba 1500 elemental analyser with acetanilide used as the calibration standard. Replicate analyses indicated a precision of ±0.1% in well-mixed samples (1 Standard Deviation, SD). For $\delta^{13}C$ analysis a Carlo Erba 1500 EA online to a VG TripleTrap was used. This setup also included a secondary cryogenic trap in the mass spectrometer for samples with very low carbon content. The mean standard deviation on replicate $\delta^{13}C$ analyses of laboratory standard broccoli (BROC1) and soil (SOILB) was between 0.1 and 0.4‰. The carbon isotope composition of the TOC within the samples is referred to as $\delta^{13}C_{TOC}$.

Two different methods are commonly used for calculating CIE magnitude. For example, in some instances, the average of $\delta^{13}C_{TOC}$ values preceding the CIE are taken and subtracted from the average of $\delta^{13}C_{TOC}$ values during the CIE (Domingo et al., 2009; Fig. 1). This averaging approach inevitably leads to some smoothing of the peak CIE magnitude at the very start of the PETM, especially if there was a relatively rapid transient negative spike at the onset. Instead, here we use a "maximum CIE" approach that identifies the most positive $\delta^{13}C_{TOC}$ value immediately prior to the negative $\delta^{13}C_{TOC}$ shift (Fig. 1, point c), and the most negative $\delta^{13}C_{TOC}$ value at the base of the PETM (Fig. 1, point d; Table 1). This maximum CIE approach is appropriate for a comparison between sections which have varying degrees of noise superimposed on the CIE, most likely due to the inclusion and reworking of variable amounts of older, non-CIE related organic material. It assumes that this reworking most likely smooths and dampens the actual magnitude of the CIE.

Regression analysis was used to assess whether there was a significant logarithmic correlation between $\delta^{13}C_{TOC}$ values and % weight of organic carbon (wt%TOC; Fig. 4) for the continental sections of Claret, Tendrui, and Esplugafreda. If correlation was not significant (95% confidence interval; low r^2), we have tentatively assumed that $\delta^{13}C_{TOC}$ values are independent of lithological change. For all sections, wt%TOC remained low (generally < 1% TOC); independence of wt%TOC and lithological change was assessed using the student's *t*-test at the 95% confidence interval (Tables A1 to A6 of the supplementary material). Where $p < 0.05$, a significant difference between wt%TOC and different lithologies may be observed, as discussed in our results, otherwise wt%TOC was considered independent of lithological change. Comparison with carbonate records (where present) was also used to assess similarity, increasing confidence in the $\delta^{13}C_{TOC}$ records reflecting a primary signal and thus atmospheric CO_2 values. A *t*-test on each section, comparing $\delta^{13}C_{TOC}$ values during the CIE to those before the CIE, determines if a significant shift in $\delta^{13}C_{TOC}$ values occurred during the CIE (Table 2).

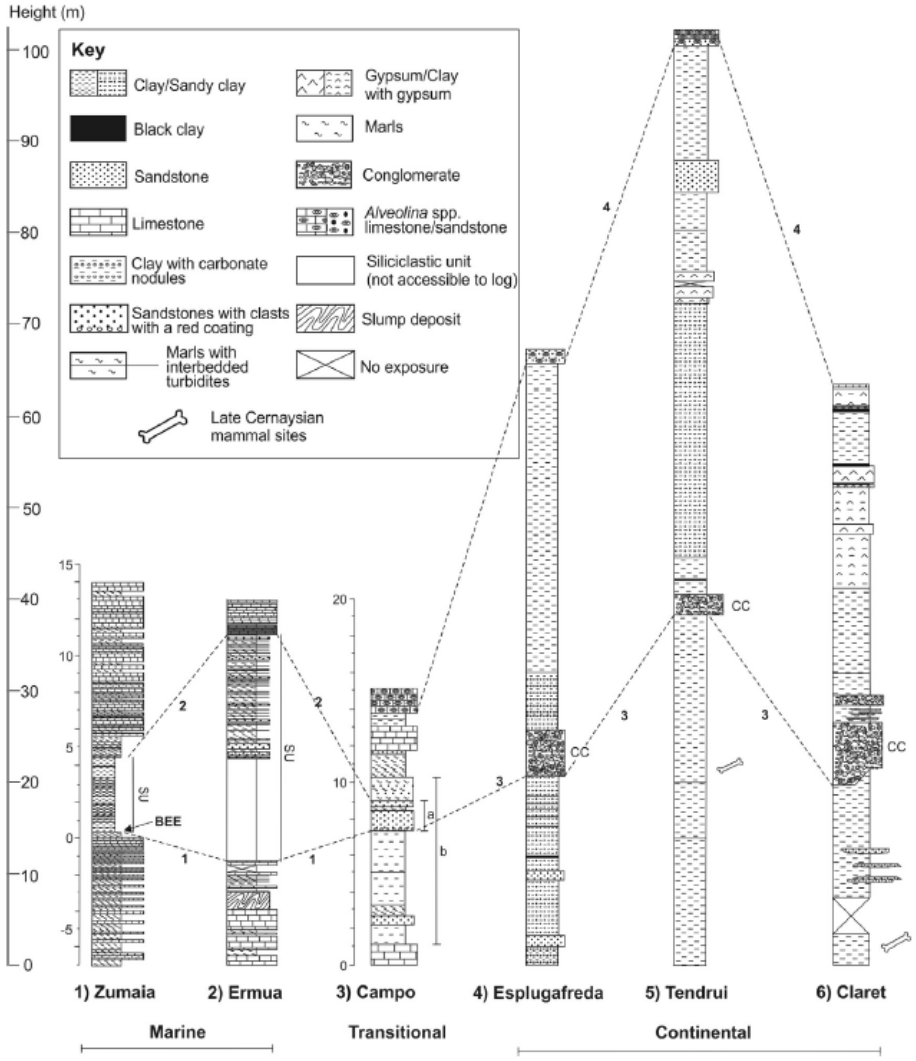

Fig. 3. Lithological logs, with proposed correlation points from the marine to continental realm (West to East), from Schmitz and Pujalte (2003), based upon carbon isotope stratigraphy and lithology. Note different scales used for Zumaia and Campo. BEE = Benthic Extinction Event. Numbered/lettered lines indicate proposed tie points/key lithological features: (1&2) Bottom and top of the marine Siliciclastic Unit (SU on figure), respectively (Schmitz et al., 2001). Using isotope stratigraphy and lithology the Siliciclastic Unit has been suggested to experience a lateral change of facies towards a more detritic nature and can be linked to two sandstone beds at the transitional section of Campo (Schmitz and Pujalte, 2003). (3) Bottom of the Claret Conglomerate (CC on figure: Schmitz and Pujalte, 2007). (4) *Alveolina* Beds associated with a marine transgression throughout the entire terrestrial region (Molina et al. 2000, 2003). (a) Sandstone beds interpreted to be the distal equivalent of the Claret Conglomerate (Schmitz and Pujalte, 2003). (b) Continental interval of the Campo section (Schmitz and Pujalte, 2003).

Table 1
The $\delta^{13}C_{TOC}$ data used for calculating the magnitude of the CIE in this study. Superscripted numbers in the case of Campo refer to the values taken for the CIE calculation as pre-CIE values vary depending on where the onset of the CIE is placed. Total number of samples means all samples from this study and those used from Domingo et al. (2009), upon which all statistical analysis has been conducted. Number of samples indicates the new samples for which $\delta^{13}C_{TOC}$ data has been generated in this study.

Section	Total no. of samples	No. of samples this study	Min. $\delta^{13}C_{TOC}$ (‰)	Max. $\delta^{13}C_{TOC}$ (‰)	CIE calculation values (‰)		CIE magnitude
					Pre-CIE	Body-CIE	
Claret	98	20	−27.8	−21.7	−23.3	−26.8	3.5
Tendrui	94	28	−26.7	−22.9	−24.7	−26.4	1.7
Esplugafreda	80	80	−26.5	−21	−21.9	−26	4.1
Campo	34	34	−28.9	−21.3	$-23.5^{1}/-26.2^{2}$	−28.3	2.1^{1}–4.8^{2}
Ermua	46	46	−29.5	−22.4	−22.4	−27.2	4.8
Zumaia	77	77	−28.4	−23.9	−24.3	−28.4	4.1

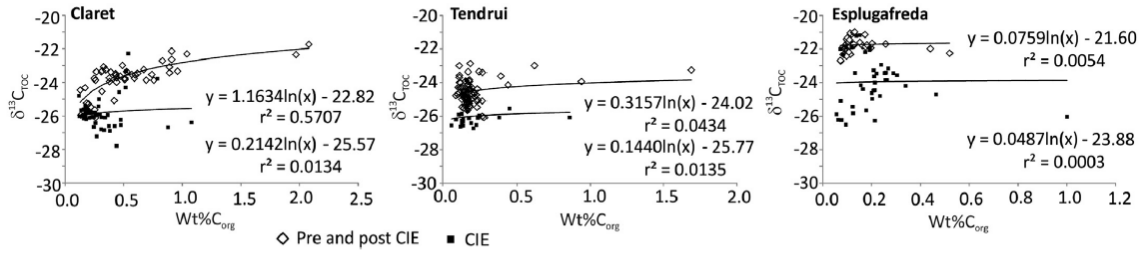

Fig. 4. Regression analysis plots. Cross plots showing correlations between $\delta^{13}C_{TOC}$ and weight % organic carbon (wt%TOC) for each continental section studied.

Table 2
Associated statistical tests performed on the data (regression analysis and *t*-tests) comparing $\delta^{13}C$ and wt%TOC. For regression analysis, pre- and post-CIE values were combined, and CIE values were analysed separately to determine if a logarithmic relationship was observed in any of the sections. *t*-tests were conducted comparing only pre-CIE values to CIE values to determine if a statistically significant shift was recorded. For this second analysis post-CIE values were ignored, as they do not return to pre-CIE values, and as such may bias the test.

Section	Data used for regression analysis	R^2 values comparing $\delta^{13}C_{TOC}$ and wt%TOC	Data used for comparison in *t*-tests	*t*-test results for $\delta^{13}C_{TOC}$ values
Claret	Pre/post CIE	0.571	Pre/during CIE	$t = 12.3198$
	During CIE	0.013		$p < 0.001$
Tendrui	Pre/post CIE	0.043	Pre/during CIE	$t = 10.3572$
	During CIE	0.014		$p < 0.001$
Esplugafreda	Pre/post CIE	0.005	Pre/during CIE	$t = 7.08471$
	During CIE	0.0003		$p < 0.001$
Campo			Pre/during CIE	$t = 3.66633$
				$p < 0.001$
Ermua	Not calculated due to the nature of the sections (continental-marine, or entirely, marine).		Pre/during CIE	$t = 13.7016$
				$p < 0.001$
Zumaia			Pre/during CIE	$t = 10.9268$
				$p < 0.001$

To define the magnitude of any CIE, the start, or onset, of the CIE in any given section must be determined. The onset of the CIE in this study is defined by a negative isotope shift of at least ca. 2‰ to continuous values of < -25‰. For Claret, Esplugafreda, Ermua, and Zumaia this resulted in an unambiguous identification of the CIE onset. However, Tendrui and Campo proved more challenging and, as such, to confirm that the shift observed was in fact the CIE associated with the PETM, the onset of the CIE in this study was compared to previously published data and lithological tie points (Fig. 3). Finally, a return to less negative values, similar to those preceding the event, was used to determine the termination of the CIE. The $\delta^{13}C_{TOC}$ results for all 6 sections are presented in Fig. 5 (continental sections) and Fig. 6 (marine sections; also Tables A7 to A12 of the supplementary material).

3. Results

The $\delta^{13}C_{TOC}$ CIE magnitudes range between 1.7 to 4.8‰ among the six sections (Table 1). The highest recorded $\delta^{13}C_{TOC}$ CIE magnitude for the continental sections is that of Esplugafreda (4.1‰), whilst for the marine sections it is Ermua (4.8‰). Using the defined parameters for the CIE onset, combined with correlative data from previous studies (Schmitz and Pujalte 2003, 2007; Pujalte et al., 2009), we suggest a CIE magnitude of 2.1‰ at Campo (Fig. 6). However, interpretation of the CIE onset at Campo was more difficult due to its stepped nature (Fig. 6), leading to a range of potential CIE magnitudes, depending on where the onset was placed (2.1–4.8‰). Among the continental sections of Claret, Tendrui, and Esplugafreda the magnitude of the CIE varies, despite their proximity (Table 1), but in the case of Claret and Tendrui, the onset of the excursion occurs prior to the deposition of the Claret Conglomerate, and the peak of the CIE occurs after conglomerate deposition (Fig. 5). Comparison between the marine sections illustrates variability in terms of the magnitude, onset, and shape of the CIE profiles (Fig. 6).

Regression analysis was conducted to determine if a significant logarithmic correlation between $\delta^{13}C_{TOC}$ and wt%TOC is present for the continental sections, in either pre- plus post-CIE sediments or CIE sediments. For most of the sections a significant correlation was not observed ($r^2 \leqslant 0.19$, Table 2, Fig. 4), although the pre- and post-CIE correlation coefficient for Claret is 0.57, indicating a possible logarithmic relationship between the $\delta^{13}C_{TOC}$ and wt%TOC of the samples in this section. A similar relationship has been observed by Wing et al. (2005), Wynn et al. (2005) and Wynn (2007), who suggested that a logarithmic relationship may imply further decomposition of organic matter after burial. Care must be taken when interpreting results where such a logarithmic relationship is observed. The dependence of wt%TOC on lithology was assessed using the students *t*-test. Results indicate that wt%TOC may be dependent on certain lithological types in the sections (Tables A1–A6 of the supplementary material). Although we observe statistically significant differences between some pairs of lithologies, they do not necessarily correspond to the lithologies observed throughout the CIEs. Furthermore, those differences do not exhibit consistency among sections. This would be indicative of the independence of the wt%TOC and the sampled lithology. Further statistical tests comparing pre-CIE to CIE $\delta^{13}C_{TOC}$ values demonstrate that statistically significant differences occur between CIE $\delta^{13}C_{TOC}$ values and those from before the CIE (Table 2) in all sections. The $\delta^{13}C$ CIE magnitudes are consistently higher in the marine sections than previously published data based on carbonates (Table 3), whilst the opposite is true for continental sections; both methods however show no apparent relationship between magnitude of the CIE and depositional environment. This verifies the results of previous studies in this region using the $\delta^{13}C$ values of carbonates, which also illustrate no observable relationship between the magnitude of CIE and depositional environment (Schmitz et al. 1997, 2001; Molina et al., 2003, Schmitz and Pujalte 2003, 2007).

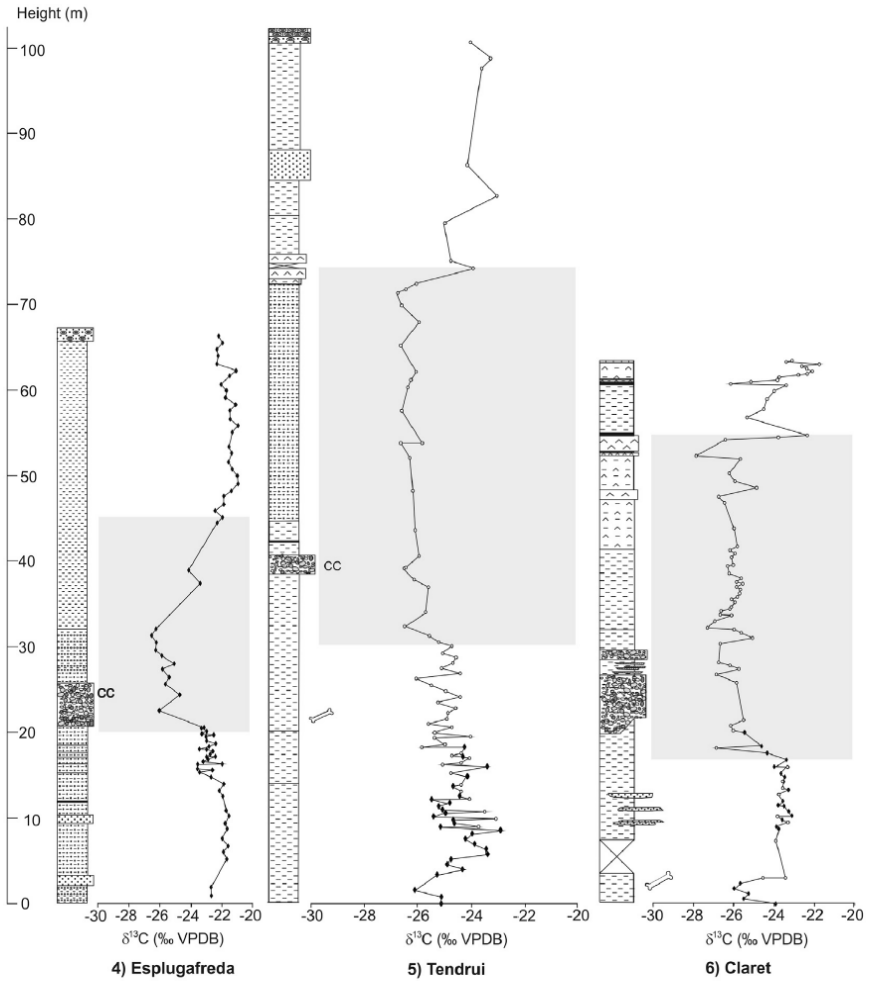

Fig. 5. Continental $\delta^{13}C_{TOC}$ data. Lithology and $\delta^{13}C_{TOC}$ for the continental sections only. Grey boxes indicate inferred CIEs associated with the PETM; clear circles indicate previously published data (Domingo et al., 2009), filled diamonds indicate new data from this study. See Fig. 3 for lithological key.

Table 3
Comparison of $\delta^{13}C_{TOC}$ CIE magnitude calculated using different methods and previously published $\delta^{13}C$ measured from carbonates. Method 1 refers to the method used in this study (see text for an explanation; termed "maximum CIE" approach); Method 2 refers to the method used in previous studies (termed "average CIE" approach. [1] Schmitz and Pujalte (2007); [2] Schmitz and Pujalte (2003); [3] Schmitz et al. (2001); [4] Schmitz et al. (1997).

Section	Setting	Published CIE magnitudes for carbonate carbon (‰ VPDB)	CIE magnitude calculation		Difference
			Method 1 (‰ VPDB)	Method 2 (‰ VPDB)	
Claret	Continental	6.0–7.0[1]	3.5	1.9	1.6
Tendrui		6.0–7.0[2]	1.7	1.4	0.3
Esplugafreda		6.0–7.0[2]	4.1	2.0	2.1
Campo	Transitional	–	2.1–4.8	1.0–2.9	1.5
Ermua	Marine	5.0[3]	4.8	3.8	1.0
Zumaia		2.0[4]	4.1	1.7	2.4

4. Discussion

4.1. Magnitude of CIE

There is low but sufficient TOC (ca. 0.2–2%) within the sediments through all six sections to generate high-resolution isotope curves from which the PETM can be identified. Differences in carbon sources or even changes in source(s) through the PETM in each section could contribute to the recorded differences in the magnitude of the CIE between sections. Some will comprise primarily marine organic matter (e.g., Zumaia and Ermua), some exclusively continental organic matter (e.g., Claret, Tendrui,

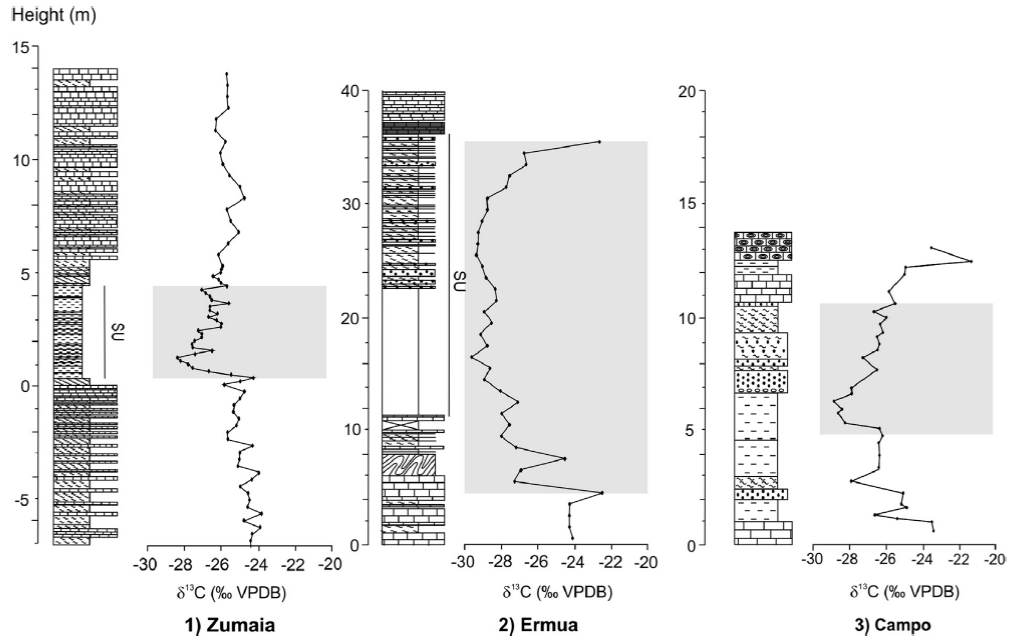

Fig. 6. Marine $\delta^{13}C_{TOC}$ data. Lithology and $\delta^{13}C_{TOC}$ for the marine and transitional sections only. Grey boxes indicate inferred CIEs associated with the PETM. See Fig. 3 for lithological key. Note different scales used throughout.

and Esplugafreda), and one likely comprises mixed organic matter sources (e.g., Campo). It is widely known that $\delta^{13}C$ values can vary dramatically with changing sources due to differences in isotopic fractionation during initial photosynthetic fixation of carbon (O'Leary, 1981; Diefendorf et al., 2010), subsequent biochemical partitioning of carbon amongst different compound classes (Hayes, 2001), and differential degradation of isotopically distinct compound classes (Lockheart et al., 1997). To some extent, these issues can be negated in well-mixed sediments of varying provenance, although even in these settings the isotopic signature of sediments can be biased by organic matter degradation and selective preservation, as well as the introduction of bacterial organic matter (Bowen et al., 2004; Magioncalda et al., 2004; Poole et al., 2004; Wynn et al., 2005; Smith et al., 2007).

The magnitude of the $\delta^{13}C_{TOC}$ CIE at Zumaia, Ermua, and Campo ranges from 2.1 to 4.8‰, comparable to marine CIEs recorded elsewhere (2‰ to 5.5‰: Zachos et al., 2005; Schmitz and Pujalte, 2007; Bowen and Zachos, 2010; McInerney and Wing, 2011; Tipple et al., 2011). Schmitz et al. (2001) measured a ca. 5‰ excursion in carbonate $\delta^{13}C$ values at Ermua, whilst here we report a $\delta^{13}C_{TOC}$ excursion of 4.8‰. However, at Zumaia, only a 1.5 to 2‰ excursion is recorded by bulk carbonate (Schmitz et al., 1997), whilst the $\delta^{13}C_{TOC}$ excursion is 4.1‰.

Calculation of the magnitude of the CIE at Campo is more difficult, possibly due to the potential for alternating continental and marine organic matter sources before, during, and after the CIE interval. Several studies have suggested that Campo was located in a shallow marine setting before and after the CIE, but that continental deposition dominated during the CIE (Molina et al., 2000; Schmitz and Pujalte, 2003). Molina et al. (2003) attempted to identify the PETM CIE using carbonate $\delta^{13}C$ stratigraphy at Campo, but they concluded that diagenetic overprinting made this impossible. Schmitz and Pujalte (2003) also attempted to identify the PETM CIE using soil carbonate $\delta^{13}C$ values. However, no magnitude was calculated due to low sample resolution making determination of the CIE challenging, although they did tentatively identify the onset (Section 4.2). Results from this study record a stepped nature of the onset, which means that our 2.1‰ estimate for the magnitude of the CIE is tentative at Campo.

The three continental records (Claret, Tendrui, and Esplugafreda) show broadly similar $\delta^{13}C_{TOC}$ magnitudes (Fig. 5, Table 1). Domingo et al. (2009) published the first $\delta^{13}C_{TOC}$ results for Claret and Tendrui, and demonstrated that in both cases the magnitude of the CIE was smaller and the onset occurred earlier than that previously recorded in soil carbonate nodules (carbonates $\delta^{13}C = 6$–7‰) from the same and neighbouring sections of the Pyrenees (Schmitz and Pujalte 2003, 2007). Here we also show the magnitudes of the CIE to be smaller than that of carbonate $\delta^{13}C$ data (3.5‰ at Claret, 1.7‰ at Tendrui, and 4.1‰ at Esplugafreda), and other studies have also reported smaller PETM CIEs from $\delta^{13}C_{TOC}$ than carbonate $\delta^{13}C$ (e.g. Smith et al., 2007).

Studies of continental records will always be biased by changes in fractionation and reworking of organic matter, as well as changes in sedimentation rate, all of which can affect the magnitude and profile shape to varying degrees. The greater the number of records available for comparison however, the better informed any conclusions pertaining to localised and global changes will be. The data presented in this study add six new PETM records to this discussion and are derived entirely from sections from neighbouring basins within the same sediment routing system, therefore allowing more direct comparison of magnitudes. So far the data from this transect suggest that for a given system, the difference between continental (average this study: 3.1 ± 1.25‰, average other studies: 4.7 ± 1.5‰; McInerney and Wing, 2011) and marine (average this study: 3.7 ± 1.40‰, average other studies: 2.8 ± 1.3‰ McInerney and Wing, 2011) organic carbon CIEs could be minimal.

4.2. Onset and recovery from the CIE

Our higher-resolution $\delta^{13}C_{TOC}$ records suggest differences in the timing of the CIE onset in the Iberian continental settings, compared to the carbonate $\delta^{13}C$ data obtained by Schmitz and Pujalte (2003, 2007), where lower-resolution analysis of soil carbonate nodules placed the onset of the CIE within and above the Claret Conglomerate. The discrepancy between our CIE onsets and those recorded in soil carbonate nodules may be due to sampling resolution, or the time taken for soil development, with the carbonate data recording the isotopic composition of local soil CO_2, in turn reflecting plant respiration and fractionation (Cerling, 1991). Hence, it is expected that the isotopic composition of soil-nodule carbonate follows that of organic carbon causing a delay in the record of the CIE onset in carbonate nodules due to the more protracted time of soil formation. The incorporation of CO_2 with pre-CIE $\delta^{13}C$ values into the carbonate could result in a smoothed record and apparently later onset. Furthermore, a paucity of carbonate $\delta^{13}C$ data directly below the Claret Conglomerate may also mean that previous studies have not detected the true onset of the CIE.

Sedimentological studies carried out by Schmitz and Pujalte (2003, 2007) indicated that the Claret Conglomerate formed as a series of alluvial megafans, which in conjunction with carbonate $\delta^{13}C$ data, were suggested to be induced by extreme hydrological changes related to the onset of the PETM (Schmitz and Pujalte, 2007). Here we show that the onset of the $\delta^{13}C_{TOC}$ CIE occurs prior to the deposition of the Claret Conglomerate in the Claret and Tendrui sections, and in the lower few metres of the Claret Conglomerate at Esplugafreda. Because peak CIE values occur after the conglomerate deposition (Domingo et al., 2009), and the onset of the CIE has been suggested to occur in ca. 15 kyr (Bowen et al., 2006), our revised records indicate a small time-lag (<15 kyr) in the response of the landscape and depositional system, to the climate perturbation (previously assumed to be coincident with onset of the CIE). This is in agreement with Domingo et al. (2009) who estimated a time-lag between the onset of the CIE and the deposition of the Claret Conglomerate of around 4–9 kyr based on sedimentation rates calculated for the Claret and Tendrui sections. This time-lag is potentially seen in the comparison of the continental and continental–marine records; the source of the Claret Conglomerate has been mapped and suggested to originate "more than 10 km to the north of the present day outcrops" (Schmitz and Pujalte, 2007; Fig. 2). Comparing this to the CIE recorded at each section potentially shows how the onset of the CIE records this time-lag. If deposition of the Claret Conglomerate is time transgressive then it would be expected that the stratigraphic lag recorded between the onset of the CIE and the Claret Conglomerate would vary between sections accordingly. This appears to be the case for these sections (Figs. 5 and 6); Esplugafreda is geographically nearest to the alluvial megafans suggested to be responsible for Claret Conglomerate deposition (Fig. 2), whilst the sections of Claret, Tendrui, and Campo are more distal respectively. Consequently Esplugafreda appears to have a briefer stratigraphic lag between the onset of the CIE and the deposition of the Claret Conglomerate than the lags at Claret, Tendrui and Campo. However, scouring probably removed some of the underlying strata during conglomerate deposition, such that even our higher-resolution record remains imperfect, complicating the comparison of any lag time between the onset of the CIE and Claret Conglomerate deposition.

Two sandstone beds separated by a marly interval occur at Campo ca. 6 m above the lithological change from marine to continental deposits; these beds have previously been interpreted as the lateral equivalent of the Claret Conglomerate (Schmitz and Pujalte, 2007) and, specifically, progression of the megafan conglomeratic deposits into lower energy environments. Pujalte et al. (2009) suggested that the Paleocene–Eocene boundary coincides with the base of the sandstone beds, interpreted to be the lateral equivalent of the Claret Conglomerate, based upon extensive mapping of the area, biostratigraphy, and carbonate $\delta^{13}C$ data. Our $\delta^{13}C_{TOC}$ data support several different interpretations, due to the stepped nature of the profile; however, when compared to Pujalte et al. (2009), the onset of the CIE as recorded by $\delta^{13}C_{TOC}$ occurs just below the sandstone units, at ca. 5 m height (Fig. 6). We suggest that this is analogous to the situation at Claret and Tendrui, where the onset of the CIE occurs prior to the Claret Conglomerate.

Differences are also recorded in the timing of the onset of the CIE in the marine realm. Schmitz et al. (2001) concluded that the onset of the CIE at Zumaia, based upon a carbonate record, occurs simultaneously with the lithological change to siliciclastic deposits, directly above a thick limestone bed (ca. 0.75 m thick) and coincident with a marl bed (ca. 0.30 m thick), inferring that the sedimentological change was brought about by the PETM. The onset of the CIE at Zumaia derived from $\delta^{13}C_{TOC}$ values occurs at the top of the ca. 0.30 m marl unit coincident with the start of siliciclastic deposition. This later onset suggests that the sedimentological changes may have occurred prior to the onset of the CIE.

At Ermua, however, the onset of the CIE occurs within the limestones below the lithological change to predominantly siliciclastic deposition (Fig. 6). This contradicts the findings of Schmitz et al. (2001), who found the CIE onset occurred simultaneously with siliciclastic deposition. However, Schmitz et al. (2001) also suggested that the carbonate isotope signals at Ermua had been diagenetically altered to a much greater extent than those of surrounding sections (e.g., Zumaia and Trabakua). Previous studies have suggested that where diagenetic overprinting is observed, isotopic analyses on organic matter could give more reliable results (Molina et al., 2003), due to organic matter being more resistant to acidic degradation than carbonate material. The onset of the CIEs at Ermua and Zumaia, therefore, both appear to be rapid, but occur at different lithological horizons, which is contrary to that shown by Schmitz et al. (2001). If the onset of the CIE associated with the PETM is assumed to be globally synchronous, this indicates that the lithological beds previously used to correlate between sections may in fact be diachronous events within the study area, and as such a time transgressive element may have to be considered. Alternatively, it may reflect limitations for the TOC-derived $\delta^{13}C$ records; for example, the apparently later CIE at Zumaia could be a consequence of organic matter source mixing associated with the sedimentological changes. Further analysis of $\delta^{13}C_{n\text{-alkanes}}$ may also help to constrain the differences recorded in $\delta^{13}C_{TOC}$ at these sections.

Recovery from the CIE in the Claret and Tendrui sections has previously been discussed as occurring coincident with a gypsum layer, suggesting a return to drier conditions and intense evaporation rates towards the end of the PETM (Domingo et al., 2009). However, a comparison of CIE recovery in relation to the stratigraphic framework for other sections is lacking. A marker bed associated with a marine transgressive event in the early Eocene, known as the *Alveolina* Beds, occurs in all continental and continental–marine sections (Claret, Tendrui, Esplugafreda and Campo, respectively). The time transgressive nature of this transgression is recorded in the isotope records at each section. Fig. 2 illustrates section location in relation to the Bay of Biscay; the transgression occurred in a south-easterly direction across the region and, as such, the CIE recovery in relationship to this marker bed can be assessed. As would be expected, the CIE recovery occurs much closer to the *Alveolina* Beds at sections geographically closer to the source of the transgression. As such, Campo records the CIE recovery closest to the *Alveolina* Beds (ca. 2 m below), whilst the more distal sections of Claret, Tendrui, and Esplugafreda

record the recovery from the CIE much further below the *Alveolina* Beds (ca. 20–25 m).

Comparison can also be made between the CIE recovery and the top of the Siliciclastic Unit at Ermua and Zumaia. Ermua is interpreted as a base-of-slope apron, whilst Zumaia is bathyal in nature. The Siliciclastic Unit is interpreted as the product of increased continental erosion coupled with reduced hydrodynamic energy of freshwater entering the ocean (Schmitz et al., 2001). Ermua records the recovery almost coincident with the top of the Siliciclastic Unit, whilst at Zumaia recovery from the CIE occurs within the Siliciclastic Unit itself. Schmitz and Pujalte (2003) showed an enhanced kaolinite influx in the Siliciclastic Unit at both sections. This enhanced kaolinite signal closely parallels the CIE, terminating coincidentally with the top of the Siliciclastic unit at Ermua but within the Siliciclastic Unit at Zumaia. Schmitz and Pujalte (2003) argued that the increase in kaolinite content reflects deeper physical continental erosion and thus, an enhancement of terrestrial runoff, consistent with other low and mid-latitude investigations (Schmitz and Pujalte, 2003; Handley et al., 2012; Stassen et al., 2012). Therefore, these sections show a clear synchroneity between the lithological expression of the PETM and the CIE within these marine sections.

For the continental sections and the continental–marine section at Campo, the presence and cause of a time-lag between the onset of the CIE and the sedimentological response has fundamental implications for how we decode the impact of abrupt climate forcing and the sedimentary record. Assuming the near-geologically instantaneous uptake of the atmospheric carbon isotopic signature by terrestrial vegetation, and the subsequent deposition of this vegetation in terrestrial sediments, there are two potential explanations for the time-lag between the recorded bulk organic CIE and the observed sedimentological response to warming in these sediments. First, there was a genuine lag between the input of light carbon to the atmosphere and the expression of its full forcing effect on the climate system in terms of warming and hydrological change (Pagani et al., 2006; Secord et al., 2010; Rohling et al. 2012). To fully account for the time-lags observed between carbon isotope and sedimentological records in these sections, this would assume that the sedimentological response to changing hydrological regimes is near-instantaneous. Second, the observed time-lag is largely due to the timescales of response of sediment source and routing systems to a shift in hydrological regime. Given the relatively short timescales involved, of the order of 10 kyr or less, it is likely that some component of both these mechanisms is operating, and the deconvolution of each of these is challenging. Indeed, the interesting constraint for future studies is rather understanding the *speed* with which these alluvial fan sediment systems are responding to rapid climate change. This study presents new and remarkably well-resolved constraints on the maximum response time of the systems of ~10 kyr, which should be a target for future sedimentological and geomorphological studies.

4.3. CIE profiles

The profiles recorded for each section vary with respect to the length of the CIE onset and recovery, and also to the general shape of the main body of the CIE. All profiles are generally triangular-shaped (Fig. 1.1) as presented by Zachos et al. (2008), or box-shaped (Fig. 1.2) as proposed by Bowen and Zachos (2010), although it is accepted that the shape is most likely influenced by reworking and sediment mixing. The CIEs recorded at Zumaia and Campo are similar to those recorded by Zachos et al. (2008) from three deep-sea sections in the Southern Ocean, Central Pacific and South Atlantic. Specifically, all records document a relatively rapid CIE onset, followed by a gradual return to pre-CIE $\delta^{13}C$ values (Fig. 1.1). In contrast, the sections of Claret, Tendrui (both continental), and Ermua (marine) are similar to those of Bowen and Zachos (2010), in that all achieve a semi-stable state following the rapid onset, before finally recording a relatively rapid return to pre-CIE $\delta^{13}C$ values (Fig. 1.2). The Esplugafreda section is more difficult to interpret due to low sample resolution in the recovery section of the CIE profile, although, data around the onset appear to follow the box profile of Bowen and Zachos (2010) in that a continued negative excursion is recorded post-onset.

Sedimentation rates are important in determining the shapes of the CIE profiles; higher sedimentation rates may lead to the onset of the CIE appearing more gradually, and vice versa. Such rates are notoriously challenging to determine for continental settings due to a lack of robust age control. For the marine sections, Schmitz et al. (2001) apply different sedimentation rates to the Siliciclastic Unit at Zumaia and Ermua based on carbon isotope stratigraphy. Their carbonate isotope results suggest the Siliciclastic Unit formed synchronously at both sections, and as such a much higher sedimentation rate is calculated for Ermua (Siliciclastic Unit thickness ca. 20 m), than that for Zumaia (Siliciclastic Unit thickness ca. 5 m). Our higher-resolution data agree with the carbonate $\delta^{13}C$ data at Zumaia, but not at Ermua where our $\delta^{13}C_{TOC}$ data suggest an earlier onset of the CIE, an observation in agreement with previous work (Orue-Etxebarria et al., 1996) where the base of the Siliciclastic Unit at Zumaia was correlated with the base of the slump deposit seen at Ermua using sequence stratigraphy. This may suggest even higher sedimentation rates recorded at Ermua than previously calculated.

In our study, the CIE at Zumaia and potentially Campo follow the classical profile, but all the other sections do not. The fact that both profiles are present within the same and neighbouring basins clearly indicates that localised factors, such as changing sedimentation rates, differential compaction, or depositional hiatuses in the record, are contributing to profile shape, likely in marine and terrestrial settings.

5. Conclusions

$\delta^{13}C_{TOC}$ and TOC data from six sections spanning a continental to marine transect through the PETM in northern Spain are presented. These data represent the highest-resolution $\delta^{13}C$ records for these sections to date, and the first organic data from four of the sections (Esplugafreda, Campo, Ermua and Zumaia). Regression analyses indicate that $\delta^{13}C_{TOC}$ values are independent of wt%TOC, suggesting that lithological changes have not impacted the isotopic records of the continental sections, and *t*-tests indicate the CIE is of statistically significant magnitude. The magnitude of the CIE amongst the six sites is variable, ranging from 1.7 to 4.8‰, with no consistent relationship between magnitude and depositional environment. The continental sections in this study record a greater CIE magnitude than the average recorded for marine sections globally, although there is no offset between the terrestrial and marine CIEs within this given depositional system. Different CIE profile shapes are recorded for different sections, fitting both the triangular profile described by Zachos et al. (2008) and the box profile proposed by Bowen and Zachos (2010). The variability in both CIE magnitude and shape, within a single terrestrial to continental margin depositional system, clearly demonstrates the significant effects that organic matter reworking and transport can have on the preserved carbon isotope signals.

The onset of the CIE appears to have occurred prior to the base of the Claret Conglomerate in most of the continental sections, whilst at the marine section of Ermua the CIE onset occurred prior to the base of the Siliciclastic Unit. This is in contrast to previous studies which have placed the CIE above or coincident with lithological changes in both the continental and marine realms. Our data, therefore, suggest that a lag occurred between the onset of

the PETM and changes in the weathering/erosional regime, similar to findings of previous workers (e.g. Handley et al., 2012).

Acknowledgements

This study forms part of the PhD research of H.R.M., funded by Plymouth University (School of Geography, Earth, and Environmental Sciences), and was partially supported by the Plan Nacional I + D project CGL2009-09000/BTE (Spain). L.D. acknowledges a former postdoctoral fellowship of the Fundación Española para la Ciencia y la Tecnología – FECYT and Spanish Ministerio de Educación and an ongoing postdoctoral fellowship of the University of California Santa Cruz. This work is a contribution from the research group UCM-CAM 910161 "Geologic Record of Critical Periods: Paleoclimatic and Paleoenvironmental Factors". T.D.J. acknowledges funding from a Royal Society Dorothy Hodgkin Fellowship; R.D. was supported by the Elspeth Matthews Fund (GSL), and R.D.P. acknowledges the Royal Society Wolfson Research Merit Award. We would also like to thank Victoriano Pujalte, for guidance in accessing sampling sites, Enrique Cantero for assistance in sampling, and Chris Kendrick for assistance with TOC and $\delta^{13}C_{TOC}$ analysis. Finally we thank the two anonymous reviewers for their helpful comments, many of which have improved the final paper.

Appendix A. Supplementary material

Supplementary material related to this article can be found online at http://dx.doi.org/10.1016/j.epsl.2013.06.016.

References

Baceta, J.I., Pujalte, V., Dinares-Turell, J., Payros, A., Orue-Etxebarria, X., Bernaola, G., 2000. The Paleocene/Eocene boundary interval in the Zumaia section (Gipuzkoa, Basque Basin): Magnetostratigraphy and high resolution lithostratigraphy. Rev. Sociedad Geol. España 13, 375–391.

Beerling, D.J., 1996. Ecophysiological responses of woody plants to past CO_2 concentrations. Tree Physiol. 16, 389–396.

Bowen, G.J., Zachos, J.C., 2010. Rapid carbon sequestration at the termination of the Palaeocene–Eocene Thermal Maximum. Nat. Geosci. 3, 866–869.

Bowen, G.J., Beerling, D.J., Koch, P.L., Zachos, J.C., Quattlebaum, T., 2004. A humid climate state during the Palaeocene/Eocene Thermal Maximum. Nature 432, 495–499.

Bowen, G.J., Bralower, T.J., Delaney, M.L., Dickens, G.R., Kelly, D.C., Koch, P.L., Kump, L.R., Meng, J., Sloan, L.C., Thomas, E., Wing, S.L., Zachos, J.C., 2006. Eocene hyperthermal event offers insight into greenhouse warming. EOS Trans. AGU 87, 165–169.

Cerling, T.E., 1991. Carbon-dioxide in the atmosphere – evidence from Cenozoic and Mesozoic paleosols. Am. J. Sci. 291, 377–400.

Cui, Y., Kump, L.R., Ridgwell, A.J., Charles, A.J., Junium, C.K., Diefendorf, A.F., Freeman, K.H., Urban, N.M., Harding, I.C., 2011. Slow release of fossil carbon during the Palaeocene–Eocene Thermal Maximum. Nat. Geosci. 4, 481–485.

Dickens, G.R., 2003. Rethinking the global carbon cycle with a large, dynamic and microbially mediated gas hydrate capacitor. Earth Planet. Sci. Lett. 213, 169–183.

Dickens, G.R., 2011. Down the Rabbit Hole: Toward appropriate discussion of methane release from gas hydrate systems during the Paleocene–Eocene Thermal Maximum and other past hyperthermal events. Clim. Past 7, 831–846.

Dickens, G.R., O'Neil, J.R., Rea, D.K., Owen, R.M., 1995. Dissociation of oceanic methane hydrate as a cause of the carbon isotope excursion at the end of the Paleocene. Palaeogeography 10, 965–971.

Dickens, G.R., Paull, C.K., Wallace, P., 1997. Direct measurement of in situ methane quantities in a large gas-hydrate reservoir. Nature 385, 426–428.

Diefendorf, A.F., Mueller, K.E., et al., 2010. Global patterns in leaf C-13 discrimination and implications for studies of past and future climate. Proc. Natl. Acad. Sci. USA 107, 5738–5743.

Domingo, L., López-Martínez, N., Leng, M.J., Grimes, S.T., 2009. The Paleocene–Eocene Thermal Maximum record in the organic matter of the Claret and Tendruy continental sections (South-central Pyrenees, Lleida, Spain). Earth Planet. Sci. Lett. 281, 226–237.

Dunkley Jones, T., Ridgwell, A., Lunt, D., Maslin, M.A., Schmidt, D.N., Valdes, P.J., 2010. A Palaeogene perspective on climate sensitivity and methane hydrate instability. Philos. Trans. R. Soc., Math. Phys. Eng. Sci. 368, 2395–2415.

Edwards, T.W.D., Graf, W., Trimborn, P., Stichler, W., Lipp, J., Payer, H.D., 2000. Delta C-13 response surface resolves humidity and temperature signals in trees. Geochim. Cosmochim. Acta 64, 161–167.

Handley, L., Pearson, P.N., McMillan, I.K., Pancost, R.D., 2008. Large terrestrial and marine carbon and hydrogen isotope excursions in a new Paleocene/Eocene boundary section from Tanzania. Earth Planet. Sci. Lett. 275, 17–25.

Handley, L., Crouch, E.M., Pancost, R.D., 2011. A New Zealand record of sea level rise and environmental change during the Paleocene–Eocene Thermal Maximum. Palaeogeogr. Palaeoclimatol. Palaeoecol. 305, 185–200.

Handley, L., O'Halloran, A., Pearson, P.N., Hawkins, E., Nicholas, C.J., Schouten, S., McMillan, I.K., Pancost, R.D., 2012. Changes in the hydrological cycle in tropical East Africa during the Paleocene–Eocene Thermal Maximum. Palaeogeogr. Palaeoclimatol. Palaeoecol. 329, 10–21, http://dx.doi.org/10.1016/j.palaeo.2012.02.002.

Hayes, J.M., 2001. Fractionation of carbon and hydrogen isotopes in biosynthetic processes. Stable Isotope Geochem. 43, 225–277.

Koch, P.L., Zachos, J.C., Gingerich, P.D., 1992. Correlation between isotope records in marine and continental carbon reservoirs near the Paleocene–Eocene boundary. Nature 358, 319–322.

Lockheart, M.J., VanBergen, P.F., Evershed, R.P., 1997. Variations in the stable carbon isotope compositions of individual lipids from the leaves of modern angiosperms: Implications for the study of higher land plant-derived sedimentary organic matter. Org. Geochem. 26, 137–153.

Lopez-Martinez, N., Pelaez-Campomanes, P., 1999. New mammals from South-Central Pyrenees (Tremp Formation, Spain) and their bearing on late Paleocene marine–continental correlations. Bull. Soc. Gèol. France 170, 681–696.

Lopez-Martinez, N., Smith, R., Pelaez-Campomanes, P., Smith, T., 2006. The acme of the micromammal Paschatherium across the Paleocene–Eocene boundary in continental Europe. Micropaleontology 52, 267–280.

Magioncalda, R., Dupuis, C., Smith, T., Steurbaut, E., Gingerich, P.D., 2004. Paleocene–Eocene carbon isotope excursion in organic carbon and pedogenic carbonate: Direct comparison in a continental stratigraphic section. Geology 32, 553–556.

McCarren, H., Thomas, E., Hasegawa, T., Röhl, U., Zachos, J.C., 2008. Depth dependency of the Paleocene–Eocene carbon isotope excursion: Paired benthic and terrestrial biomarker records (Ocean Drilling Program Leg 208, Walvis Ridge). Geochem. Geophys. Geosyst. 9, Q10008.

McInerney, F.A., Wing, S.L., 2011. The Paleocene–Eocene Thermal Maximum: A perturbation of carbon cycle, climate, and biosphere with implications for the future. Annu. Rev. Earth Planet. Sci. 39, 489–516.

Molina, E., Angori, E., Arenillas, I., Simonetta, M., Schmitz, B., 2000. Integrated stratigraphy across the Paleocene/Eocene boundary at Campo, Spain. GFF 122, 106–107.

Molina, E., Angori, E., Arenillas, I., Brinkhuis, H., Crouch, E.M., Luterbacher, H., Monechi, S., Scmitz, B., 2003. Correlation between the Paleocene/Eocene boundary and the Ilerdian at Campo, Spain. Rev. micropalèontol. 46, 95–109.

Nuñez-Betelu, K., Pujalte, V., Payros, A., Baceta, J.I., Bernaola, G., 2000. The Ilerdian parastratotype at Campo (central South Pyrenean Basin, Spain): A palynological re-study of the uppermost Paleocene and lowermost Eocene. GFF 122, 119–120.

O'Leary, M.H., 1981. Carbon isotopes in photosynthesis. Bioscience 38, 328–336.

Orue-Etxebarria, X., et al., 1996. Physical and biostratigraphic analysis of two prospective Paleocene–Eocene boundary stratotypes in the intermediate-deep water Basque Basin, Western Pyrenees: the Trabakua Pass and Ermua sections. Neues Jahrbuch Geol. Paläontol. Abhandl. 201, 179–242.

Orue-Etxebarria, X., Pujalte, V., Bernaola, G., Apellaniz, E., Baceta, J.I., Payros, A., Nuñez-Betulu, K., Serra-Kiel, J., Tosquella, J., 2001. Did the Late Paleocene thermal maximum affect the evolution of larger foraminifers? Evidence from calcareous plankton of the Campo section (Pyrenees, Spain). Marine Micropaleontol. 41, 45–71.

Pagani, M., Pedentchouk, N., Huber, M., Sluijs, A., Schouten, S., Brinkhuis, H., Sinninghe Damste, J., Dickens, G.R., Expedition 302 Scientists, 2006. Arctic hydrology during global warming at the Palaeocene/Eocene Thermal Maximum. Nature 442, 671–675.

Panchuk, K., Ridgwell, A., Kump, L.R., 2008. Sedimentary response to Paleocene–Eocene Thermal Maximum carbon release: A model–data comparison. Geology 36, 315–318.

Poole, I., van Bergen, P.F., Kool, J., Schouten, S., Cantrill, D.J., 2004. Molecular isotopic heterogeneity of fossil organic matter: Implications for δ^{13}C-biomass and δ^{13}C-palaeoatmosphere proxies. Org. Geochem. 35, 1261–1274.

Pujalte, V., Baceta, J.I., Payros, A., Orue-Etxebarria, X., Schmitz, B., 2000. Upper Paleocene–lower Eocene strata of the Western Pyrenees, Spain: A shelf-to-basin correlation. GFF 122, 129–130.

Pujalte, V., Schmitz, B., Baceta, J.I., Orue-Etxebarria, X., Bernaola, G., Dinares-Turrell, J., Payros, A., Apellaniz, E., Caballero, F., 2009. Correlation of the Thanetian–Ilerdian turnover of larger foraminifera and the Paleocene–Eocene Thermal Maximum: Confirming evidence from the Campo area (Pyrenees, Spain). Geol. Acta, 161–175.

Rohl, U., Westerhold, T., Bralower, T.J., Zachos, J.C., 2007. On the duration of the Paleocene–Eocene Thermal Maximum (PETM). Geochem. Geophys. Geosyst. 8.

Rohling, E.J., Sluijs, A., Dijkstra, H.A., Köhler, P., van de Wal, R.S.T., von der Heydt, A.S., Beerling, D.J., Berger, A., Bijl, P.K., Crucifix, M., DeConto, R., Drijfhout, S.S., Fedorov, A., Foster, G.L., Ganopolski, A., Hansen, J., Hönisch, B., Hooghiemstra, H., Huber, M., Huybers, P., Knutti, R., Lea, D.W., Lourens, L.J., Lunt, D., Masson-Demotte, V., Medina-Elizalde, M., Otto-Bliesner, B., Pagani, M., Pälike,

H., Renssen, H., Royer, D.L., Siddall, M., Valdes, P., Zachos, J.C., Zeebe, R.E., 2012. Making sense of palaeoclimate sensitivity. Nature 491, 683–691.
Schmitz, B., Pujalte, V., 2003. Sea-level, humidity, and land-erosion records across the initial Eocene Thermal Maximum from a continental–marine transect in Northern Spain. Geology 31, 689–692.
Schmitz, B., Pujalte, V., 2007. Abrupt increase in seasonal extreme precipitation at the Paleocene–Eocene boundary. Geology 35, 215–218.
Schmitz, B., Asaro, F., Molina, E., Monechi, S., von Salis, K., Speijer, R.P., 1997. High-resolution iridium, $\delta^{13}C$, $\delta^{18}O$, foraminifera and nanofossil profiles across the latest Paleocene benthic extinction event at Zumaya, Spain. Palaeogeogr. Palaeoclimatol. Palaeoecol. 133, 49–68.
Schmitz, B., Pujalte, V., Núñez-Betelu, K., 2001. Climate and sea-level perturbations during the Incipient Eocene Thermal Maximum: evidence from siliciclastic units in the Basque Basin (Ermua, Zumaia and Trabakua Pass), Northern Spain. Palaeogeogr. Palaeoclimatol. Palaeoecol. 165, 299–320.
Secord, R., Gingerich, P.D., Lohmann, K.C., MacLeod, K.G., 2010. Continental warming preceding the Paleocene–Eocene Thermal Maximum. Nature 467, 955–958.
Sluijs, A., Brinkhuis, H., Schouten, S., Bohaty, S.M., John, C.M., Zachos, J.C., Reichart, G.-J., Sinninghe Damste, J.S., Crouch, E.M., Dickens, G.R., 2007. Environmental precursors to rapid light carbon injection at the Palaeocene/Eocene boundary. Nature 450, 1218–1221.
Smith, F.A., Wing, S.L., Freeman, K.H., 2007. Magnitude of the carbon isotope excursion at the Paleocene–Eocene Thermal Maximum: The role of plant community change. Earth Planet. Sci. Lett. 262, 50–65.
Stassen, P., Thomas, E., Speijer, R.P., 2012. Integrated stratigraphy of the Paleocene–Eocene Thermal Maximum in the New Jersey Coastal Plain: Toward understanding the effects of global warming in a shelf environment. Paleoceanography 27, PA4210.
Storme, J.Y., Devleeschouwer, X., Schnyder, J., Cambier, G., Baceta, J.I., Pujalte, V., Di Matteo, A., Iacumin, P., Yans, J., 2012. The Palaeocene/Eocene boundary section at Zumaia (Basque–Cantabric Basin) revisited: new insights from high-resolution magnetic susceptibility and carbon isotope chemostratigraphy on organic matter (d13Corg). Terra Nova 24, 310–317.
Thomas, D.J., Zachos, J.C., Bralower, T.J., Thomas, E., Bohaty, S., 2002. Warming the fuel for the fire: Evidence for the thermal dissociation of methane hydrate during the Paleocene–Eocene Thermal Maximum. Geology 30, 1067–1070.
Tipple, B.J., Pagani, M., Krishnan, S., Dirghangi, S.S., Galeotti, S., Agnini, C., Giusberti, L., Rio, D., 2011. Coupled high-resolution marine and terrestrial records of carbon and hydrologic cycles variations during the Paleocene–Eocene Thermal Maximum (PETM). Earth Planet. Sci. Lett. 311, 82–92.
Ward, J.K., Harris, J.M., Cerling, T.E., Wiedenhoeft, A., Lott, M.J., Dearing, M.D., Coltrain, J.B., Ehleringer, J.R., 2005. Carbon starvation in glacial trees recovered from the La Brea tar pits, Southern California. Proc. Natl. Acad. Sci. USA 102, 690–694.
Wing, S.L., Harrington, G.J., Smith, F.A., Bloch, J.I., Boyer, D.M., Freeman, K.H., 2005. Transient floral change and rapid global warming at the Paleocene–Eocene boundary. Science 310, 993–996.
Wynn, J.G., 2007. Carbon isotope fractionation during decomposition of organic matter in soils and paleosols: Implications for paleoecological interpretations of paleosols. Palaeogeogr. Palaeoclimatol. Palaeoecol. 251, 437–448.
Wynn, J.G., Bird, M.I., Wong, V.N.L., 2005. Rayleigh distillation and the depth profile of (13)C/(12)C ratios of soil organic carbon from soils of disparate texture in Iron Range National Park. Geochim. Cosmochim. Acta 69, 1961–1973.
Zachos, J.C., Rohl, U., Schellenberg, S.A., Sluijs, A., Hodell, D.A., Kelly, D.C., Thomas, E., Nicolo, M., Raffi, I., Lourens, L.J., McCarren, H., Kroon, D., 2005. Rapid Acidification of the Ocean During the Paleocene–Eocene Thermal Maximum. Science 308, 1611–1615.
Zachos, J.C., Bohaty, S.M., John, C.M., McCarren, H., Kelly, D.C., Nielsen, T., 2007. The Palaeocene–Eocene carbon isotope excursion: Constraints from individual shell planktonic foraminifer records. Philos. Trans. R. Soc., Math. Phys. Eng. Sci. 365, 1829–1842.
Zachos, J.C., Dickens, G.R., Zeebe, R.E., 2008. An early Cenozoic perspective on greenhouse warming and carbon-cycle dynamics. Nature 451, 279–283.
Zeebe, R.E., Zachos, J.C., Dickens, G.R., 2009. Carbon dioxide forcing alone insufficient to explain Palaeocene–Eocene Thermal Maximum warming. Nat. Geosci. 2, 576–580.

Quaternary Science Reviews 29 (2010) 3489–3504

Contents lists available at ScienceDirect

Quaternary Science Reviews

journal homepage: www.elsevier.com/locate/quascirev

Striking similarities in temporal changes to spring sea ice occurrence across the central Canadian Arctic Archipelago over the last 7000 years

Simon T. Belt [a,*], Lindsay L. Vare [a], Guillaume Massé [a,b], Hayley R. Manners [a], John C. Price [a], Suzanne E. MacLachlan [c], John T. Andrews [d], Sabine Schmidt [e]

[a] Petroleum and Environmental Geochemistry Group, Biogeochemistry Research Centre, University of Plymouth, Drake Circus, Plymouth, PL4 8AA, UK
[b] LOCEAN, UMR7159 CNRS/UPMC/IRD/MNHN, 4 Place Jussieu, 75005 Paris, France
[c] National Oceanography Centre, University of Southampton, Waterfront Campus, European Way, Southampton, SO14 3ZH, UK
[d] INSTAAR and Department of Geological Sciences, University of Colorado, Boulder CO 80309, USA
[e] UMR CNRS 5805 EPOC, OASU, Université Bordeaux 1, Avenue des Facultés, 33405 Talance, France

ARTICLE INFO

Article history:
Received 30 November 2009
Received in revised form
18 June 2010
Accepted 18 June 2010

ABSTRACT

A 7000 year spring sea ice record for Victoria Strait (ARC-4) and Dease Strait (ARC-5) in the Canadian Arctic Archipelago (CAA) has been determined by quantification of the sea ice diatom-derived biomarker IP_{25} in two marine sediment piston cores obtained in 2005. The chronologies of the ARC-4 and ARC-5 cores were determined using a combination of ^{14}C AMS dates obtained from macrobenthic fossils and magnetic susceptibility measurements. The ages of the tops of the piston cores were estimated by matching chemical and physical parameters with those obtained from corresponding box cores. These analyses revealed that, while the top of the ARC-4 piston core was estimated to be essentially modern (ca. 60 cal yr BP), a few hundred years of sediment appeared to be absent from the ARC-5 piston core. Downcore changes to IP_{25} fluxes for both cores were interpreted in terms of variations in spring sea ice occurrence, and correlations between the individual IP_{25} flux profiles for Victoria Strait, Dease Strait and Barrow Strait (reported previously) were shown to be statistically significant at both 50 and 100-year resolutions. The IP_{25} data indicate lower spring sea ice occurrences during the early part of the record (ca. 7.0–3.0 cal kyr BP) and for parts of the late Holocene (ca. 1.5–0.8 cal kyr BP), especially for the two lower latitude study locations. In contrast, higher spring sea ice occurrences existed during ca. 3.0–1.5 cal kyr BP and after ca. 800 cal yr BP. The observation of, consecutively, lower and higher spring sea ice occurrence during two periods of the late Holocene, coincides broadly with the Medieval Warm Period and Little Ice Age epochs, respectively. The IP_{25} data are complemented by particle size and mineralogical data, although these may alternatively reflect changes in sea level at the study sites. The IP_{25} data are also compared to previous proxy-based determinations of palaeo sea ice and palaeoclimate for the CAA, including those based on bowhead whale remains and dinocyst assemblages. The spatial consistency in the proxy data which, most notably, indicates an increase in spring sea ice occurrence around 3 cal kyr BP, provides a potentially useful benchmark for the termination of the Holocene Thermal Maximum for the central CAA.

1. Introduction

Sea ice features prominently within the polar oceans by contributing to, and being influenced by, the Earth's climate. The enhanced albedo of sea ice relative to the open oceans results in a dramatic reduction of solar radiation at the Earth's surface, and this insulation strongly influences changes in climate both locally and globally. Further, during melting, the outflow of low-salinity surface water impacts on the climate by influencing deep oceanic circulation. The climate system also influences the transport of heat and moisture to the Polar Regions and thus the formation and mobility of sea ice (e.g. Aagaard and Carmack, 1989; Thomas and Dieckmann, 2010). This strong relationship between sea ice and global climate provides a strong motivation for the determination of temporal and spatial changes to polar sea ice cover, especially as there has been such a dramatic decline in the extent and thickness of Arctic sea ice in summer months over the last 30 years; an observation that is starting to be observed for winter sea

* Corresponding author. Tel.: +44 1752 584799; fax: +44 1752 584709.
E-mail address: sbelt@plymouth.ac.uk (S.T. Belt).

0277-3791/$ – see front matter © 2010 Elsevier Ltd. All rights reserved.
doi:10.1016/j.quascirev.2010.06.041

ice as well (e.g. Parkinson et al., 1999; Serreze et al., 2003; Rigor and Wallace, 2004; Meier et al., 2005; Comiso, 2006; Stroeve et al., 2008). Such spatial and temporal sea ice data is pivotal in informing predictive climate models, for which an evaluation of the relative contributions of natural and anthropogenic influences provides further motivation for investigation. However, in order to better contextualise the recent rapid changes to polar sea ice extent and thickness, and to provide a more comprehensive dataset for modelling studies, greater temporal and spatial historical sea ice records are urgently needed (e.g. Smith et al., 2003).

The recent (last 30 years) sea ice record has been rigorously determined via passive microwave satellite imagery (e.g. Parkinson et al., 1999; Serreze et al., 2003; Rigor and Wallace, 2004; Meier et al., 2005; Comiso, 2006; Stroeve et al., 2008). Prior to the 1970s, sea ice records rarely extend beyond the 19th century and the few records that do exist are based on archived material including ships' logs and other maritime records (e.g. Divine and Dick, 2006). In reality, these historical records represent the exceptional cases and are not diverse, spatially. Longer term records of sea ice cover (e.g. for the Holocene) are also rare, although proxy-based studies are beginning to be reported, and these are commonly based on the occurrence and distributions of physical, chemical and biological tracers within marine sediments. For example, spatial and temporal sea ice reconstructions for the Canadian Arctic Archipelago (CAA) have been derived from distributions of large mammal bones (Dyke et al., 1996b) together with occurrences of marine molluscs (Dyke et al., 1996a) and driftwood (Dyke and Morris, 1990; Dyke et al., 1997). The presence/absence of calcareous microfossils such as foraminifera has also been employed as a proxy for previous sea ice cover (e.g. Rahman and de Vernal, 1994; Cronin et al., 1995; Wollenburg and Kuhnt, 2000; Knudsen et al., 2008) though abundances and species diversity are often very low in the Arctic, with only *Neogloboquadrina pachyderma* dominating within planktic communities at higher latitudes. Dissolution of aragonite/carbonate foraminifera is a further limitation of this method (e.g. Wollenburg and Kuhnt, 2000; Gregory et al., in press). Some descriptions of diatom-based sea ice determinations for the North Atlantic have appeared recently (e.g. Justwan and Koç, 2008; Justwan et al., 2008), although this approach has received greater attention in the Antarctic (e.g. Gersonde and Zielinski, 2000; Hodell et al., 2001; Crosta et al., 2008; Denis et al., 2009).

Perhaps the most widespread method used in palaeo sea ice studies (to date) for the Arctic is based on the occurrence and distributions of dinoflagellate cysts. These organic-walled dinocysts are highly resistant to degradation and are well preserved in marine sediments (e.g. Voronina et al., 2001; de Vernal et al., 2001, 2005; Mudie et al., 2006; Ledu et al., 2008; McKay et al., 2008). This stability, combined with well characterised species diversity has permitted the reconstruction of sea surface conditions including temperatures, salinity and sea ice cover using the modern analogue technique (MAT). In addition to these biological proxies, the accumulation of 'foreign' ice rafted debris (IRD; e.g. quartz) has been used as a proxy for Arctic drift sea ice (e.g. Darby, 2003; Moros et al., 2006; Andrews and Eberl, 2007; Andrews, 2009; Andrews et al., 2009). Despite the advances made through these studies, further proxy-based palaeo sea ice investigations and calibrations of existing proxies are still needed.

In recent years, we have developed a new proxy for palaeo sea ice, which is based on the occurrence and distribution of a monounsaturated highly branched isoprenoid (HBI) lipid (IP_{25}) biosynthesised by sea ice diatoms during the spring bloom period (April–May), and deposited in underlying sediments following ice melt in the summer. The strict requirement for these conditions of sea ice formation, spring diatom bloom and subsequent ice melt is, in part, illustrated by the absence of IP_{25} in Arctic marine sediments under ice-free waters or permanent ice conditions (Belt et al., 2007; Müller et al., 2009), with the presence of sedimentary IP_{25} best reflecting spring sea ice occurrence (Vare et al., 2009). On the basis of sediments analysed thus far, IP_{25} would appear to be stable in marine sediments for at least 30 kyr (Belt et al., 2007; Massé et al., 2008; Andrews et al., 2009; Müller et al., 2009; Vare et al., 2009). By analysing the variable fluxes of IP_{25} in well-dated marine sediment cores, long term sea ice records for North Iceland (Massé et al., 2008; Andrews et al., 2009), Fram Strait (Müller et al., 2009), the Barents Sea (Vare et al., 2010) and Barrow Strait in the Canadian Arctic Archipelago (CAA; Fig. 1) (Vare et al., 2009) have been determined. For the CAA, spring sea ice occurrence was shown to be relatively low in the early part of the Holocene (ca. 10–4 cal kyr BP), then increased between ca. 4–3 cal kyr BP, and was highest and most variable after ca. 3 cal kyr BP (Vare et al., 2009), although these were only expressed as qualitative outcomes. In the current study, we provide new sea ice records for two further locations in the CAA (Victoria Strait and Dease Strait, Fig. 1), interpret these alongside our previously reported data for Barrow Strait, provide suggestions as to how the qualitative data may potentially be interpreted more quantitatively, and discuss the outcomes with respect to the climate history of the CAA over the past ca. 7 cal kyr BP.

2. Regional setting

2.1. The Canadian Arctic Archipelago (CAA) and sea ice

The CAA is a complex array of islands, with narrow channels interconnecting larger basins between numerous islands (Fig. 1). This study concentrates on locations in Dease Strait, Victoria Strait and Barrow Strait, which connect the western and eastern regions, collectively known as the Northwest Passage. The channels represent a major gateway for freshwater flow from the Arctic Ocean to the North Atlantic Ocean, while water circulation through Barrow Strait is influenced by eastward flow from the Canada Basin and westward flow from Baffin Bay. A major change in the marine circulation involving a switch in the dominance of Atlantic and Arctic waters occurred at ca. 6.0 cal kyr BP for eastern Baffin Island, but later (ca. 2–4 kyr BP) for more westerly regions including Barrow Strait (Williams et al., 1995). The Laurentide and Innuitian ice sheets covered the entire CAA during the Last Glacial Maximum (LGM) (Dyke et al., 2002), with recession of the ice margin in the central region beginning ca. 10 cal kyr BP (Dyke et al., 1996a; Dyke, 1999, 2008). The rate of this ice sheet recession was variable, spatially, but for the central channels described here, the final remnants of ice disappeared ca. 7–8 cal kyr BP, following a rapid increase in temperature (Dyke et al., 1996a; Dyke, 1999). In the modern age, the CAA is characterised by seasonal sea ice cover, with ice formation beginning in September followed by melting from April–June.

3. Methods

3.1. Field methods

The current study is based on the analysis of three piston cores (ARC-3, ARC-4 and ARC-5; 99.2 mm internal diameter), collected during the CCGS *Amundsen* ArcticNet cruise (August/September 2005). Summaries of each core are shown in Table 1. Each core was divided on-board into 100-cm sections plus a shorter section at the top. Sections were longitudinally split, with one half archived at the British Ocean Sediment Core Research Facility (BOSCORF, University of Southampton, UK). The remaining halves were sub-sectioned at a 1 cm resolution and each horizon was further divided, with one half freeze-dried, the other stored in a cold room (+4 °C). For dating purposes, box cores were also collected at ARC-4 and ARC-5.

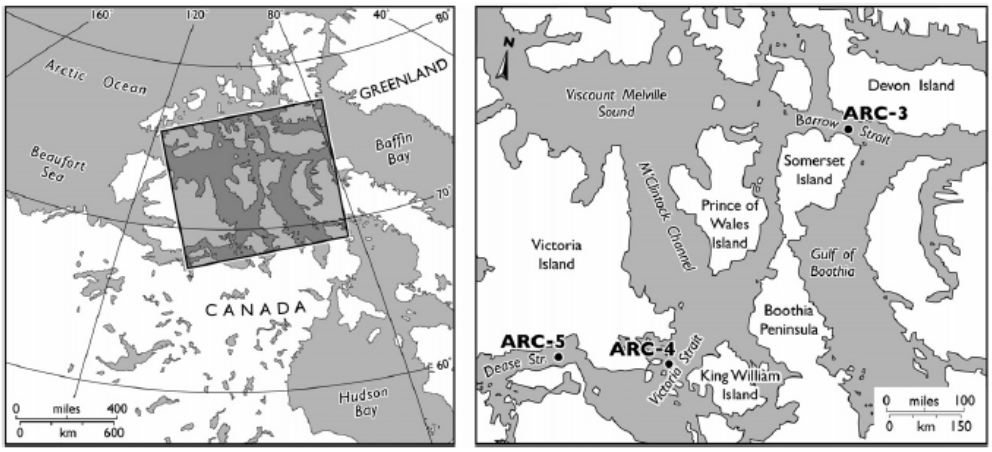

Fig. 1. Map of the Canadian Arctic Archipelago and the sampling locations (ARC-3,4,5) described in the current study.

3.2. Dating of the sediment sequences

We previously determined an age/depth model for ARC-3 based on ^{14}C AMS analyses of bivalve, gastropod and scaphopod shells obtained from ten sediment horizons (Vare et al., 2009). For the current study, we adopted a similar approach to construct an age/depth model for ARC-4, and obtained ^{14}C AMS dates from seven horizons (Beta Analytic, USA; Table 2). Conventional radiocarbon ages were converted to calibrated ages (cal kyr BP) with the CALIB 5.0.1 program (Stuiver and Reimer, 1993), using the calibration dataset Marine04, which incorporates a global ocean reservoir correction of 400 yr. An additional regional marine reservoir correction (ΔR) of 290 ± 40 yr was also applied, taken from Arctic Bay, NW Baffin Island (McNeely et al., 2006). Typical ΔR values for the eastern CAA, taken from the marine reservoir correction database (http://intcal.qub.ac.uk/marine/), range from 180 ± 80 yr to 435 ± 56 yr. Since only one horizon from the ARC-5 core provided sufficient carbonate material for ^{14}C AMS dating, we determined an age/depth model for this core based mainly by matching the magnetic susceptibility profiles of ARC-4 and ARC-5 and using a series of tie points to identify equivalent ages and using ARC-4 as a reference core. Magnetic susceptibility measurements were taken with a GEOTEK multi-sensor core logger.

3.3. Laboratory methods

For biomarker analyses, an internal standard (7-hexylnonadecane; 0.1 μg) was added to sub-samples of freeze-dried sediment material (ca. 1 g), before being extracted using dichloromethane/methanol (3 × 3 mL; 2:1 v/v) and ultrasonication. Following removal of the solvent from the combined extracts using nitrogen, the resulting total organic extracts (TOE) were purified using column chromatography (silica), with hydrocarbons (hexane; 6 mL) collected as a single fraction. The sea ice biomarker IP_{25} was identified using gas chromatography-mass spectrometry (GC–MS) on the basis of its characteristic retention time and mass spectrum (Belt et al., 2007; Vare et al., 2009). Relative sedimentary abundances of IP_{25} were determined on the basis of the magnitudes of its GC/MS responses with those of the internal standard, with these ratios corrected according to the mass of sediment analysed. Analytical reproducibility (±7%) was determined as described previously (Vare et al., 2009).

Total organic carbon (TOC) and total nitrogen (N) of the sediment horizons were determined using ca. 10–20 mg of sediment, using a LECO 900 CHN analyser. Inorganic carbonates were removed with hydrochloric acid (10%; 1 mL; Vare et al., 2009). Acetanilide was used as a calibration standard.

To determine the inorganic geochemical properties of ARC-4, evenly-spaced (10 cm) sediment horizons were selected and subjected to a combined nitric, hydrochloric and hydrofluoric acid total digest, followed by quantitative analysis of individual metals by inductively coupled plasma-optical emission spectroscopy (ICP-OES).

Particle size analyses were undertaken using a Malvern Mastersizer 2000 laser particle sizer as described previously (Vare et al., 2009). Individual distributions of particle sizes were calculated using previously reported methods (Friedman and Sanders, 1978) according to the following classifications – clay: < 2 μm; silt: 2–63 μm; sand (coarse): 63 μm–2 mm. Dry sediment densities were determined for all horizons using % water content and fixed sediment specific gravity (2.65 g cm^{-3}). Particle size measurements were also carried out in conjunction with sediment mineralogy determinations for ARC-4 using X-ray Diffraction (XRD) methods (Eberl, 2003, 2004; Andrews and Eberl, 2007; Andrews, 2009). Briefly, ca. 1 g of sediment (<2 mm–sand, silt, and clay) from 10-cm spaced horizons were combined with ZnO (ca. 0.1 g) before being ground in a McCrone mill (5 min; 4 mL methanol). Following drying and sieving (0.5 mm), fractions were side packed into aluminium

Table 1
Summary of cores and core locations described in the current study.

Sediment Core	ArcticNet stations Location	Water depth (m)	Date of collection	Latitude (N)	Longitude (W)
ARC-3	4 – Barrow Strait	347	24-08-2005	74°16.05′	91°06.38′
ARC-4	6 – Victoria Strait	61	27-08-2005	69°09.94′	100°41.72′
ARC-5	7 – Dease Strait	112	30-08-2005	68°59.45′	106°34.27′

Table 2
Summary of radiocarbon age determinations for the ARC-4 and ARC-5 cores.

Radiocarbon age determinations for ARC-4 and ARC-5							
Core location	Depth (cm)	Material dated (all fragments)	Laboratory sample no. (Beta)	Measured radiocarbon age (yr BP)	Conventional radiocarbon age (yr BP)	2-sigma calibrated age range (cal kyr BP)	Mid-point calibrated age (cal kyr BP)
ARC-4	68.5	Bivalve fragments	250068	1970 ± 40	2420 ± 40	1.86–1.56	1.71
ARC-4	90.5	Bivalve fragments	253521	2240 ± 40	2670 ± 40	2.15–1.86	2.01
ARC-4	131.5	Bivalve fragments	250069	2470 ± 40	2890 ± 40	2.43–2.12	2.27
ARC-4	160.5	Bivalve fragments	253522	2600 ± 40	3010 ± 40	2.62–2.30	2.46
ARC-4	227.5	Bivalve fragments	253523	3130 ± 40	3550 ± 40	3.26–2.92	3.09
ARC-4	317.5	Bivalve fragments	253524	4240 ± 40	4650 ± 40	4.70–4.34	4.52
ARC-4	383.5	Forams (Nodosaria spp.)	254653	7930 ± 40	5880 ± 40	5.88–6.16	6.01
ARC-5	322.5	Bivalve fragments	250070	5640 ± 40	6050 ± 40	6.29–6.01	6.15

sample holders against frosted glass and loaded into a 40 sample carousel. XRD analyses were obtained between 5° and 65° (2-theta; 0.02° steps; 2 s counting integration). The resulting 3000 intensities were processed using "Rockjock", an Excel macro program that uses the "Solver" to match a set of internal mineral standards against the observed XRD pattern (Eberl, 2003). A degree-of-fit (DOF) statistic was calculated and the pattern matching terminated when 5 iterations changed by less than 0.001 or 0.0001 (Eberl, 2003).

Estimates of sediment accumulation rates for box core sediment material were derived by measurement of the excess or unsupported activity of ^{210}Pb (^{210}Pb$_{xs}$) which is incorporated rapidly into the sediment from atmospheric fallout and water column scavenging (Appleby and Oldfield, 1992 and references therein). ^{210}Pb, ^{226}Ra and ^{137}Cs activities were measured using a low background, high-efficiency, well-shaped γ detector exhibiting good reproducibility (Schmidt et al., 2007, 2009). Calibration of the γ detector was achieved using IAEA standards (RGU-1, RGTh-1). ^{210}Pb$_{xs}$ was calculated by subtracting the measured activity supported by its parent isotope, ^{226}Ra, from the total ^{210}Pb activity in the sediment. Errors in ^{210}Pb$_{xs}$ were calculated by propagation of errors in the corresponding pair (^{210}Pb and ^{226}Ra) and represented graphically.

In addition to climate controls on sediment inputs, another important factor, given the relatively shallow waters from which the cores were extracted (Table 1), is the impact of glacioisostatic rebound on seafloor and oceanographic processes. Observations and dating of raised beaches throughout the CAA indicates that over the course of the last 8–9 cal kyr BP, waters have shallowed by 100–150 m or so, depending on location (Andrews, 1970; Dyke, 1998; Dyke and Peltier, 2000; Dyke et al., 2005). The half-life of the rebound is ca. 2 kyr, so shallowing of water depths would have decreased exponentially to the present. Thus, in addition to influences of climate change, we predict that the cores will also record the impact of progressively shallowing water depths.

4. Results

4.1. Core chronologies

The starting point for constructing age/depth profiles for the three cores described in the current study has been the determination of ^{14}C AMS-based age data for carbonate material obtained from individual sediment horizons. For the ARC-3 core (Barrow Strait) characterised previously, the ^{14}C AMS data covered virtually the entire core length, including a relatively recent date of ca. 400 cal yr BP (Vare et al., 2009). In contrast, for the ARC-4 core (Victoria Strait), the youngest of the seven ^{14}C AMS dates measured corresponded to ca. 1700 cal yr BP. In order to address whether the surface of the ARC-4 piston core was (relatively) recent or otherwise, we conducted two complementary methods of analysis.

Firstly, we compared the ^{210}Pb$_{xs}$ activities of the piston core and the corresponding box core to see if they could be matched. Using the assumptions of constant flux and constant sediment accumulation rate (the CF:CS method; Appleby and Oldfield, 1992; Schmidt et al., 2009), the ^{210}Pb$_{xs}$ profile for the ARC-4 box core yielded a mean sedimentation rate of 0.16 cm yr^{-1} (Fig. 2). Significantly, the ^{210}Pb$_{xs}$ content of the surface sediment from the ARC-4 piston core coincided with that of the box core at ca. 8.5 cm (Fig. 2), indicating that only a few cm had been lost through coring. To corroborate these observations and interpretations further, we measured ^{137}Cs levels in the ARC-4 cores. Peak ^{137}Cs activity, corresponding to maximum deposition in 1963 (Andersen et al., 2000), was observed at ca. 7 cm for the ARC-4 box core (Fig. 2) in excellent agreement with that predicted using the estimated sedimentation rate (0.16 cm yr^{-1}) and mixed layer (0.5 cm) derived from the ^{210}Pb data, combined with the core collection date (2005). In addition, ^{137}Cs was observed in the upper section of the ARC-4 piston core. Applying the same offset (8.5 cm) to the piston core ^{137}Cs data reveals excellent overlap with those obtained from the related box core, with both profiles showing diminishing ^{137}Cs activity with depth (Fig. 2).

Secondly, by comparing the down-core profiles (piston & box cores) of a series of other chemical and physical parameters, the extent of any overlap could also be identified. For example, inspection of the down-core profiles of TOC, particle sizes (e.g. % clay & sand) and Ca/Fe, indicated a small loss from the top of the ARC-4 piston core of ca. 8–10 cm (Fig. 3). By using an estimated value of 8.5 cm for the loss of material from the top of the ARC-4 piston core, together with the mean sediment rate determined from the ^{210}Pb$_{xs}$ data (box core; Fig. 2), we estimate the age of the surface of the ARC-4 core to be ca. 60 cal yr BP. This age estimate was combined with the seven ^{14}C AMS dates obtained from shell material isolated from individual horizons downcore to derive an age/depth model via a 3rd order polynomial fit (Fig. 4). This fit was extrapolated to ca. 7 cal kyr BP, corresponding to ca. 1 kyr beyond the oldest ^{14}C AMS-dated horizon (383.5 cm; ca. 6 cal kyr BP).

We were not able to carry out an analogous age/depth model determination for ARC-5 (Dease Strait) since sufficient shell fragment material for ^{14}C AMS analysis was only available from a single sediment sub-sample (Table 2), despite examination of over 400 individual horizons. Instead, we constructed an age/depth model for ARC-5 by correlating magnetic susceptibility (MS) data between cores ARC-4 and ARC-5. This correlation allowed us to extrapolate the ^{14}C AMS-based chronology established for ARC-4 to ARC-5, thereby providing a framework for the downcore MS peaks. In total, nine tie points were identified (Fig. 5). The dates of these tie points were then used together with the single ^{14}C AMS determination for ARC-5 to construct an age/depth model based on a 3rd order polynomial fit as used previously for ARC-4 (Fig. 4). In contrast to ARC-4, the polynomial fit to the (largely) MS-derived dates suggested that a more substantial section of the core top had been lost through

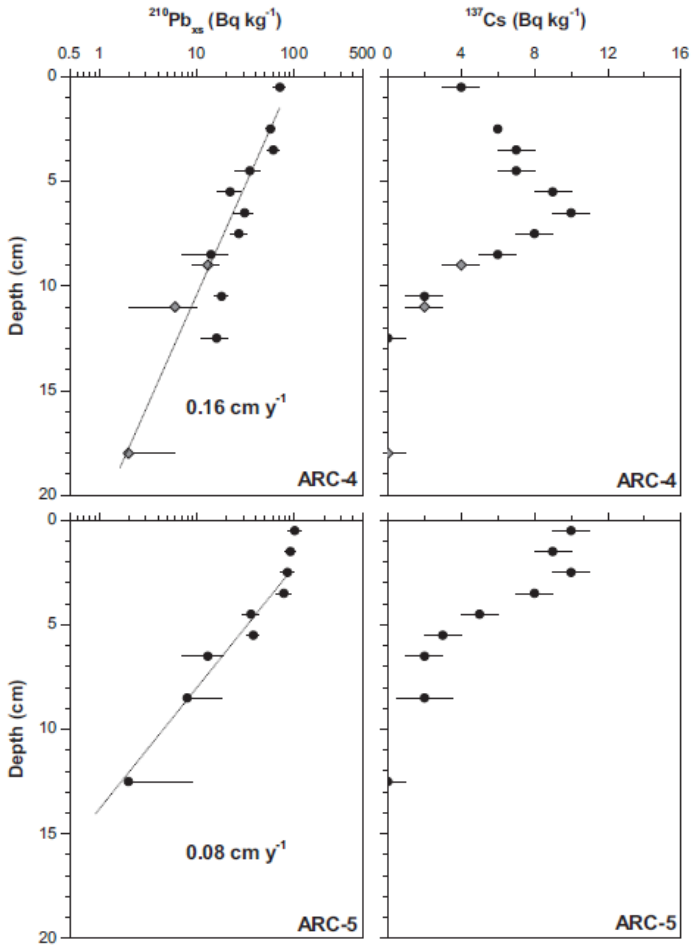

Fig. 2. $^{210}Pb_{xs}$ and ^{137}Cs data (circles) obtained from ARC-4 and ARC-5 box cores with mean accumulation rates. The related $^{210}Pb_{xs}$ and ^{137}Cs data for the near-surface material from the ARC-4 piston core (diamonds) have been offset by 8.5 cm to illustrate the estimate of the amount of sediment lost from the surface of this core. No $^{210}Pb_{xs}$ or ^{137}Cs was detected in the ARC-5 piston core.

coring or, at least, was absent, with the top of the piston core estimated as ca. 580 cal yr BP (Fig. 4). In support of this outcome, no $^{210}Pb_{xs}$ or ^{137}Cs was detected in the top section of the ARC-5 piston core. Since $^{210}Pb_{xs}$ was detected in the corresponding box core down to ca. 13 cm (Fig. 2), we estimate that at least this amount of sediment was lost from the top of the ARC-5 piston core and probably more. In addition, the $^{210}Pb_{xs}$ profile for the box core suggested a mean sedimentation rate of ca. 0.08 cm yr^{-1} for the upper ca. 13 cm (at least) below a mixed layer of ca. 2 cm. This lower sedimentation rate for ARC-5 relative to that estimated for ARC-4 (0.16 cm yr^{-1}) is further demonstrated through the observation of a shallower depth for the peak ^{137}Cs activity (Fig. 2), with the lowest detection level at ca. 8 cm corresponding to the earliest ^{137}Cs input in 1950. If the $^{210}Pb_{xs}$-derived sedimentation rate is extrapolated to 580 cal yr BP (intercept of polynomial fit to the piston core data), this provides an estimate of ca. 45 cm of missing sediment from the top of the ARC-5 piston core. As such, the loss of material from the top of the ARC-5 core is estimated to be at least 13 cm and probably closer to 45 cm.

4.2. Bulk sediment geochemistry

Although the determination of past spring sea ice occurrence for the central CAA is based primarily on IP_{25} biomarker profiles obtained for the ARC-4 and ARC-5 cores, we anticipated that the decrease in relative sea level at the core sites over the last 8 kyr would probably have resulted in some overprinting of any climatic signal in the physical nature of the cores. Therefore, in addition to the IP_{25} analyses, we also determined the bulk organic matter and particle size distributions for ARC-4 and ARC-5 and, in addition, quantitatively measured inorganic elements and mineralogical features of the ARC-4 core, in order to either provide complementary proxy data to the IP_{25} fluxes and/or to assess for any major changes in sediment provenance.

Firstly, we determined the inorganic element composition of ARC-4 by acid digestion of sediments followed by analysis by ICP-OES, with the aim of investigating any possible lithogenic changes to the sediment material (Croudace et al., 2006). Ti/Rb was

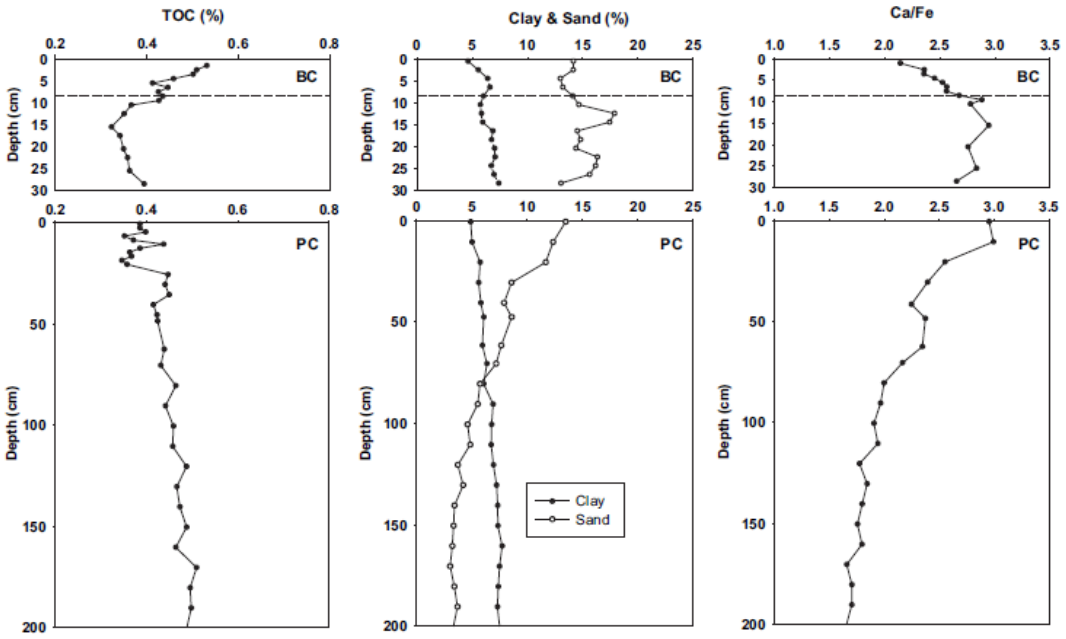

Fig. 3. Downcore profiles of TOC, particle sizes (clay and sand %) and Ca/Fe for the box core (BC) and piston core (PC) obtained from Victoria Strait (ARC-4) used to estimate the degree of overlap between the two cores. The horizontal dashed lines at 8.5 cm indicate the offset between the two cores based on the $^{210}Pb_{xs}$ data (Fig. 2).

extremely consistent, indicating deposition of geochemically similar material downcore as observed previously for ARC-3 (Vare et al., 2009), while the Al composition decreased slightly towards the top of the core but with a mean value (2.5%) within the typical range for marine sediments (Chester, 1990; O'Brien et al., 2006). In contrast to these lithogenic indicators, Ca/Fe ratios, proposed as an indication of palaeo productivity (Croudace et al., 2006), showed a substantial increase after ca. 3.0 cal kyr BP, after an interval of consistency in the lower section of the core (Fig. 6). Inorganic element analysis of ARC-5 was not performed.

Secondly, we determined particle size distributions for both ARC-4 and ARC-5. By the laser particle sizer method, the silt fraction was

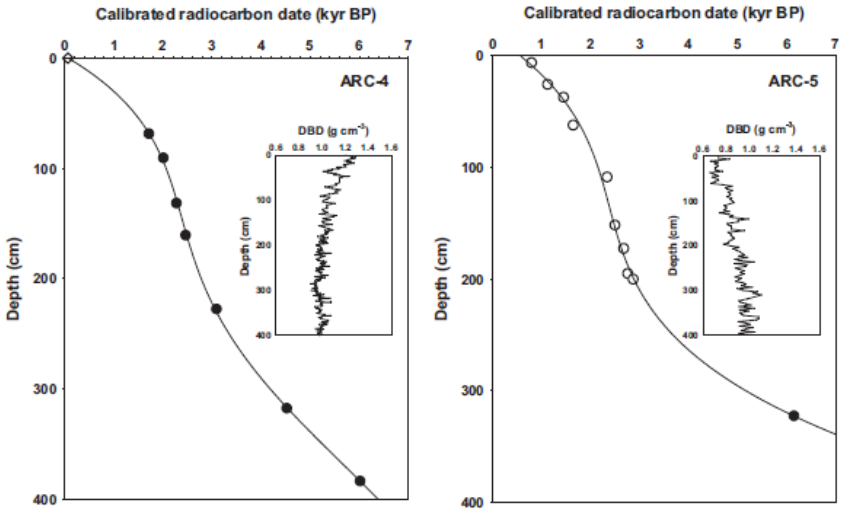

Fig. 4. Age/depth profiles for ARC-4 and ARC-5. For both profiles, solid circles refer to ^{14}C AMS dates; for ARC-4, the open diamond corresponds to the estimate of the age of the core-top based on the $^{210}Pb_{xs}$ and other composition data shown in Figs. 2 and 3; for ARC-5, the open circles correspond to ages derived from the matched (ARC-4 & ARC-5) magnetic susceptibility data (Fig. 5). Inset: Sediment dry bulk densities (DBD).

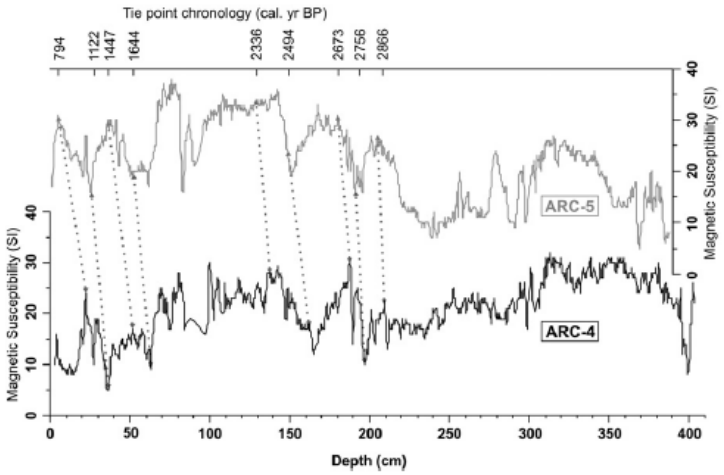

Fig. 5. Comparison of magnetic susceptibility (MS) data from ARC-4 and ARC-5. Ages of individual horizons from ARC-4 (^{14}C AMS dates) permit the establishment of an age model for ARC-5 by matching of the MS records. Dashed lines show points of correlation between MS data.

identified as the major component in each case, representing 80–90% and >90% for ARC-4 and ARC-5, respectively (Fig. 7). The most substantial change identified for either core was seen in the sand fraction for ARC-4, which increased steadily from ca. 2% in the 7.0–3.0 cal kyr BP interval to ca. 14% at the surface of the core. Particle size distributions were also determined for ARC-4 using XRD. Notably, the silt fraction was identified as the major component (mean 86%), with smaller amounts of sand and clay. The sediment shows a strong enhancement in the % sand beginning at ca. 3 cal kyr BP (3%), increasing to 14% at the core-top, in excellent agreement with the particle sizer method as expected. XRD analysis also shows that the non-clay mineral fraction shows a steady but non-linear increase from the base of the core to ca. 2.5 cal kyr BP, after which there is a steady increase to ca. 87 wt%. In contrast, both clay-sized particles and clay minerals decrease in wt% toward the present. Closer examination of the non-clay mineral composition reveals the presence of felsic and carbonate minerals including quartz and dolomite, both of which have increased over the last 7 cal kyr BP. In contrast, the dominant clay mineral (illite) decreased upcore from ca. 12 to 6 wt% (Fig. 6).

Thirdly, we measured the TOC composition of each core to determine whether any potentially significant changes in the input/retention of organic material may influence the IP_{25} flux profiles. For each of ARC-4 and ARC-5, the TOC content was relatively low (<1%), with no major alterations downcore (Fig. 7) indicating that variations in IP_{25} fluxes were unlikely to be influenced by changes in TOC or due to significant degradation. In addition, we derived downcore C/N ratios (where possible) to identify whether there were any major changes to the sources of organic matter (OM). Consistent with the TOC data, C/N profiles for ARC-5 showed little change downcore, with values (C/N ca. 6–10; data not shown) indicative of OM of largely marine origin (Meyers, 1994; Stein and Macdonald, 2004). The corresponding values for ARC-4 could not be determined in many cases since the nitrogen levels were below or too close to the limit of detection.

4.3. Sea ice biomarker - IP_{25}

In the current study, we analysed for the sea ice biomarker IP_{25} in each of ARC-4 and ARC-5 at a ca. 3 cm sampling interval, which corresponds to an effective age resolution of ca. 20–100 yr. In order to allow us to make comparisons between the cores, and to keep the analyses within reasonable ranges defined by the age/depth models, we limited the oldest age for analysis of IP_{25} and other proxy data to 7 cal kyr BP (i.e. 1 kyr extrapolated beyond the oldest ^{14}C AMS date; Table 2). IP_{25} concentration profiles for ARC-4 and ARC-5 show relatively little variation downcore (Fig. 8) other than some elevated levels in the upper horizons. However, concentration versus depth profiles can be potentially misleading with respect to quantitative interpretation of IP_{25} data, since they do not adequately reflect the influences of any changes in bulk sediment properties (e.g. density) or accumulation rates seen for each core. These are important factors, since a key feature of the IP_{25} proxy is its annual production cycle by sea ice algae followed by deposition and incorporation into underlying sediments following sea ice melt. Therefore, in order to provide more meaningful assessments of sedimentary IP_{25} that more accurately represent deposition on a consistent (annual) timescale, we converted all IP_{25} concentrations to annual fluxes, by combining individual sediment concentrations with sediment densities and accumulation rates derived from dry bulk density data and age/depth models (Fig. 4), respectively (Müller et al., 2009; Vare et al., 2009, 2010). The resulting IP_{25} flux profiles for the ARC-4 and ARC-5 cores (Fig. 9) have a number of common features with some differences as follows. Firstly, the detection of IP_{25} in each of the ARC-4 and ARC-5 horizons analysed (Fig. 9), indicates the occurrence of (at least) partial spring sea ice conditions on bidecadal – centennial timescales. A similar observation and interpretation was made previously for ARC-3 (Fig. 9; Vare et al., 2009). For each of ARC-4 and ARC-5, the IP_{25} fluxes are consistently below the median values for virtually the entire interval from ca. 7.0 cal kyr BP to ca. 3.5 cal kyr BP (Fig. 9). Brief exceptions to this general trend occur for ARC-4 during two short intervals ca. 5.9–5.7 cal kyr BP and ca. 3.8–3.6 cal kyr BP, during which times, the IP_{25} fluxes are slightly above the median. After ca. 3.0 cal kyr BP, the IP_{25} fluxes increase sharply in both cores, and higher than median values are sustained before declining again below the median at ca. 1.8–1.5 cal kyr BP, reaching values seen at the beginning of the record. Finally, for ARC-4, the IP_{25} fluxes increase above the median during the last 500–600 yr (Fig. 9). We are unable to make a firm related observation for ARC-5 due to the reduced dataset caused by the loss of the core-top during coring,

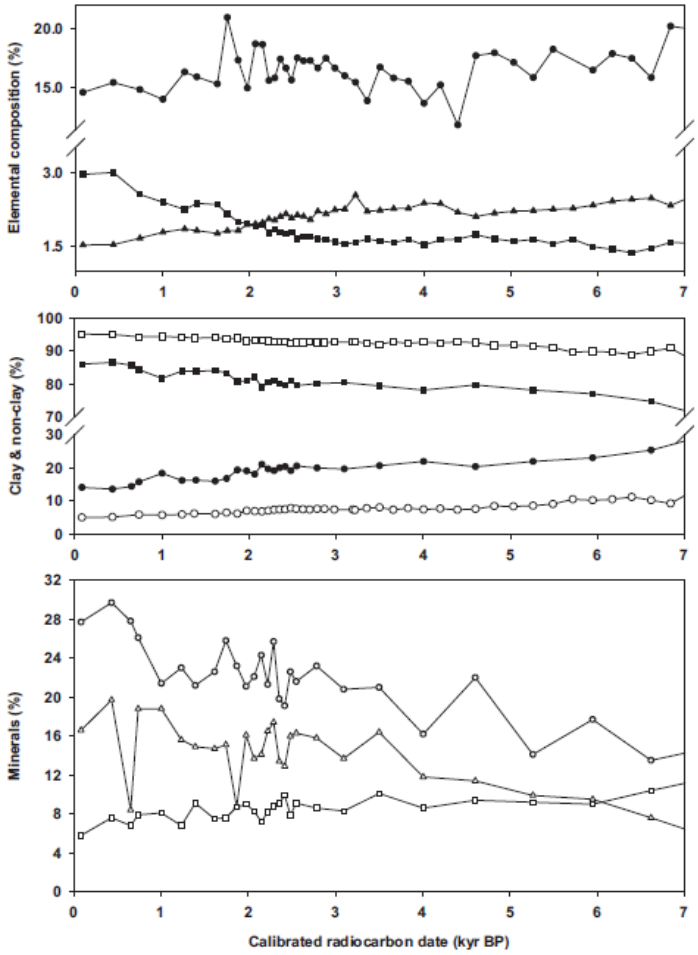

Fig. 6. Elemental and mineralogical data for ARC-4. Top plot:(● = Ti/Rb; ▲ = Al; ■ = Ca/Fe). Middle plot: clay (XRD = ●; particle sizer = ○) and non-clay (XRD = ■; particle sizer = □) size distributions. Lower plot: Main minerals (Quartz = ○; Dolomite = Δ; Illite = □).

although there is some evidence for increased IP_{25} fluxes after ca. 600 cal yr BP (Fig. 9).

These temporal changes to the IP_{25} fluxes in the ARC-4 and ARC-5 cores broadly parallel those reported for ARC-3 previously (Vare et al., 2009) and the data for the latter are presented again here for further comparison (Fig. 9). For example, the relatively low (below median) IP_{25} fluxes observed for ARC-4 and ARC-5 during the mid-Holocene (ca. 7.0–3.5 cal kyr BP) are also seen in the ARC-3 IP_{25} flux profile. This is followed by an interval beginning ca. 3.0–2.8 cal kyr BP, where the IP_{25} fluxes remain higher than the median, before declining ca. 2.0–1.5 cal kyr BP depending on the core location. However, in contrast to ARC-4 and ARC-5, in the case of ARC-3, the magnitude of this decline is less dramatic, and IP_{25} fluxes do not fall below the median. For all three cores, there is a period in the late Holocene (beginning ca. 700–500 cal yr BP) where IP_{25} fluxes again increase.

In order to make these cross-core comparisons more quantitative, we re-expressed the IP_{25} flux data on two common timescales using the Analyseries program v 2.03 (Paillard et al., 1996). Initially, we chose a sampling interval of 100 yr, since this corresponded to the lowest resolution in any of the three cores. The resulting IP_{25} flux profiles (Fig. 10), further highlight the similarities and differences described previously. All 100-yr IP_{25} flux profiles are strongly correlated with that between ARC-4 and ARC-5 being the most striking ($r = 0.86$; $p < 0.0001$). The corresponding correlations between ARC-3 and ARC-4 ($r = 0.72$; $p < 0.0001$) and between ARC-3 and ARC-5 ($r = 0.70$; $p < 0.0001$) are also significant; the slightly poorer correlations involving ARC-3 likely due to differences in the three profiles since ca. 2 cal kyr BP, although all correlations are likely to be influenced to some degree by the accuracy of the core chronologies. A higher resolution between ARC-3 and ARC-4 was also achievable and, at a 50-yr interval, ARC-3 and ARC-4 were also significantly correlated ($r = 0.70$; $p < 0.0001$).

5. Discussion

Previously, reconstructions of palaeoclimate for the Canadian Arctic region during the Holocene have been derived mainly from

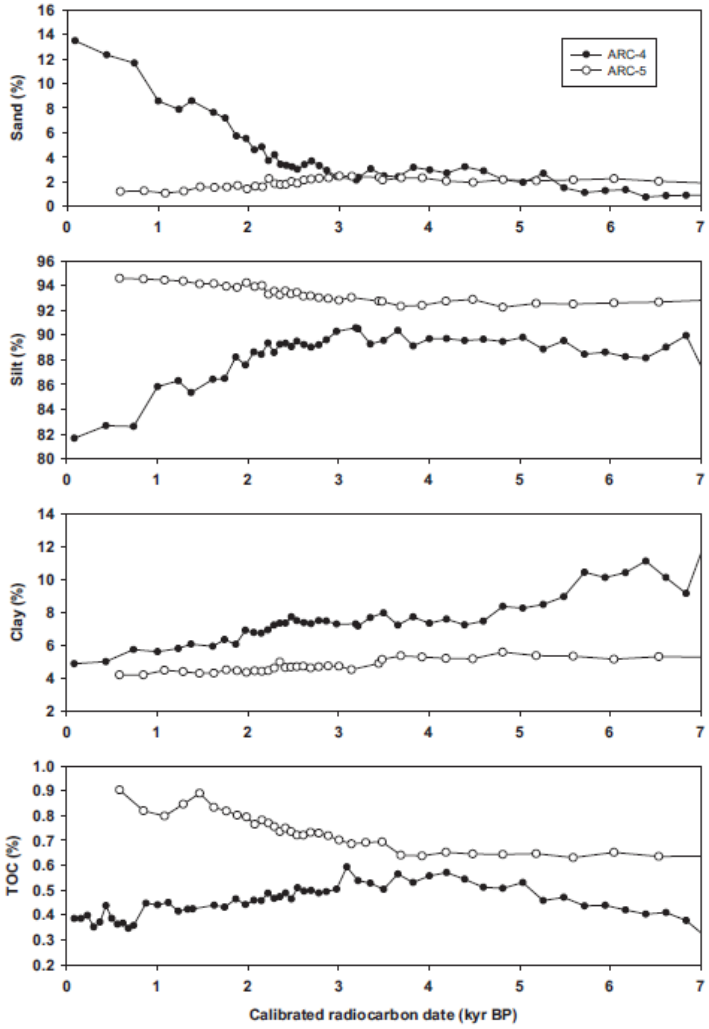

Fig. 7. TOC and particle size data for ARC-4 and ARC-5 piston cores.

proxy-based analyses of lacustrine and marine sediments, ice cores and archive/observational records. These include evidence from the Agassiz ice cap melt data (Koerner and Fisher, 1990), microfossil assemblage distributions, including diatoms (e.g. Smith, 2002; LeBlanc et al., 2004; Podritske and Gajewski, 2007), calcareous microfossils (e.g. Knudsen et al., 2008; Gregory et al., in press), dinoflagellate cysts (Levac et al., 2001; Mudie et al., 2001, 2005, 2006; Ledu et al., 2008), and pollen records (e.g. Gajewski, 1995; Zabenskie and Gajewski, 2007; Peros and Gajewski, 2008, 2009). Analysis of dinoflagellate cysts, foraminifera and diatoms in Arctic sediments have been used to infer sea surface temperature and sea ice conditions, but this approach has been limited largely to Baffin Bay and the eastern region of the Canadian Arctic (e.g. Levac et al., 2001; Mudie et al., 2005; Ledu et al., 2008), although some studies for the western region, including the Mackenzie Shelf in the Beaufort Sea (Richerol et al., 2008) and the Alaskan margin in the eastern Chukchi Sea (McKay et al., 2008) are beginning to be reported.

The most comprehensive evidence for sea ice conditions within the CAA comes from archival records such as bowhead whale remains (Dyke et al., 1996b; Savelle et al., 2000), marine mollusc assemblages (Dyke et al., 1996a), and the presence of driftwood located on raised beaches (Dyke et al., 1997). For example, Dyke et al. (1996b) and Savelle et al. (2000) interpreted the abundances of bowhead whale remains to suggest a period of maximum postglacial warmth between 10.5 and 8.5 cal kyr BP, followed by severe ice conditions at 8.5–5.0 cal kyr BP, with the central channels of the CAA effectively plugged with ice throughout the year. Bowhead whale remains reappeared within the CAA after ca. 5.0 cal kyr BP, indicative of lower summer sea ice conditions, before a further decline in numbers after 3.0 cal kyr BP, suggestive of a return to enhanced sea ice cover. In contrast, bowhead whales only really populated the western region of the CAA during the early and late Holocene (Dyke and Savelle, 2001). These observations have recently been complemented by biomarker (IP_{25})

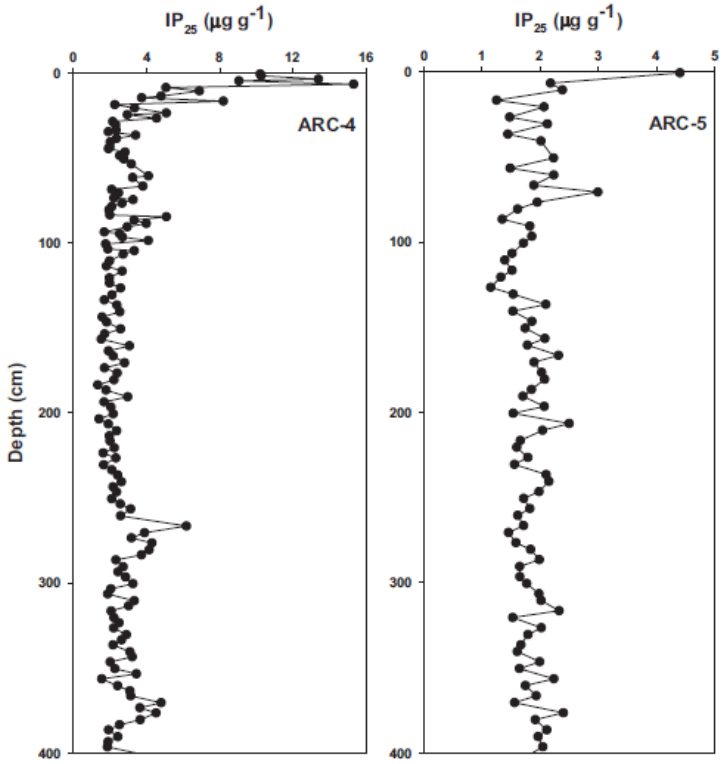

Fig. 8. Downcore concentration profiles of IP_{25} in ARC-4 and ARC-5.

derived sea ice data obtained from Barrow Strait (Vare et al., 2009) and we add to this evolving dataset here following determination of temporal changes to IP_{25} fluxes for Victoria Strait and Dease Strait.

The continuous occurrence of the IP_{25} biomarker back to 7 cal kyr BP for all three study locations (Barrow Strait, Victoria Strait and Dease Strait, Fig. 1), provides further confirmation of the retreat of the main ice margins within the central CAA channels by this time (Dyke, 1999; Dyke et al., 2002; Kaufman et al., 2004), since sea ice formation and melt must have occurred in order for sedimentary deposition of IP_{25} to have taken place. IP_{25} data reported previously for Barrow Strait also indicated that retreat of the main ice sheets for this region was complete by ca. 10 cal kyr BP (Vare et al., 2009), and this is possibly also the case too for both Victoria Strait and Dease Strait since IP_{25} was detected in all sediment horizons to the base of each core. However, the reliability of the age models for these two locations prior to 7.0 cal kyr BP are not sufficiently high to permit this same conclusion to be drawn with complete confidence.

The observation of continuous, non-zero values for the IP_{25} fluxes, also demonstrates the absence of extended periods of ice-free conditions or permanent ice cover, at least within the sampling intervals investigated (Müller et al., 2009). One question that remains, however, is to what extent variations in IP_{25} fluxes can be interpreted further in terms of changes to sea ice conditions in a general sense or, more quantitatively, with respect to sea ice occurrence. For example, while the conditions responsible for an absence of IP_{25} are readily understood for the two extreme scenarios of ice-free waters and permanent ice cover (Müller et al., 2009), establishing whether there is a minimum or threshold sea ice occurrence before IP_{25} is produced and detected is less clear at present. In addition, IP_{25} production may be controlled to some extent by localised conditions such as snow cover or nutrients, both of which have been reported to influence sea ice algal biomass (Mundy et al., 2005; Gradinger, 2009; Różańska et al., 2009). However, despite some clear evidence for nitrate limitation on sea ice-derived biomass (Gradinger, 2009; Różańska et al., 2009), anomalies to this general trend also exist, likely as a result of other biological and physical influences (Różańska et al., 2009). In addition, influences of environmental parameters on bulk biomass production may not extend to individual species or lipids, including IP_{25}. Further, while short-term biomass production is generally lower under high snow cover conditions (Mundy et al., 2005; Różańska et al., 2009), the accompanying thermal insulation of sea ice can result in a lengthening of the algal growth season (Mundy et al., 2005), with the potential for some compensation to otherwise lower productivity. To date, an evaluation of all of the potential influences on sea ice algal biomass and individual lipid production is prevented by the absence of detailed time series studies from point locations which are logistically prohibitive (Mundy et al., 2005) and unlikely to ever be pan-Arctic. For palaeo studies based on sedimentary analyses, both spatial and temporal smoothing of individual influences that may exist on a seasonal or annual basis also deserve consideration, especially for temporal resolutions of >20 yr as presented here. Given the difficulties in firmly establishing all of the possible influences on IP_{25} production

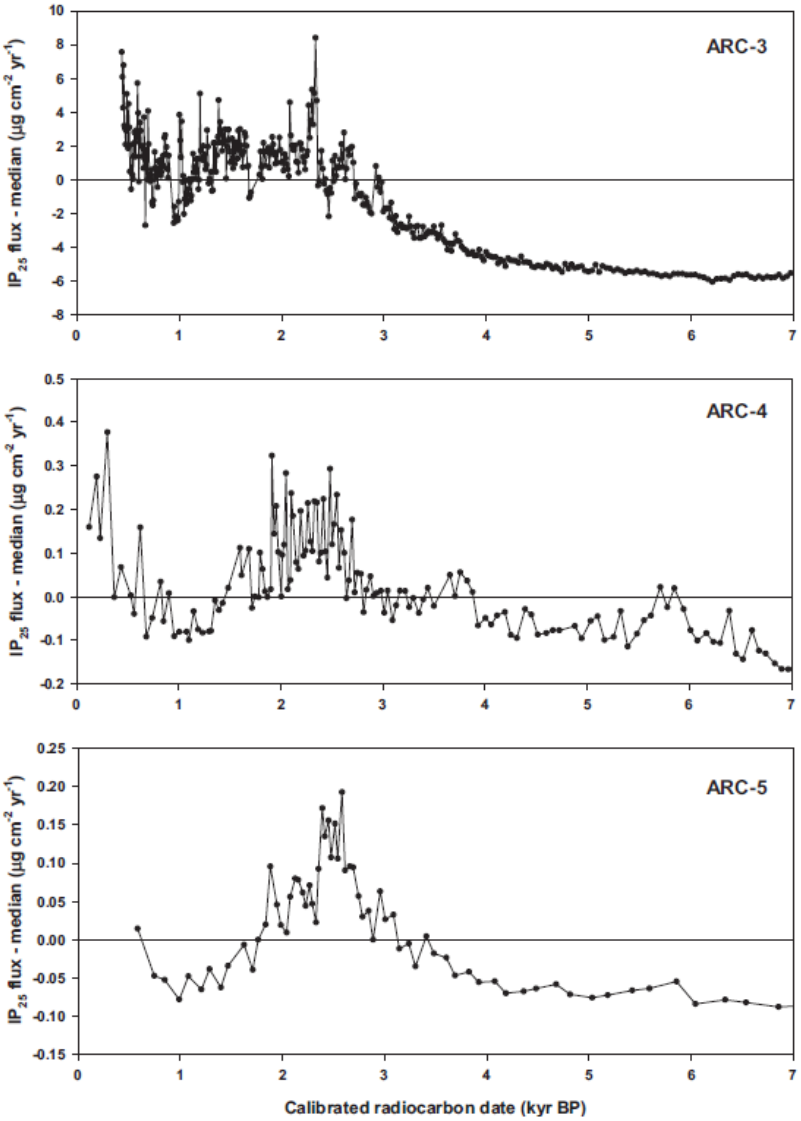

Fig. 9. IP_{25} flux profiles (value – median) for ARC-3 (Barrow Strait), ARC-4 (Victoria Strait) and ARC-5 (Dease Strait).

in sea ice and deposition in the sedimentary record, a more realistic approach to evaluating the significance of variable IP_{25} in sediments would be to calibrate abundances or fluxes against known sea ice conditions or by cross comparison with other sea ice proxies. To date, this has been done with some success with palaeo sea ice studies from north Iceland (Massé et al., 2008; Andrews et al., 2009) and the Barents Sea (Vare et al., 2010).

Currently, modern core-top data for IP_{25} do not exist, preventing quantitative calibrations against known sea ice conditions to be made. Increased IP_{25} fluxes are therefore generally interpreted qualitatively in terms of higher occurrences of spring sea ice. However, since some factors responsible for IP_{25} formation/deposition are understood, it is possible to offer some further interpretations of IP_{25} flux data, especially for the CAA where the timings of sea ice formation and melt are reasonably well known. For example, sea ice formation in the CAA begins in September with melting taking place (May–June) after the peak diatom bloom and IP_{25} production in April (Belt et al., 2007, 2008; T. Brown, personal communication). As such, the observation of IP_{25} deposition in underlying sediments most likely reflects the occurrence of at least 8 months yr^{-1} sea ice (Sept–April). An upper limit of ca. 11 months yr^{-1} can also be proposed given the additional requirement of summer ice melt following the diatom bloom. If this range of 8–11 months yr^{-1} is accepted as part of the requirement

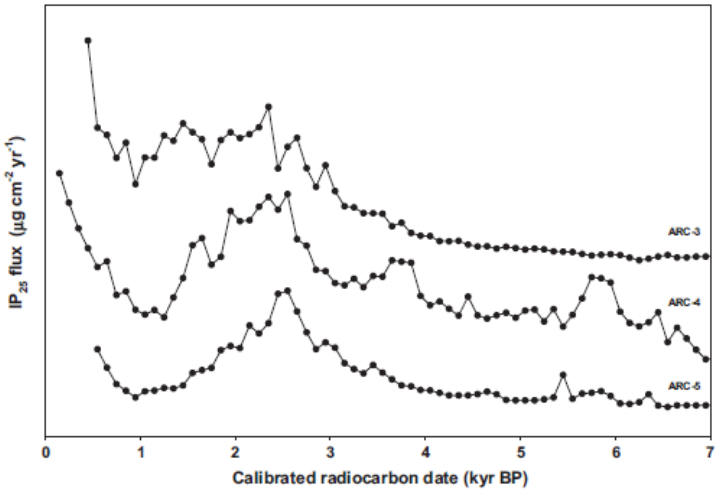

Fig. 10. 100-yr averaged IP_{25} flux datasets for ARC-3, ARC-4 and ARC-5. The individual datasets have been offset for illustrative purposes only. Flux ranges are as follows: ARC-3: 0.6–14.0 µg cm^{-2} yr^{-1}; ARC-4: 0.02–0.4 µg cm^{-2} yr^{-1}; ARC-5: 0.03–0.3 µg cm^{-2} yr^{-1}.

for IP_{25} to be formed and deposited in sediments, then changes in IP_{25} fluxes observed downcore may reflect variations in the frequency of these conditions during a sampling interval (typically 20–100 yr), rather than a more extreme presence/absence of sea ice on an annual basis. As a consequence, relatively small but consistent changes to periods of sea ice cover from e.g. 8 months yr^{-1} (IP_{25} present) to 6 months yr^{-1} (IP_{25} absent) may have strong influences on the observed IP_{25} flux profiles. Therefore, changes to IP_{25} fluxes might be best interpreted in terms of variations in frequency of 8–11 months yr^{-1} sea ice, with higher fluxes indicating relatively frequent occurrence. Lower fluxes would indicate a higher frequency of <8 months yr^{-1} sea ice, although identification of to what extent the sea ice period falls below this threshold value is less reliable. Such conclusions should be considered with caution, however, and further calibrations using modern core-top material should be carried out before existing IP_{25} flux datasets are re-expressed in these terms. For the purposes of the current study, a qualitative interpretation of IP_{25} fluxes in terms of more/less spring sea ice occurrence is used.

The close agreement between the three IP_{25} profiles indicates a significant degree of consistency in spring sea ice occurrence across the central CAA since ca. 7 kyr BP, despite the core locations being separated by up to 800 km (Barrow Strait – Dease Strait) and representing quite distinct locations within the Northwest Passage. Thus, the early – mid Holocene (from ca. 7 to 3 cal kyr BP) for all three locations is characterised by relatively low spring sea ice occurrence, followed by an interval beginning at ca. 3 cal kyr BP where elevated IP_{25} fluxes indicate higher frequencies of spring sea ice. Evidence is also provided for a return to lower spring sea ice occurrence after ca. 2.0–1.5 cal kyr BP, though this is most evident for the two lower latitude locations (ARC-4 and ARC-5; Victoria Strait and Dease Strait; Fig. 1), discussed in more detail later. The observation of, consecutively, relatively low and high (and variable) spring sea ice occurrence in the early and middle-late Holocene is consistent with a sea ice duration profile for northern Baffin Bay, based on dinocyst assemblages, which showed that a key low-to-high sea ice transition occurred at ca. 4.5 kyr BP (Levac et al., 2001). Dinocyst assemblage data have also shown that for Lancaster Sound, east of Barrow Strait, a shift towards cooler summer temperatures and higher sea ice conditions took place ca. 2.9 cal kyr BP (Ledu et al., 2008). Interestingly, in both of these cases, sea ice duration was variable, but was estimated to fall within the range 7–11 months yr^{-1} since ca. 6.5 cal kyr BP, in reasonable agreement with the hypothesis presented here, that sedimentary IP_{25} occurrence reflects sea ice duration of ca. 8–11 months yr^{-1} for the CAA. Finally, with respect to the western region of the CAA, an elevation in seasonal sea ice observed for ARC-4 and ARC-5 at ca. 3.0 cal kyr BP may provide further evidence for an association between climate conditions and declining Palaeoeskimo populations on Victoria Island around this time as suggested previously (Savelle and Dyke, 2002). Changes in sea ice and more general influences of climate on paleoeskimo populations throughout the Canadian Arctic have also been reported (Mudie et al., 2005).

These interpretations of the IP_{25} data for the three locations in the central CAA are both in agreement with, and at first sight, contradictory to, those obtained from analysis of bowhead whale remains in raised beach deposits throughout the archipelago (Dyke et al., 1996b; Savelle et al., 2000). For example, both the fossil and biomarker (for Barrow Strait, at least; Vare et al., 2009) records indicate low sea ice conditions during the early Holocene as evidenced by relatively high numbers of bowhead whale remains and low IP_{25} fluxes, respectively (Dyke et al., 1996b; Vare et al., 2009). Similarly, the two proxies suggest that since ca. 3 cal kyr BP, sea ice conditions were much higher than for the early – mid Holocene, with some returns to lower sea ice frequency, particularly from ca. 1.5 to 0.8 cal kyr BP, prior to establishment of modern (and high) sea ice conditions. The exception to these general agreements between the two datasets occurs in the mid-Holocene where, for example, the virtual absence of bowhead whale remains from ca. 8 to 5 cal kyr BP, attributed to impenetrable or permanent sea ice conditions, contradicts the relatively low (below median) fluxes of IP_{25} indicative of lower seasonal sea ice occurrence. Previously, Vare et al. (2009) noted these same differences based on IP_{25} data for Barrow Strait only, and proposed a number of potential explanations for this apparent discrepancy, including differences between the proxies themselves and what they represent. They also considered spatial variations in effective sampling locations between the two proxies and the possible limitations of the

bowhead whale data given some relatively low sample numbers (Vare et al., 2009). The most satisfactory of these alternative explanations, however, was considered to be the likely differences between the proxies themselves, but this was not particularly elaborated on. Here, we attempt to rationalise the apparent anomaly between the two records further, by consideration of what we believe to be the key differences between the two proxies.

With respect to the biomarker-based approach, IP_{25} is currently believed to originate from relatively thin landfast or drift ice (typically first year ice) conditions capable of providing the necessary environment for sea ice diatom growth in the spring. Following summer melt, the sea ice bearing diatoms are released into the water column and subsequently deposited in sediments with release of IP_{25} (Belt et al., 2007; Vare et al., 2009). It is unlikely that significant (if any) IP_{25} production and deposition into underlying sediments would result from thick multiyear pack ice or from permanent ice cover conditions. Indeed, sedimentary IP_{25} has recently been shown to be present in Arctic sediments during intervals of seasonal sea ice, yet absent for periods of permanent ice cover, at least for northern Fram Strait (Müller et al., 2009). In contrast, while the migratory preference of bowhead whales for an ice-edge habitat is likely associated with a number of factors, including a lack of competition for food from other whales (since bowheads can survive the harsh ice conditions), and protection from predators such as the killer whale (Dyke et al., 1996b), this association is probably not so limited to a particular ice type (e.g. Laidre et al., 2008). However, permanent ice cover conditions would prevent access to channels and/or would lead to entrapment resulting in low numbers. Associations between bowhead whale numbers and changes in mortality rates, low food supply or insufficient ice were previously considered unlikely alternative explanations for observed low frequencies for a number of reasons (Dyke et al., 1996b).

In recent decades, the central CAA channels have been characterised by a combination of first year and multiyear ice with a high degree of short-term (years) variability in the distribution between the two (e.g. Maxwell, 1981; Kwok, 2006). However, although summer sea ice clearance occurs at least to some extent from most of the region via the major peripheral gateways (e.g. McClure Strait, Lancaster Sound), the relatively narrow and shallow central channels including M'Clintock Strait experience extreme sea ice build up resulting in a so-called sea ice plug or drain trap (Dyke et al., 1996b; Howell et al., 2008). Since the occurrence of first year ice (formation and melt) and multiyear ice (in situ formation and drifting) are neither mutually exclusive nor necessarily associated, it is feasible for the two scenarios to occur independently or co-exist, and the observed short-term variability in sea ice type within the central CAA in recent decades is testimony to this (Maxwell, 1981; Kwok, 2006). Indeed, lower first year sea ice cover in the CAA, attributed (in part) to a longer melt season in recent years, has not always been accompanied by lower multiyear ice in the CAA, since open water conditions have enabled transfer of the latter from the Arctic Ocean via the northern channels (Howell et al., 2009). More specifically, despite overall reductions in Arctic sea ice conditions in recent decades, the sea ice drain trap in M'Clintock Strait and Peel Sound has continued to form as a result of both in situ ice formation and advection of multiyear ice facilitated by higher west-to-east winds and warmer, more open water conditions (Howell et al., 2008). Therefore, within the resolvable time periods for proxy-based analyses (decadal – centennial), it is plausible that during intervals of relatively low seasonal sea ice conditions in the mid-Holocene (low IP_{25} fluxes), the central channels may have remained effectively blocked with multiyear ice, preventing intrusion into and across this region by bowhead whales, as was observed from ca. 8.0 to 5.0 cal kyr BP (Dyke et al., 1996b). Conversely, intermittent flushing of the central channels, even if infrequent, may account for the small numbers of bowhead whales that did enter the central channels during this interval and somewhat higher numbers from ca. 5.0 to 3.0 cal kyr BP (Dyke et al., 1996b). Indeed, the observation of rafted driftwood provides further evidence for at least some occurrence of mobile ice/water conditions during the middle Holocene (Dyke and Morris, 1990). In contrast, permanent landfast ice would have prevented deposition of driftwood as reported recently for the northeast coast of Ellesmere Island by ca. 5 cal kyr BP and somewhat later within Clements Markham Inlet (England et al., 2008). These observations, along with our proxy data and the reporting of elevated frequencies of driftwood in the central CAA in the later Holocene (Dyke et al., 1997) indicate that these channels became increasingly impacted by sea ice over the last 5 cal kyr BP, and especially so since ca. 3 cal kyr BP.

During the latter part of the record (since ca. 1.5–2.0 cal kyr BP), both the biomarker and bowhead whale fossil records suggest a period of relatively low sea ice conditions, with a return to elevated occurrences after ca. 800 cal yr BP. Although temporal ranges for the so-called Medieval Warm Period (MWP) and the Little Ice Age (LIA) for the northern hemisphere are not particularly well defined (Hughes and Diaz, 1994; Broecker, 2001; Grove, 2001), and appear to be influenced significantly by location (e.g. Mayewski et al., 2004), the interval of lower IP_{25} fluxes (especially for ARC-4 and ARC-5) and a reoccurrence of bowhead whale remains, interpreted as reflecting low sea ice conditions, coincides broadly with the general timescale for the MWP (Grove and Switsur, 1994; Matthews and Briffa, 2005; Podritske and Gajewski, 2007; Wanner et al., 2008). Similarly, higher IP_{25} fluxes in all three records and a paucity of bowhead whale remains after ca. 500–800 cal yr BP align well with the LIA interval, and further evidence for the occurrence of both periods comes from other biotic proxy studies from the CAA, including those derived from lacustrine pollen (e.g. Zabenskie and Gajewski, 2007; Peros and Gajewski, 2008, 2009), diatom (LeBlanc et al., 2004; Podritske and Gajewski, 2007) and chironomid (e.g. Porinchu et al., 2009) records.

Zabenskie and Gajewski (2007) provided evidence for a warming event at ca. 750–900 yr BP based on pollen distributions in a lacustrine core obtained from North West Boothia Peninsula, with cooler conditions either side of this interval. This study, which also indicated a relatively warm mid-Holocene consistent with the IP_{25} data presented here, was complemented by diatom analyses of the same core, which revealed a greater diversity in species composition from ca. 1.15 kyr BP to 0.6 kyr BP suggestive of a warmer climate (LeBlanc et al., 2004). Conversely, diatom species diversity was significantly lower before and after (0.6–0.15 kyr BP) this interval, indicative of cooler conditions (LeBlanc et al., 2004). Other pollen and diatom records for the central CAA also reveal the occurrence of relatively warm intervals ca. 2.0–1.0 kyr BP (e.g. Podritske and Gajewski, 2007; Peros and Gajewski, 2008, 2009), although it remains unclear whether some of the temporal discrepancies that exist between the individual records are due to real differences in climate conditions or if they reflect uncertainties in core chronologies and/or interpretations of individual proxies. Clearly, such uncertainties also exist with the IP_{25} proxy data presented here, in part due to difficulties in the modelling of core chronologies, especially for relatively short (e.g. centennial) timescales, which are particularly influenced by estimates of and/or variations in ΔR. Lacustrine chironomid records, used to infer mean summer air temperatures, also identify the occurrence of cooler conditions between 1100 and 1600 AD (ca. 850–350 cal yr BP) for southeast Victoria Island (proximal to ARC-4), in good agreement with other proxy air temperature determinations based on biogenic silica and treeline zone studies (Porinchu et al., 2009).

This reduction in spring sea ice conditions during the MWP is less apparent for Barrow Strait (ARC-3) which is both north and east of Victoria Strait (ARC-4) and Dease Strait (ARC-5). Previously, Vare et al. (2009) noted some depletion in IP_{25} fluxes between ca. 1.2–0.8 cal kyr BP, before an increase during the last 400 yr of the record (ca. 0.8–0.4 cal kyr BP), but it would appear from the additional data presented here, that this reduction is not as marked as for the two south-westerly locations (Figs. 6 and 7). Although sea ice represents only one component of the climate system, it is known that the timings of the initiation and termination of the HTM for the western Arctic are spatially variable (Kaufman et al., 2004). Such conclusions may be influenced to some extent by the accuracies of core chronologies and by the responses of individual proxies to climate changes (e.g. Viau et al., 2006), but most studies indicate a degree of heterogeneity in the timing of these events with, for example, a delay in the initiation of the HTM in the eastern region of the Canadian Arctic resulting from the cooling effects of the residual Laurentide Ice Sheet (LIS), despite hemispheric forcing (Kaufman et al., 2004). In the neoglacial, a coupled ocean-atmospheric system has been suggested to explain the advance of glaciers and intense cooling noted for Baffin Island in the eastern region (Miller et al., 2005), with increased influxes of Arctic cold waters contributing to the marine component and likely increase in sea ice around Baffin Island and the CAA (e.g. Osterman and Nelson, 1989; Andrews et al., 1993; Dyke et al., 1996a; Miller et al., 2005; Gregory et al., in press). The palaeo sea ice data presented previously (Vare et al., 2009) and again here, for Barrow Strait, provide evidence for this hypothesis, with relatively high and sustained IP_{25} fluxes since ca. 3 cal kyr BP, and only a small decline during the MWP (Vare et al., 2009). This apparent 'buffering' of the climate system in the eastern region is not so evident in the west, where the HTM paralleled the summer insolation anomaly (Kaufman et al., 2004).

Overall, the observation of elevated IP_{25} fluxes, ascribed here to a greater frequency of seasonal sea ice occurrence after ca. 3.0 cal-kyr BP for all three study locations, is consistent with a general degree of cooling in the CAA compared to the early and mid-Holocene reported previously in numerous other studies (e.g. Bradley, 1990; Fisher et al., 1995; Gajewski, 1995; Gajewski and Atkinson, 2003; Kaufman et al., 2004; Miller et al., 2005; Ledu et al., 2008). Any climatic interpretation of the grain-size and XRD data is rendered difficult because of the overprinting on the sediment records of the lowering of sea levels throughout the Holocene. Thus, changes in grain-size and mineralogy probably reflect the increased erosion and transport of coarse sediments under shallowing water conditions by wave action, bottom currents, and sea ice rafting.

6. Conclusions

This study provides biomarker and other proxy evidence for the occurrence of variable spring sea ice conditions for three locations in the central CAA over the last 7 kyr, with no indication of prolonged periods of either ice-free waters or permanent ice cover. Despite the temporal variability in the proxy-based data, there is remarkable consistency in the IP_{25} flux profiles for the three study sites, suggestive of related spring sea ice conditions at each location throughout the 7 kyr interval. All three records indicate relatively low spring sea ice occurrence from ca. 7.0 to 3.0 cal kyr BP, with higher spring sea ice frequency since 3.0 cal kyr BP. Exceptionally, in this latter interval, periods of lower than median sea ice occurrence existed during the Medieval Warm Period, with the evidence for this being clearer for the lower latitude sites (Victoria Strait and Dease Strait). These periods of relatively low and high spring sea ice occurrence may, alternatively, reflect more quantitatively, the frequency changes to the annual period of sea ice occurrence that represents a minimum or threshold level in order for IP_{25} (and sea ice diatoms) to be produced (ca. 8 months yr^{-1}). This alternative (quantitative) interpretation will require further calibration of IP_{25} fluxes against known sea ice occurrence in the future. In any case, given the pivotal role that sea ice plays in contributing to, and is influenced by, changes in climate, and the need to pinpoint both spatial and temporal Holocene climate variations (Kaufman et al., 2004; Viau et al., 2006), a useful benchmark for the termination of the Holocene Thermal Maximum for the central CAA, as defined by increases in seasonal sea ice occurrence, might be considered to be ca. 3.0 cal kyr BP.

Acknowledgements

This work was supported by the Natural Environmental Research Council (NERC), UK (NE/D013216/1) and the National Science Foundation (NSF-ATM-0502515), USA. The fieldwork was conducted within the framework of ArcticNet, a Canadian Network of Centres of Excellence (http://www.arcticnetulaval.ca). We are particularly grateful to the officers and crew of the CCGS Amundsen and to A. Rochon (ISMER-UQAR) and co-workers for help in obtaining the sediment cores described in this study. We also thank A. Fisher, A. Tonkin and R. Hartley (University of Plymouth) for elemental analysis, TOC and particle size determinations, and to Tom Cronin (USGS) and two anonymous referees for providing helpful suggestions during the reviewing of this paper.

References

Aagaard, K., Carmack, E., 1989. The role of sea ice and other fresh water in the Arctic circulation. Journal of Geophysical Research 94, 14,485–14,498.
Andersen, T.J., Mikkelsen, O.A., Møller, A.L., Pejrup, M., 2000. Deposition and mixing depths on some European intertidal mudflats based on ^{210}Pb and ^{137}Cs activities. Continental Shelf Research 20, 1569–1591.
Andrews, J.T., 1970. A Geomorphological Study of Post-glacial Uplift with Particular Reference to Arctic Canada. Institute of British Geographers, London.
Andrews, J.T., 2009. Seeking a Holocene drift ice proxy: non-clay mineral variations from the SW to N-central Iceland shelf: trends, regime shifts, and periodicities. Journal of Quaternary Science 24, 664–676.
Andrews, J.T., Eberl, D.D., 2007. Quantitative mineralogy of surface sediments on the Iceland shelf, and application to down-core studies of Holocene ice-rafted sediments. Journal of Sedimentary Research 77, 469–479.
Andrews, J.T., Dyke, A.S., Tedesco, K., White, J.W., 1993. Meltwater along the Arctic margin of the Laurentide Ice Sheet (8–12 ka): stable isotopic evidence and implications for past salinity anomalies. Geology 21, 881–884.
Andrews, J.T., Belt, S.T., Olafsdottir, S., Massé, G., Vare, L.L., 2009. Sea ice and diamte variability for NW Iceland/Denmark Strait over the last 2000 cal yr BP. The Holocene 19, 775–784.
Appleby, P.G., Oldfield, F., 1992. Application of lead-210 to sedimentation studies. In: Ivanovich, M., Harmon, R. (Eds.), Uranium Series Disequilibrium-Application to Environmental Problems: Applications to Earth, Marine, and Environmental Sciences, second ed. Oxford Press, London, pp. 731–778.
Belt, S.T., Massé, G., Rowland, S.J., Poulin, M., Michel, C., LeBlanc, B., 2007. A novel chemical fossil of palaeo sea ice: IP_{25}. Organic Geochemistry 38, 16–27.
Belt, S.T., Massé, G., Vare, L.L., Rowland, S.J., Poulin, M., Sicre, M.-A., Sampei, M., Fortier, L., 2008. Distinctive ^{13}C isotopic signature distinguishes a novel sea ice biomarker in Arctic sediments and sediment traps. Marine Chemistry 112, 158–167.
Bradley, R.S., 1990. Holocene paleoclimatology of the Queen Elizabeth islands, Canadian high arctic. Quaternary Science Reviews 9, 365–384.
Broecker, W.S., 2001. Was the medieval warm period global? Science 291, 1497–1499.
Chester, R., 1990. Marine Geochemistry. Unwin Hyman Ltd, London.
Comiso, J.C., 2006. Abrupt decline in the Arctic winter sea ice cover. Geophysical Research Letters 33, L18504.
Cronin, T.M., Holtz Jr., T.R., Stein, R., Spielhagen, R., Fütterer, D., Wollenburg, J., 1995. Late quaternary paleoceanography of the Eurasian basin, Arctic Ocean. Paleoceanography 10, 259–281.
Crosta, X., Denis, D., Ther, O., 2008. Sea ice seasonality during the Holocene, Adelie Land, east Antarctica. Marine Micropaleontology 66, 222–232.
Croudace, I.W., Rindby, A., Rothwell, R.G., 2006. ITRAX: description and evaluation of a new multi-function X-ray core scanner. In: Rothwell, R.G. (Ed.), New Techniques in Sediment Core Analysis. Geological Society, London, pp. 51–63.
Darby, D.S., 2003. Sources of sediment found in the sea ice from the western Arctic Ocean, new insights into processes of entrainment and drift patterns. Journal of Geophysical Research 108 (3257).

Denis, D., Crosta, X., Schmidt, S., Carson, D.S., Ganeshram, R.S., Renssen, H., Bout-Roumazeilles, V., Zaragosi, S., Martin, B., Cremer, M., Giraudeau, J., 2009. Holocene glacier and deep water dynamics, Adelie Land region, East Antarctica. Quaternary Science Reviews 28, 1291–1303.

de Vernal, A., Henry, M., Matthiessen, J., Mudie, P.J., Rochon, A., Boessenkool, K., Eynaud, F., Grøsfjeld, K., Guiot, J., Hamel, D., Harland, R., Head, M.J., Kunz-Pirrung, M., Levac, E., Loucheur, V., Peyron, O., Pospelova, V., Radi, T., Turon, J.-L., Voronina, E., 2001. Dinoflagellate cyst assemblages as tracers of sea-surface conditions in the northern North Atlantic, Arctic and sub-Arctic seas: the new 'n = 677' database and application for quantitative palaeoceanographic reconstruction. Journal of Quaternary Science 16, 681–698.

de Vernal, A., Hillaire-Marcel, C., Darby, D., 2005. Variability of sea-ice cover in the Chukchi Sea (western Arctic Ocean) during the Holocene. Paleoceanography 20, PA4018.

Divine, D.V., Dick, D., 2006. Historical variability of sea ice edge position in the Nordic Seas. Journal of Geophysical Research 111, C01001.

Dyke, A.S., 1998. Holocene delevelling of Devon Island, Arctic Canada: implications for ice sheet geometry and crustal response. Canadian Journal of Earth Sciences 35, 885–904.

Dyke, A.S., 1999. Last Glacial maximum and deglaciation of Devon island, Arctic Canada: support for an Innuitian ice sheet. Quaternary Science Reviews 18, 393–420.

Dyke, A.S., 2008. The Steensby Inlet ice Stream in the context of the deglaciation of northern Baffin island, eastern Arctic Canada. Earth Surfaces Processes and Landforms 33, 573–592.

Dyke, A.S., Dale, J.E., McNeely, R.N., 1996a. Marine molluscs as indicators of environmental change in glaciated North America and Greenland during the last 18 000 years. Geographie Physique et Quaternaire 50, 125–184.

Dyke, A.S., Hooper, J., Savelle, J.M., 1996b. A history of sea ice in the Canadian Arctic Archipelago based on postglacial remains of the bowhead whale (*Balaena mysticetus*). Arctic 49, 235–255.

Dyke, A.S., England, J., Reimnitz, E., Jetté, H., 1997. Changes in driftwood delivery to the Canadian Arctic Archipelago: the hypothesis of postglacial oscillations of the transpolar drift. Arctic 50, 1–16.

Dyke, A.S., Andrews, J.T., Clark, P.U., England, J.H., Miller, G.H., Shaw, J., Veillette, J.J., 2002. The Laurentide and Innuitian ice sheets during the last Glacial maximum. Quaternary Science Reviews 21, 9–31.

Dyke, A.S., Dredge, L.A., Hodgson, D.A., 2005. North American deglacial marine- and lake-limit surfaces. Geographie physique et Quaternaire 59, 155–185.

Dyke, A.S., Morris, T.F., 1990. Postglacial history of the bowhead whale and of driftwood penetration: implications for paleoclimate, central Canadian Arctic. Geological Survey of Canada, 17. Paper 89–24.

Dyke, A.S., Peltier, W.R., 2000. Forms, response times and variability of relative sea-level curves, glaciated North America. Geomorphology 32, 315–333.

Dyke, A.S., Savelle, J.M., 2001. Holocene history of the Bering Sea bowhead whale (Balaena mysticetus) in its Beaufort Sea summer ground off Southwestern Victoria island, western Canadian Arctic. Quaternary Research 55, 371–379.

Eberl, D.D., 2003. User Guide to RockJock: a Program for Determining Quantitative Mineralogy from X-ray Diffraction Data. United States Geological Survey, Open File Report 03–78, Washington, DC, 40 pp.

Eberl, D.D., 2004. Quantitative mineralogy of the Yukon River system: variations with reach and season, and determining sediment provenance. American Mineralogist 89, 1784–1794.

England, J.H., Lakeman, T.R., Lemmen, D.S., Bednarski, J.M., Stewart, T.G., Evans, D.J.A., 2008. A millennial-scale record of Arctic Ocean sea ice variability and the demise of the Ellesmere Island ice shelves. Geophysical Research Letters 35, L19502.

Fisher, D.A., Koerner, R.M., Reeh, N., 1995. Holocene climate records from Agassiz ice cap, Ellesmere island, NWT, Canada. Holocene 5, 19–24.

Friedman, G.M., Sanders, J.E., 1978. Principles in Sedimentology. Wiley, New York.

Gajewski, K., 1995. Modern and Holocene pollen assemblages from some small Arctic Lakes on Somerset island, NWT, Canada. Quaternary Research 44, 228–236.

Gajewski, K., Atkinson, D.A., 2003. Climatic change in northern Canada. Environmental Reviews 11, 69–102.

Gersonde, R., Zielinski, U., 2000. The reconstruction of late quaternary Antarctic sea-ice distribution – the use of diatoms as a proxy for sea ice. Palaeogeography, Palaeoclimatology, Palaeoecology 162, 263–286.

Gradinger, R., 2009. Sea-ice algae: major contributors to primary production and algal biomass in the Chukchi and Beaufort Seas during May/June 2002. Deep-Sea Research II 56, 1201–1212.

Gregory, T.R., Smart, C.W., Hart, M.B., Massé, G., Vare, L.L., Belt, S.T., 2010. Holocene palaeoecology and dissolution of foraminifera in Barrow Strait, Canadian Arctic. Journal of Quaternary Science, in press, doi:10.1002/jqs.1367.

Grove, J.M., 2001. The initiation of the "Little ice age" in regions round the north atlantic. Climatic Change 48, 53–82.

Grove, J.M., Switsur, R., 1994. Glacial geological evidence for the medieval warm period. Climate Change 26, 143–169.

Hodell, D.A., Kanfoush, S.L., Shemesh, A., Crosta, X., Charles, C.D., Guilderson, T.P., 2001. Abrupt cooling of Antarctic surface waters and sea ice expansion in the south atlantic sector of the Southern Ocean at 5000 cal yr B.P. Quaternary Research 56, 191–198.

Howell, S.E.L., Tivy, A., Yackel, J.J., McCourt, S., 2008. Multi-year sea ice conditions in the western Canadian Arctic Archipelago region of the Northwest Passage: 1968–2006. Atmosphere-Ocean 46, 229–242.

Howell, S.E.L., Duguay, C.R., Markus, T., 2009. Sea ice conditions and melt season duration variability within the Canadian Arctic Archipelago: 1979–2008. Geophysical Research Letters 36, L10502.

Hughes, M.K., Diaz, H.F., 1994. Was there a 'Medieval Warm Period', and if so, where and when? Climate Change 26, 109–142.

Justwan, A., Koç, N., Jennings, A.E., 2008. Evolution of the Irminger and East Icelandic Current systems through the Holocene, revealed by diatom-based sea surface temperature reconstructions. Quaternary Science Reviews 27, 1571–1582.

Justwan, A., Koç, N., 2008. A diatom based transfer function for reconstructing sea ice concentrations in the North Atlantic. Marine Micropaleontology 66, 264–278.

Kaufman, D.S., Ager, T.A., Anderson, N.J., Anderson, P.M., Andrews, J.T., Bartlein, P.J., Brubaker, L.B., Coats, L.L., Cwynar, L.C., Duvall, M.L., Dyke, A.S., Edwards, M.E., Eisner, W.R., Gajewski, K., Geirsdottir, A., Hu, F.S., Jennings, A.E., Kaplan, M.R., Kerwin, M.N., Lozhkin, A.V., MacDonald, G.M., Miller, G.H., Mock, C.J., Oswald, W.W., Otto-Bliesner, B.L., Porinchu, D.F., Ruhland, K., Smol, J.P., Steig, E.J., Wolfe, B.B., 2004. Holocene thermal maximum in the western Arctic (0–180 degrees W). Quaternary Science Reviews 23, 529–560.

Knudsen, K.L., Stabell, B., Seidenkrantz, M.S., Eiriksonn, J., Blake Jr., W., 2008. Deglacial and Holocene conditions in northernmost Baffin Bay: sediments, foraminifera, diatoms and stable isotopes. Boreas 37, 346–376.

Koerner, R.M., Fisher, D.A., 1990. A record of Holocene summer climate from a Canadian high-Arctic ice core. Nature 343, 630–631.

Kwok, R., 2006. Exchange of sea ice between the Arctic Ocean and the Canadian Arctic Archipelago. Geophysical Research Letters 33, L16501.

Laidre, K.L., Stirling, I., Lowry, L.F., Wiig, Ø., Heide-Jørgensen, M.P., Ferguson, S.H., 2008. Quantifying the sensitivity of Arctic marine mammals to climate-induced habitat change. Ecological Applications Supplement 18, S97–S125.

LeBlanc, M., Gajewski, K., Hamilton, P.B., 2004. A diatom-based Holocene palaeoenvironmental record from a mid-arctic lake on Boothia Peninsula, Nunavut, Canada. The Holocene 14, 417–425.

Ledu, D., Rochon, A., de Vernal, A., St-Onge, G., 2008. Palynological evidence of Holocene climate change in the eastern Arctic: a possible shift in the Arctic oscillation at the millennial time scale. Canadian Journal of Earth Sciences 45, 1363–1375.

Levac, E., De Vernal, A., Blake, W., 2001. Sea-surface conditions in northernmost Baffin Bay during the Holocene: palynological evidence. Journal of Quaternary Science 16, 353–363.

Massé, G., Rowland, S.J., Sicre, M.-A., Jacob, J., Jansen, E., Belt, S.T., 2008. Abrupt climate changes for Iceland during the last millennium: evidence from high resolution sea ice reconstructions. Earth and Planetary Science Letters 269, 565–569.

Matthews, J.A., Briffa, K.R., 2005. The 'Little ice age': re-evaluation of an evolving concept. Geografiska Annaler A 87, 17–36.

Maxwell, J.B., 1981. Climatic regions of the Canadian Arctic islands. Arctic 34, 225–240.

Mayewski, P.A., Rohling, E.E., Stager, J.C., Karlén, W., Maasch, K.A., Meeker, L.D., Meyerson, E.A., Gasse, F., van Kreveld, S., Holmgren, K., Lee-Thorp, J., Rosqvist, G., Rack, F., Staubwasser, M., Schneider, R.R., Steig, E.J., 2004. Holocene climate variability. Quaternary Research 62, 243–255.

McKay, J.L., de Vernal, A., Hillaire-Marcel, C., Not, C., Polyak, L., Darby, D., 2008. Holocene fluctuations in Arctic sea-ice cover: dinocyst-based reconstructions for the eastern Chukchi Sea. Canadian Journal of Earth Sciences 45, 1377–1397.

McNeely, R., Dyke, A.S., Southon, J.R., 2006. Canadian Marine Reservoir Ages, Preliminary Data Assessment. Geological Survey Canada, Open File 5049, pp.3.

Meier, W., Stroeve, J., Fetterer, F., Knowles, K., 2005. Reductions in Arctic sea ice cover no longer limited to summer. Eos, Transactions of the American Geophysical Union 86, 326–327.

Meyers, P.A., 1994. Preservation of elemental and isotopic source identification of sedimentary organic matter. Chemical Geology 114, 289–302.

Miller, G.H., Wolfe, A.P., Briner, J.P., Sauer, P.E., Nesje, A., 2005. Holocene glaciations and climate evolution of Baffin island, arctic Canada. Quaternary Science Reviews 24, 1703–1721.

Moros, M., Andrews, J.T., Eberl, D.D., Jansen, E., 2006. The Holocene history of drift ice in the northern North Atlantic – Evidence for different spatial and temporal modes. Palaeoceanography 21, PA2017.

Mudie, P.J., Harland, R., Matthiessen, J., De Vernal, A., 2001. Marine dinoflagellate cysts and high latitude Quaternary paleoenvironmental reconstructions: an introduction. Journal of Quaternary Science 16, 595–602.

Mudie, P.J., Rochon, A., Levac, E., 2005. Decadal-scale sea ice changes in the Canadian Arctic and their impact on humans during the past 4,000 years. Environmental Archaeology 10, 113–126.

Mudie, P.J., Rochon, A., Prins, M.A., Soenarjo, D., Troelstra, S.R., Levac, E., Scott, D.B., Roncaglia, L., Kuijpers, A., 2006. Late Pleistocene-Holocene marine geology of Nares Strait region: Palaeoceanography from foraminifera and dinoflagellate cysts, sedimentology and stable isotopes. Polarforschung 74, 169–183.

Müller, J., Masse, G., Stein, R., Belt, S.T., 2009. Variability of sea-ice conditions in the Fram Strait over the past 30 000 years. Nature Geoscience 2, 772–776.

Mundy, C.J., Barber, D.G., Michel, C., 2005. Variability of snow and ice thermal, physical and optical properties pertinent to sea ice algae biomass during spring. Journal of Marine Systems 58, 107–120.

O'Brien, M.C., Macdonald, R.W., Melling, H., Iseki, K., 2006. Particle fluxes and geochemistry on the Canadian Beaufort Shelf: implications for sediment transport and deposition. Continental Shelf Research 26, 41–81.

Osterman, L.E., Nelson, A.R., 1989. Latest Quaternary and Holocene paleoceanography of the eastern Baffin Island continental shelf, Canada: benthic foraminiferal evidence. Canadian Journal of Earth Science 26, 2236–2248.

Paillard, D., Labeyrie, L., Yiou, P., 1996. Macintosh program Performs time-series analysis. Eos. Transactions of the American Geophysical Union 77, 379.

Parkinson, C.L., Cavalieri, D.J., Gloersen, P., Zwally, H.J., Comiso, J.C., 1999. Arctic sea ice extents, areas, and trends, 1978–1996. Journal of Geophysical Research 104, 20837–20856.
Peros, M.C., Gajewski, K., 2008. Holocene climate and vegetation change on Victoria Island, western Canadian Arctic. Quaternary Science Reviews 27, 235–249.
Peros, M.C., Gajewski, K., 2009. Pollen-based reconstructions of late Holocene climate from the central and western Canadian Arctic. Journal of Paleolimnology 41, 161–175.
Podritske, B., Gajewski, K., 2007. Diatom community response to multiple scales of Holocene climate variability in a small lake on Victoria Island, NWT, Canada. Quaternary Science Reviews 26, 3179–3196.
Porinchu, D.F., MacDonald, G.M., Rolland, N., 2009. A 2000 year midge-based paleotemperature reconstruction from the Canadian Arctic archipelago. Journal of Paleolimnology 41, 177–188.
Rahman, A., de Vernal, A., 1994. Surface oceanographic changes in the eastern Labrador Sea: Nannofossil record of the last 31 000 years. Marine Geology 121, 247–263.
Richerol, T., Rochon, A., Blasco, S., Scott, D.B., Schell, T.M., Bennett, R.J., 2008. Evolution of paleo sea-surface conditions over the last 600 years in the Mackenzie Trough, Beaufort Sea (Canada). Marine Micropaleontology 68, 6–20.
Rigor, I.G., Wallace, J.M., 2004. Variations in the age of Arctic sea-ice and summer sea ice extent. Geophysical Research Letters 31, L09401.
Różańska, M., Gosselin, M., Poulin, M., Wiktor, J.M., Michel, C., 2009. Influence of environmental factors on the development of bottom ice protest communities during the winter-spring transition. Marine Ecology Progress Series 386, 43–59.
Savelle, J.M., Dyke, A.S., 2002. Variability in Palaeoeskimo occupation on south-western Victoria Island, Arctic Canada: causes and consequences. World Archaeology 33, 508–522.
Savelle, J.M., Dyke, A.S., McCartney, A.P., 2000. Holocene bowhead whale (*Balaena mysticetus*) mortality patterns in the Canadian Arctic Archipelago. Arctic 53, 414–421.
Schmidt, S., Jouanneau, J.-M., Weber, O., Lecroart, P., Radakovitch, O., Gilbert, F., Jezequel, D., 2007. Sedimentary processes in the Thau Lagoon (South France): from seasonal to century time scales. Estuarine Coastal Shelf Science 72, 534–542.
Schmidt, S., Howa, H., Mouret, A., Lombard, F., Anschutz, P., Labeyrie, L., 2009. Particle fluxes and recent sediment accumulation on the Aquitanian margin of Bay of Biscay. Continental Shelf Research 29, 1044–1052.
Serreze, M.C., Maslanik, J.A., Scambos, T.A., Fetterer, F., Stroeve, J., Knowles, K., Fowler, C., Drobot, S., Barry, S.G., Haran, T.M., 2003. A record minimum arctic sea ice extent and area in 2002. Geophysical Research Letters 30 (1110).
Smith, I.R., 2002. Diatom-based Holocene paleoenvironmental records from continental sites on northeastern Ellesmere Island, high Arctic, Canada. Journal of Paleolimnology 27, 9–28.
Smith, L.M., Miller, G.H., Otto-Bliesner, B., Shin, S.-I., 2003. Sensitivity of the Northern Hemisphere climate system to extreme changes in Holocene Arctic sea ice. Quaternary Science Reviews 22, 645–658.
Stein, R., Macdonald, R.W., 2004. The Organic Carbon Cycle in the Arctic Ocean. Springer, Berlin.
Stroeve, J., Frei, A., McCreight, J., Ghatak, D., 2008. Arctic sea-ice variability revisited. Annals of Glaciology 48, 71–81.
Stuiver, M., Reimer, P.J., 1993. Extended ^{14}C data-base and revised CALIB 3.0 ^{14}C age calibration program. Radiocarbon 35, 215–230.
Thomas, D.N., Dieckmann, G.S., 2010. Sea Ice, second ed. Wiley Blackwell Publishing.
Vare, L.L., Massé, G., Gregory, T.R., Smart, C.W., Belt, S.T., 2009. Sea ice variations in the central Canadian Arctic Archipelago during the Holocene. Quaternary Science Reviews 28, 1354–1366.
Vare, L.L., Massé, G., Belt, S.T., 2010. A biomarker-based reconstruction of sea ice conditions for the Barents Sea in recent centuries. The Holocene 40, 637–643.
Viau, A.E., Gajewski, K., Sawada, M.C., Fines, P., 2006. Millennial-scale temperature variations in North America during the Holocene. Journal of Geophysical Research 111, D09102.
Voronina, E., Polyak, L., de Vernal, A., Peyron, O., 2001. Holocene variations of sea-surface conditions in the southeastern Barents Sea, reconstructed from dinoflagellate cysts assemblages. Journal of Quaternary Science 16, 717–726.
Wanner, H., Beer, J., Bütikofer, J., Crowley, T.J., Cubasch, U., Flückiger, J., Goose, H., Grosjean, M., Joos, F., Kaplan, J.O., Küttel, M., Müller, S.A., Prentice, C., Solomina, O., Stocker, T.F., Tarasov, P., Wagner, M., Widmann, M., 2008. Mid- to Late Holocene climate change: an overview. Quaternary Science Reviews 27, 1791–1828.
Williams, K.M., Short, S.K., Andrews, J.T., Jennings, A.E., Mode, W.N., Syvitski, J.P.M., 1995. The eastern Canadian Arctic at ca.6 ka BP: a time of transition. Géographie Physique et Quaternaire 49, 13–27.
Wollenburg, J.E., Kuhnt, W., 2000. The response of benthic foraminifers to carbon flux and primary production in the Arctic Ocean. Marine Micropaleontology 40, 189–231.
Zabenskie, S., Gajewski, K., 2007. Post-Glacial climate change on Boothia Peninsula, Nunavet, Canada. Quaternary Research 68, 261–270.

8.2 PUBLISHED ABSTRACTS

Manners, H.R., Grimes, S.T., Sutton, P.A., Domingo, L., Pancost, R.D., Leng, M.J., Twitchett, R.T., Hart, M.B., Taylor, K.W.R. 2013. 26th International Meeting Organic Geochemistry abstract proceedings 2, p 346-347.

26th IMOG *-Vol.2-*

AN ORGANIC GEOCHEMICAL MULTI-PROXY STUDY OF THE PALAEOCENE-EOCENE THERMAL MAXIMUM: EVIDENCE FROM NORTHERN SPAIN

Hayley MANNERS[1*], Stephen GRIMES[1], Paul SUTTON[1], Laura DOMINGO[2], Phil JARDINE[3], Richard PANCOST[4], Melanie LENG[5,6], Robert DULLER[7], Kyle TAYLOR[4], Richard TWITCHETT[1], Malcolm HART[1]

1. *School of Geography, Earth and Environmental Sciences, Plymouth University, Devon, PL4 8AA, UK*
2. *Earth & Planetary Sciences Department, University of California Santa Cruz, USA*
3. *School of Geography, Earth and Environmental Sciences, University of Birmingham, Edgbaston, Birmingham, B15 2TT, UK*
4. *Organic Geochemistry Unit, University of Bristol, Bristol, BS8 1TS, UK*
5. *University of Leicester, Department of Geology, University Road, Leicester, LE1 7RH, UK*
6. *NERC Isotope Geosciences Laboratory, Kingsley Dunham Centre, Keyworth, Nottingham, NG12 5GG*
7. *School of Environmental Sciences, University of Liverpool, Nicholson Building, Liverpool, L69 3GP*

**Corresponding author: Hayley.manners@plymouth.ac.uk*

The Palaeocene – Eocene Thermal Maximum (PETM), a hyperthermal event that occurred ca. 56 Ma, has been attributed to the release of substantial amounts of isotopically light carbon. This release had a major impact on the atmosphere, biosphere, and hydrosphere. The amount, duration and mechanism(s) of carbon release are a subject of considerable debate, since the magnitude and profile of the Carbon Isotope Excursion (CIE), associated with this event, differ between locations on a global scale. High resolution organic carbon isotope profiles ($\delta^{13}C_{TOC}$) of six PETM sections in northern Spain are presented, spanning a 450 km transect from continental (Claret, Tendrui, and Esplugafreda sections) to marine (Campo, Zumaia, and Ermua sections) environments. These data represent the highest resolution $\delta^{13}C_{TOC}$ records for these sections, and allow for comparison of the magnitude, profile shape, and relative timing of the onset of the CIE across a linked sediment routing system. Results indicate that no systematic variation in the magnitude of the CIE is recorded between the continental and marine realms, and profile shape varies between the sections. This contributes

additional understanding regarding the rate and timing of the PETM carbon release, and the mode and rapidity of carbon drawdown during the recovery phase.

The continental section of Claret and the marine section of Zumaia have been analysed further using $\delta^{13}C$ values of higher plant-derived *n*-alkanes to resolve the magnitude, profile shape, and onset of the CIE in a localised system. The magnitude of the $\delta^{13}C_{n\text{-alkane}}$ CIE is an agreement with the $\delta^{13}C_{TOC}$ records at both sections, and is similar between sections (Claret ~4‰, Zumaia ~5‰). This contradicts global records that suggest a difference in CIE magnitude between the continental organic carbon and marine carbonate carbon records ($\delta^{13}C$ marine 2.5 - 4‰, $\delta^{13}C$ terrestrial 6 - 8‰; Bains *et al.* 1999; Bowen *et al.* 2001; Schmitz and Pujalte 2003). This is particularly significant when considering that the global discrepancy between records is from sites as disparate as the Arctic (Schouten *et al.* 2007) and the South Atlantic ocean (Zachos *et al.* 2005) with potentially very different influences, whereas the data presented here is from within a linked sediment routing system. This data may therefore help to calibrate any perceived differences at other sections of the CIE associated with the PETM, which in turn would allow for more accurate models of future climate projections.

Profile shape is important as different profile shapes have been observed globally and are intriguing as they may suggest different carbon drawdown methods being observed. At Claret, both $\delta^{13}C_{TOC}$ and $\delta^{13}C_{n\text{-alkane}}$ records suggest a box-shaped profile, however at Zumaia $\delta^{13}C_{TOC}$ data suggest a triangular shaped profile, whilst $\delta^{13}C_{n\text{-alkane}}$ data records a box-shaped profile similar to that at Claret. In this localised setting, this cannot be explained by different carbon sequestration methods, so instead this is interpreted as sediment re-working and alternating continental and marine carbon sources, which may be biasing the marine record. Palynological analyses is being conducted at Claret and Zumaia, and used to test this reworking hypothesis at Zumaia, both in terms of pollen assemblages throughout the sections, and reworking of older more thermally mature sediment being washed in, which may also have an effect on profile shape.

Higher plant-derived biomarker analysis will serve to further test these results, which will provide the first data of this type in northern Spain, and could have implications for our understanding of the PETM.

REFERENCES

Bains, S., *et al.* 1999. Science 285, 724-727. Bowen *et al.* 2001. University of Michigan Papers on Palaeontology 33 73 - 88. Schmitz, B. and V. Pujalte 2003.Geology 31, 689-692.Schouten, S., *et al.* 2007.Earth and Planetary Science Letters 258, 581-592. Zachos, J. C., *et al.* 2005. Science 308, 1611-1615.

Manners, H.R., Grimes, S.T., Sutton, P.A., Domingo, L., Pancost, R.D., Leng, M.J., Twitchett, R.T., Hart, M.B., Taylor, K.W.R. 2012. AGU Fall Meeting, control ID 1480481.

1745h

PP34A-08

An organic geochemical multi-proxy study of the Palaeocene-Eocene Thermal Maximum: Evidence from northern Spain

***Manners, H R**
hayley.manners@plymouth.ac.uk
Centre for Research in Earth Sciences, Plymouth University, Plymouth, United Kingdom
Grimes, S
Stephen.grimes@plymouth.ac.uk
Centre for Research in Earth Sciences, Plymouth University, Plymouth, United Kingdom
Sutton, P
p.a.sutton@plymouth.ac.uk
Biogeochemistry Research Centre, Plymouth University, Plymouth, United Kingdom
Domingo, L
ldomingo@ucsc.edu
Earth and Planetary Sciences Department, University of California Santa Cruz, Santa Cruz, CA, USA
Pancost, R D
r.d.pancost@bristol.ac.uk
Organic Geochemistry Unit, University of Bristol, Bristol, United Kingdom
Leng, M J
mjl@bgs.ac.uk
Department of Geology, University of Leicester, Leicester, United Kingdom
Twitchett, R J
richard.twitchett@plymouth.ac.uk
Centre for Research in Earth Sciences, Plymouth University, Plymouth, United Kingdom
Hart, M B
m.hart@plymouth.ac.uk
Centre for Research in Earth Sciences, Plymouth University, Plymouth, United Kingdom
Taylor, K W
kyle.taylor@bristol.ac.uk
Organic Geochemistry Unit, University of Bristol, Bristol, United Kingdom

The Palaeocene - Eocene Thermal Maximum (PETM), a hyperthermal event that occurred ca. 56 Ma, has been attributed to the release of substantial amounts of isotopically light carbon, affecting the atmosphere, biosphere, and hydrosphere. Debate concerning the amount, duration and mechanism(s) of carbon release are topical, with the magnitude and profile of the Carbon Isotope Excursion (CIE) associated with this event proving pivotal as different records occur globally. Continental records generally record a higher CIE magnitude than marine records (continental δ13C 6 - 8‰, marine δ13C 2.5 - 4‰)1,2,3. This difference was recently proposed to be due to a change in plant communities from mixed angiosperm (flowering plants)/gymnosperm (evergreen plants) flora to a predominantly

angiosperm flora4,5, believed to be coincident with the onset of the PETM, indicating that the continental realm may be recording an artificially large CIE due to a change in the plant isotopic fractionation pathway. High resolution organic carbon isotope profiles (δ13CTOC) of six PETM sections in northern Spain are presented that span a transect from continental (Claret, Tendrui, and Esplugafreda sections) to marine (Campo, Zumaia, and Ermua sections) environments. These data represent the highest resolution δ13CTOC records for these sections, and allow for comparison of the magnitude, profile shape, and relative timing of the onset of the CIE across a linked sediment routing system. Results indicate that no systematic variation in the magnitude of the CIE is recorded between the continental and marine realms, and profile shape varies across the sections, adding further data to debates around the rate and timing of the PETM carbon release and the mode and rapidity of carbon drawdown during the recovery phase. The continental section of Claret and the marine section of Zumaia have been further compared using δ13C values of higher plant-derived n-alkanes to further constrain the magnitude, profile shape, and onset of the CIE in a localised system. Preliminary results for Claret suggest that the continental δ13CTOC records a lower magnitude excursion than δ13Cn-alkane data, where excursions of up to 8‰ are recorded - one of the largest continental excursions recorded to date. In comparison, there is good agreement between the δ13CTOC and δ13Cn-alkane records for the marine section of Zumaia, where an excursion of ca. 4‰ occurs in both proxies. The apparent enhancement in magnitude of the continental CIE is particularly significant, because unlike other sites4, there is no biomarker evidence for vegetation change, e.g. the average chain length of the n-alkanes, in either the Claret or Zumaia sections. Higher plant-derived biomarker and palynological analysis will serve to further test these results, which will provide the first data of this type in northern Spain, and could have implications for our understanding of the PETM. References 1. Bains, S. *et al.* 1999. Science, 285, (5428) 724-727. 2. Bowen, G. J. *et al.* 2001. University of Michigan Papers on Palaeontology, 33, 73 - 88. 3. Schmitz, B. and Pujalte, V. 2003. Geology. 689-692. 4. Smith, F. A. *et al.* 2007. Earth and Planetary Science Letters, 262, (1-2) 50-65. 5. Schouten, S. *et al.* 2007. Earth and Planetary Science Letters, 258, (3-4) 581 - 592.

DE: [0473] BIOGEOSCIENCES / Palaeoclimatology and palaeoceanography
DE: [1041] GEOCHEMISTRY / Stable isotope geochemistry
DE: [1055] GEOCHEMISTRY / Organic and biogenic geochemistry
SC: Palaeoceanography and Palaeoclimatology (PP)
MN: 2012 Fall Meeting

Manners, H.R., Grimes, S.T., Sutton, P.A., Domingo, L., Pancost, R.D., Leng, M.J., Taylor, K.W.R., Twitchett, R.T., Hart, M.B., Lopez-Martinez, N., 2011. 25th International Meeting Organic Geochemistry abstract proceedings, p 67.

O-09

A high resolution compound specific carbon isotope study of the PETM in northern Spain

Hayley Manners[1], Stephen Grimes[1], Paul Sutton[1], Laura Domingo[2,3], Richard Pancost[4], Melanie Leng[5], Kyle Taylor[4], Richard Twitchett[1], Malcolm Hart[1], Nieves López-Martínez[3]

[1]University of Plymouth, Plymouth, United Kingdom, [2]University of California Santa Cruz, Santa Cruz, United States of America, [3]Universidad Complutense de Madrid, Madrid, Spain, [4]University of Bristol, Bristol, United Kingdom, [5]NERC Isotope Geosciences Laboratory, Nottingham, United Kingdom (corresponding author: hayley.manners@plymouth.ac.uk)

The Palaeocene/Eocene Thermal Maximum (PETM) occurred approximately 55 Ma, lasting for 100 – 200 Kyr, initiating a period of global warming, biotic extinction, migration and turnover, and fundamental changes in the carbon and hydrological cycles[1]. Marine and terrestrial sediments record the event, however discrepancy between the carbon isotope excursion (CIE) measured in the two realms has been observed ($\delta^{13}C$ marine 2.5 - 4‰, $\delta^{13}C$ terrestrial 6 - 8‰)[2,3,4]. Two hypotheses have recently been proposed for this discrepancy – the "marine modification" and the "plant community change" hypothesis[5]. The plant community change hypothesis states that the magnitude of the CIE is greater in the terrestrial realm owing to major changes in floral composition during the PETM, from mixed angiosperm (flowering plants)/gymnosperm (conifers) flora to a predominantly angiosperm flora [5,6]. To date, evidence for the plant community change hypothesis has been observed in North America[5] and the Arctic[6]. Presented here are preliminary results from eight sections in Northern Spain spanning the Palaeocene/Eocene boundary. Sections from (East to West) Claret, Tendrui, Esplugafreda, and Berganuy represent the terrestrial realm; La Cinglera and Campo a shallow marine setting, and Zumaia and Ermua a deep marine environment.

High resolution section sampling enabled the onset of the CIE at all sections to be assessed in more detail than previously reported. Total organic carbon (TOC) $\delta^{13}C$ along this transect illustrate that the CIE associated with the PETM varies in magnitude between ca. 2 and 5‰; however there appears to be no correlation between magnitude and depositional environment. Preliminary results from compound specific carbon isotope analysis of higher molecular weight *n*-alkanes at Claret follow a similar trend to TOC $\delta^{13}C$ data at this site (see Fig.1). However, the results suggest that the bulk $\delta^{13}C$ records a lower magnitude excursion than the *n*-alkane data where excursions of up to 8‰ are being found. This apparent enhancement in the magnitude of CIE is particularly significant when results for average chain length (ACL) are considered, as thus far, no change in ACL has been recorded for the Claret section. This could suggest that there is no appreciable reconfiguration of terrestrial higher plant biota coincident with the PETM at the Claret site, which would indicate that the plant community change is not responsible for overestimation of the CIE in the terrestrial realm.

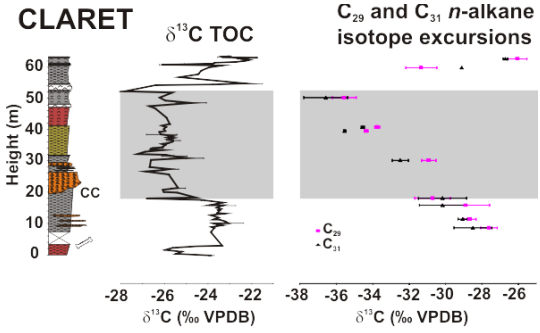

Fig. 1 Bulk and *n*-alkane $\delta^{13}C$ data

References

1. Bowen, G. J. *et al.* 2006. *EOS Trans. AGU*, **87**, (17) 165 - 169.
2. Bains, S. *et al.* 1999. *Science*, **285**, (5428) 724-727.
3. Bowen, G. J. *et al.* 2001. *University of Michigan Papers on Palaeontology*, **33**, 73 - 88.
4. Schmitz, B. and Pujalte, V. 2003. *Geology*. 689-692.
5. Smith, F. A. *et al.* 2007. *Earth and Planetary Science Letters*, **262**, (1-2) 50-65.
6. Schouten, S. *et al.* 2007. *Earth and Planetary Science Letters*, 258, (3-4) 581 – 592.

Manners, H.R., Grimes, S.T., Sutton, P.A., Domingo, L., Pancost, R.D., Leng, M.J., Taylor, K.W.R., Twitchett, R.T., Hart, M.B., Lopez-Martinez, N., Berichte Geol. B.-A., 85 (ISSN 1017-8880) – Climate and Biota of the Early Palaeogene abstract proceedings, p113.

A high resolution compound specific carbon isotope study of the PETM in Northern Spain

Hayley Manners[1], Stephen Grimes[1], Paul Sutton[1], Laura Domingo[2,3], Richard Pancost[4], Melanie Leng[5], Kyle Taylor[4], Richard Twitchett[1], Malcolm Hart[1], Nieves López-Martínez[3]

1. SoGEES, University of Plymouth, Drake Circus, Devon, PL4 8AA, UK
2. Earth & Planetary Sciences Department, University of California Santa Cruz, USA
3. Departamento de Palaeontología, Universidad Complutense de Madrid, Spain
4. Organic Geochemistry Unit, University of Bristol, Bristol, BS8 1TS, UK
5. NERC Isotope Geosciences Laboratory, BGS, Nottingham NG12 5GG, UK

The Palaeocene/Eocene Thermal Maximum (PETM) occurred approximately 55 Ma, lasting for 100 – 200 Kyr, initiating a period of global warming, biotic extinction, migration and turnover, and fundamental changes in the carbon and hydrological cycles[1.] Marine and terrestrial sediments record the event, however discrepancy between the carbon isotope excursion (CIE) measured in the two realms has been observed ($\delta^{13}C$ marine 2.5 - 4‰, $\delta^{13}C$ terrestrial 6 - 8‰)[2,3,4]. Two hypotheses have recently been proposed for this discrepancy – the "marine modification" and the "plant community change" hypothesis[5]. The plant community change hypothesis states that the magnitude of the CIE is greater in the terrestrial realm owing to major changes in floral composition during the PETM from mixed angiosperm (flowering plants)/gymnosperm (conifers) flora, to a purely angiosperm flora [5,6]. To date, the plant community change hypothesis has been tested in North America and the Arctic. Presented here are preliminary results from eight sections in Northern Spain spanning the Palaeocene/Eocene boundary. The sections from East to West are Claret, Tendrui, Esplugafreda, and Berganuy in the terrestrial realm, La Cinglera and Campo, which collectively represent a shallow marine setting, and Zumaia and Ermua, which are deep marine sections.

Total organic carbon (TOC) $\delta^{13}C$ along this transect illustrate that the CIE associated with the PETM varies in magnitude between ca. 2 and 5‰; however there appears to be no direct link between magnitude and depositional environment. Furthermore, due to the high resolution nature of the $\delta^{13}C$ data, the onset of the CIE at all sections can be assessed in more detail than could previously be achieved from the carbonate isotope record. Preliminary results from compound specific carbon isotope analyses of higher molecular weight *n*-alkanes from all 8 sections appear to support the bulk $\delta^{13}C$ data. However, the results suggest that the bulk $\delta^{13}C$ records a lower magnitude excursion than the *n*-alkane data in the northern Spain PETM sections, as excursions of up to 8‰ are being found in the *n*-alkane $\delta^{13}C$ data. This apparent enhancement in the magnitude of CIE is particularly significant when considering the average chain length results, as thus far they record no observable change in those sections analysed. This could suggest that there is no appreciable reconfiguration of terrestrial higher plant biota coincident with the PETM across Northern Spain, indicating that plant community change is not responsible for overestimation of the CIE in the sections analysed.

[1] Bowen, G. J. *et al.* 2006. *EOS Trans. AGU*, **87**, (17) 165 - 169. [2] Bains, S. *et al.* 1999. *Science*, **285**, (5428) 724-727. [3] Bowen, G. J. *et al.* 2001. *University of Michigan Papers on Palaeontology*, **33**, 73 - 88. [4] Schmitz, B. and Pujalte, V. 2003. *Geology*. 689-692. [5] Smith, F. A. *et al.* 2007. *Earth and Planetary Science Letters*, **262**, (1-2) 50-65. [6] Schouten, S. *et al.* 2007. *Earth and Planetary Science Letters*, **258**, (3-4) 581-592.

Manners, H.R., Grimes, S.T., Sutton, P.A., Twitchett, R.T., Hart, M.B., Pancost, R.D., Domingo, L., Lopez-Martinez, N., 2010. Polish Geological Institute (ISBN 978-83-924869-6-1) – 1st students international geological conference, Krakow, 16th – 19th April, Abstract p30.

Understanding the sensitivity of the Earth's climate to CO_2 forcing: comparative organic geochemistry of hyperthermal events

Hayley MANNERS[1], Stephen GRIMES[1], Paul SUTTON[1], Richard TWITCHETT[1], Malcolm HART[1], Richard PANCOST[2], Laura DOMINGO[3], Nieves LÓPEZ-MARTÍNEZ[3]

1. School of Geography, Earth and Environmental Sciences, University of Plymouth, Devon, PL4 8AA; hayley.manners@plymouth.ac.uk
2. Organic Geochemistry Unit, University of Bristol, Bristol, BS8 1TS; r.d.pancost@bristol.ac.uk
3. Catedrática de Palaeontología, Universidad Complutense de Madrid, 28040 MADRID (España); lauradomingo@geo.ucm.es

The Palaeocene/Eocene Thermal Maximum (PETM) occurred approximately 55 Ma ago, lasting for 100 – 200 Kyr, initiating a period of global warming, biotic extinction and migration, and fundamental changes in the carbon and hydrological cycles (Bowen *et al.* 2006). During the PETM it is estimated that 4500 Gt of carbon was released into the environment, causing global temperature rises of up to 9°C (Bowen *et al.* 2006), comparable to that released if the entire fossil fuel resource base was burned (Smith *et al.* 2007), thus understanding this event is of significant topical importance. The most widely accepted theory as to how the event occurred remains the release of methane hydrates, which were subsequently oxidised to carbon dioxide. Marine and terrestrial sediments record the event, however discrepancy between the carbon isotope excursion (CIE) measured in the two realms has been observed ($\delta^{13}C$ marine 2.5 to 4 ‰ difference, as compared to 6 to 8 ‰ difference for terrestrial $\delta^{13}C$). Two hypotheses have recently been proposed for this discrepancy – the "marine modification" and the "plant community change" hypothesis (Smith *et al.* 2007). The plant community change hypothesis states that the true magnitude of the CIE is overestimated in the terrestrial realm owing to major changes in floral composition during the PETM from gymnosperms (conifers) to angiosperms (flowering plants) (Smith *et al.* 2007; Schouten *et al.* 2007). This hypothesis will be tested as angiosperms in the present day are known to be ca. 2.5 – 6 ‰ more depleted in ^{13}C than conifers; if the same discrimination occurred in Palaeocene-Eocene vegetation then the records would be in agreement. To date, the plant community change hypothesis has been tested in North America and the Arctic. I will test the hypothesis across a terrestrial to marine transect in Northern Spain. A series of *n*-alkanes will be extracted and analysed, to measure the average chain length and $\delta^{13}C$, also biomarkers characteristic of the different types of flora during the event will be measured to determine whether a change in the dominant flora occurred.

Bowen G. J., *et al.*, 2006. Eos: Transactions of the American Geophysical Union, vol. 87: 165 – 169. Smith F.A., *et al.*, 2007. EPSL 262, 50-65. Schouten S., *et al.*, 2007. EPSL 258, 581-592

Manners, H.R., Grimes, S.T., Sutton, P.A., Twitchett, R.T., Hart, M.B., Pancost, R.D., Domingo, L., Lopez-Martinez, N., 2010. Carbon System Science Geochemistry Group Research in Progress Meeting, London, March 4th.

Understanding the sensitivity of the Earth's climate to CO_2 forcing: comparative organic geochemistry of hyperthermal events

Hayley Manners*, Stephen Grimes*, Paul Sutton*, Richard Twitchett*, Malcolm Hart*, Richard Pancost**, Laura Domingo***, Nieves López-Martínez***

* School of Geography, Earth and Environmental Sciences, University of Plymouth, Devon, PL4 8AA. ** Organic Geochemistry Unit, University of Bristol, Bristol, BS8 1TS. *** Catedrática de Palaeontología, Universidad Complutense de Madrid, 28040 MADRID (España). hayley.manners@plymouth.ac.uk

The Palaeocene/Eocene Thermal Maximum (PETM) occurred approximately 55 Ma, lasting for 100 – 200 Kyr, initiating a period of global warming, biotic extinction and migration, and fundamental changes in the carbon and hydrological cycles [1]. During the PETM it is estimated that 4500 Gt of carbon was released into the environment, causing global temperature rises of up to 9°C [1], comparable to that released if the entire fossil fuel resource base was burned [2], thus understanding this event is of significant topical importance. The most widely accepted theory as to how the event occurred remains the release of methane hydrates, which were subsequently oxidised to carbon dioxide. Marine and terrestrial sediments record the event, however discrepancy between the carbon isotope excursion (CIE) measured in the two realms has been observed ($\delta^{13}C$ marine 2.5 - 4 ‰, $\delta^{13}C$ terrestrial 6 - 8 ‰). Two hypotheses have recently been proposed for this discrepancy – the "marine modification" and the "plant community change" hypotheses [2]. The plant community change hypothesis states that the true magnitude of the CIE is overestimated in the terrestrial realm owing to major changes in floral composition during the PETM from gymnosperms (conifers) to angiosperms (flowering plants) [2, 3]. This hypothesis will be tested as angiosperms in the present day are known to be ca. 2.5 – 6 ‰ more depleted in ^{13}C than conifers; if the same discrimination occurred in Palaeocene-Eocene vegetation then the records would be in agreement. To date, the plant community change hypothesis has been tested in North America and the Arctic. I will test the hypothesis across a terrestrial to marine transect in Northern Spain. A series of *n*-alkanes will be extracted and analysed to measure the average chain length and $\delta^{13}C$, also biomarkers characteristic of the different types of flora during the event will be measured to determine whether a change in the dominant flora occurred.

G.J. Bowen *et al.*, (2006) Eos: Transactions of the American Geophysical Union 87, 165 - 169. F.A. Smith *et al.*, (2007) EPSL 262, 50-65 S. Schouten *et al.*, (2007) EPSL 258, 581-592.